



저작자표시-비영리-변경금지 2.0 대한민국

이용자는 아래의 조건을 따르는 경우에 한하여 자유롭게

- 이 저작물을 복제, 배포, 전송, 전시, 공연 및 방송할 수 있습니다.

다음과 같은 조건을 따라야 합니다:



저작자표시. 귀하는 원저작자를 표시하여야 합니다.



비영리. 귀하는 이 저작물을 영리 목적으로 이용할 수 없습니다.



변경금지. 귀하는 이 저작물을 개작, 변형 또는 가공할 수 없습니다.

- 귀하는, 이 저작물의 재이용이나 배포의 경우, 이 저작물에 적용된 이용허락조건을 명확하게 나타내어야 합니다.
- 저작권자로부터 별도의 허가를 받으면 이러한 조건들은 적용되지 않습니다.

저작권법에 따른 이용자의 권리는 위의 내용에 의하여 영향을 받지 않습니다.

이것은 [이용허락규약\(Legal Code\)](#)을 이해하기 쉽게 요약한 것입니다.

[Disclaimer](#)

공학박사학위논문

기구 위상 및 치수 통합 합성 기법 개발과 이를 응용한 차량 현가 장치 개념설계

**Development of Unified Topology and Dimension Synthesis
Methodology for Linkage Mechanisms and its Application
to Conceptual Design of Vehicle Suspensions**

2017년 8월

서울대학교 대학원

기계항공공학부

김 서 인

기구 위상 및 치수 통합 합성 기법 개발과 이를 응용한 차량 현가 장치 개념설계

Development of Unified Topology and Dimension Synthesis
Methodology for Linkage Mechanisms and its Application
to Conceptual Design of Vehicle Suspensions

지도교수 김 윤 영

이 논문을 공학박사 학위논문으로 제출함

2017년 5월

서울대학교 대학원

기계항공공학부

김 서 인

김서인의 공학박사 학위논문을 인준함

2017년 6월

위 원 장 : 조 맹 효

부위원장 : 김 윤 영

위 원 : 박 종 우

위 원 : 윤 병 동

위 원 : 박 준 홍

ABSTRACT

Development of Unified Topology and Dimension Synthesis Methodology for Linkage Mechanisms and its Application to Conceptual Design of Automobile Suspensions

Suh In Kim

School of Mechanical and Aerospace Engineering

The Graduate School

Seoul National University

Topology optimization of rigid-link mechanisms, a methodology for obtaining linkages that satisfy a set of user defined kinematic requirements without any a priori baseline design, is a new paradigm that can be usefully employed in industries such as automotive or aerospace engineering. In previous research, however, the methodology has been limited to simple planar linkages.

In this research, a new formulation for synthesizing the topology and dimension of linkages is proposed. To design topology of link mechanisms by using the optimization method, a formulation which represents the DOF (Degree-of-Freedom) in differentiable form has to be considered. Herein, the DOF is the minimum number of actuators that is required to decide the position of the all link components. In

previous research, motion compliance and load stiffness have been employed to avoid deficient-DOF state and redundant-DOF state, respectively. To this end, the motion compliance is the system flexibility under displacement excitation such as motion drive, and the load stiffness is the system rigidity under force excitation such as external resistance forces. However, in aspect of the multi-objective optimization, implementation of the DOF control by using the two functions, the motion compliance and load stiffness, contradictive to each other is quite particular about heuristic weighting factor decision issue. Meanwhile, as the work transmittance efficiency function suggested in this thesis is exploited to control the system DOF, there is no issue related to the preference decision between two objective functions. That is, only a unified objective function is used to avoid the deficient- and the redundant-DOF states. Therefore, it is possible to design complicated systems, unlike the previous research which is hard to consider it due to difficulties of the DOF control.

Our approach is validated through several case studies. In the planar design case, benchmark type four-bar linkages and automotive steering systems are considered. For spatial linkage synthesis problems, automotive suspension mechanisms are designed by the suggested method. To find a better solution in suspension design, we employed a simultaneous topology and shape optimization method. As a result, a new type suspension mechanism is obtained by the unified topology and dimension synthesis method, especially when a smaller design space compared with nominal one is provided. To analyze the behavior of the newly designed suspension system,

the screw-axis theory is applied. From this investigation, it is found that a new special module is included in the new-concept suspension and it works as a conventional link component. In this research, according to this property of the newly proposed concept, it will be called a “hidden link” suspension. It is also shown that the suspension installation space can be reduced compared with nominal multi-link type suspensions by exploiting the hidden link module.

The synthesized suspension mechanism is the first successful industrial result obtained by the unified topology and dimension synthesis method. Especially, the proposed method can provide new insight to engineers who want to enhance the product quality by making use of totally different conceptual designs as shown in this research. In the near future, it will be possible to apply the suggested linkage synthesis method to other practical problems, beyond the automotive industry problems, to find more advanced mechanisms.

**Keywords: Rigid-body mechanism, Topology optimization, Vehicle Suspension,
Hidden link suspension mechanism**

Student Number: 2011-20691

CONTENTS

ABSTRACT	i
CONTENTS.....	iv
LIST OF TABLES	viii
LIST OF FIGURES.....	ix

CHAPTER 1

INTRODUCTION.....	1
1.1 Motivation: review of conventional synthesis methods	3
1.2 Previous researches for unified synthesis of mechanisms.....	10
1.3 Main contributions of this thesis	20

CHAPTER 2

TOPOLOGY OPTIMIZATION METHOD FOR LINKAGE MECHANISMS	25
2.1 Definition of problem.....	27
2.2 Modeling, analysis, and formulation.....	32
2.2.1 Modeling and Analysis.....	32
2.2.2 Objective function	37
2.3 Mechanism synthesis by the proposed formulation	46
2.3.1 Synthesis of Grashof-type four-bar linkage mechanisms.....	46

2.3.2 Synthesis of steering linkage mechanisms	50
2.4 Post-processing	56
2.4.1 Step 1: Binarizing.....	56
2.4.2 Step 2: Pruning.....	56
2.4.3 Step 3: Simplification.....	57
2.5 Summary	62

CHAPTER 3

SPATIAL VEHICLE SUSPENSION DESIGN BY USING SIMULTANEOUS TOPOLOGY AND SHAPE OPTIMIZATION.....85

3.1 Review of recently developed suspension design methods.....	87
3.2 Ground structure model and kinematic analysis	90
3.2.1 Spatial ground structure composed of bars and springs	90
3.2.2 Nonlinear finite element analysis of spatial bar elements	92
3.2.3 Rigid-body motion and constraint of the hub-carrier	97
3.2.4 Governing equations for kinematic analysis	101
3.3 Optimization based formulation for mechanism synthesis	104
3.3.1 Design variables and interpolation	104
3.3.2 Work transmittance efficiency based formulation.....	106
3.3.3 Design sensitivity analysis for design optimization	112
3.4 Suspension mechanism synthesis by the proposed method	114
3.4.1 Recovery of double wishbone and multilink suspensions.....	114

3.4.2 Synthesis of suspensions satisfying R&H requirements	119
3.4.3 Interpretation of the optimized suspension layouts	126
3.5 Summary	132

CHAPTER 4

NEW CONCEPT SUSPENSION INCLUDING HIDDEN LINK MODULE 145

4.1 Overview	145
4.2 A new concept obtained from topology optimization.....	147
4.2.1 A special module included in the new concept.....	147
4.2.2 Strategy for interpretation of the special module	149
4.3 Force transmission analysis.....	152
4.3.1 Introduction of the screw axis theory	153
4.3.2 Force transmission analysis of the RSR-limb	159
4.3.3 Suggestion of hidden link concept	164
4.3.4 Validation of the hidden link concept.....	166
4.4 Nonlinear effects of the hidden link suspension.....	174
4.4.1 Effective length of the hidden link in nonlinear motion.....	176
4.4.2 Prediction of the effective length of the hidden link	181
4.4.3 Design guide line of the hidden link suspension	186
4.5 Summary	192

CHAPTER 5 CONCLUSIONS 211

APPENDIX A

REMEDIES FOR THE MESH DEPENDENCY ISSUE	216
A.1 Overview	216
A.2 Coarse-to-fine mesh converting approach.....	218
A.3 Simultaneous topology and shape optimization approach	222

APPENDIX B

WRENCH SCREW ANALYSIS	231
B.1 Overview	231
B.2 Wrench screw of arm component.....	232
B.3 Wrench screw of RSR limb module	237

APPENDIX C

VIRTUAL PRODUCT DEVELOPMENT FOR VALIDATION OF HIDDEN LINK CONCEPT	242
C.1 Overview	242
C.2 Virtual Product development process	243

REFERENCES.....	248
ABSTRACT (KOREAN).....	259
ACKNOWLEDGEMENTS.....	262

LIST OF TABLES

Table 2.1 Parameters used at post-processing and comparison of the results.....	64
Table 3.1 Optimized values of the design parameters for Cases 3 and 4 (All satisfy the R&H constraints specified by (3.41) and (3.42)).	134

LIST OF FIGURES

CHAPTER 2

Figure 2.1 Design domain and problem description for synthesizing (a) the Grashof-type linkage systems generating desired paths and (b) an automobile steering mechanisms satisfying Ackermann condition.	65
Figure 2.2 The proposed ground structure based rigid-body mechanism synthesis model comprised of nonlinear bar elements and zero-length springs.	66
Figure 2.3 Representation of (a) various rigid-body configurations and (b) link connections to the ground by using the employed bar-spring model.	67
Figure 2.4 Possible occurrence of circuit defects depending on the employed numerical solvers. (a) Stable linkage configuration at input crank angle (θ_{in}) equal to 225° (b) Converged linkage configuration by the Newton-Raphson algorithm at $\theta_{in} = 236.25^\circ$ (c) Converged linkage configuration by the Levenberg-Marquardt algorithm at $\theta_{in} = 236.25^\circ$	68
Figure 2.5 Illustration of linkage systems having different degrees of freedom (a) DOF = 2, (b) DOF = 0, and (c) DOF = 1.	69
Figure 2.6 Three Grashof-type four-bar linkage mechanisms to be recovered by the proposed optimization formulation (a) Case 1, (b) Case 2, and (c) Case 3 (Q: end-effector position).	70
Figure 2.7 Iteration history and intermediate layouts for Case 1.	71

Figure 2.8 Iteration history and intermediate layouts for Case 2.	72
Figure 2.9 Iteration history and intermediate layouts for Case 3.	73
Figure 2.10 Layouts before and after the application of the proposed three-step post-processing algorithm (In the directly-converged results, the gray levels in the links correspond to the design variable values. In the post-processed results, only the thick lines represent the results).	74
Figure 2.11 The effects of ε in equation (2.15) on the solution convergence. A path involving a crunode is illustrated as an example.	75
Figure 2.12 Schematic illustration of the Ackermann condition (Four tires and wheel axles are indicated in the figure).	76
Figure 2.13 (a) Design domain for steering system synthesis (b) Two bar-spring ground models with 6 by 3 and 7 by 3 discretizations.	77
Figure 2.14 Intermediate and the final layouts for the synthesis of steering systems satisfying the Ackermann condition. (n_i : iteration number)	78
Figure 2.15 Iteration histories for the steering system synthesis problem.	79
Figure 2.16 Comparison of (a) a typical four-bar linkage (for an automobile steering system) and (b) the optimized linkages by the proposed method. (c) The 9-bar linkage in (b) divided into two 6-bar linkages for the interpretation of the result. .	80
Figure 2.17 Comparison of the optimized and reference linkage mechanisms.	81
Figure 2.18 Kinematically equivalent systems. (a) configuration after Step 2 and (b) configuration after Step 3.	82
Figure 2.19 The processes of simplification algorithm consisting of (a) grouping, (b)	

joint identification, and (c) reconfiguration applied to the mechanism shown in Figure 2.19 (a).....83

Figure 2.20 The application of the three processes of Step 3 post-processing to (a) the layout obtained by post-processing Step 2 for Case 3, (b) grouping, (c) joint identification, and (d) reconfiguration.84

CHAPTER 3

Figure 3.1 (a) Ground structure model composed of spatial bar elements and spring elements (spring elements are not shown). (b) Double wishbone suspension constructed from the ground structure. (c) Zoomed in view of the ground structure model with artificial zero-length springs. (d) Representation of a link and an arm by using the bar-spring ground structure model.....135

Figure 3.2 Undeformed (X,Y,Z) and deformed (x,y,z) configurations of a spatial bar element with two end-nodes.136

Figure 3.3 (a) Five-link suspension modeled by ADAMS (left) and by the present bar-spring ground structure model (right). (b) (left) Trajectories of (q_X, q_Y) and (right) those of $(\theta_1, \theta_2, \theta_3)$ or the 5-link suspension shown (a) when its Z-direction motion (q_Z) of the wheel center is prescribed as Eq. (3.37).137

Figure 3.4 The planar mechanism behavior with a bar element of an intermediate design variable $\xi = \xi_{\text{int}}$, (say $\xi_{\text{int}} = 0.5$). — : $\xi = \xi_{\text{max}} = 1.0$, --- : $\xi = \xi_{\text{int}}$. (a) Mechanism in a quasi-redundant DOF state and (b) mechanism in a quasi-deficient

DOF state.138

Figure 3.5 The iteration histories of (a) the mean transmittance efficiency ($\bar{\eta}$) and

(b) the path error measures for Design Case 1. ($\psi_{t^*}^{(1)} = |q_X(t^*) - \hat{q}_X(t^*)|$,

$\psi_{t^*}^{(2)} = |q_Y(t^*) - \hat{q}_Y(t^*)|$, $\psi_{t^*}^{(3)} = |\theta_1(t^*) - \hat{\theta}_1(t^*)|$, $\psi_{t^*}^{(4)} = |\theta_2(t^*) - \hat{\theta}_2(t^*)|$

$\psi_{t^*}^{(5)} = |\theta_3(t^*) - \hat{\theta}_3(t^*)|$).....139

Figure 3.6 Intermediate and final suspension layouts with their configurations for different wheel-center stroke values (\hat{q}_Z) for Design Case 1 to synthesize a double wishbone suspension mechanism (n_i : iteration number).140

Figure 3.7 Intermediate and final suspension layouts with their configurations for different wheel-center stroke values (\hat{q}_Z) for Design Case 2 to synthesize a 5-link suspension mechanism (n_i : iteration number).141

Figure 3.8 Evolutions of the suspension mechanism layouts by the proposed synthesis method for Design Cases 3 and 4 (n_i : iteration number). The last two rows show the post-processed synthesized mechanism configurations at $\hat{q}_Z = 0$ mm and $\hat{q}_Z = 100$ mm142

Figure 3.9 The iteration histories for Design Case 3. (a) The work transmittance efficiency and (b) some design parameters.143

Figure 3.10 Illustration of the synthesized suspensions (a) for Design Case 3 and (b) Design Case 4. The two-dimensional schematic representation of the optimized suspensions can facilitate the kinematic chain analyses.144

CHAPTER 4

Figure 4.1 Topology optimization result for Design Case L and Design Case S. 194

Figure 4.2 Schematic illustration of the topology optimization results (a) Result obtained from the Design Case L and (b) Result obtained from the Design Case S.

..... 195

Figure 4.3 Two grouping strategies for investigating role of the new component. (a) Two groups composed of three links and remained one, respectively. (b) Two groups composed of two links, respectively. Each group can be considered as an arm component with revolute and ball joint. 196

Figure 4.4 An example motion for explaining the screw axis theory. (a) Two configurations before and after movement. (b) Decoupled motions corresponding to translation and rotation about an axis. (c) Another motion view in perpendicular to the rotational axis. 197

Figure 4.5 Twist and wrench screw description for RS (arm) component. (a) Twist screws of each joint and (b) Wrench screws corresponding to reciprocal screws of the twist screws. 198

Figure 4.6 Twist and wrench screw description for RSR-limb. (a) Twist screws of each joint and (b) Wrench screws corresponding to reciprocal screws of the twist screws. 199

Figure 4.7 Load path of the supporting force imposed on the knuckle through the RSR-limb and equivalent force. (a) Description of the load flow from the frame (car-body) to the knuckle (wheel). (b) A constraint force equivalent to the forces applied

on the knuckle in (a).....	200
Figure 4.8 A new suspension proposed with a RSR-limb and its instantaneously equivalent system. (a) Newly suggested vehicle suspension including the RSR-limb and (b) Instantaneously equivalent system of the newly designed suspension in (a).	201
Figure 4.9 Comparison of the compliance behavior of the two suspensions in Figure 4.8(a) and (b). Amount of the response is depicted through bar plot.	202
Figure 4.10 Configuration of the suspension (left) and constraint forces imposed on the knuckle (right) through the hidden link module and the real link for vertical stroke motions from -100 mm to 100 mm. (a) Hidden link suspension and multi-link suspension with the link length of (b) 200 mm, (c) 400 mm, and (d) 600 mm. (M: mount point of the real link in multi-link suspensions).....	203
Figure 4.11 Comparison of the kinematic motion of the knuckle in vertical stroke. Circular marker corresponds to the motion of the new concept suspension in Figure 4.8(a), and other curves are that of the suspension in Figure 4.8(b). Length of the link corresponding to the hidden link is 200 mm, 400 mm, 600 mm, and 800 mm, respectively.....	204
Figure 4.12 Variation of the RMS error value, defined in Eq. (4.19), according to the variation of the length of the link employed instead of the hidden link as shown in Figure 4.8(b).....	205
Figure 4.13 (a) Arc trajectory of the ball joint of the RSR-limb and (b) Radius of the circle which includes the arc trajectory of the ball joint. (c) Configuration of a cone	

which takes the circular path as the base plane, where the vertex of the cone is located at the intersection point of the extended line of the hidden link and the rotation axis of the frame-attached arm in RSR-limb.206

Figure 4.14 (a) A hidden link suspension corresponding to the initial configuration of the parameter study. (b) The equivalent multi-link suspension of (a) obtained by the proposed effective length calculation method. (c) A hidden link suspension with hard points 10 mm moved in $-Y$ direction by the parameter study. (d) The equivalent multi-link suspension of (c).207

Figure 4.15 Three dimensional view of the error plot and (b) 2D plane view of the error plot. Minimum error set is the line connecting the minimum error points. Ideal line is a set of points representing $X=Y$ (identity) in the 2D plane view.208

Figure 4.16 Design case study considering layout problem, where a zone depicted by the red dotted box is not allowed to mount any hard points. (a) A multi-link suspension and (b) A hidden link suspension.209

Figure 4.17 Comparison of the kinematic motion of the multi-link suspension in Figure 4.15(a) and hidden link suspension in Figure 4.15(b). In motion curves, hidden link (Initial Design) is the analysis result of the suspension in Figure 4.15(b), and hidden link (Optimized Design) corresponds to the result after adjusting the hard point locations by the chassis geometry optimization.210

APPENDIX A

Figure A.1 Ground structure and design results for the various mesh grids. (a) 7 by 3 mesh grid, (b) 9 by 3 mesh grid, (c) 13 by 3 mesh grid, and (d) 7 by 5 mesh grid, and (e) 13 by 5 mesh grid.....224

Figure A.2 Result of the coarse-to-fine mesh grid approach in 13 by 5 mesh grid, where the initial guess based on the converged result of 7 by 3 grid mesh shown in Figure A.1(a) is applied. For each case, (a) $\Delta\xi_{\text{init}} = 0.3$, (b) $\Delta\xi_{\text{init}} = 0.15$, and (c) $\Delta\xi_{\text{init}} = 0.10$ is allocated as the initial guess controlling parameter.....225

Figure A.3 Result of the coarse-to-fine mesh grid approach in 12 by 5 mesh grid, where the initial guess based on the converged result of 6 by 3 grid mesh (i.e. 9-bar linkage shown in Figure 2.14) is applied. For each case, (a) $\Delta\xi_{\text{init}} = 0.3$ and (b) $\Delta\xi_{\text{init}} = 0.15$ is allocated as the initial guess controlling parameter.....226

Figure A.4 Comparison of the post-processed result shown in Figure A.3.227

Figure A.5 Reference linkage mechanism configuration and output path trajectory.228

Figure A.6 Ground structure employed for the optimization and post-processed result obtained from the optimization. (a) 5 by 5 mesh grid result for pure topology optimization and (b) 3 by 3 mesh grid result with simultaneous topology and shape optimization.....229

Figure A.7 Iteration history for comparing pure topology optimization (5 by 5 mesh grid) and simultaneous topology and shape optimization (3 by 3 mesh grid).....230

APPENDIX C

Figure C.1 Half car model of the hidden link suspension mechanism developed by the commercial software ADAMS/Car. (a) Suspension model with rig module, (b) without rig module.244

Figure C.2 Full vehicle model of the hidden link suspension mechanism developed by the commercial software ADAMS/Car. (a) Chassis and car body, (b) with only chassis components.245

Figure C.3 (a) Developed 1/4-sized hidden link suspension CAD model and (b) its vertical stroke motion.....246

Figure C.4 (a) Prototype manufactured by the SLA type 3D printer (b) its vertical stroke motion.....247

CHAPTER 1

INTRODUCTION

The mechanism is a system that converts a given input motion into a desired output motion, while the structure constitutes and supports the mechanism. A system in which an energy source is combined with a mechanism-structure system is called a machine [1], in which the mechanism transmits energy from the input actuator to the output point in the desired form, such as rotary motion. The mechanical system called mechanisms have variety of configurations. For example, linkage, pinion-gear, cam-follower, and fluid machinery like as a torque converter. The majority are based on rigid bodies, and among them the linkage has many applications.

The linkage mechanisms are traditionally applied to industrial fields where repetitive work is required, and they are also employed in harsh work environments where high reliability is required. In particular, when using the linkage mechanisms, compared with robotic systems, engineers can have advantages of simple configuration with less actuators/controllers, light weight, cheap cost, etc. That is

why the linkage is still used in many industrial fields. Representative applications of the linkage mechanisms are vehicle suspensions, morphing mechanisms of the airfoils, landing gears of the aircraft, and front attachments of the construction equipment. However, in spite of the various and important industrial application examples, there is no systematic and creative design methods for the mechanisms. To this end, “experience-based design method” or “trial-and-error based conventional design methods” are still employed for the mechanism synthesis.

In this research, a mechanism design method is developed to avoid the repetitive design iterations. The suggested method based on recently proposed topology optimization methods will be developed and verified for the planar linkage mechanisms in first. And then, it will be extended to three-dimensional problems for applying it to vehicle suspension design problems. Also, by employing this new design paradigm, a new-concept suspension entirely different with conventional ones is derived.

The proposed method is expected to be applied into various industrial fields in the near future, as it is a systematic and creative method for constructing linkage systems unlike the tedious and time-consuming conventional design methods. Before introducing a new mechanism synthesis method, the traditional mechanism design techniques which have been applied for a long time in industrial applications will be reviewed. After that, the recently proposed topology optimization techniques for the mechanisms will also be introduced briefly.

1.1 Motivation: review of conventional synthesis methods

Mechanism synthesis methods are divided into a topology synthesis corresponding to concept design and a dimension synthesis corresponding to detailed design. In the topology synthesis (or called number synthesis in classical literature), designers enumerate all possible kinematic chains constructed by number of links and joints. After finding the kinematic chains, ground link is selected by deciding ground pivot joints. Otherwise, in the dimension synthesis, it is assumed that kinematic chain and ground link fixed to the base is provided. The goal of the dimension synthesis is finding the proper geometry of the components for achieving desired performances.

In general, above two processes are implemented sequentially, but they should be repeated if the design result does not satisfy the given design conditions. Therefore, time-cost problems arise from trials and errors, and it is almost impossible to consider all design candidates through this iterative procedure. As a result, the trial and error process is limited to only few candidates, resulting in a very local sub-optimal solution. This research is presented to resolve this problem. Before looking at the proposed solution, it is worth reviewing the conventional design methods to explain how the proposed method differs from them.

Literature review of the number synthesis methods

First, the topology of the kinematic chain that constitutes the mechanism is determined through the number synthesis, usually by enumeration. To this end, for example, there was an attempt to derive a mechanism having one degree-of-freedom

from the kinematic structures consisting of 10 links, and the result shows 230 unique structures [2]. For such an enumeration a kinematic structure representation technique, called Franke's notation, was employed. Generally, enumeration method based on it is defined as the graphical technique among the number synthesis methods. The background of the concept is well described in the review paper [3]. On the other hand, as computer-based methods have emerged, more efficient enumeration has become possible, and numerical methods based on theory of graphs are developed. Generally, in the number synthesis including the computer-based enumeration, it is necessary to derive independent kinematic chains by separating isomorphism. In order to solve this problem, a research was carried out to distinguish isomorphism by utilizing the inherent invariance of the link-to-link matrix [4]. Meanwhile, a way to construct and compare by using the code-representation of the kinematic chain to check the isomorphism was also developed. To this end, the canonical form of the upper triangular matrix was constructed through permutation, and isomorphism was analyzed by vectorizing the corresponding components into the form of 1-D code [5]. Besides the number synthesis methods for the linkages, there is another method called building block approach, which is used to build topologies considering various components such as gear and cam [6, 7]. The building block approach is sometimes categorized into type synthesis, not into the number synthesis, but they can also be employed to the initial concept design to determine topology of the mechanisms.

Literature review of the dimension synthesis methods

Dimension synthesis is a process of determining the joint position/direction of a kinematic chain after finishing the number synthesis. The method can be divided into two categories, one involving the concept of a precision point, and the other not including it, where the precision point refers to output points specified by the designer so that the end-effector passes them precisely. Typically, there is a limit to the number of precision points that can be specified since it must pass the point mathematically without errors. For four-bar linkages, a solution with four precision points is infinite, but the number of solutions with five precision points is finite. To put it in more detail, according to Burmester's theorem, there are a myriad of dyads passing through four specified precision points. Here, the dyad corresponds to a part constituting half of a four-bar linkage (a four-bar linkage can be constructed by connecting the two dyads at one point). Thus, if any two of the myriad dyad candidates passing through four precision points are selected, a four-bar link with designated four precision points can be synthesized. Also, a four-bar linkage mechanism passing through the five precision points can be obtained through the four precision point linkage design procedures. First, generate two four-point sets which are extracted from the five precision points. Then, find candidate dyads for each set. If the candidate solutions of each set have the common solution dyads, it will be possible to synthesis a four-bar linkage passing through the five precision points. Theoretically, there can be zero, two, or four common dyads. If there are two common ones, it is possible to combine one four-bar linkage having the five

precision points. On the other hand, if there is no common dyads, constructing a four-bar linkage having the given five precision points is impossible by the Burmester's theorem. For more detailed classical theories related to Burmester's theorem, see [8].

For the four-bar linkages, one can also deal with the precision points without employing the Burmester's theorem. For the general program based on the Newton-solver, there is a "Displacement Matrix" method introduced in [9]. From the Displacement Matrix method, a four-bar linkage that passes through five precision points can be synthesized just as employing the Burmester's theorem. The number of the precision points of the four-bar linkage is limited to five in the Burmester's theorem, however the number of geometry design parameters are larger than five in four-bar linkages. Then, how many precision points can be handled with the general programming methods? It has been found that the computational methods can handle the precision points up to nine points for the four-bar linkages [10]. In this case, 1442 candidates exist for the given nine precision point equations, and the candidate solutions, corresponding to the configuration of the linkages, can be obtained by using a continuation method type solver. After solving the equations, each obtained candidate solutions should be checked if they are possible to be constructed in the physical world. If it is possible to realize the solution, one can have the four-bar linkages passing through the nine precision points. However, it is not always possible to derive the answer through the given nine points due to branch defects and order defects.

Meanwhile, if the characteristics of curves is exploited properly, it may possible

to derive a four-bar linkage that passes more than nine points. In [11], more than 10 points were dealt with, however the design could not pass the points correctly. That is, the points are no longer the precision points. There are other methods which do not consider the precision points. Optimization methodologies for dealing with multiple (approximately exact) points are representative methods which do not consider the precision points. Among the optimization techniques, SPS (Selective Precision Synthesis) method adopted the concept of accuracy neighborhoods in which different design relaxation conditions are given for each point [12]. In SPS method, “Search technique” was applied for optimization, and it was confirmed that a suitable solution could be derived without sensitivity information. Other various dimension synthesis (or design optimization) methodologies are well described in [1].

Limitations of the conventional methods

In traditional design techniques, the conceptual design (number synthesis) and the detailed design (dimension synthesis) steps are fully separated, and most of the dimension syntheses are limited to the four-bar linkages. If the four-bar linkage does not satisfy the desired condition, the dimension synthesis must be repeated for the other linkages such as six-bar linkages. If the alternative still does not satisfy the given design condition, designers has to do it repeatedly until they get a proper solution. This trial-and-error procedure is tedious and time-consuming works, and the designers nearly impossible to get a creative solution until they tried dimension

synthesis for the whole candidates obtained from the number synthesis. Under this background, researches have been presented that integrate the number and dimension synthesis.

Remedy for the conventional methods

For integrating number and dimension syntheses, a methodology which can numerically deal with the number synthesis is required. A proposed methodology is the number synthesis method using the concept of Link-to-link Adjacency Matrix (LAM). If the number of links is given, the linking relation between the links can be expressed by the LAM. In [13], system characteristics were anticipated from the LAM matrix, and then a proper kinematic chain was obtained through the optimization of the LAM-matrix based performance evaluations. After success of the parameterization of the kinematic chain for the integrated optimization, the method was expanded to include the geometrical information. Various coupler curves were derived at a certain error level by performing LAM based connection design and dimensional optimization with GA [14]. It is the first advanced study that enables automatic synthesis, which shows possibilities of designing the mechanism without any baseline design and intuition. However, the concept design process takes considerable time, and the type of mechanism is limited only to the planar six-bar linkages using the revolute joints. Of course, it is an algorithm have high potential, but it is not realistic in aspects of the computational cost. So, engineers need an efficient automatic synthesis method which can cover a number of design cases, and

the topology optimization was one of the alternatives for this problem. In this viewpoint, the following chapter will briefly introduce the history of the topology optimization researches for the automatic synthesis of linkage mechanisms.

1.2 Previous researches for unified synthesis of mechanisms

Topology optimization has been developed based on structural design [15] and extended to the design of multi-physics systems including compliant mechanism design [16] and rigid body mechanism design [17]. In particular, the effectiveness of the methodology has been well proved and firmly established as a reliable design tool in structure design field. However, in the field of rigid-body mechanisms, the topology optimization technique is applied to only some textbook design problems, and the topology optimization methodology is not applied to practical mechanism design problems. That is, it is in very low-level compared with the successful structural topology optimization, which has been applied to industrial problems for aircrafts [18], vehicles [19], and architectures [20, 21]. Then, what is the main difference between the structural design and the rigid-body mechanisms? In structure problems, the topology optimization has been rapidly developed and applied to the industry because there were three underlying techniques; minimization of compliance formulation, material penalization interpolation scheme, and filter developments for mesh independency [22]. References and recent trends are well documented in textbook [23] and review papers [24, 25]. Meanwhile, there are still some key issues which has to be solved in the topology optimization of the rigid-body mechanism. **In this chapter, the key issues will be briefly introduced, and researches which have been conducted to solve the problem will be discussed.**

Issues in topology optimization of rigid-body mechanisms

First, since **formulation of the design problem**, one of the most important parts in design optimization, has not been clearly established in the field of topology optimization of rigid-body mechanisms, the design technique could not be applied to complicated and practical problems. In recent years, however, a formulation based on energy was suggested [26], and it has been employed as the standard one for the rigid-body mechanisms. For example, the formulation has been applied to the advanced design problems for ground vehicles [27, 28] and aero-vehicles [29]. In this thesis, principle of the energy-based formulation and its utility will be dealt with. Then, how to solve various design problems through the formulation will also be discussed. Details are introduced in the next sub-chapter for overview and the main chapter of this thesis.

Second, **modeling issue** is remained in the topology optimization of rigid-body mechanisms. Mechanisms can be divided into planar, spherical, and spatial mechanisms. In planar mechanisms, revolute joints, translational joints, and various composite joints consisting of revolute and translational joints are employed. When the problem is extended in three dimensions, more types of joints should be considered; for example, ball joints, S-S joints, and universal joints. However, the majority of existing studies are limited to the planar mechanism design problems, among which revolute joint is the only joint type applied to. In this thesis, as the process of extending the methodology into three dimensional problems, ball joints, revolute joints, and S-S joints are employed. Although all types of joints are not

covered in research, it is able to handle a variety of design candidates in vehicle suspension design problems, including double wishbone and multilink type suspensions. In this review, the modeling issues for the topology optimization of linkage mechanisms will be briefly introduced. And the three-dimensional model for the vehicle suspension mechanisms will be dealt with in the main chapter.

In addition to the above-mentioned two core issues, there are a number of remained challenges for the automatic linkage synthesis. In particular, the problem of global optimum convergence and numerical issues related to stability are the representative issues. The studies including these issues will be summarized in the following paragraphs in historical order.

Research in early stage

The first attempt to optimize the rigid-body mechanisms by using the topology optimization was implemented by Felter [30]. He developed modeling and the formulation for 0-1 design for the first time, but the research was in the basic level. Then, Kawamoto and his colleagues proposed a planar mechanism synthesis model based on nonlinear FEM method, and also proposed formulation for DOF (Degree-of-Freedom) constraint and global optimum. The contents is well-defined in Kawamoto's doctoral dissertation [31]. In the first research proposed by Kawamoto and his colleagues, an enumeration technique rather than optimization was employed [32]. They applied FEM truss based model to form a "ground structure", which is containing a number of linkage mechanism candidates. They considered several

design criteria such as symmetric configuration, then find the all possible solutions satisfying the given design conditions by the enumeration. After considering the candidate solutions, they could find the best solution, a converter mechanism, appropriate to the provided objective function. This study can be regarded as a cornerstone of the modeling technique for the topology optimization. They have shown, through subsequent study, that it is possible to synthesize linkage mechanisms by using the gradient-based optimization for the same ground structure model [17]. In this process, a new formulation for controlling DOF (Degree of Freedom) was suggested in addition to the modeling, which is a completely new part different from the topology optimization of structures or other physics systems. As will be discussed in the main section (Chapter 2), the degree of freedom corresponds to a discretized integer value, which has to be considered for the mechanism design problems. For this reason, it is necessary to convert to a DOF expression in differentiable form when applying the gradient-based optimization. In [17], Kawamoto et al. proposed a formulation for the DOF control in order to optimize based on design sensitivity information. Their research was quite successful and proved the possibilities of applying the proposed method in the synthesis of one-dimensional motion mechanisms, such as a converter/inverter. However, a highly-nonlinear function was introduced in procedure of DOF expression to continuous differentiable form, which makes the design more difficult with the nonlinearity inherent in the large-motion of mechanism systems. In particular, the high-nonlinearity induces local convergence problems, accordingly it is difficult to obtain

an appropriate solution in a gradient-based approach. To resolve this problem, Stolpe and Kawamoto introduced a branch-and-bound method, one of the global optimization techniques [33]. The design space was divided, relaxed, and approximately evaluated according to the relaxation. Then, the design was performed by searching or discarding the divided spaces. By iteratively doing these procedures, a suitable global solution could be obtained. To this end, this research has a very important meaning because the proposed method reliably assures the most proper answer, however it has a limitation in that it causes a problem of dramatically increasing the time cost. In particular, since the formulation of SAND (Simultaneous Analysis and Design) method is applied instead of NAND (Nested Analysis and Design), the design cost increases greatly when the number of state variables increases. Therefore, it is difficult to apply it to general problems, such as multiple time step problems, because the number of state variables is proportionally increased according to the increase of the time steps. This method has not been applied in the subsequent studies of other researchers. Instead, the other studies have been carried out in order to develop other DOF representation techniques to reduce the nonlinearity issues. In addition to the one-dimensional motion transformation problem such as the converter, Kawamoto also investigated problems with general paths [34]. He applied the above-mentioned continuous DOF expression with gradient-based optimization method, and proved the possibility of unified synthesis of the mechanisms through various planar mechanism design examples. These studies are the earliest attempt of topology optimization for the general rigid-body

mechanism designs, especially for linkage mechanisms. Subsequent studies have been conducted following the Kawamoto and his colleagues, for improvement of modeling, development of the new formulation, and application of various optimization algorithms. Also, applicability in industrial problems has been examined. These researches in the second generation was implemented for a decade.

Second generation research

There is a study of automatic mechanism synthesis based on SBM (Spring-connected Block Model) performed by Kim et al. [35]. Unlike the FE truss-based model, the SBM adopts a multi-body model consisting of rigid bodies and springs. As will be seen later, the SBM is not a simple alternative for mechanism syntheses, but a potentially extendable model for multiple joint types. The SBM controls the stiffness of springs connecting two blocks to design existence of rigid-joints between the blocks. If there are enough stiffness representing rigid-connection or revolute joints, it could be interpreted as the joints of linkage mechanisms.

Otherwise, Ohsaki and Nishiwaki introduced the same nonlinear FEM model [36] as applied in Kawamoto's researches, where the most difference thing between two researches is employed function for the DOF constraint of the mechanisms. The method in [36] is very similar to that applied in topology optimization for compliant mechanism designs [16]. First, the phenomenon that occurs when the DOF is in deficient-state could be expressed by one physical quantity value, and the other phenomenon that appears when the DOF is in redundant-state could be expressed by

another physical quantity value. Then, In order to prevent each situation from appearing, the physical quantities corresponding to each phenomenon should be controlled during the optimization. In [36], by employing this method, it was possible to derive a mechanism with a suitable one degree of freedom, which corresponds to not deficient- or redundant-DOF state in the design case with one actuator case. But, as mentioned in early stage research of Kawamoto in [17], deciding upper bound of constraint related to the designated physical quantity, mean compliance in [17], is very complicated.

Nam et al. also applied the similar method for controlling the DOF with GSBM (Generalized Spring-connected Block Model) [37]. They used slightly different physical quantities for controlling the DOF condition, and applied both physical quantities to multi-objective optimization formulation. To this end, a weighted sum formulation was employed. High-nonlinearity problems mentioned in previous researches of Kawamoto was quite relaxed by applying the physical quantity-based DOF control method, so that various design problems could be dealt with. However, there still remains a problem of user intervention in adjusting the preferences, such as the weighting factors or the upper bound of the constraints, in order to control the respective physical quantity. It is a major obstacle for the methodology which has to be resolved to consider complex and real industrial problems, such as automotive steering and suspension problems.

State-of-the-art covered in recent research

The work transmittance efficiency function to be covered in this paper corresponds to a unified function that integrates two state representation functions employed for the DOF control in previous researches. This method has been proposed by Kim and Kim, and its potential was proved in the planar linkage design problems [26]. They employed the nonlinear FE-based ground structure model used in Kawamoto's study, and solved various four-bar linkage problems by applying the work transmittance efficiency function to the DOF control. Also, they dealt with the design of the steering systems of the vehicle, which was the first study to go beyond simple design examples. There was one difference in the modeling compared with the Kawamoto's work. They designed a ground fixed point by introducing a zero-length artificial spring which is the same with applied one in SBM. In other words, the boundary condition of the problem was parameterized and designed automatically. For more information, see Chapter 2.

The DOF control based on the work transmittance efficiency function was also applied to the SBM. Kang et al. introduced DSBM (Double Spring-connected Block Model) that modified SBM for various joint types, and succeeded in deriving proper linkage mechanisms by applying the work transmittance efficiency function for the DOF control [38]. The DSBM was proposed to improve the limitations of conventional FE-based ground structures or SBMs that can deal with revolute joint only. In addition to the revolute joints, the DSBM can handle translation joint and various composite joints. To this end, the composite joints include various joints such

as a double integrated cross slider joint and a double separated cross slider joint, as well as a rotation-and-translation joint. They set a unit module corresponding to the “pin-in-slot” as the basis of the model, and by combining the presence or absence of these units, it was possible to design not only existence of joints but also the types of joints.

From the FE-based model research and the modified SBM model research, the work transmittance efficiency function has been proved as a generalized method that can be applied any model. Unlike the existing DOF control methodology, it was shown that the newly suggested DOF control method is very intuitive and powerful to be applied for the complex problems such as vehicle steering design problems. As a result, the methodology could be extended to three-dimensional real problems, such as vehicle suspension design problems which requires a number of complex design criteria [27, 28]. For more information, see Chapter 3. Particularly, one of the suspensions derived from this process has been found to have the advantage of space saving, which will be discussed in Chapter 4.

Another work to apply the work transfer efficiency function is to combine the GSBM and the Fourier transformation-based path description method [39], where Han et al. applied “Discretized Fourier Transformation” to express the path drawn by the output point of the mechanisms, and they could define the characteristics of the curve by using it. When extracting and designing the characteristics of a curve, through the Fourier analysis, it has an advantage that non-prescribed timing problems can be handled. To this end, the non-prescribed timing problem means that

there is no pre-defined timing between the input position and output position. The output point is just required to pass through the point regardless of the input link position, so that designers can synthesize linkage mechanisms when they only know shape of the desired path.

Through the afore-mentioned studies, it has been confirmed that the work transmittance efficiency function is a reliable DOF description method that can be universally applied to various models and problems. Also, it has been considered that the modification of the SBM is one of the next generation research issues for the mechanism design with various joint types.

Alternatives for automatic synthesis of mechanisms

Ohsaki and his colleagues have proposed mechanism design techniques based on similarity of buckling phenomenon and mechanism motion [40]. Also, there are other researches which shows that it is possible to design mechanisms based on evolution [41] and big database [42], respectively. Among them, Coros et al. designed linkage mechanisms through the big database, for providing motion to animation characters [42]. In the future, it is expected that various technologies besides conventional machinery design can be applied to the mechanism designs.

1.3 Main contributions of this thesis

In this thesis, below three themes are implemented for the first time.

Theme 1: A unified synthesis algorithm for a simultaneous number and dimension synthesis of link mechanisms is developed and verified. Especially, the work transmittance efficiency function which merges “motion compliance” and “load stiffness” concepts of previous research is suggested as the DOF constraint representation function. Therefore, heuristics for deciding scaling factors between two contradictive functions, compliance and stiffness, no longer concerns the users.

Theme 2: Developed design method is applied to industrial problems including automotive steering system and three-dimensional vehicle suspension. Application of the topology optimization technique for the steering and suspension systems is the first attempt which has never been reported in previous research.

Theme 3: A new concept suspension is found by using the proposed link mechanism synthesis method. The meaning of the obtained result is investigated through the screw axis theory, by which hidden link effect included in the result is discovered. By using module which has the hidden link effect, suspension install space can be reduced dramatically.

The above-mentioned themes will be introduced in main Chapters.

• Development of the methodology for unified synthesis of the linkages

In Chapter 2, development of an automatic mechanism synthesis algorithm will be introduced in detail. Especially, a methodology for controlling the degree of freedom which is one of the biggest issues in mechanism synthesis algorithm will be discussed. The degree of freedom, minimum number of actuators required to determine the position of the mechanism components, is the value of which is expressed as a discrete integer value. However, the discretized value is very disadvantageous in optimization, and is particularly difficult to handle as an objective function when applying sensitivity-based optimization algorithms. In general, topology optimization is a problem of dealing with many variables, so that the sensitivity information is used to efficiently finding a solution in a multivariable large-scale space. Therefore, dealing with the integer type quantity, i.e. the degree of freedom, could be the biggest problem in gradient-based topology optimization. Previous studies mentioned in Chapter 1.2 have proposed various methods to solve this problem. In this paper, this problem is resolved by a method based on **work transmittance efficiency function**, unlike previous studies. The work transmittance efficiency function is **a powerful method which expresses the degree of freedom with only a unified function without any heuristic scaling factors**. In Chapter 2, the concept of the work efficiency function will be introduced, by which synthesis process of various planar linkage mechanisms will also be considered. After that, implications of the efficiency function will be investigated by focusing on convergence history of the developed algorithm.

• Applying the developed method into 3D vehicle suspension design problems

In Chapter 3, the automatic mechanism synthesis method based on the work transmittance efficiency function proposed in Chapter 2 will be extended into a practical problem in three dimensions, which is the vehicle suspension design problem. To extend the topology optimization into spatial mechanism design problems, a model including ball joints, revolute joints, and links is introduced. In order to confirm whether the proposed three-dimensional modeling and optimization formulation based on the efficiency function can be applied to the suspension design problems, a benchmark type problem is considered. In the benchmarking problem, the target trajectories of the traditional suspensions such as double wishbone and multilink are provided, and then optimization is implemented to find the solution tracing the given motion. After validation through the benchmark problem, the methodology will also be applied to actual design problems. In the practical problem, input factors related to the driving performance (ride comfort and handling performances) are considered, which is commonly applied in automotive industry. At this time, two design spaces for the same requirements are provided, but the one is much smaller than another one. From the actual design problems with these two design domains, it will be possible to examine effectiveness of the suggested design methodology. In Chapter 3, modeling, formulation, and design requirements related to the ride and handling will be introduced in detail, to verify the possibility of applying the suggested design algorithm into practical design problems.

• Analysis of the newly design suspension by the constraint force analysis

In Chapter 4, a specific component included in the newly suggested suspension, which appears in the result of the topology optimization when the small design domain is applied, will be intensively studied. The geometrical feature of the new component is RSR-limb in topological aspect, which is the same as one used in parallel manipulators. But, this configuration which is composed of two revolute joints and a ball joint has not been reported in the automotive industry for the vehicle suspensions. The component is obtained in the topology optimization for the suspension mechanisms for the first time. In the viewpoint of the kinematic chain analysis, it has the effect of restricting one degree of freedom as conventional link components, so that it can be applied to the traditional suspensions instead of the link components. In Chapter 4, a multi-link type suspension with this special module, RSR-limb, will be investigated through the constraint force analysis, by which it is possible to identify the role of the newly suggested component. Fortunately, the reason why the component is obtained in the narrow design domain can be explained through the suggested constraint force analysis with several proofs. The effectiveness is also verified in system-level through the elasto-kinematic system analysis. From the in-depth analysis for the RSR-limb, the hidden link concept will be introduced. After investigation of the newly suggested component based on the force analysis, nonlinear effects will also be considered for providing the design guideline of the newly suggested suspension to mechanism designers.

In Chapter 5, the achievements in this research will be summarized, from the

methodology development to applications. Through the suspension design problems, the possibility of applying the topology optimization into practical problems is demonstrated. However, there are remained issues for advanced design problems. Limitations of the currently proposed method and future works for further development will be discussed.

CHAPTER 2 ¹

TOPOLOGY OPTIMIZATION METHOD FOR LINKAGE MECHANISMS

In spite of increasing interest in gradient-based topology optimization of linkage mechanisms, it is still difficult to solve practical, realistic problems. Besides the apparent difficulty resulting from high nonlinearity, the optimization problem faces other major difficulties: difficulty to satisfy the discrete Degree-Of-Freedom (DOF) condition with continuous design variables and lack of intrinsic mechanisms to generate distinct black-and-white layouts. To deal with the DOF issue, a new formulation which maximizes a single objective function, the energy transmittance efficiency, is proposed. It is shown that the efficiency function maximization handles DOF-redundancy and deficiency simultaneously. To obtain distinct linkage layouts,

¹ This chapter previously appeared as an article in International Journal for Numerical Methods in Engineering. The original citation is as follows: S.I. Kim and Y.Y. Kim, Topology optimization of planar linkage mechanisms, Int. J. Numer. Methods Eng., 98 (2014) 265-286.

a common practice is to introduce an artificial mass constraint and/or to remove unnecessary links during optimization. However, any artificial mass constraint is not used, but post-processing of the optimized result is employed to obtain the final layout by a special post-processing algorithm. In this study, the linkage design model consists of nonlinear ground bars and zero-length springs. The springs are used to fix bar-connecting nodes to the ground, generating pinned joints. After verifying the effectiveness of the proposed approach for four-bar linkage synthesis, an automobile steering mechanism satisfying the Ackermann condition is synthesized. The steering mechanism problem is solved here for the first time.

2.1 Definition of problem

Rigid-body mechanisms such as automobile suspension and steering systems may be better designed if a systematic optimization method is available. Type, number (topology) and dimension syntheses are usually performed in a sequential order. Motivated by the success of the topology optimization method in structures, some attempts [17, 26-28, 31-37, 39] have been recently made for simultaneous syntheses of linkage numbers and dimensions. The present work is also along the latter track because the present work is concerned with the gradient-based topology optimization of planar linkage mechanisms generating desired paths. Among others, some practical design problems such as an automobile steering mechanism satisfying the Ackermann condition is now solved in this research. To solve such problems requires quite different formulations from existing ones. To pinpoint the main technical contributions of the present work, it is worth giving a brief review of earlier related studies.

Kawamoto and his colleagues first attempted to synthesize one-directional force converters/inverters and also short-path non-Grashof type linkages in the framework of the topology optimization [17, 31-34]. They suggested a nonlinear-bar based ground model and used both gradient and non-gradient optimizers. On the other hand, the spring-connected rigid-block model that employs rigid blocks and zero-length elastic springs [43-45] has also been suggested [35, 37-39, 46-48]. Interesting alternative approaches have been also suggested by other researchers [36, 40, 49-52]. In spite of these efforts, it is still difficult to use any of these methods for practical

industrial design problems and in fact, no paper reports practical case studies. Because many optimization iterations would be required in this type of problems, the use of a non-gradient-based optimization algorithm may not be preferred. When gradient-based methods are used, one of the critical issues is that accurate satisfaction of the desired DOF (typically 1 DOF) is very difficult without causing other numerical problems. Another critical issue is that it is difficult to obtain distinct black-and-white linkage layouts.

First, the DOF issue needs to be considered. Recall that the DOF issue arises because gradient-based methods must deal with integer-valued DOF's by using real-valued variables. If optimized linkage mechanisms cannot satisfy the required DOF [1], they would be obsolete. In Ref. [1], a compliance function representing the redundant state of DOF was considered but it was found difficult to decide appropriate upper bounds for the function. Alternatively, the Maxwell equation was applied directly and the sigmoid function was used to count the number of bars and nodes [17]. Because the function typically varies very rapidly, it tends to yield many local solutions. So it appears that an integer-type algorithm such as the branch-and-bound algorithm needs to be used to solve a certain class of problems (see [33]). Alternatively, the satisfaction of the DOF by considering strain energy, displacement, etc. was suggested [36, 37]. It is equivalent to simultaneous control of rigidity and flexibility. The idea behind these approaches is as follows. If the DOF of an optimized system is not redundant, the system stiffness would resist any perturbation. On the other hand, no strain energy will be stored in the system during motion if it

is not deficient. (Note that the same arguments do not apply to compliant mechanisms.) Unlike in earlier attempts [36, 37], a new unified approach which simultaneously deals with the DOF-redundancy and deficiency is proposed in this research.

In the present formulation, a single function called the work transmittance efficiency function is maximized to satisfy the correct DOF. The main motivation of using the work transmittance efficiency function (η) is that two separate conditions, the DOF non-redundancy and non-deficiency conditions, can be handled by maximizing the function alone. No artificial weighting factor to adjust the relative contributions of the two conditions is needed. In Chapter 2.2, how the two conditions can be met through the maximization of η will be shown. Because the DOF is handled by using an objective function, other desired kinematic conditions such as the satisfaction of the desired path at an end-effector are treated as constraint equations.

Now the second issue, to obtain distinct black-and-white linkage layouts, will be discussed. Typically, the penalization of material or geometrical variables such as the cross sectional areas of domain-discretizing nonlinear bars and/or the stiffnesses of zero-length springs would certainly help push distinct black-and-white images. The penalization scheme will be more effective if a mass constraint [23, 53] is used. Nevertheless, there is no guarantee to yield distinct images in linkage design problems unlike in structural compliance minimization problems that have natural mass constraints. To this end, it is not possible to determine in advance the total mass

of an optimal linkage mechanism (equivalently, the total number of links). In an attempt to avoid the use of an artificial mass constraint, one may eliminate floating elements (bars or blocks that do not contribute to the realization of the desired path) during optimization iterations as done in [37]. But this method does not always guarantee distinct linkage layouts at convergence. Based on these observations, a different approach is taken in this research: an optimal mechanism layout is found without too much worrying about distinct black-and-white images, and then post-process the results to identify optimized linkage layouts. To this end, a specially-devised post-processing method suitable for mechanism synthesis is newly developed. After converged design variables (taking on values between 0 and 1) are replaced by 0 or 1 by a simple rule, two main post-processing algorithms are applied. One of the main algorithms is a pruning algorithm developed to eliminate floating elements. Then a so-called simplification algorithm is devised to group bars having the same angular motions and to generate the linkage elements made of the least number of discretizing bars.

The effectiveness of the proposed work-transmittance efficiency based formulation is tested and the proposed post-processing algorithm is also verified by using an example to find known Grashof-type four-bar linkages that produce desired paths at their end effectors. The test problems to be considered are sketched in Figure 2.1(a). The design domain will be discretized by 3×3 ground bars having zero-length springs at their ends. After the verification of the proposed methods, the synthesis of an automobile steering mechanism satisfying the Ackermann condition

[54] is considered. The problem is illustrated in Figure 2.1(b) where 6×3 and 7×3 ground bar models incorporating zero-length springs are employed. To confirm the effectiveness of the proposed formulation and the post-processing algorithm, the performance of the mechanisms obtained by the present approach will be compared with that of a reference steering mechanism.

In the next section, modeling, analysis and formulation will be presented. Because the DOF issue will be treated as the minimization of an objective function, the requirement that an end-effector follows a prescribed path will be treated as constraints. Then, Chapter 2.3 presents how to formulate specific design problems by stating the corresponding constraint equations along with the objective function. In the section, Grashof-type four-bar linkages and automobile steering systems will be synthesized. The optimized linkage mechanisms will be identified as the results of the application of the proposed post-processing algorithm. The detailed accounts of the algorithm will be given in Chapter 2.4, and findings of this study will be summarized in Chapter 2.5.

2.2 Modeling, analysis, and formulation

2.2.1 Modeling and Analysis

The ground-structure model consisting of nonlinear elastic bar elements [31, 55, 56] is used to discretize the design domain for linkage mechanism synthesis. As shown in Figure 2.2, nodes are first located in a two-dimensional array and all possible node combinations are considered to fill the design domain with nonlinear bar elements from which an optimal mechanical chain can be constructed. The areas (A) of bar elements are interpolated between A_{\min} and A_{\max} . While the values of A control the presence of bars in the domain, we also introduce variables (k) controlling the stiffnesses of zero-length springs connecting nodes to the ground. By assigning the maximum spring stiffness value (k_{\max}), one can realize a ground pivot at the corresponding node location because it fixes end points of the links to the ground. In the present study, sliding joints are not considered. Therefore, both the horizontal and vertical stiffnesses of the springs are simultaneously controlled by k . When k takes on the minimum value (k_{\min}), the corresponding node is treated to be dis-connected from the ground. Figure 2.3 briefly illustrates the realization of various mechanism components and joint conditions when two sets of variables take on their minimum or maximum values. The usefulness of the zero-length springs in topology optimization was demonstrated in structure and mechanism design problems [37, 43]. A similar approach was also considered in Ref. [57].

For further discussions, let us introduce some symbols used to denote bars and

others with a reference to Figure 2.2. Let $L_{i,m}$ ($i \neq m$) denote the nonlinear bar connecting node i and node m ($i, m \in \{1, 2, \dots, N_n\}$) where N_n is the total number of nodes used to discretize a given design domain. It is often convenient to use a single-index notation L_j ($j \in \{1, 2, \dots, N_\ell\}$) for the bar elements where N_ℓ is the total number of bars. (The symbols $L_{i,m}$ and L_j will be used interchangeably.) The length of L_j will be denoted by l_j with its initial length, $l_{j,0}$ and the area of L_j is expressed by A_j . Because the value of the variable A_j can be used to denote the existence of L_j , one may interpolate it as a function of the design variable ξ_j^A ($\xi_{\min}^A \leq \xi_j^A \leq \xi_{\max}^A = 1$) as

$$A_j = A_0 \left(\xi_j^A \right)^p \quad (2.1)$$

where A_0 denotes a nominal bar cross sectional area and p is the penalization constant. The value of $p=3$ will be used throughout this study. Likewise, the stiffness of the zero-length spring will also be interpolated as a function of ξ_i^k ($\xi_{\min}^k \leq \xi_i^k \leq \xi_{\max}^k = 1$) to represent various joint conditions:

$$k_i = k_0 \left(\xi_i^k \right)^p \quad (2.2)$$

where k_0 is a nominal stiffness value. For a later use, we define $k_{\max} = k_0$ and $k_{\min} = k_0 \left(\xi_{\min}^k \right)^p$. Note that the bar element L_j should simulate a rigid

connection when $A_j = A_{\max} = A_0$ and disconnection between its end nodes when

$A_j = A_{\min} = A_0 \left(\xi_{\min}^A \right)^p$. Therefore, the value of A_0 and ξ_{\min}^A should be

properly selected. Similar arguments are applied to the selection of k_0 and ξ_{\min}^k .

The actual values of A_0 , k_0 , ξ_{\min}^A , and ξ_{\min}^k will be specified when design case studies are considered later. For a later use, it is convenient to define the following symbols:

$$\boldsymbol{\xi}^A = \left\{ \xi_1^A, \xi_2^A, \dots, \xi_{N_\ell}^A \right\}^T \quad (2.3)$$

$$\boldsymbol{\xi}^k = \left\{ \xi_1^k, \xi_2^k, \dots, \xi_{N_n}^k \right\}^T \quad (2.4)$$

To calculate the current location of nodes and bars during motions, the discretizing bars are modeled by geometrically-nonlinear bar elements (but with linear material behavior assumed). More detailed accounts of the analysis for this kind of problems can be found in earlier works [31, 55, 56], but only a few important equations are listed here. To this end, the detailed FE-based description will be dealt with in Chapter 3, where three-dimensional ground structure is employed with rigid body corresponding to wheel for general suspensions.

$$E_j = \frac{l_j^2 - l_{j,0}^2}{2l_{j,0}^2} \quad (j=1,2,\dots,N_\ell) \quad (2.5)$$

$$S_j = CE_j \quad (j=1,2,\dots,N_\ell) \quad (2.6)$$

$$F_j = A_j S_j \quad (j=1,2,\dots,N_\ell) \quad (2.7)$$

In equations (2.5-2.7), E_j and S_j denote the Green-Lagrange strain and the 2nd Piola-Kirchhoff stress of the bar element j , respectively and C , the stress-strain modulus, corresponds to Young's modulus in small deformation. The internal force in the bar element j along its longitudinal direction with respect to its local coordinates is denoted by F_j . The nonlinear finite element analysis is implemented by an iterative method utilizing the tangent stiffness (see, e.g. [55, 56]).

Because the kinematic motion of the bars involves very large motion, some special care must be taken. For example, consider the case when buckling occurs. Figure 2.4 shows a four-bar linkage where positions of the input crack link are marked by a set of thin (red) lines. In Figure 2.4(a), the same linkage configuration is obtained stably either by the Newton-Raphson (NR) algorithm or the Levenberg-Marquardt (LM) algorithm until the angle of the input crack link (with respect to the vertical axis) reaches 225° , say, corresponding to the analysis step $t-1$. At the next step t when the angle becomes 236.25° , two different configurations could be obtained depending on the selected nonlinear solver; see Figure 2.4(b,c). Although two configurations are different, they are all correct solutions. This type of multiple solutions is due to truss buckling and it is very similar to the circuit defect in rigid-body mechanisms [1]. Note that linkage mechanisms can have two or more than two configurations without the violation of kinematic constraints and these configurations are included in each circuit (e.g. multiple configurations in crank-slide mechanisms [31, 58]). However, jumping to another circuit (associated with

the circuit defect) should be avoided in linkage mechanisms, for the system of interest should move without discontinuity. If the circuit transition is required to take place, then the linkage system should be dis-assembled and re-assembled to have another configuration except a bifurcation case. This undesirable circuit transition, equivalently, buckling in finite element analysis, can occur during simulations. For example, Figure 2.4(b) is the next step configuration of Figure 2.4(a) obtained from the NR algorithm. To avoid this problem, we use the LM algorithm with a proper initial guess.

It was shown earlier that the NR algorithm cannot prevent the circuit defect [59]. So, the use of the LM algorithm was suggested [31, 58] with an additional linear buckling constraint at every step. The approach was successful in the examples discussed in the studies. In the present study, however, an additional special attention is paid to initial guesses for ensuring stable results by the LM method. To explain the proposed strategy to select initial guesses, let us see how they were selected in the previous researches; the converged solution at the analysis time step $t-1$ during the optimization iteration stage n_{iter} was used as the initial guess for the LM algorithm at the step t for the same iteration stage $n_{iter} - 1$. The problem is that in design optimization involving very large displacements, this strategy can be often ineffective. This is because the initial guess for the next step may be very near another circuit, not the circuit of the previously-converged solution. In this case, the buckling as illustrated in Figure 2.4(b) could occur. This problem may be better

circumvented if input motion is varied continuously and a method such as the arc-length method is used [60-62]. However, its implementation appears quite complicated. A popular remedy to find converged configurations tracing the original circuit is to use a continuation method that decreases the penalty parameter related to the circuit transition [63], but it is quite time-consuming. In the present study, we use a simpler algorithm, the LM algorithm, but suggest the use of an alternative strategy for initial guesses (without imposing any additional constraint). Specifically, the converged solution at the analysis step t of the optimization iteration stage $n_{\text{iter}} - 1$ is used as an initial guess at the analysis step t of the iteration stage n_{iter} . The main reason to suggest this modification is as follows. Because we use a gradient-based optimizer, MMA (the Method of Moving Asymptote) [64] with small move limits, the converged solution at the step t of the iteration stage $n_{\text{iter}} - 1$ would be closer to the solution at the step t of the iteration stage n_{iter} than the converged solution at the step $t-1$ of the iteration stage n_{iter} . All numerical problems considered in this study were solved by this approach and good convergence without the circuit defect was observed.

2.2.2 Objective function

One of the key aspects in the study is the use of an alternative objective function that is critical for stable convergence. A linkage mechanism that generates a target path at its end effector will be found within the selected discretization of a given design

domain. In formulating optimization problems, we propose to deal with the DOF issue by minimizing the proposed objective function while a given target path to be traced by the end-effector of the optimized linkage mechanism is treated as constraint equations. Unlike earlier approaches [36, 37] that use separate conditions to control DOF-redundancy and deficiency, a single objective function is proposed in this study; the validity of the proposed single-objective function approach will be justified with supporting arguments.

The degree of freedom (DOF) represents the number of the actuators required to control a mechanism; a linkage system having the DOF equal to the number of given actuators can have a unique configuration for prescribed actuator locations except in some special cases such as bifurcations (Bifurcation occurs when two or more than two circuits overlap on a point of the configuration space of a rigid-body mechanism). If a system has a redundant DOF, i.e. if there are fewer input sources than necessary, its configuration becomes easily perturbed under arbitrary external disturbances because of insufficient stiffness. Figure 2.5(a) shows the redundant DOF case. When the a linkage system has a deficient DOF, i.e. if there are more input sources than necessary, the system cannot move without deformations in links. The situation is illustrated in Figure 2.5(b) and in fact, the system represents a structure, corresponding to a compliant mechanism. Once a mechanism layout is known, its DOF can be calculated by Gruebler's equation or Maxwell's equation [1, 17]. According to these equations, the DOF's of the systems shown in Figure 2.5(a,b,c) are 2, 0 and 1, respectively. When an input motion is specified at an input link, the

0-DOF system cannot move without deformation and the 2-DOF system cannot resist any external force, except some singular configuration cases. The 1-DOF system shown in Figure 2.5(c) is a schematic representation of a four-bar linkage mechanism.

Note that it is difficult to use Gruebler's or Maxwell equation for topology optimization formulated by real-valued variables because the discrete DOF cannot be precisely determined especially in intermediate mechanisms appearing during topology optimization iterations. Nevertheless, the following observations can be made by examining the behavior of the systems in Figure 2.5. The DOF-deficient system in Figure 2.5(b) is too stiff while the DOF-redundant system in Figure 2.5(a) has no resistance under an arbitrary external force. Based on this observation, we will examine the structural rigidity of a mechanism when it is subjected to an external force. As an external force, we propose to use a force applied in the direction connecting the target position of the end-effector at the current step and that at the next step. This approach will be explained in more details below.

Let us now consider the proposed objective function formulated in terms of the real-valued design variables. As a means to satisfy the desired DOF, the following energy transmittance efficiency function (η) is proposed:

$$\eta = W^{\text{out}} / W^{\text{inp}} \quad (2.8)$$

where W^{inp} denotes the work done by an actuator, while W^{out} is the work done by the system against the external force through the movement of the loaded point

from its initial position to the current position. The use of the efficiency function is not a new concept; efficiency and similar concepts (e.g. mechanical/geometrical advantages) have been used in the design of “compliant” mechanisms [16, 65-70]. However, it has not been used for the design of rigid-body mechanisms, as proposed here. Surprisingly, its use turns out to resolve the DOF issue if an additional external force introduced to control the DOF is properly selected. We give the reasons for its effectiveness below and also confirm it with numerical examples.

While the formula in equation (2.8) is a generic form, the specific formula to be used needs more attention. To this end, we will investigate how to define an external force properly for the DOF control. Actually, the external force may be somewhat arbitrary as long as it can disturb the movement of the end-effector. Perhaps the best way to “keep” perturbing a mechanism system is to apply an external force \mathbf{F}^{ext} at its end-effector in a direction opposite to the direction tracing the desired target path. For instance, the applied force \mathbf{F}^{ext} at the analysis step t^* is defined as

$$\mathbf{F}_{t^*}^{\text{ext}} = F_0 \frac{\hat{\mathbf{r}}_{t^*-1} - \hat{\mathbf{r}}_{t^*}}{\|\hat{\mathbf{r}}_{t^*-1} - \hat{\mathbf{r}}_{t^*}\|} \quad (t^* = 1, 2, \dots, T) \quad (2.9)$$

where T is the last analysis step to complete a given input motion and F_0 , the magnitude of the applied force. The position $\hat{\mathbf{r}}_t$ denotes the prescribed position of the end-effector at analysis step t . In what follows, the symbol \mathbf{r}_t will be used to denote the position vector of the end-effector point of an intermediate mechanism designed at the optimization iteration step (n_{iter}). The external force defined here

has the meaning of resistance and is similar to the counter load used to make the design problem well-posed in compliant mechanism design [69].

Let us now define $W_{t^*}^{\text{out}}$ as the total external work by $\mathbf{F}_{t^*}^{\text{ext}}$ as the result of the movement of the end effector from the analysis step $t=1$ up to $t=t^*$ ($1 \leq t^* \leq T$).

$$W_{t^*}^{\text{out}} = \sum_{t=1}^{t^*} (\mathbf{r}_{t-1} - \mathbf{r}_t)^T \mathbf{F}_t^{\text{ext}} = \sum_{t=1}^{t^*} (\mathbf{r}_{t-1} - \mathbf{r}_t)^T \left(F_0 \frac{\hat{\mathbf{r}}_{t-1} - \hat{\mathbf{r}}_t}{\|\hat{\mathbf{r}}_{t-1} - \hat{\mathbf{r}}_t\|} \right) \quad (2.10)$$

The expression in equation (2.10) denotes the summation of the incremental work done by the external force from $t=1$ to $t=t^*$. Precisely speaking, the output work defined in (2.10) needs additional minor term, small deformation of the structure due to their flexibility with respect to the external force, to be the exact output work as described in [66]. However, the additional terms could be neglected in large-motion and almost rigid-body behaviors, since the term is too minor. When they are not considered, it becomes easier to calculate the output work.

In a problem to design Grashof-type linkages that go through full-cyclic motions, the relations that $\hat{\mathbf{r}}_T = \hat{\mathbf{r}}_0$ and $\mathbf{r}_T = \mathbf{r}_0$ hold. Here, the subscript “o” stands for the un-deformed, original configuration.

Because the motion of an input actuator (or link) causes elastic deformation of a mechanism and the motion at its end effector, the following energy relation holds

$$W_{t^*}^{\text{inp}} = U_{t^*}^{\text{int}} + W_{t^*}^{\text{out}} \quad (1 \leq t^* \leq T) \quad (2.11)$$

where $W_{t^*}^{\text{inp}}$ is the work done by an input actuator and $U_{t^*}^{\text{int}}$, the strain energy stored at time t^* in the mechanism system that consists of nonlinear elastic bars

and zero-length springs. No energy dissipation is considered here. Because $U_{t^*}^{\text{int}}$ can be evaluated from the finite element analysis, it is convenient to express the transmittance efficiency function η_{t^*} at $t = t^*$ as

$$\eta_{t^*} = \frac{W_{t^*}^{\text{out}}}{W_{t^*}^{\text{inp}}} = \frac{W_{t^*}^{\text{out}}}{W_{t^*}^{\text{out}} + U_{t^*}^{\text{int}}} \quad (1 \leq t^* \leq T) \quad (2.12)$$

Equation (2.10) indicates that $W_{t^*}^{\text{out}}$ is always positive and finite as the mechanism end-effector traces the desired path. Accordingly, the minimization of the strain energy of the mechanism system at each step t^* is equivalent to the maximization of the efficiency. The strain energy is stored in the system by two sources, the external force and the input displacement.

Let us now explain how the strain energy minimization controls DOF-redundancy and deficiency. When an external force is applied to a system, the compliance minimization equivalent to the strain energy minimization is used to find the stiffest structure as done in structural topology optimization. Therefore, the strain energy minimization under the suggested external force ($\mathbf{F}_{t^*}^{\text{ext}}$) will effectively suppress DOF-redundancy. On the other hand, the system flexibility can be achieved by reducing the strain energy induced by the displacement input prescribed at an input link; then, most of the input energy $W_{t^*}^{\text{inp}}$ at each step t^* will be converted to $W_{t^*}^{\text{out}}$ (see equation (2.11)) as the elastic deformation is reduced. Therefore, DOF-redundancy and DOF-deficiency can be simultaneously prevented by maximizing

the transmittance efficiency function alone. The proposed single-objective function approach may be compared with those using multi-objective functions [36, 37]. In the present approach, there is no need to adjust weighting factors for the two conditions. While the strain energy minimization is equivalent to the efficiency function maximization, the use of the efficiency function is preferred because it is so normalized to vary between 0 and 1 (under the assumption of positive output work) and its value is a direct indicator to tell how well the DOF conditions are met. For instance, the efficiency function value larger than a certain value (say, 0.9) at convergence would indicate that the designed system is a rigid-body mechanism satisfying the desired DOF.

Another advantage of the proposed efficiency function based approach is that the design variables at convergence tend to approach either 0 (no bar) or 1 (existence of a bar) because the system would behave just like a rigid-body mechanism during its entire motion. Therefore, any bar participating in the formation of a rigid-body linkage mechanism should be sufficiently stiff to minimize the stored energy. The use of the standard penalization scheme as expressed as $p \geq 1$ in equations (2.1-2.2) would also help because the strain energy minimization under an external force is considered. However, there is a situation where the maximization of the efficiency function cannot effectively suppress intermediate design variables. When a set of bars forms a rigid body, such as a delta triplet, more bars than necessary may be used. This situation may be avoided if a mass constraint is used. However, it is not possible to choose a specific mass constraint ratio in advance for rigid-body mechanism

synthesis. Furthermore, the use of a tight mass constraint needed to yield the simplest skeletal mechanism layout would eliminate reinforcing bars necessary to form a stable link mechanism, resulting in some instability, such as structural buckling different from the buckling mentioned in Chapter 2.2.1. Due to these difficulties originating from an artificial mass constraint, we will not use it but newly develop a post-processing algorithm to extract the simplest skeleton layout from the converged configuration. This algorithm should be also able to eliminate the so-call floating bars that do not actually contribute to the realization of the desired motion. The latter process is necessary because no implicit penalization will be used to suppress such bars. The details on the proposed post-processing algorithms will be given in Chapter 2.4.

Back to the objective function used to synthesize Grashof-type linkages, the efficiency function defined in equation (2.8) should be maximized for all analysis time steps, $t^* = 1, 2, \dots, T$. This means that the DOF condition is imposed to be satisfied during the whole analysis time steps. Another advantage of maximizing the efficiency function at every step is that the Grashof-rotatability condition can be satisfied through the efficiency maximization when full-cyclic motions are considered. Since the input link cannot reach the limit position (also called the singular position [63]) in a system that doesn't satisfy the rotatability condition, the efficiency maximization will impose the condition to be fulfilled; a system that violates the condition would produce large deformation in the system, yielding a small efficiency value as it passes through the limit position. Because linkage

geometry data are needed to check the condition, it is very difficult to impose as an explicit constraint equation in the real-variable based topology optimization setting. Therefore, imposing the Grashof-rotatability condition implicitly through the proposed efficiency function is an efficient way for the topology optimization based mechanism synthesis.

Based on the above-mentioned arguments, the following objective function will be utilized in setting up an optimization problem for mechanism synthesis:

$$\bar{\eta} = \frac{1}{T} \sum_{t^*=1}^T \eta_{t^*} \quad (2.13)$$

The function $\bar{\eta}$ is the mean value of the efficiency functions for all analysis time steps. The desired kinematic conditions (no DOF-redundancy, etc.) are satisfied if $\bar{\eta}$ reaches 1. Using $\bar{\eta}$, the following minimization problem is proposed for mechanism synthesis:

$$\begin{aligned} & \underset{\xi^A \in \mathbf{R}^{N_\ell}, \xi^k \in \mathbf{R}^{N_n}}{\text{Minimize}} && 1 - \bar{\eta} \\ & \text{Subject to} && \psi_{t^*}(\xi^A, \xi^k) \leq \varepsilon \quad (t^* = 1, 2, \dots, T) \end{aligned} \quad (2.14)$$

In formulation (2.14) ψ_{t^*} is a performance function at step t^* . It represents the distance between the reference path and the actual path traced in path-generation problems and the Ackerman error in a steering design problem.

2.3 Mechanism synthesis by the proposed formulation

In this section, we will use the proposed formulation given in Section 2 for actual syntheses of some mechanisms. In the first part of this section, we will mainly consider how the proposed formulation works in recovering some known mechanisms the end-effector trajectories of which are prescribed for given input motions. The second part is concerned with the synthesis of an optimal steering mechanism that satisfies the Ackermann condition. Unless stated otherwise, the following numerical values are used:

$$\begin{aligned} A_0 &= 1 \text{ m}^2 & \varepsilon &= 10^{-2} \sim 10^{-1} \\ C &= 10^3 \text{ N / m}^2 & \xi_{\min}^A &= 10^{-4} \\ k_0 &= 10^3 \sim 10^4 \text{ N / m} & \xi_{\min}^k &= 10^{-4} \\ F_0 &= 1 \text{ N} \end{aligned}$$

Note that a too large value of F_0 would perturb the optimization problem away from the desired objective while a too small value would not produce the desired effect. After several numerical experiments, the value of F_0 equal to $O(10^{-3})A_0C$ is found be effective in general. Thus, this value of F_0 is used in all problems considered in this paper.

2.3.1 Synthesis of Grashof-type four-bar linkage mechanisms

The goal of path generation is to find a linkage that produces a desired output motion subject to a given input motion. In this section, we will check if known four-bar

linkage mechanisms can be recovered by the proposed formulation. It appears that mechanism syntheses involving full cyclic input motions were very difficult by most of currently-available gradient-based topology optimization methods, but we show how effectively the present approach handles such problems. As examples, we consider three cases in which input links return to their original configurations after cyclic motions. Three known mechanisms and the trajectories of their end-effectors are illustrated in Figure 2.6. In these test problems, the end points of input crank links and the output points are so selected as to exactly match the nodes of the ground bar model. The three selected output paths are: a path generated on a joint (Case 1), a simply-connected path generated by a coupler (Case 2) and a multiply-connected path (having a crunode [38]) generated by a coupler (Case 3). A square design domain ($D_x = 1 \text{ m}$, $D_y = 1 \text{ m}$) is used for the mechanism synthesis and discretized by geometrically-nonlinear ground bars connecting uniformly-discretized 9-nodes as illustrated in Figure 2.2 and Figure 2.6.

Referring to Figure 2.2, $L_{1,4}$ is the input crank link with its area fixed to A_{\max} and we fix node 1 to the ground by assigning $k_1 = k_{\max}$. The end-effector (i.e., output) node for Cases 1 and 2 is node 8 while it is node 2 for Case 3. Obviously, no zero-length spring is used for output nodes and node 4 that is connected to the input link. Except the link and the nodes mentioned above, the design variables ξ_j^A and ξ_i^k are assigned to all links and zero-length springs, respectively. Although we consider ideal cases where solutions are guaranteed to exist under the selected

discretization, we can check the effectiveness of the optimization formulation proposed in section 2.2.2.

To find the four-bar linkage mechanisms in Figure 2.6 by the proposed formulations given by (2.14), the constraint equation ψ_t should be stated. If the desired path at the end-effector location Q at time step t is denoted by $\hat{\mathbf{r}}_t^Q$, then ψ_t can be expressed as

$$\psi_t = \left\| r_t^Q(\xi^A, \xi^k) - \hat{\mathbf{r}}_t^Q \right\| \quad (t=1, 2, \dots, T) \quad (2.15)$$

The input crack motion going through 360° is discretized by 11.25° for all problems considered in this section, which corresponds to $T=32$. The method of moving asymptotes [64] was used as a gradient-based optimizer. The sensitivities were obtained by the direct method but the details will not be given here because the procedure is a standard one.

The iteration histories and intermediate layouts are shown in Figures 2.7, 2.8 and 2.9 for Cases 1, 2 and 3, respectively. Figure 2.10 shows how the final layouts are identified from the converged layouts shown in Figures 2.7-2.9. The converged layouts in Figures 2.7-2.9 still have some intermediate variables but their contributions in tracing the desired path are insignificant. Most of them are the floating links as pointed by Nam et al. [37]. These links can be easily identified and eliminated by the three-step post processing algorithm newly developed in Chapter 2.4. Clearly, the final layouts in Figure 2.10 are identical to those in Figure 2.6 that are used to generate desired paths at their end-effectors.

From Figures 2.7-2.9, one can see that the desired paths are almost exactly recovered at convergence while the efficiency functions reach values close to 1. Except for Case 3 exhibiting somewhat slow convergence, the convergence behavior for all three cases appears to be typical when MMA [29] is used as a gradient-based optimizer. In the MMA algorithm, the original optimization problem stated by equation (2.14) is converted to the following problem:

$$\begin{aligned} \text{Max}_{\tilde{\mu} \in \mathbf{R}^T} \quad & \text{Min}_{\xi^A \in \mathbf{R}^{N_\ell}, \xi^k \in \mathbf{R}^{N_n}} \quad (1 - \bar{\eta}^a) + \sum_{t=1}^T \mu_t (\psi_t^a - \varepsilon) \\ & + c \left\{ \sum_{t=1}^T \max(\psi_t^a - \varepsilon, 0) \right\} + d \left\{ \sum_{t=1}^T [\max(\psi_t^a - \varepsilon, 0)]^2 \right\} \end{aligned} \quad (2.16)$$

where $\tilde{\mu}_t$ is the Lagrangian multiplier. Symbols c and d denote linear and quadratic penalty parameters, respectively. Approximations of functions $\bar{\eta}$ and ψ_t are denoted by $\bar{\eta}^a$ and ψ_t^a , respectively. In this paper, the values of c and d are selected to be 1000 and 0, respectively. Thereby, the MMA algorithm tries to satisfy the constraint equation given by ψ_t using the linear penalty formulation, as is apparent from Figures 2.7-2.9. The slow convergence for Case 3 may be due to the difficulty in tracing a path involving a crunode. To see why this happens and how the related problem can be relieved by the proposed formulation (2.14), consider Figure 2.11. Recall that ψ_t defined in equation (2.15) must be satisfied for all t 's within an error bound of ε by equation (2.14). This means that any path lying within a circle of diameter 2ε around target points can be accepted. Figure 2.11(a) indicates the allowable zone. Figure 2.11(b) shows a candidate path that could satisfy

equation (2.14) without actually tracing the exact target path. However, the transmittance efficiency function in this case cannot be close to 1 because the suggested path in Figure 2.11(b) would require rather large elastic energy to be stored in the system. This also suggests that the efficiency function can be effective to help find a desired linkage mechanism.

2.3.2 Synthesis of steering linkage mechanisms

In this section, we consider the synthesis of an automobile steering system. There are several conditions to design actual systems, but the underlying kinematic condition applicable in low-speed steering will be considered here. The condition is known as the Ackermann condition [54]. Figure 2.12 shows 4 wheels and also the extended lines of the wheel axles. Referring to Figure 2.12, the Ackermann condition can be stated in terms of θ_{OWD} , the steering angle of an outer front wheel and θ_{IWD} , the steering angle of an inner front wheel as

$$g_{\text{Acker}}(\theta_{\text{IWD}}, \theta_{\text{OWD}}) = \frac{1}{\tan \theta_{\text{OWD}}} - \frac{1}{\tan \theta_{\text{IWD}}} - \frac{T_r}{W_b} = 0 \quad (2.17)$$

where T_r and W_b denote axle track and wheelbase. This condition prevents the lateral slip motion of each tire. It is also known that a car satisfying (2.17) does not fall into a state of out-of-control. However, equation (2.17) is valid only at low speed because no centrifugal force is taken into account. Despite of this limitation, the condition may be useful enough to design a realistic, practically-useful mechanism.

To solve this problem, a design domain illustrated in Figure 2.13(a) is considered. Two ground structure models in different discretizations are shown in Figure 2.13(b). The ratio $r = T_r/W_b$ is chosen to be 1.6/2.6 because typical sedans have this ratio. Rigid modules representing tires and wheels are also modeled by bar elements with their areas equal to $A = A_0$ but no design variable is assigned to these non-design elements. Also, the zero-length springs attached to the nodes belonging to these rigid modules are non-design elements and the stiffnesses are chosen to k_{\min} except kingpin positions. The nodes at the kingpin positions are made to serve as ground pivots by imposing $k = k_0$. To facilitate the design optimization, the left and right halves of an optimized layout are enforced to be symmetric to each other. Because this problem does not have any explicit input motion, we define ψ_t as the error in satisfying the Ackermann condition (2.17):

$$\psi_t = \psi_t(\theta_{\text{OWD},t}) = \left\| \frac{\theta_{\text{IWD},t} - \hat{\theta}_{\text{IWD},t}(\theta_{\text{OWD},t})}{\hat{\theta}_{\text{IWD},t}(\theta_{\text{OWD},t})} \right\| \quad (t = 1, 2, \dots, T) \quad (2.18)$$

where $\theta_{\text{IWD},t}$ and $\theta_{\text{OWD},t}$ are the steering angles of the outer and inner wheels at time step t . The symbol $\hat{\theta}_{\text{IWD},t}(\theta_{\text{OWD},t})$ is an inner angle $\theta_{\text{IWD},t}$ satisfying $g_{\text{Ackermann}}(\theta_{\text{IWD}}, \theta_{\text{OWD}}) = 0$ when $\theta_{\text{OWD}} = \theta_{\text{OWD},t}$. The range of the input angle varying from $\theta_{\text{OWD}} = 0^\circ$ to $\theta_{\text{OWD}} = 30^\circ$ is discretized by 5° , yielding $T = 6$. The value of ε appearing in equation (2.15) is taken to be 0.1, implying that the

relative error of $\hat{\theta}_{\text{IWD},t}$ for all time steps in satisfying the Ackermann condition is smaller than 10%.

To explain how the external force in equation (9) can be defined for this problem, note that the position vector $\hat{\mathbf{r}}$ is associated with the point Q marked in Figure 2.13(b). Since Q rotates about point O, the kingpin location, Q makes a circular motion. Because θ_{OWD} increases up to 30° , $\hat{\theta}_{\text{IWD}}$ is found to increase up to 41.85° by equation (2.17). Therefore, $\hat{\mathbf{r}}$ appearing in equation (2.9) traces an arc of radius 0.2 m centered at O. Then, the external force can be precisely defined through equation (2.9).

Figure 2.14 shows the intermediate and final layouts during optimization iterations when ground structures of different discretizations are used. It also shows the final layouts that are identified after the application of the post-processing algorithm. The algorithm will be explained in the next section. In case when the 7×3 ground structure is used, the optimized layout turns out to be a 6-bar linkage. On the other hand, the optimized layout is a 9-bar linkage when the 6×3 ground structure is employed. The difference in the results is due to different discretization; vertical links can appear along the center of the design domain only when the 7×3 ground structure model is used. Therefore, the 6-bar linkage cannot be obtained in the 6×3 ground structure model. This means that the discretization-dependency, usually known as the mesh-dependency in structural optimization problems, also appears in mechanism synthesis. Further discussion for the mesh dependency issue

is well established in APPENDIX A.2. In Figure 2.14, the system configurations for $\theta_{\text{OWD}} = 15^\circ$ and 30° are also illustrated. Figure 2.15 shows the iteration histories; the transmittance efficiency functions have almost approached the maximum value of 1, meaning that the optimized rigid-body mechanisms satisfy the correct DOF.

For the results from the both ground structures, we need to check their similarity. Two configurations obtained in each ground structure looks quite different, and it is the above-mentioned mesh dependency problem. But, they could be considered as the same one in the topological aspect. Each result corresponds to the 6-bar and the 9-bar linkage, however the 9-bar linkage is possible to be divided into two 6-bar linkages as shown in Figure 2.16(c), and it means that DOF of the 9-bar linkage is equal to 0. Then, how can it satisfy the mobility condition? The 9-bar result in Figure 2.16(b) is the special one, so-called an over-constrained mechanism, which has the more degree of the mobility than the predicted one through the conventional DOF calculation method. It is well-known in kinematics that the over-constrained mechanisms have the redundant constraints which is self-satisfied automatically for all input conditions, so that the motions will not be changed even though the redundant component is removed. In Figure 2.16(c), two 6-bar linkages share the same input and output links, but fortunately the relation between the input and output angle is the same in the both linkages. Therefore, one of them could be deleted without change of the steering performances. The exceptional case of the DOF calculation due to the redundant constraint is introduced in [1], and the similar configurations compared with 9-bar linkage in Figure 2.16 can be found in [71, 72].

From the obtained over-constrained linkage results, we can see that our suggestion, energy-based DOF control method, has a powerful advantage. In conventional DOF calculation, the over-constrained constraints should be considered through self-checking algorithms, e.g. generalized coordinate partitioning method in [63]. However, the work-transmittance efficiency function based DOF control method do not need to employ that kinds of the additional algorithms to check the exceptional DOF case studies. From this viewpoint, we expect that it will be possible to apply the proposed efficiency function-based design method to the construction equipment or commercial vehicle system design problems, which requires over-constrained linkage systems to resist large forces.

Next, it will be interesting to compare the performance of the optimized linkage mechanisms obtained by the proposed method against a typical four-bar steering linkage mechanism. They are shown in Figure 2.16. The four-bar linkage in Figure 2.16(a) has two main design parameters, the trapezoidal angle φ and the arm length s . A common method of parameter tuning is to make the extended lines of both arms meet at the center of the rear axle [54], which is depicted in Figure 2.16(a). If this condition is imposed, there remains only one parameter, s . To compare the performance of the linkages shown in Figure 2.16, the absolute value of the Ackermann error defined as $(\theta_{\text{IWD}} - \hat{\theta}_{\text{IWD}}) / \hat{\theta}_{\text{IWD}}$ is plotted as a function of the input angle θ_{OWD} in Figure 2.17. To calculate the error, the standard kinematic analysis [63, 73] by using the rigid-body layouts that are extracted from the finite

element models was carried out. In case of the four-bar linkage, several values of the parameter s were tried. In the process of the kinematic analysis, the deformations of the link elements are ignored. It was checked that the negligence of the deformation causes little difference in the actual motion of the linkages. Figure 2.17 shows that the conventional four-bar linkage mechanisms tuned with several parameters exhibit more than 10 % errors while both of the two optimized linkage mechanisms have about 2 % errors. This comparison indeed shows the effectiveness of the proposed formulation. While the maximum error of the 9-bar linkage is larger than that of the 6-bar linkage, the former appears to outperform the latter for small values of θ_{OWD} . Interestingly, a 6-bar linkage similar to the optimized one here is regarded as an advanced steering system in the automobile industry [54]. Although not pursued here, subsequent sizing optimization would further improve the kinematic performance of the optimized 6-bar and the 9-bar linkages.

2.4 Post-processing

In this section, a three-step post-processing algorithm is developed to identify rigid-body link mechanisms out of the converged layout from the optimization formulation, equation (2.14). To make sure that the post-processing does not affect the performance of the optimized mechanism, the values of the objective function before and after the application of the post-processing will be checked.

2.4.1 Step 1: Binarizing

Step 1 in the post-processing algorithm is trivial; the real-valued design variables are simply binarized to 0 or 1. If the value of a design variable is larger than or equal to 0.5, the value of 1 is assigned to it. Otherwise, the value of 0 is assigned. For actual implementation, 10^{-4} is used instead of 0 in order to utilize the available ground structure model. The layouts after applying the Step 1 post-processing are illustrated in Figure 2.10 for the cases of four-bar linkages.

2.4.2 Step 2: Pruning

The Step 2 post-processing is to remove redundant elements that do not contribute to generate the desired motion. These elements, referred to as floating elements in Nam et al [37], can appear because there is no mass constraint. To eliminate these unnecessary redundant linkage elements, we observe that they should not participate in the transmission of the external applied force applied at the end-effector. Thus, the

magnitudes of internal forces in all elements are checked. If internal forces are smaller than a certain value, the corresponding elements are regarded to be redundant and eliminated. The pruning process can be written as

$$\text{If } |F_{i,t^*}| \leq \zeta F_0, \text{ then set } \xi_i^A = \xi_{\min}^A \quad (i = 1, 2, \dots, N_\ell) \quad (2.19)$$

where F_{i,t^*} is the internal force in the element i at time step t^* . The symbol ζ is a parameter to prune off redundant elements. One may check (2.19) throughout all analysis time steps, but we consider only one time step. The typical value chosen was $t^* = 6$ for the present study. As stated in Eq. (2.19), the actual implementation of the elimination is to assign a small value ξ_{\min}^A to the corresponding design variables. The post-processed layouts by the Step 2 pruning process are shown in Figure 2.10 for the four-bar problems.

2.4.3 Step 3: Simplification

The final step (Step 3) is mechanism simplification. This process is to remove some reinforcing links not affecting the motion of the end-effector and thus to make the optimized linkage system as simple as possible.

To illustrate why this step is needed, consider Figure 2.18. The two systems in Figure 2.18 are kinematically equivalent as long as the same input motions are prescribed in the same input link and the end-effector locations are the same. The

difference is that one system has the simplest configuration while the other does not. Note that the system in Figure 2.18(a) can turn into the system having the simplest configuration in Figure 2.18(b) if $L_{1,5}, L_{4,6}, L_{5,6}, L_{5,7}$ and $L_{4,7}$ are removed and $L_{4,5}$ is inserted to connect nodes 4 and 5. Because layouts obtained after the Step 2 processing may look like the system in Figure 2.18(a) having a complex configuration, we aim to convert such systems into systems having the simplest configurations as shown in Figure 2.18(b) through the Step 3 processing.

Step 3 consists of three processes, (a) grouping, (b) joint identification, and (c) reconfiguration. We will explain these processes by showing how a layout shown in Figure 2.19(a) can be simplified. The layout may be viewed as a linkage mechanism obtained after Step 2. The first process in Step 3 is to form a single rigid body by grouping together a set of link elements that move at the same angular velocity. To this end, we first calculate the angular displacement $\Delta\theta_{i,m}$ of link $L_{i,m}$ between time step t^*-1 and t^* . (A typical value of t^* in this study was 6):

$$\Delta\theta_{i,m} = \left| \cos^{-1} \left\{ \frac{x_m(t^*) - x_i(t^*)}{l_{i,m,0}} \right\} - \cos^{-1} \left\{ \frac{x_m(t^*-1) - x_i(t^*-1)}{l_{i,m,0}} \right\} \right| \quad (2.20)$$

In equation (2.20), $l_{i,m,0}$ represents the initial length of element $L_{i,m}$ connecting node i and node m and $x_m(t^*)$ denotes the x coordinate of node m at time t^* .

After $\Delta\theta_j$'s are calculated for all elements, they are sorted by their magnitudes in

the ascending order and stored as an array. Then, we check if there is a finite jump between $\Delta\theta_{j'}^{sorted}$ and $\Delta\theta_{j'+1}^{sorted}$, where $\Delta\theta_{j'}^{sorted}$ denotes the sorted $\Delta\theta$ value of the component j' in the array. If $\Delta\theta_{j'+1}^{sorted} - \Delta\theta_{j'}^{sorted} > \delta_{tol}$ (a prescribed value), then the corresponding elements are declared to belong to different rigid bodies. Otherwise, they are declared to belong to the same rigid-body. Referring to Figure 2.19 (a), there are four rigid bodies identified by this grouping process. For instance, the link elements $L_{4,6}, L_{4,7}, L_{5,6}, L_{5,7}, L_{6,7}$ belong to the same rigid body (group 4) because they have virtually the same $\Delta\theta$ values.

There is a special case where the above-mentioned grouping process cannot be directly used. As an example, consider the case when $l_{1,2,0} = l_{4,5,0}$ and $l_{1,5,0} = l_{2,4,0}$ in the linkage mechanism shown in Figure 2.19(a). In this case, links $L_{1,2}, L_{2,4}, L_{4,5}$, and $L_{1,5}$ form a parallelogram in which $\Delta\theta_{1,2} = \Delta\theta_{6,7}$ ($\Delta\theta_{4,6} = \Delta\theta_{4,7} = \Delta\theta_{5,6} = \Delta\theta_{5,7}$) and $\Delta\theta_{1,5} = \Delta\theta_{2,4}$ ($= \Delta\theta_{2,3} = \Delta\theta_{3,4}$). Although the rigid link $L_{1,2}$ and the rigid body formed by $L_{6,7}$ (and $L_{4,6}, L_{4,7}, L_{5,6}, L_{5,7}$) should be identified as different rigid bodies, the above-mentioned grouping algorithm will declare, in this special situation, that the two rigid bodies are the same rigid body. After grouping through the examination of their angular displacements, therefore, one must further check if an identified rigid body indeed consists of links that are actually connected. To avoid erroneous grouping, an algorithm to check common nodes will be used. To this end, we form a linear adjacency matrix \mathbf{A} [74]

for a group, and use a TSP program such as “shortestpath” followed by “biograph” in MATLAB to check if all links in the group indeed belong to the same rigid body. If no path connecting a certain node to another node is found by a TSP program, then it is an indication that two or more rigid bodies are erroneously included in the group. In the special case considered earlier ($l_{1,2,0} = l_{4,5,0}$ and $l_{1,5,0} = l_{2,4,0}$), for example, the application of the TSP algorithm to the adjacency matrix of a set of links $L_{1,5}, L_{2,3}, L_{2,4}$ and $L_{3,4}$ that are initially-assumed to belong to the same group finds no connecting path. Therefore, the original group consisting of $L_{1,5}, L_{2,3}, L_{2,4}$ and $L_{3,4}$ will be decomposed into two groups (rigid bodies): a group consisting of $L_{1,5}$ and the other group consisting of $L_{2,3}, L_{2,4}$ and $L_{3,4}$. There are a few other cases where such erroneous grouping may occur. Therefore, the link connectivity checking by using the TSP algorithm should be included as a part of the grouping process. Our experiences show that rigid-body groups directly identified by the grouping process typically do not involve more than 5 or 7 nodes, so that the computational cost of solving the TSP problem is negligible compared to other computational costs.

The next process is joint identification. It is needed for the next “reconfiguration” process to remove elements that work only as structurally-reinforcing elements without affecting system kinematics. By noting that a joint node should be shared by two or more rigid groups, we search for shared nodes. Referring to Figure 2.19(b), node 2 appears both in Group 1 and Group 2 and node 4, both in Group 2 and Group

3. Therefore, node 2 and node 4, marked with the bracket “{ }” in Figure 2.19(b), are identified as joint nodes. For the subsequent reconfiguration process, it is also necessary to identify pivot nodes. By the proposed modeling and the definition of the ground spring, any node connected to the maximum stiffness spring (i.e. $\xi^k = 1$) becomes a ground pivot. In Figure 2.19(b), node 5 is a ground pivot, which is indicated by angle brackets as $\langle 5 \rangle$. The locations of the non-design pivot and the end-effector are nodes 1 and 3, respectively. For subsequent discussions, joint nodes, an end-effector, and nodes of ground pivots will be called essential nodes.

The last process in the simplification algorithm is to reconfigure each of the identified rigid-bodies by connecting only its essential nodes. For instance, only $L_{4,5}$, the link connecting a joint (node 4) and a pivot (node 5), will be selected to represent Group 3 as depicted in Figure 2.19(c).

To illustrate how the three processes in Step 3 are applied, let us revisit Case 3 in Section 2.3.1. Figure 2.20 shows the details of how the final layout obtained from the post-processed layout by Step 2 can be further processed by the three consecutive processes in Step 3.

Table 2.1 summarizes the values of the parameters ζ and δ_{tol} for all problems considered in this paper. It also compares the efficiency values ($\bar{\eta}$) before and after the application of the proposed post-processing algorithm. The fact that $\bar{\eta}_{\text{opt}} \approx \bar{\eta}_{\text{post}}$ implies that the post-processing algorithm maintains the linkage layouts originally found by the optimization formulation.

2.5 Summary

The synthesis of planar rigid-body link mechanisms was considered in the frame of ground-structure topology optimization. As in earlier researches, we also used real-valued design variables and a nonlinear-bar base ground model. Compared with the existing efforts based on the topology optimization idea, the following new attempts were made.

Firstly, we demonstrated a new possibility to handle the discrete DOF-condition by maximizing the transmittance efficiency function. The concept of transmittance efficiency has already been used for the synthesis of “compliant” mechanisms, but its use for the synthesis of rigid-body mechanisms, as proposed here, is apparently very promising; it was shown that the difficult issue of satisfying a discrete DOF in an optimization formulation using real-valued design variables can be resolved. Indeed, the transmittance efficiency maximization is shown to DOF-redundancy and deficiency simultaneously. Especially to control the DOF-redundancy, an external force that could perturb a system being synthesized is introduced. An external force is applied in the direction connecting the target position of the end-effector at the current step and that at the next step. The use of the efficiency function was also shown to help yield distinct black-and-white layouts. Because the objective function handles the DOF conditions, the requirement that an end-effector of a synthesized mechanism traces a desired path is treated as a constraint equation.

Secondly, we do not use any mass constraint because it is not possible to select a specific value in advance. However, the mechanism synthesis without any mass

constraint would yield floating or reinforcing links that do not actually participate in producing a desired motion although the synthesized mechanism produces a desired motion. To identify the simplest rigid-body link mechanism from the results obtained by the topology optimization formulation, therefore, we newly developed a systematic 3-step post-processing algorithm consisting of binarizing, pruning, and simplification. After giving the details of the algorithm, we demonstrated how each step in the algorithm processes the optimized linkage layout to the final one.

Using the proposed method, we synthesized the Grashof-type four-bar linkages for which input links go through full cyclic motions. As the output motions of their end-effectors, three representative motions including the motion involving a crunode were considered. While these problems were to recover the already-known linkage mechanisms, they certainly showed the effectiveness of the proposed approach using the transmittance efficiency function and the 3-step post-processing algorithm. A challenging problem was to synthesize an automobile steering mechanism satisfying the Ackermann condition. This problem, which has not been solved earlier in the existing literature, was solved by the proposed approach. Depending on how the design domain is discretized, different linkage mechanisms were obtained but they were shown to outperform a nominal four-bar linkage mechanism.

Table 2.1 Parameters used at post-processing and comparison of the results.

	λ	δ	$\bar{\eta}_{opt}$	$\bar{\eta}_{post}$
Design Test 1	0.200	0.010	0.9805	0.9985
Design Test2	0.200	0.010	0.9956	0.9985
Design Test3	0.200	0.010	0.9677	0.9987
Steering (7 by 3)	0.050	0.010	0.9544	0.9825
Steering (6 by 3)	0.050	0.010	0.9739	0.9845

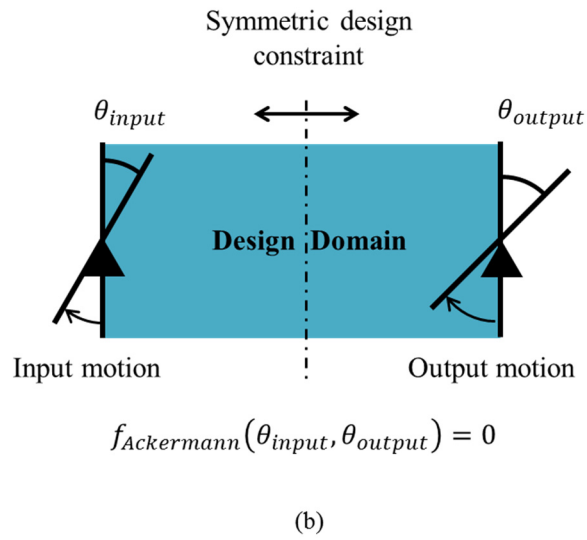
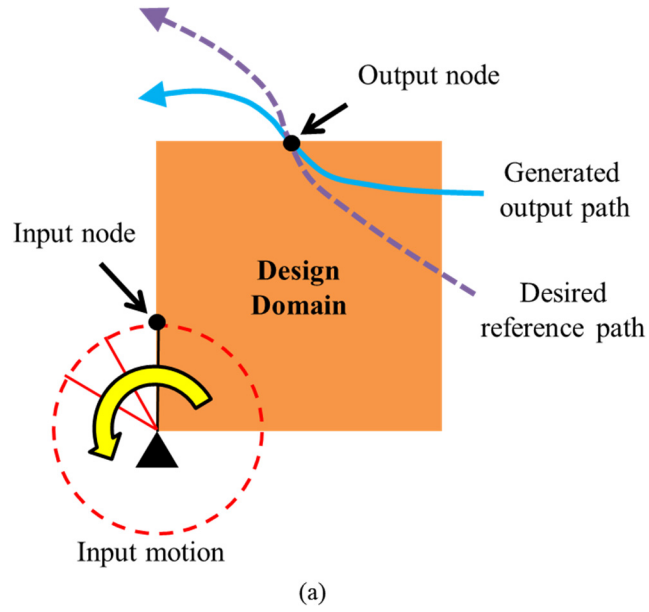


Figure 2.1 Design domain and problem description for synthesizing (a) the Grashof-type linkage systems generating desired paths and (b) an automobile steering mechanisms satisfying Ackermann condition.

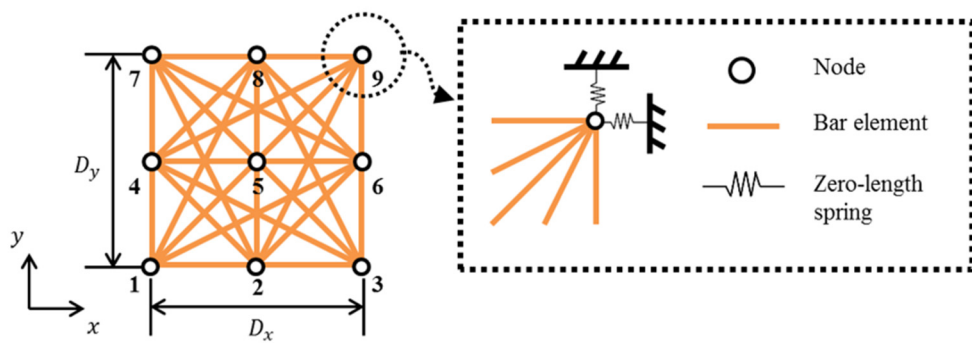
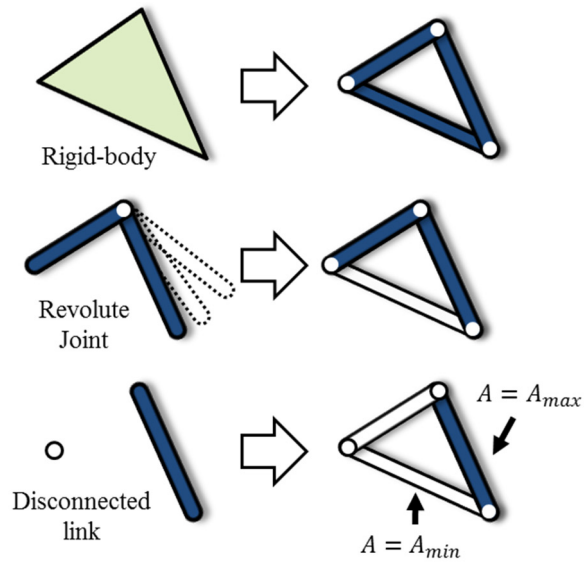
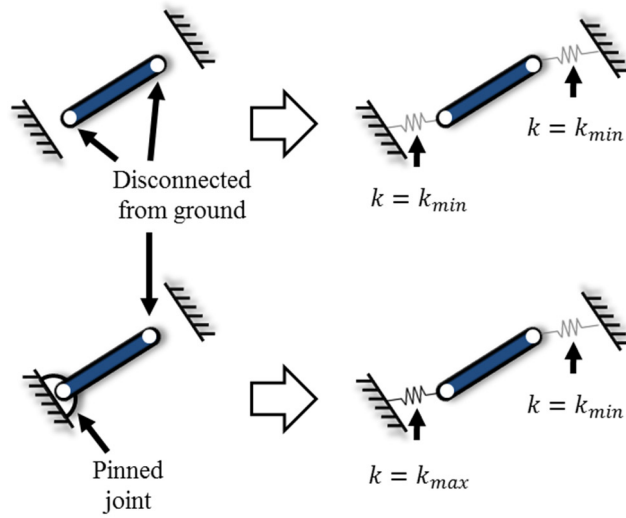


Figure 2.2 The proposed ground structure based rigid-body mechanism synthesis model comprised of nonlinear bar elements and zero-length springs.



(a)



(b)

Figure 2.3 Representation of (a) various rigid-body configurations and (b) link connections to the ground by using the employed bar-spring model.

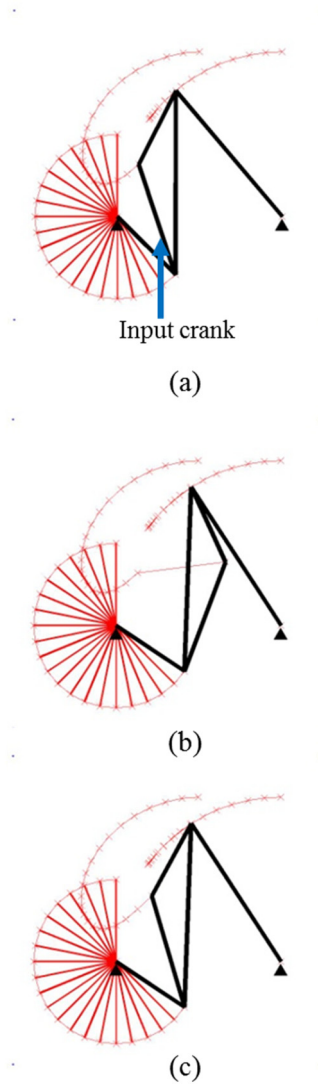


Figure 2.4 Possible occurrence of circuit defects depending on the employed numerical solvers. (a) Stable linkage configuration at input crank angle (θ_{in}) equal to 225° (b) Converged linkage configuration by the Newton-Raphson algorithm at $\theta_{in} = 236.25^\circ$ (c) Converged linkage configuration by the Levenberg-Marquardt algorithm at $\theta_{in} = 236.25^\circ$.

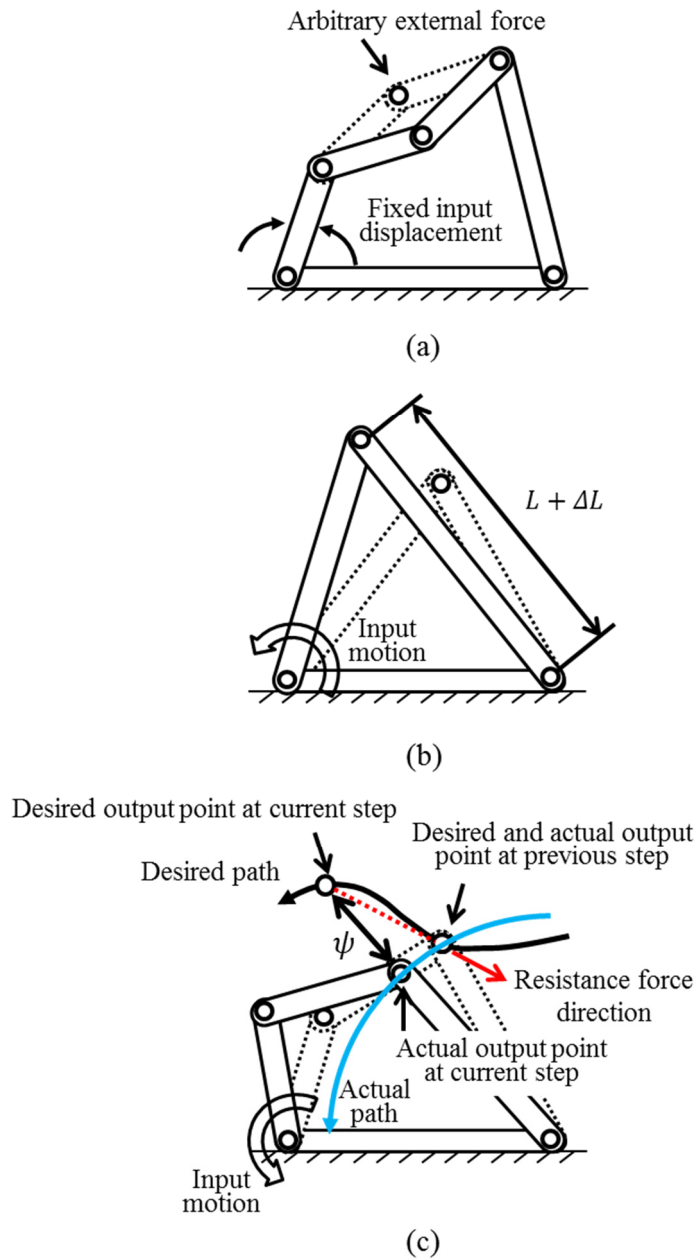


Figure 2.5 Illustration of linkage systems having different degrees of freedom (a) DOF = 2, (b) DOF = 0, and (c) DOF = 1.

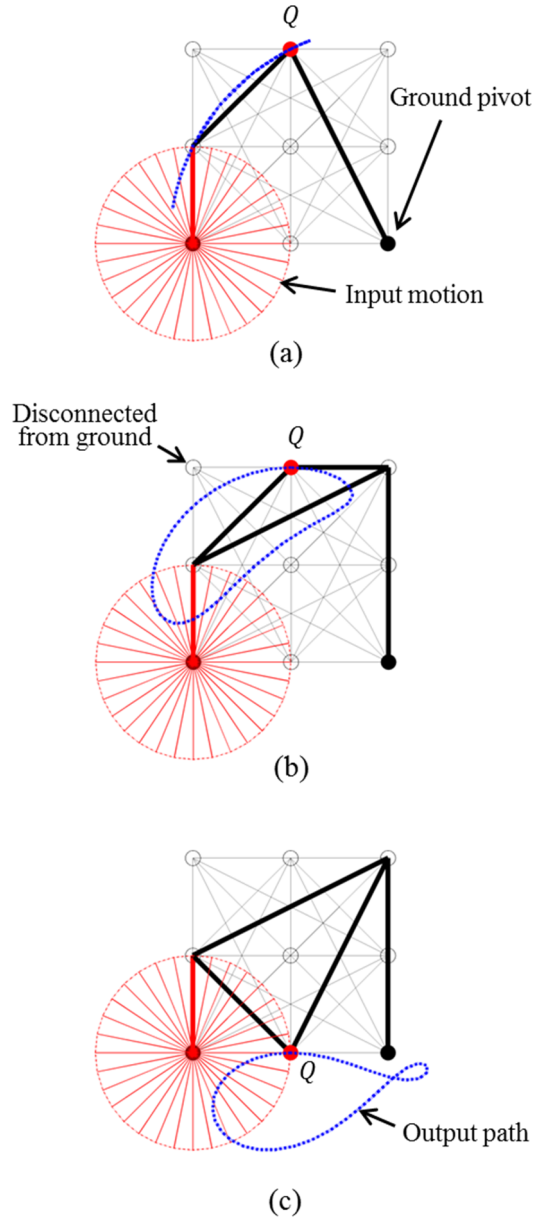


Figure 2.6 Three Grashof-type four-bar linkage mechanisms to be recovered by the proposed optimization formulation (a) Case 1, (b) Case 2, and (c) Case 3 (Q : end-effector position).

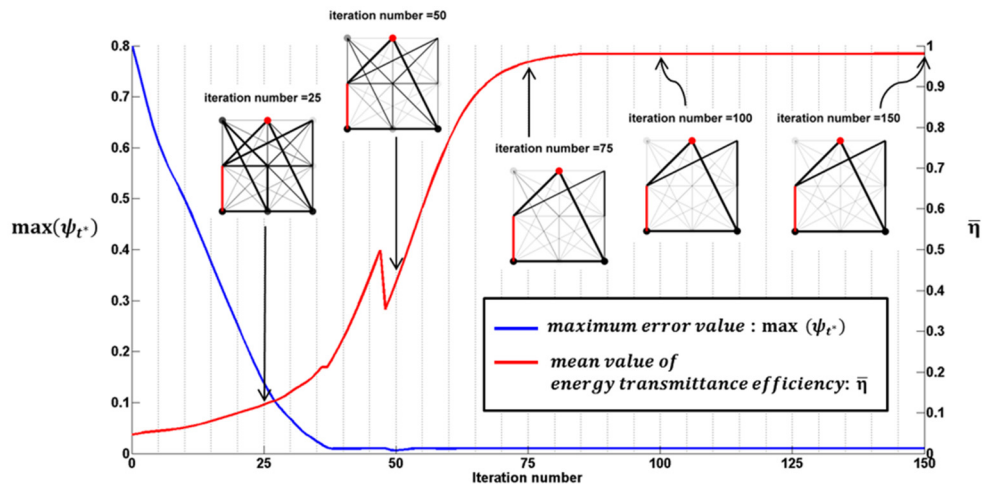


Figure 2.7 Iteration history and intermediate layouts for Case 1.

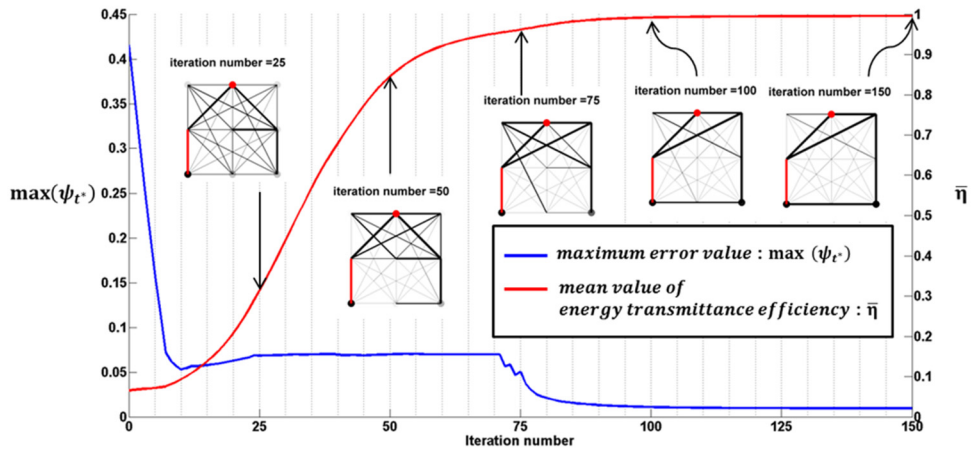


Figure 2.8 Iteration history and intermediate layouts for Case 2.

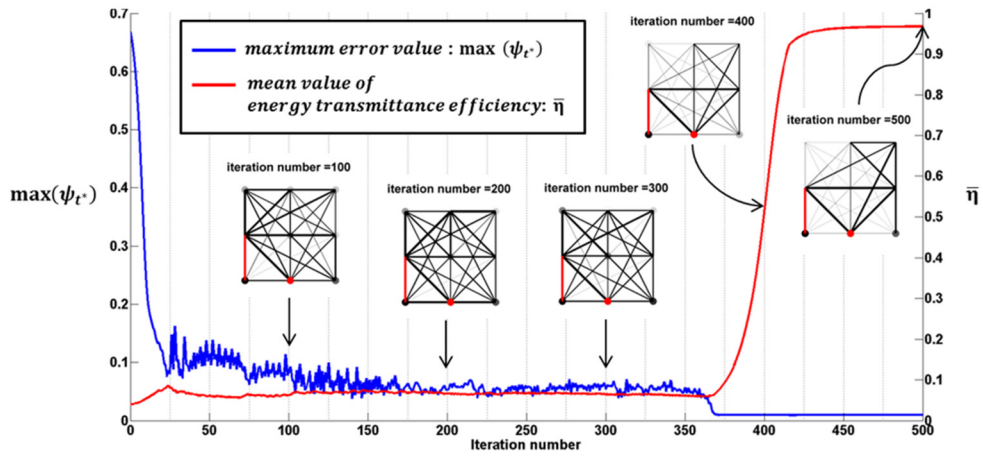


Figure 2.9 Iteration history and intermediate layouts for Case 3.


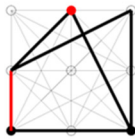
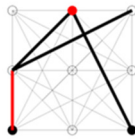
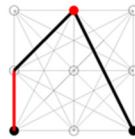

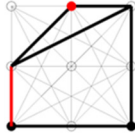
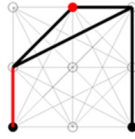
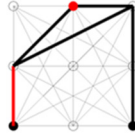
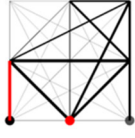
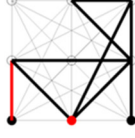
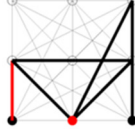
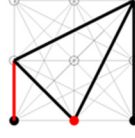
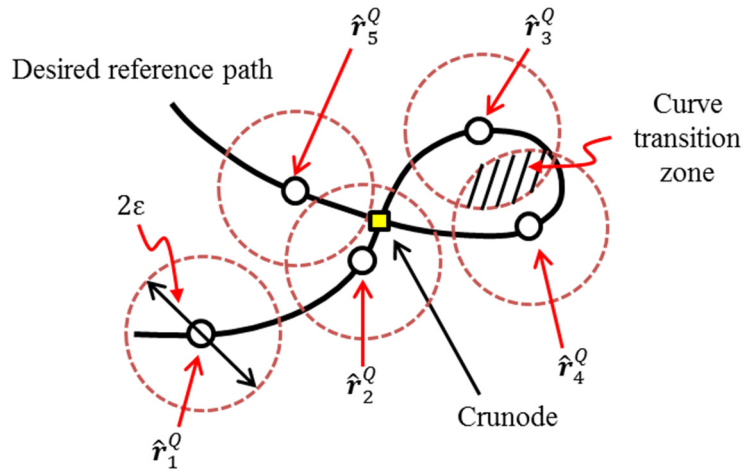
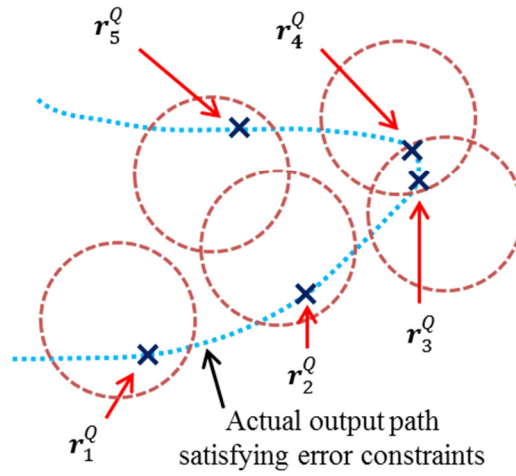
Case	Converged by equations (14,15)	Post processing		
		STEP 1	STEP 2	STEP 3
Case 1				
Case 2				
Case 3				

Figure 2.10 Layouts before and after the application of the proposed three-step post-processing algorithm (In the directly-converged results, the gray levels in the links correspond to the design variable values. In the post-processed results, only the thick lines represent the results).



(a)



(b)

Figure 2.11 The effects of ε in equation (2.15) on the solution convergence. A path involving a crunode is illustrated as an example.

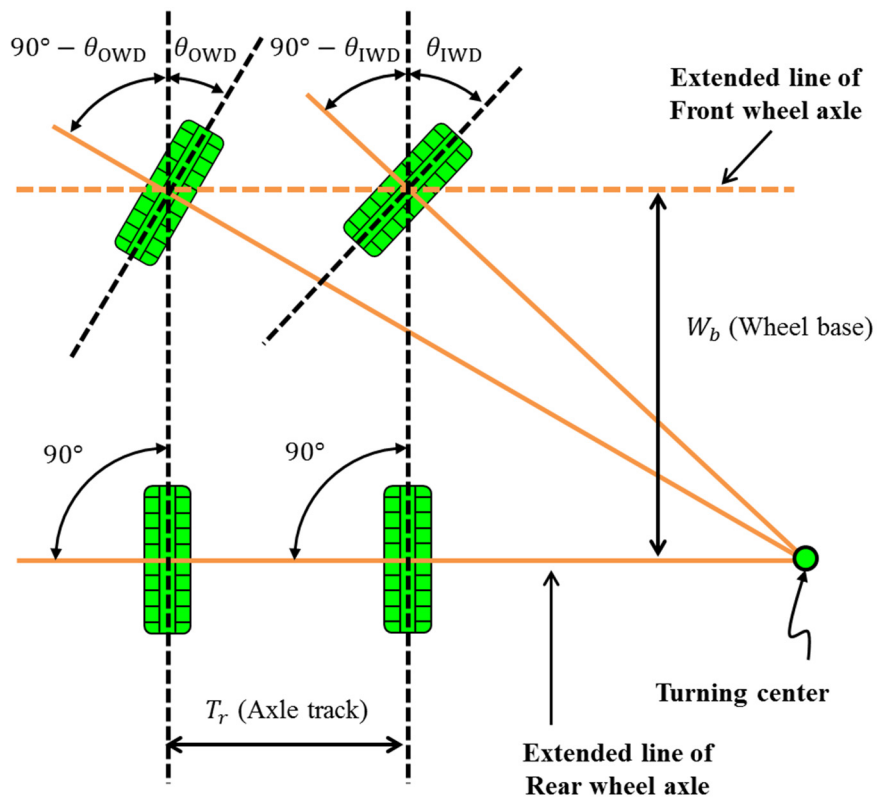


Figure 2.12 Schematic illustration of the Ackermann condition (Four tires and wheel axles are indicated in the figure).

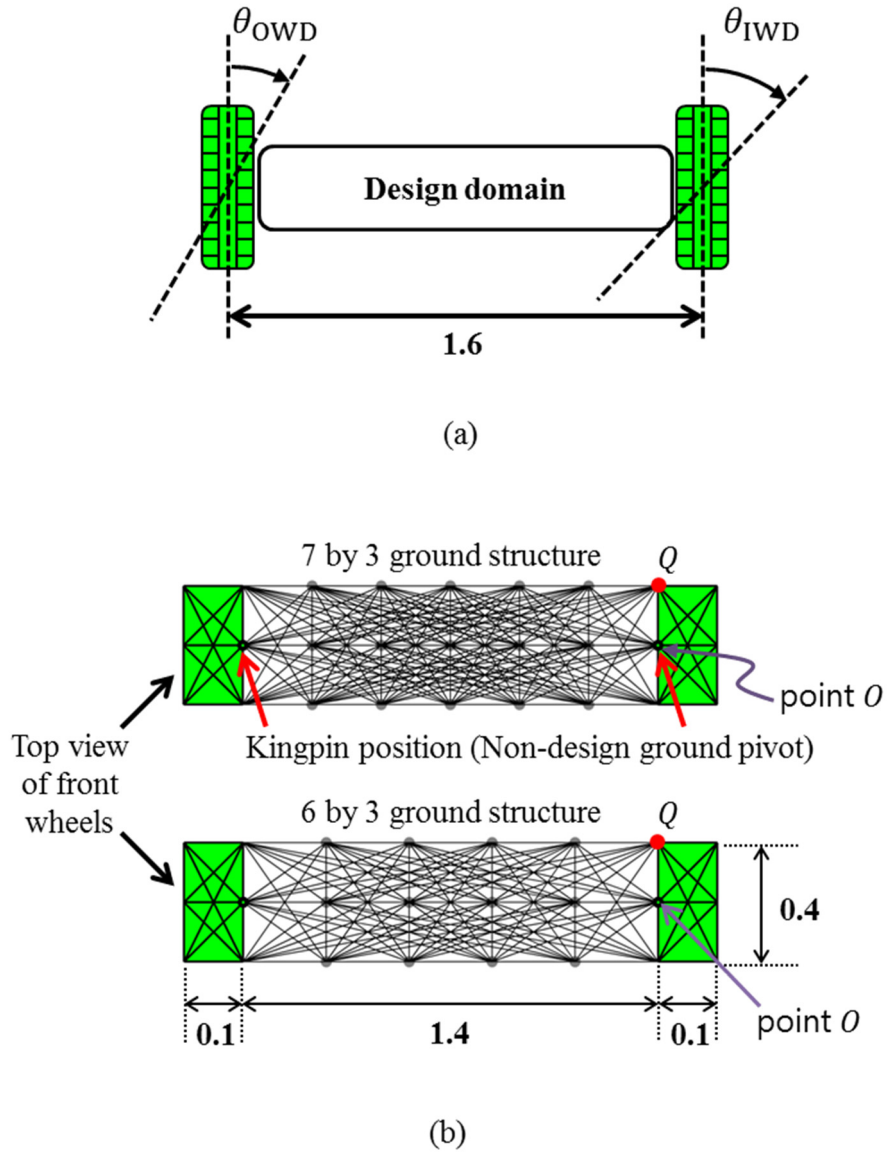


Figure 2.13 (a) Design domain for steering system synthesis (b) Two bar-spring ground models with 6 by 3 and 7 by 3 discretizations.

Iteration number	7 by 3 ground structure Converged $n_i = 300$	6 by 3 ground structure Converged $n_i = 209$
$n_i = 0$		
$n_i = 10$		
$n_i = 20$		
$n_i = 50$		
$n_i = 100$		
Converged		
Result after post processing		
$\alpha = 15^\circ$		
$\alpha = 30^\circ$		

Figure 2.14 Intermediate and the final layouts for the synthesis of steering systems satisfying the Ackermann condition. (n_i : iteration number)

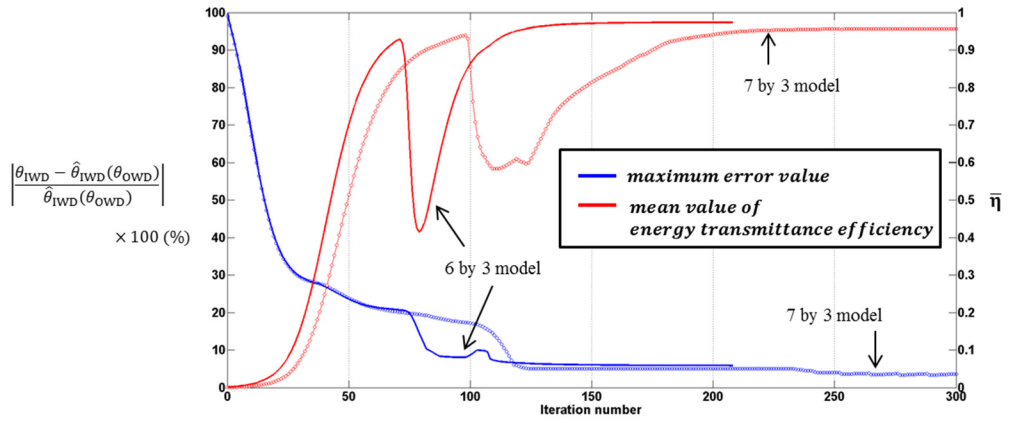


Figure 2.15 Iteration histories for the steering system synthesis problem.

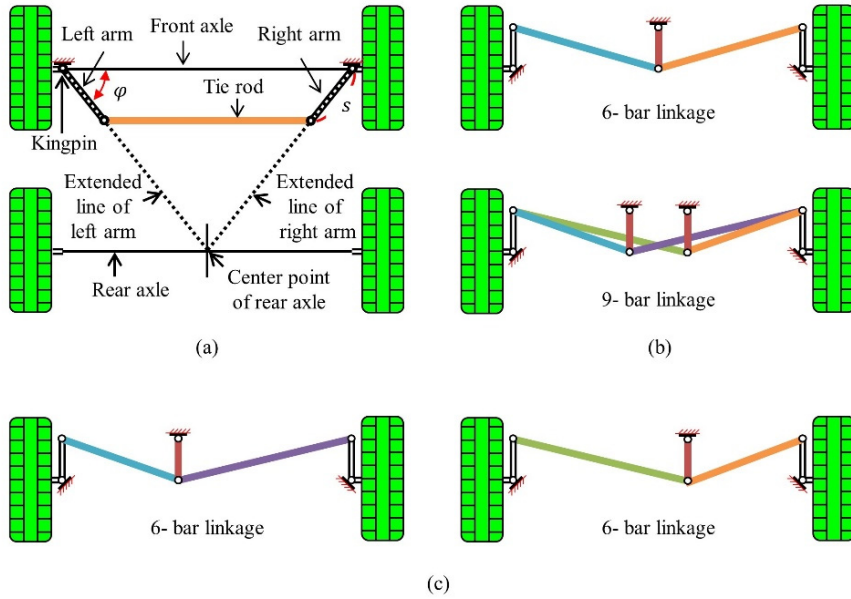


Figure 2.16 Comparison of (a) a typical four-bar linkage (for an automobile steering system) and (b) the optimized linkages by the proposed method. (c) The 9-bar linkage in (b) divided into two 6-bar linkages for the interpretation of the result.

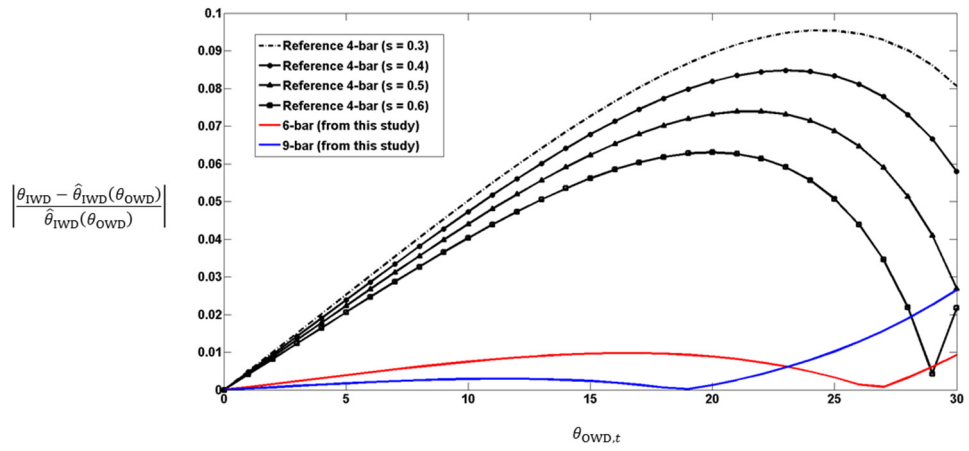
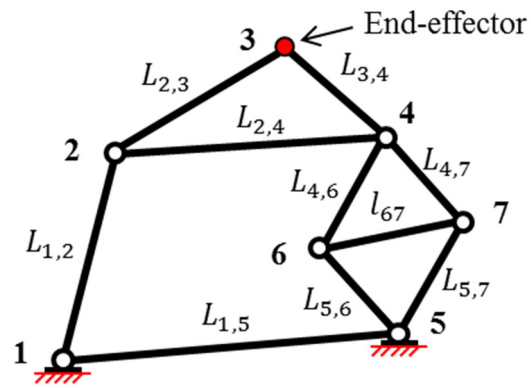
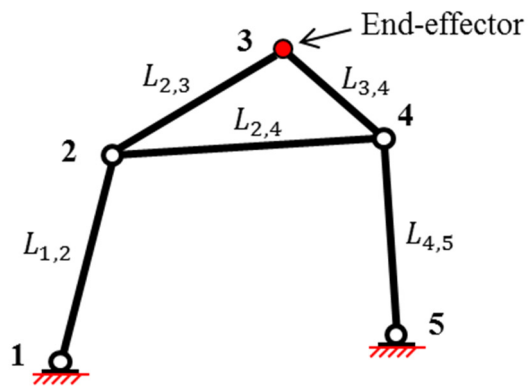


Figure 2.17 Comparison of the optimized and reference linkage mechanisms.



(a)



(b)

Figure 2.18 Kinematically equivalent systems. (a) configuration after Step 2 and (b) configuration after Step 3.

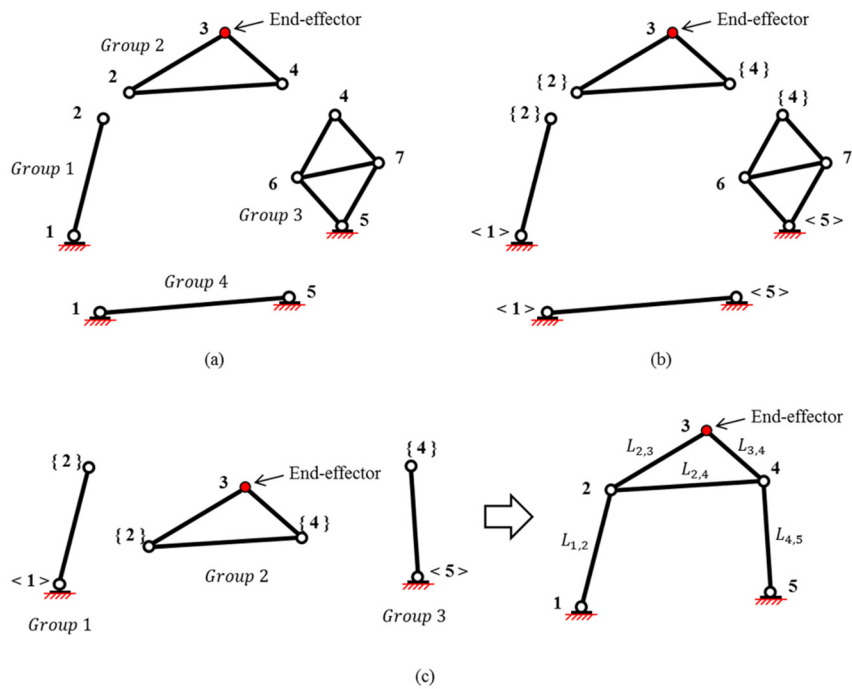


Figure 2.19 The processes of simplification algorithm consisting of (a) grouping, (b) joint identification, and (c) reconfiguration applied to the mechanism shown in Figure 2.19 (a).

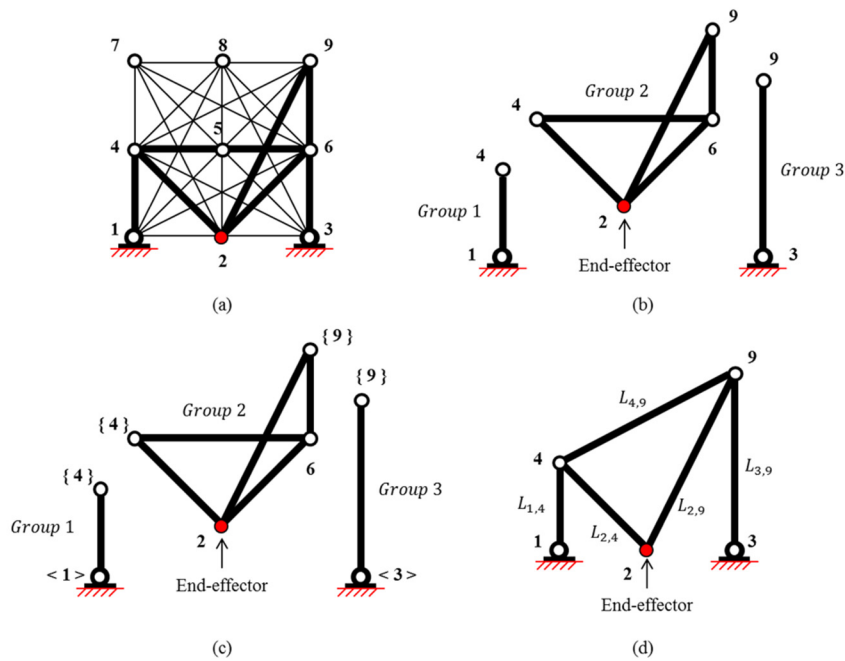


Figure 2.20 The application of the three processes of Step 3 post-processing to (a) the layout obtained by post-processing Step 2 for Case 3, (b) grouping, (c) joint identification, and (d) reconfiguration.

CHAPTER 3 ²

SPATIAL VEHICLE SUSPENSION DESIGN BY USING SIMULTANEOUS TOPOLOGY AND SHAPE OPTIMIZATION

Because suspensions critically affect the ride and handling performance of a vehicle, considerable efforts have been made to improve their design by an optimization method. In this research, a topology optimization based method for suspension synthesis is suggested by employing a three-dimensional model constructed with nonlinear bars and zero-length springs that discretize the three-dimensional space between the chassis frame and the wheel of a vehicle. For the optimization, cross-

² This chapter previously appeared as an article in International Journal for Numerical Methods in Engineering. The original citation is as follows: S.I. Kim, S.W. Kang, Y.-S. Yi, J. Park, and Y.Y. Kim, Topology optimization of vehicle rear suspension mechanisms, Int. J. Numer. Methods Eng., Special Issue on Advanced Topology Optimization (2017).

sections of the bars and stiffness values of the springs are used as the design variables and if necessary, the nodal positions of the bar elements are also employed as shape optimization variables for simultaneous topology and shape optimization. To demonstrate the validity of the proposed approach, two types of design problems were solved: recovery of known suspension mechanisms for a given set of trajectories of a wheel and synthesis of unknown suspension mechanisms satisfying several design constraints typically used in automobile industry. Through these examples, possibilities to design new advanced suspensions by the proposed optimization method are clearly demonstrated.

3.1 Review of recently developed suspension design methods

The design of vehicle suspensions is an important part of chassis design. Because ride and handling performances are mainly determined by the kinematics of vehicle suspension systems, there are a number of studies on optimal tuning of key parameters of the suspension systems [75, 76]. In these studies, mechanical and geometric parameters were mainly allowed to vary while the type (topology) of vehicle suspension systems was given or fixed. Because optimal designs by these approaches were performed within given topologies of suspension systems, the design space was limited. On the other hand, some studies attempted to find new-concept suspensions by number synthesis [77, 78]. In these attempts, they tried to find suspension topology, but no systematic suspension design method to simultaneously determine the number and dimension of a vehicle suspension was established.

In this study, a goal of research is to simultaneously determine the optimal number of links and the dimensions of vehicle suspension linkage mechanisms that satisfy desired ride and handling performances evaluated by their rigid-body kinematics. To fulfill this goal, it is proposed to set up the simultaneous synthesis of vehicle suspension mechanisms as a topology optimization problem in which optimization iterations can start without any specific baseline design. Because the synthesis method aims to find general linkage mechanisms, it should be able to find various linkage suspension systems, including double wishbone, dual-link, and 5-link suspensions, depending on design criteria. For practical consideration of suspension

design, suspensions should be synthesized in reasonable time. Therefore, it is aimed to set up the topology optimization problem for suspension synthesis by using a numerically efficient gradient-based optimizer. Note that the synthesized suspension mechanisms in operation can be treated as a system of rigid bodies for their kinematic analysis.

In this study, the kinematic synthesis of three-dimensional rear wheel suspension mechanisms will be dealt with. No dynamics or compliance will be considered. Also, the steering system is not considered because 4-wheel steering vehicles is not in consideration. To solve the mechanism synthesis problem as a topology optimization problem, the ground model shown in Figure 3.1(a) will be used. Spatial bar elements are used to discretize the three-dimensional space between the chassis frame of a vehicle and its hub carrier; a three-dimensional suspension mechanism is to be designed in the space. The spatial bar elements can have nonlinear deformations due to geometric nonlinearity, similar to planar bar elements employed in Chapter 2. The bar elements are connected to each other by ball joints at the nodes marked by filled circles in Figure 3.1(a) and they are also connected to the frame by zero-length springs or the hub-carrier. The stiffness of bar and spring elements are made to vary as functions of continuous design variables, which have values between 0 and 1. If a design variable controlling the stiffness of a bar element is sufficiently close to 0 or 1, the bar element represents a disconnected state or a rigid link state, respectively. On the other hand, if the design variable controlling spring stiffness is sufficiently close to 0 or 1, the corresponding node is free to move or rigidly connected to the

frame, respectively.

While the details of the employed model and the kinematic analysis by nonlinear finite elements will be explained in Chapter 3.2, it is pointed out that the ground model in Figure 3.1(a) is capable to represent suspension mechanisms made of links, ball and revolute joints. Thereby, fairly general three-dimensional suspension mechanisms can be formed as the result of the proposed topology optimization. However, struts will not be considered in the present model because it cannot be represented by the ground model employed. In Chapter 3.3, the topology optimization formulation to synthesize a three-dimensional suspension mechanism and the sensitivity analysis will be presented. Then the validity of the proposed approach will be demonstrated in Chapter 3.4 by dealing with two types of design problems: recovery of known real wheel suspension mechanisms for a given set of trajectories of a wheel and synthesis of unknown rear wheel suspension mechanisms under a given set of design constraints related to key ride and handling performances. As the ride related design criteria, anti-features such as anti-lift are also considered. It is also attempted to synthesize a suspension mechanism by considering the roll steering characteristics governing both the stability and agility of vehicles.

3.2 Ground structure model and kinematic analysis

This section presents a three-dimensional ground structure model needed to build an optimal spatial vehicle suspension mechanism in a specified space. For kinematic analysis of suspension systems, nonlinear finite element analysis is employed to facilitate mechanism synthesis. In planar mechanism synthesis, similar approaches were used as described in Chapter 2. The ground-structure model also employs zero-length elastic spring elements to attach the bar elements to the ground.

3.2.1 Spatial ground structure composed of bars and springs

Figure 3.1(a) illustrates the ground model occupying a parallelepiped design domain of $[D_x \times D_y \times D_z]$ with $D_x = D_y = 0.5$ m and $D_z = 0.3$ m. The design domain is a spatial region in which a vehicle suspension mechanism is supposed to be located. It should be connected to the chassis frame (or sub-frame) of a vehicle and the hub carrier attached to the hub and wheel module. The design domain is discretized by spatial bar (or truss) elements as shown in Figure 3.1(a). In the discretized mesh grid, bar elements connecting the discretizing nodes (illustrated in blue and yellow circles) are allowed to deform only along their lengthwise directions. In Figure 3.1, the nodes denoted by yellow circles are rigidly attached to some points of the hub-carrier and those denoted by blue circles are connected to the frame by zero-length springs. Therefore, the latter nodes represent a set of candidate hard points.

It will be now explained how a suspension system can be represented by the model

depicted in Figure 3.1(a). The left illustration in Figure 3.1(b) illustrates a double wishbone suspension represented by the ground model consisting of a set of bars and springs; the bars denote rigid links and their nodes are rigidly connected to the frame or the hub carrier by ball joints. (The hard points are connected through zero-length springs of full stiffness in actual modeling. This modeling will be explained below in more details.) To interpret the kinematics of the model, the right-hand side illustration in Figure 3.1(b) is prepared; it demonstrates how two arms of the double wishbone suspension are represented by bars and nodes attached to the frame and the hub carrier. Two colored triangles are used to denote the two arms. The upper and lower arms are represented by two and three bars, respectively and they all behave as if they are connected to the hub carrier by a spherical joint and to the frame by a revolute joint. Note that the axes of the revolute joints are indicated by red dotted lines passing through the nodes attached to the frame. In case of the lower arm, it is represented by three bars one of which is redundant because their end nodes attached to the frame are all along the same revolute joint axis.

Then, it needs to be explained by using Figure 3.1(c) how bar elements can be connected to the ground (i.e., the frame or the hub carrier). Here, blue double lines represent spatial bar elements and black open circles denote the ground-structure discretizing nodes, which can work as candidate hard points. They are connected to the chassis frame (ground in the figure) through the zero-length springs by which the connectivity between node and frame is defined. For the gradient-based topology optimization of suspension mechanisms, the cross sectional area (A) of bar elements

and the stiffness (k) of spring elements are varied as functions of continuous real design variables and they are bounded by $A_{\min} \leq A \leq A_{\max}$ and $k_{\min} \leq k \leq k_{\max}$. If $A = A_{\min}$ or $A = A_{\max}$, the corresponding bar is regarded to disappear or to behave as a rigid bar, respectively. If $k = k_{\min}$ or $k = k_{\max}$, the corresponding spring has nearly zero or full stiffness values representing the states of disconnection or rigid connection to the ground (by a ball joint), respectively. Figure 3.1(d) shows some illustrative cases in which A and k take on their lower or upper bound values. It also shows their equivalent mechanisms, indicated by “link (S-S joint)” and “Arm (R-S module)” where R and S stand for revolute and spherical joints, respectively. The examples in Figure 3.1(d) suggest that depending on the values of A and k , different mechanisms can be represented. Therefore, the full control of these values for the three-dimensional model shown in Figure 3.1(a) can yield various desired suspension mechanisms. Formulations to find desired suspension mechanisms by the topology optimization will be presented in Chapter 3.3.

3.2.2 Nonlinear finite element analysis of spatial bar elements

Nonlinear bar elements will be employed to discretize the suspension design domain and their cross-sectional areas will be varied during mechanism synthesis. The element is the same as the one employed for planar mechanism synthesis in Chapter 2. However, the elements will be used for three-dimensional spatial ground structure modeling unlike the Chapter 2. Also, the elements will be modeled to interact with a

rigid representing “wheel” for suspension mechanism representation, so that description of the mechanical behavior of spatial bar elements will be shown in this section again with detailed expression.

Because large rotation is involved in the motion of a linkage mechanism, the bar elements should be able to express the effects of geometrical nonlinearity. To this end, the Green-Lagrange strain \mathbf{E} , the 2nd Piola-Kirchhoff stress tensor \mathbf{S} , and the St. Venant nonlinear material model which involves the modulus of elasticity tensor \mathbf{C}^{SE} will be used. Because many books on continuum mechanics (see, e.g., [18]) deal with these quantities in detail, key equations will be simply written based on the total Lagrangian formulation to describe mechanics involving geometric nonlinearity:

$$\mathbf{F} = \frac{\partial \mathbf{x}}{\partial \mathbf{X}} \quad (3.1)$$

$$\mathbf{E} = 0.5(\mathbf{F}^T \mathbf{F} - \mathbf{I}) \quad (3.2)$$

$$\mathbf{S} = \mathbf{C}^{\text{SE}} : \mathbf{E} \quad (3.3)$$

$$(\mathbf{F}^{\text{int}}) \cdot \delta \mathbf{u} = \int_V (\mathbf{S} : \delta \mathbf{E}) dV \quad (3.4)$$

$$\mathbf{K}^{\text{tan}} \Delta \mathbf{u} = \frac{d}{d\varepsilon} \left[\mathbf{F}^{\text{int}}(\mathbf{u} + \varepsilon \Delta \mathbf{u}) \right]_{\varepsilon=0} \quad (3.5)$$

In the above equations, \mathbf{X} and \mathbf{x} denote the un-deformed and deformed configurations of a bar element, respectively and \mathbf{F} , the deformation gradient tensor. Equation (3.4) defines the internal force vector \mathbf{F}^{int} through the variational principle where \mathbf{u} denotes displacement field and quantities with δ denoting

virtual quantities (such as virtual displacement $\delta \mathbf{u}$). Equation (3.5) defines the tangent stiffness \mathbf{K}^{tan} where $\Delta \mathbf{u}$ denotes incremental displacement (arbitrary perturbed displacement for linearization). The tangent stiffness corresponds to the Jacobian matrix of multi-variable nonlinear equations.

If a spatial bar element is assumed to deform only in its lengthwise direction, as shown in Chapter 2 for dealing with planar mechanism synthesis, much simplification can be possible in Equations (3.1-3.5). In this case, only nonzero strain in \mathbf{E} is the normal strain defined along the lengthwise direction of a bar, which is simply denoted by E :

$$E = \frac{l^2 - l_0^2}{2l_0^2} \quad (3.6)$$

where l_0 and l denote the initial and deformed length of a bar, respectively. With E in Equation (3.6), Equations (3.3) and (3.4) can be replaced by

$$S = CE \quad (3.7)$$

$$(\mathbf{F}_{\text{bar}}^{\text{int}}) \cdot \delta \mathbf{u} = \int_V S(\delta E) dV \quad (3.8)$$

where C is the modulus of elasticity component corresponding to the lengthwise direction, S is the 2nd Piola-Kirchhoff stress corresponding to normal stress in longitudinal direction of a bar element and $\mathbf{F}_{\text{bar}}^{\text{int}}$, the internal force vector. Because the finite element method will be used for the kinematic analysis of a mechanism system, subsequent discussion will be based on a discretized model consisting of nonlinear bar elements allowing lengthwise deformation only. We also assume that

strain is uniform in each bar.

First, consider the configurations of the spatial bar element j having two nodes i and $m (\neq i)$ before and after deformation shown in Figure 3.2. The Cartesian coordinates of node k in the un-deformed and deformed configurations are denoted by $\mathbf{X}_k = \{X_k, Y_k, Z_k\}^T$ and $\mathbf{x}_k = \{x_k, y_k, z_k\}^T$, respectively. The three-dimensional displacement vector of node k is denoted by $\mathbf{u}_k = \{u_k, v_k, w_k\}^T$. To denote the bar element j , either “ j ” or “ (i, m) ” is used interchangeably. When the (i, m) notation is used, i and m denote two end nodes of the bar j . So, the bar lengths at the deformed and undeformed states will be represented by $l_{j,0} = l_{i,m,0}$ and $l_j = l_{i,m}$, respectively. They can be calculated as $l_{j,0} = \|\mathbf{X}_i - \mathbf{X}_m\|_2$, $l_j = \|\mathbf{x}_i - \mathbf{x}_m\|_2$.

To calculate $\mathbf{F}_{j,\text{bar}}^{\text{int}}$, the internal force vector in the bar j , Equation (3.8) can be used. Because strain and stress in each bar are assumed to be uniform, it can be simply calculated as

$$\mathbf{F}_{j,\text{bar}}^{\text{int}} = \frac{A_j S_j \Delta \mathbf{x}_j}{l_{j,0}} \quad (j = 1, \dots, N_\ell) \quad (3.9)$$

where A_j is the cross section of the bar element j , and S_j is the 2nd Piola-Kirchhoff stress. The total numbers of nodes and bar elements used to construct a ground-structure model are denoted by N_n and N_ℓ , respectively. The vector $\Delta \mathbf{x}_j$

in (3.9) is defined as

$$\Delta \mathbf{x}_j = \{x_i - x_m, y_i - y_m, z_i - z_m, x_m - x_i, y_m - y_i, z_m - z_i\}^T \quad (3.10)$$

To explicitly write the tangent stiffness matrix $\mathbf{K}_{j,\text{bar}}^{\text{tan}}$ of the bar element j , Equation (3.5) is used with \mathbf{K}^{tan} replaced by $\mathbf{K}_{j,\text{bar}}^{\text{tan}}$ and $\Delta \mathbf{u}$ replaced by $\Delta \mathbf{u}_j = \{\Delta u_i, \Delta v_i, \Delta w_i, \Delta u_m, \Delta v_m, \Delta w_m\}^T$, which is the incremental displacement vector of the bar element j having the end nodes i and m . If \mathbf{F}^{int} in Equation (3.5) is replaced by $\mathbf{F}_{j,\text{bar}}^{\text{int}}$ in Equation (3.9), the following equations can be obtained:

$$\left[\mathbf{K}_{j,\text{bar}}^{\text{tan}} \right] \Delta \mathbf{u}_j = \frac{d}{d\varepsilon} \left[\mathbf{F}_{j,\text{bar}}^{\text{int}} \left(\mathbf{u}_j + \varepsilon \Delta \mathbf{u}_j \right) \right]_{\varepsilon=0} \quad (3.11)$$

$$\mathbf{K}_{j,\text{bar}}^{\text{tan}} = \frac{A_j C}{l_{j,0}} \left[\left(\frac{\Delta \mathbf{x}_j}{l_{j,0}} \right) \left(\frac{\Delta \mathbf{x}_j}{l_{j,0}} \right)^T + E_j \mathbf{B} \right] \quad (3.12)$$

In Equation (3.12), E_j denotes a simplified Green-Lagrange strain corresponding to the axial stretch of the bar element j . The matrix \mathbf{B} in (3.12) is given by

$$\mathbf{B} = \begin{bmatrix} \mathbf{I}_3 & -\mathbf{I}_3 \\ -\mathbf{I}_3 & \mathbf{I}_3 \end{bmatrix} \quad (3.13)$$

where \mathbf{I}_3 denotes a 3 by 3 identity matrix. If the bar element is 2-dimensional elements as described in Chapter 2, the \mathbf{I}_3 needs to be converted to \mathbf{I}_2 , which is a 2 by 2 identity matrix. Also, one can see that the tangent stiffness matrix becomes the stiffness matrix of a linear finite bar element [79] when displacement is small.

Artificial zero-length spring elements illustrated in Figure 3.1(c) are assumed to have the same stiffness values for all directions. If $k_i, (X_i, Y_i, Z_i)$ and (x_i, y_i, z_i) denote the stiffness, the undeformed and the deformed coordinates of the zero-length spring element i , its internal force vector $\mathbf{F}_{i,\text{spring}}^{\text{int}}$ and tangent stiffness matrix $\mathbf{K}_{i,\text{spring}}^{\text{tan}}$ are given by

$$\mathbf{F}_{i,\text{spring}}^{\text{int}} = k_i \{x_i - X_i, y_i - Y_i, z_i - Z_i\}^T \quad (3.14)$$

$$\mathbf{K}_{i,\text{spring}}^{\text{tan}} = \text{diag}[k_i, k_i, k_i] \quad (3.15)$$

with $i = 1, 2, \dots, N_k$, where N_k is the total number of spring elements.

Once the internal forces and tangent stiffness matrices of the employed finite elements are obtained for each element, the total internal force and tangent stiffness of the system can be expressed by using an assembly operator \bigcup as

$$\mathbf{F}^{\text{int}}(\mathbf{u}) = \bigcup_{j=1}^{N_\ell} [\mathbf{F}_{j,\text{bar}}^{\text{int}}(\mathbf{u})] + \bigcup_{i=1}^{N_n} [\mathbf{F}_{i,\text{spring}}^{\text{int}}(\mathbf{u})] \quad (3.16)$$

$$\mathbf{K}^{\text{tan}}(\mathbf{u}) = \bigcup_{j=1}^{N_\ell} [\mathbf{K}_{j,\text{bar}}^{\text{tan}}(\mathbf{u})] + \bigcup_{i=1}^{N_n} [\mathbf{K}_{i,\text{spring}}^{\text{tan}}(\mathbf{u})] \quad (3.17)$$

where \mathbf{u} is the total nodal displacement vector of length $3N_n \times 1$.

3.2.3 Rigid-body motion and constraint of the hub-carrier

Nonlinear bar elements will be employed to discretize the suspension design domain and their cross-sectional areas will be varied during mechanism synthesis. The

element is the same as the one employed for planar mechanism synthesis in Chapter 2. However, the elements will be used for three-dimensional spatial ground structure modeling unlike the Chapter 2. Also, the elements will be modeled to interact with a rigid representing “wheel” for suspension mechanism representation, so that description of the mechanical behavior of spatial bar elements will be shown in this section again with detailed expression.

Because a wheel (see Figure 3.1) moves as a rigid body, its translational motion can be depicted by $\mathbf{R}_w = \{q_x, q_y, q_z\}^T$, the translation of the wheel center. It is expressed in the space-fixed coordinate system. To represent the roll, pitch, and yaw angles of the hub carrier³, the Tait-Bryant angles $\boldsymbol{\theta} = \{\theta_1, \theta_2, \theta_3\}^T$ are introduced that are defined in a coordinate system fixed at the hub carrier. Accordingly, $\mathbf{q}_w = \{q_x, q_y, q_z, \theta_1, \theta_2, \theta_3\}^T$ can be used to describe the rigid-body motion of the wheel. If \mathbf{R}_w and $\boldsymbol{\theta}$ are given, the position vector of point i on the hub-carrier can be written as

$$\mathbf{r}_{i,w} = \mathbf{R}_w + \mathbf{A}(\boldsymbol{\theta})\mathbf{s}_{i,w} \quad (3.18)$$

³ The wheel is supposed to spin relative to the hub carrier. For the present kinematic analysis, no relative spin motion is assumed to occur between the hub and the wheel.

$$\begin{aligned}
\mathbf{A}(\boldsymbol{\theta}) &= \begin{bmatrix} 1 & 0 & 0 \\ 0 & \cos\theta_1 & -\sin\theta_1 \\ 0 & \sin\theta_1 & \cos\theta_1 \end{bmatrix} \begin{bmatrix} \cos\theta_2 & 0 & \sin\theta_2 \\ 0 & 1 & 0 \\ -\sin\theta_2 & 0 & \cos\theta_2 \end{bmatrix} \begin{bmatrix} \cos\theta_3 & -\sin\theta_3 & 0 \\ \sin\theta_3 & \cos\theta_3 & 0 \\ 0 & 0 & 1 \end{bmatrix} \\
&= \begin{bmatrix} \cos\theta_2\cos\theta_3 & -\cos\theta_2\sin\theta_3 & \sin\theta_2 \\ \cos\theta_1\sin\theta_3 + \sin\theta_1\sin\theta_2\cos\theta_3 & \cos\theta_1\cos\theta_3 - \sin\theta_1\sin\theta_2\sin\theta_3 & -\sin\theta_1\cos\theta_2 \\ \sin\theta_1\sin\theta_3 - \cos\theta_1\sin\theta_2\cos\theta_3 & \sin\theta_1\cos\theta_3 + \cos\theta_1\sin\theta_2\sin\theta_3 & \cos\theta_1\cos\theta_2 \end{bmatrix}
\end{aligned} \tag{3.19}$$

In (3.18) and (3.19), $\mathbf{A}(\boldsymbol{\theta})$ denotes the transformation matrix and $\mathbf{s}_{i,w}$, the relative position vector of an arbitrary point i on the hub-carrier with respect to the hub carrier center (the same as the wheel center). The vector $\mathbf{s}_{i,w}$ can be expressed as $\mathbf{s}_{i,w} = \mathbf{r}_{i,w,0} - \mathbf{R}_{w,0}$, where $\mathbf{r}_{i,w,0}$ and $\mathbf{R}_{w,0}$ represent the position of point i and the wheel center at their initial configurations, respectively.

There are two sets of constraints to be considered for kinematic analysis. For the present suspension design problems, the vertical motion of the wheel center is given as an excitation source and it simulates a bound stroke motion imposed on a wheel (say, by a bump). The described motion can be described as the following constraint:

$$c_{w,z} = q_z - \hat{q}_z = 0 \tag{3.20}$$

where \hat{q}_z is the amount of the bound stroke imposed on the wheel center. Because the wheel displacement excitation is only in the Z direction, the displacement constraint equation (3.20) is written in scalar form. The second set of constraints is to require that the finite element nodes (which will be denoted by “ r ” below) used to form the skeleton of the ground structure in Figure 3.1(a) be attached to the nodes

(denoted by “ s ”) of the hub carrier during the whole rigid-body motion of the wheel:

$$\mathbf{c}_{s,\text{rigid}} = \mathbf{r}_{s,W} - \mathbf{x}_r = \{\mathbf{R}_W + \mathbf{A}(\boldsymbol{\theta})\mathbf{s}_{s,W}\} - (\mathbf{X}_r + \mathbf{u}_r) = 0 \quad (s, r = 1, 2, \dots, N_H) \quad (3.21)$$

where $\mathbf{X}_r = \mathbf{r}_{i,W,0}$.

Equation (3.21) states that the position vector \mathbf{x}_r of node r should be the same as the position vector $\mathbf{r}_{s,W}$ of node s . Note that $\mathbf{c}_{s,\text{rigid}}$ consists of three components $(c_{s,X,\text{rigid}}, c_{s,Y,\text{rigid}}, c_{s,Z,\text{rigid}})$. Therefore, Equation (3.21) implies $3N_H$ constraints where N_H is the total number of the hub-attached nodes.

At this point, it will be worth adding some words regarding the symbols N_α ($\alpha = \ell, n, H, k$). In the model employed in this study, springs are attached only to the nodes that are directly connected to the chassis frame (or car body). Therefore, N_k (the number of springs) is $N_k = N_n - N_H$, where N_H and N_n denote the number of the nodes attached to the hub and the number of the nodes used to discretize the ground model, respectively. For given N_n nodes for the ground model, there are $0.5N_n(N_n - 1)$ possible bar connections. However, there is no need to put bars to connect hub-attached nodes because they simply belong to a single rigid body. Therefore, the actual number of the bars in our model becomes $0.5N_n(N_n - 1) - 0.5N_H(N_H - 1)$.

For the subsequent kinematic analysis of the bar-spring system attached to the hub-carrier, it will be convenient to define the state variable vector $\boldsymbol{\mu} = \{\mathbf{q}_W^T, \mathbf{u}^T\}^T$

consisting of the nodal displacement vector \mathbf{u} of bar elements and the hub-carrier motion vector \mathbf{q}_w . The total number of variables in $\boldsymbol{\mu}$ is $3N_n + 6$ because \mathbf{q}_w representing 3 translational and 3 rotational motions has 6 variables and \mathbf{u} representing 3 displacement components for each of N_n nodes discretizing the ground structure has $3N_n$ variables.

3.2.4 Governing equations for kinematic analysis

As shall be explained in the next section, the cross-sectional areas $A_j (j=1,2,\dots,N_\ell)$ of bar elements and the stiffness of zero-length springs $k_i (i=1,2,\dots,N_k)$ will vary as functions of design variables during mechanism synthesis process. This means that a system represented by the bar-spring ground structure can represent a specific suspension mechanism if A_j and k_i are properly assigned to each of bars and springs. To find the motion of the ground structure having selected values of $A_j (j=1,2,\dots,N_\ell)$, and $k_i (i=1,2,\dots,N_k)$, the equilibrium equation of the system will be used. Treating the stroke motion of the wheel center as an input motion to the system, one can find its equilibrium state from

$$\text{Find } \mathbf{x} = \{\boldsymbol{\mu}^T, \boldsymbol{\lambda}^T\}^T \quad (3.22a)$$

$$\text{Solve } \mathbf{f}(\mathbf{x}) = \begin{Bmatrix} \mathbf{F}^{\text{net}}(\mathbf{x}) = \mathbf{F}^{\text{int}} + \mathbf{F}^{\text{con}} - \mathbf{F}^{\text{ext}} \\ \mathbf{c}(\mathbf{x}) \end{Bmatrix} = \mathbf{0} \quad (3.22b)$$

where \mathbf{c} and $\boldsymbol{\lambda}$ denote the constraint equations and the corresponding Lagrange multipliers. They are defined as

$$\mathbf{c} = \left\{ \mathbf{c}_{1,\text{rigid}}^T, \mathbf{c}_{2,\text{rigid}}^T, \dots, \mathbf{c}_{N_H,\text{rigid}}^T, c_{W,Z} \right\}^T \quad (3.23)$$

$$\boldsymbol{\lambda} = \left\{ \boldsymbol{\lambda}_{1,\text{rigid}}^T, \boldsymbol{\lambda}_{2,\text{rigid}}^T, \dots, \boldsymbol{\lambda}_{N_H,\text{rigid}}^T, \lambda_{W,Z} \right\}^T \quad (3.24)$$

The force terms (\mathbf{F}) in Eq. (3.22) are defined as

$$\mathbf{F}^{\text{int}} = \bigcup_{j=1}^{N_\ell} [\mathbf{F}_{j,\text{bar}}^{\text{int}}(\mathbf{u})] + \bigcup_{i=1}^{N_n} [\mathbf{F}_{i,\text{spring}}^{\text{int}}(\mathbf{u})] \quad (3.25a)$$

$$\mathbf{F}^{\text{con}} = \bigcup_{s=1}^{N_H} [\mathbf{F}_{s,\text{rigid}}^{\text{con}}(\boldsymbol{\mu}, \boldsymbol{\lambda})] + \mathbf{F}_{W,Z}^{\text{con}}(\boldsymbol{\mu}, \boldsymbol{\lambda}) \quad (3.25b)$$

in which \mathbf{F}^{con} denotes the vector of the constraint forces required to satisfy $\mathbf{c} = \mathbf{0}$.

The force vectors $\mathbf{F}_{s,\text{rigid}}^{\text{con}}$ and $\mathbf{F}_{W,Z}^{\text{con}}$ can be evaluated as

$$\mathbf{F}_{s,\text{rigid}}^{\text{con}} = \left[\nabla_{\boldsymbol{\mu}} (\mathbf{c}_{s,\text{rigid}}) \right] \boldsymbol{\lambda}_{s,\text{rigid}} \quad (3.26a)$$

$$\mathbf{F}_{W,Z}^{\text{con}} = \left[\nabla_{\boldsymbol{\mu}} (c_{W,Z}) \right] \lambda_{W,Z} \quad (3.26b)$$

Note that $\boldsymbol{\mu}, \mathbf{F}^{\text{net}} \in \mathbb{R}^{3N_n+6}$ and $\boldsymbol{\lambda}, \mathbf{c} \in \mathbb{R}^{3N_H+1}$.

To solve Eq. (3.22), a nonlinear solver such as the NR (Newton-Raphson) algorithm, can be used. It updates the field variable as

$$\mathbf{x}^{(k+1)} = \mathbf{x}^{(k)} - \left[\nabla_{\mathbf{x}} \mathbf{f}(\mathbf{x}^{(k)}) \right]^{-1} \mathbf{f}(\mathbf{x}^{(k)}) \quad (3.27a)$$

with

$$\nabla_{\mathbf{x}} \mathbf{f}(\mathbf{x}) = \begin{bmatrix} \nabla_{\boldsymbol{\mu}} \mathbf{F}^{\text{net}} & \nabla_{\boldsymbol{\mu}} \mathbf{c} \\ \nabla_{\boldsymbol{\lambda}} \mathbf{F}^{\text{net}} & \nabla_{\boldsymbol{\lambda}} \mathbf{c} \end{bmatrix} = \begin{bmatrix} \nabla_{\boldsymbol{\mu}} \mathbf{F}^{\text{net}} & \nabla_{\boldsymbol{\mu}} \mathbf{c} \\ (\nabla_{\boldsymbol{\mu}} \mathbf{c})^T & \mathbf{0} \end{bmatrix} \quad (3.27b)$$

where $\mathbf{x}^{(k)}$ is the variable vector at the analysis iteration step k . The specific algorithm used in this study is the Levenberg-Marquardt method, one of the NR-family solvers. The effectiveness of this method was discussed in [26]. The tangent stiffness matrix $\mathbf{K}^{\text{tan}}(\mathbf{u})$ in (3.17) will be used to evaluate $\nabla_{\boldsymbol{\mu}} \mathbf{F}^{\text{net}}$.

3.3 Optimization based formulation for mechanism synthesis

In this Chapter, a method to synthesize a vehicle suspension mechanism by using a topology optimization based formulation is proposed. For the optimization based mechanism synthesis, it needs to define the design variables for optimization, an objective function, and constraint equations. They are similar with that for the planar mechanisms synthesis in Chapter 2, however there are additional factors used for suspension mechanisms. To this end, the accurate formulation including procedure for sensitivity calculation will be written down in this section.

3.3.1 Design variables and interpolation

To find a desired suspension mechanism out of the three-dimensional bar-spring ground structure depicted in Figure 3.1 by a topology optimization method, the existences of bar and spring elements should be controlled by the design variables. As mentioned earlier, large-sized problems, such as the synthesis problems discussed here, cannot be efficiently solved with discrete variables directly representing the existences of elements. Therefore, real-valued design variables ξ_j^A and ξ_i^k ($\xi_{min} \leq \xi_j^A, \xi_i^k \leq \xi_{max} = 1$) are used to interpolate the area of the bar element j and the stiffness of the spring element i as

$$A_j = A_0 \left(\xi_j^A \right)^p \quad (j = 1, 2, \dots, N_\ell) \quad (3.28a)$$

$$k_i = k_0 \left(\xi_i^k \right)^p \quad (i = 1, 2, \dots, N_k) \quad (3.28b)$$

where A_0 and k_0 are the nominal bar cross-sectional area and spring stiffness and p is a penalization constant. The value of $p=3$ and $\xi_{\min}=0.001$ are used throughout this study as in planar mechanisms shown in Chapter 2.

Now the kinematic states when ξ_j^A and ξ_i^k have bound values will be examined. If ξ_j^A takes on its upper or lower bound value, i.e., if $A_j = A_{\max} = A_0$ or $A_j = A_{\min} = A_0 \xi_{\min}^p$, the corresponding bar element simulates the state of a rigid bar or that of no connection. If $k_i = k_{\max}$ or $k_i = k_{\min} = k_0 \xi_{\min}^p$, the corresponding node i is regarded to be rigidly-connected or disconnected to the ground (frame). So, a node i connected to the ground (frame) with a spring element of $k_i = k_{\max}$ simulates a revolute joint (in planar cases) or a spherical joint (in spatial cases). For subsequent discussions, the following notation will be used:

$$\xi^T = \left\{ \left(\xi^A \right)^T, \left(\xi^k \right)^T \right\} = \left\{ \xi_1^A, \xi_2^A, \dots, \xi_{N_l}^A, \xi_1^k, \xi_2^k, \dots, \xi_{N_k}^k \right\}$$

To demonstrate that one can properly represent any desired mechanism with the upper or lower bound values of ξ_j^A and ξ_i^k , a multi-link suspension shown in the left side of Figure 3.3(a) modeled by ADAMS is considered here. The same suspension is modeled by the ground structure in the right side of Figure 3.3(a); the bar and spring elements with the upper bound value ($\xi = \xi_{\max}$) are drawn in straight lines and circular markers (in blue), respectively. Ground structure modeling and mechanism synthesis are performed with MATLAB. The other elements not shown

in the figure have the lower bound value $\xi = \xi_{\min}$. As shown in Figure 3.3(b), the motions of the wheel center by the two models (ADAMS and Present) agree well with each other, validating the use of the ground structure model for mechanism representation.

3.3.2 Work transmittance efficiency based formulation

The goal of mechanism synthesis is to find a mechanism to convert a specified input to a desired output motion. Perhaps, it may appear natural to choose the error between the target motion and the actual motion as an objective function in optimization-based mechanism synthesis and treat the satisfaction of the desired DOF (1 for a rigid-body mechanism for a single input and a single output) as a constraint (see, Ref. [34]). However, a new formulation yielding stable convergence is proposed in Chapter 2, so that planar mechanisms generating complicated loops can be synthesized, which is otherwise difficult. The key idea is to maximize the work-transmittance efficiency as the objective function to satisfy the desired DOF requirement. Although the formulation is set up for the synthesis of planar linkage mechanisms, it can be extended for the synthesis of spatial linkage mechanisms, such as vehicle suspension mechanisms. Therefore, the formulation with the same function applied to the planar mechanisms, called “work-transmittance efficiency”, is employed for three-dimensional suspension mechanism design.

Here, Let us briefly consider the work transmittance efficiency concept again.

First, we can assume intermediate mechanisms shown in Figure 3.4, which can appear as some candidate mechanisms during a topology optimization-based synthesis. They can be realized by the bar-spring ground model if the design variables are properly assigned. For instance, those with black and gray lines correspond to bars with $\xi^\Lambda = \xi_{\max}$ and $\xi^\Lambda = 0.5$, respectively, which represent almost rigid and elastically deformable bars, respectively. Other bar elements used to form a ground structure are assumed to have $\xi^\Lambda = \xi_{\min}$, so they are not illustrated in Figure 3.4 (likewise, revolute joints attached to the ground are expressed with $\xi^k = \xi_{\max}$). If we look for a mechanism to convert a given input motion to a desired output motion, the mechanism synthesis problem could be set up without considering any external load applied at the end effector. However, it is assumed that some external load (force) \mathbf{F}^{ext} is applied at the output point or the end effector and the specific form of \mathbf{F}^{ext} is explained in Chapter 3.4. As depicted in Chapter 2, \mathbf{F}^{ext} is necessary to define the work transmittance efficiency, which will be maximized to enforce the correct DOF of a mechanism to be synthesized.

With \mathbf{F}^{ext} applied at the output point, one can calculate the output work $W_{t^*}^{\text{out}}$ done by the system against the external force during the system motion subjected to the input actuation work $W_{t^*}^{\text{inp}}$ between the initial time $t = 0$ and a certain time $t = t^*$. For example, the output work ($W_{t^*=1}^{\text{out}}$) at time step 1 corresponds to the work done against the external force from the initial configuration to the first time step

($t=1$). $W_{t^*=2}^{\text{out}}$ is the accumulated output work done from the initial state ($t=0$) to time step ($t=2$). Because the bars used to discretize the design domain behave elastically during the synthesis process, some strain energy $U_{t^*}^{\text{int}}$ can be stored in the bar-spring system if bars do not behave as rigid links. Therefore, $W_{t^*}^{\text{inp}} = U_{t^*}^{\text{int}} + W_{t^*}^{\text{out}}$ ($1 \leq t^* \leq T$) will hold. With these variables, the work transmittance efficiency function η at $t=t^*$ can be defined as

$$\eta_{t^*} = \frac{W_{t^*}^{\text{out}}}{W_{t^*}^{\text{inp}}} = \frac{W_{t^*}^{\text{out}}}{W_{t^*}^{\text{out}} + U_{t^*}^{\text{int}}} \quad (1 \leq t^* \leq T) \quad (3.29)$$

Clearly, $\eta_{t^*} = \eta(t^*)$ will be 1 if the bar with $\xi^A = 0.5$ in Figure 3.4(a) is replaced by a bar with $\xi^A = \xi_{\text{max}}$ and if the bar with $\xi^A = 0.5$ in Figure 3.4(b) is replaced by a bar with $\xi^A = \xi_{\text{min}}$, making their DOF's equal to 1. In these cases, $U_{t^*}^{\text{int}}$ will become zero for both. The Gruebler's equation [1] can be utilized to check the system DOF, but this energy interpretation is critical for efficiently performing mechanism synthesis by a gradient-based approach.

Let us now explain how maximizing the work transmittance efficiency function ensures that a mechanism has the correct DOF (equal to 1). To facilitate the explanation, we consider the mechanism from $t=1$ to $t=t^*$ without an external force applied and then apply the external force thereafter. For the intermediate mechanism in a quasi-redundant DOF state in Figure 3.4(a), the mechanism actuation stores no strain energy in the system, but the application of an

external force \mathbf{F}^{ext} does. The length of the member A_1B becomes shorter after the external force is applied and the difference between the length of A_1B and the length of A_2B corresponds to the amount of compression (The blue thin lines denote the circular paths centered at point B). Since $U_{t^*}^{\text{int}} \neq 0$, $\eta_{t^*} < 1$ (i.e., η_{t^*} is not maximized). For the intermediate mechanism in a quasi-deficient DOF state in Figure 3.4(b), the mechanism actuation stores strain energy in the system while the application of an external force \mathbf{F}^{ext} does not. In Figure 3.4(b), the length of A_2B is larger than A_1B and their difference corresponding to the elongation is the strain energy storage source (In Figure 3.4(b), the thin blue lines denote the circular paths centered at point B). Again, $\eta_{t^*} < 1$ as $U_{t^*}^{\text{int}} \neq 0$. Although the principles that make $U_{t^*}^{\text{int}}$ non-zero in quasi-redundant and quasi-deficient cases are different, they can be simultaneously suppressed by maximizing the same function η . This is a very useful result, because both DOF-redundancy and deficiency can be treated in a unified manner. Furthermore, the degree of the exact DOF satisfaction can be checked by examining the η value at the convergence of the optimization-based mechanism synthesis; if η is sufficiently close to 1, the synthesized mechanism indeed works as a rigid-body mechanism.

Let us briefly explain how the maximization of the work efficiency function equals the minimization of the strain energy stored in the system, which controls DOF-redundancy and deficiency. When an external force is applied to a system, the compliance minimization equivalent to the strain energy minimization is used to find

the stiffest structure in structural topology optimization. Therefore, the minimization of the strain energy under the external force (\mathbf{F}^{ext}) will effectively suppress DOF-redundancy. On the other hand, system flexibility can be achieved by reducing the strain energy induced by the displacement input prescribed at an input link. In this case, most of the input energy $W_{t^*}^{\text{inp}}$ at each step t^* will be converted to $W_{t^*}^{\text{out}}$ as the elastic deformation is reduced. Therefore, DOF-redundancy and deficiency can be simultaneously prevented by maximizing the transmittance efficiency function alone.

The actual actuation motion can be described by a number of time steps from $t=1$ to $t=T$ where T is the final time step. Now, one can define the “mean work-transmittance efficiency” $\bar{\eta}$ such that

$$\bar{\eta} = \frac{1}{T} \sum_{t^*=1}^T \eta_{t^*} \quad (3.30)$$

The output work $W_{t^*}^{\text{out}}$ can be calculated as

$$W_{t^*}^{\text{out}} = W_{t^*-1}^{\text{out}} - \left(\mathbf{F}_{t^*}^{\text{ext}} \right)^T (\boldsymbol{\mu}_{t^*} - \boldsymbol{\mu}_{t^*-1}) \quad (3.31)$$

with $W_{t^*=0}^{\text{out}} = 0$. As a result, definition of the efficiency function written down in (3.29-31) is exactly the same with the efficiency function employed in Chapter 2 for planar link mechanisms.

If the desired kinematic requirements for a suspension link mechanism to be synthesized are denoted by $\psi_{t^*}^{(i)} \leq \varepsilon^{(i)}$ ($i=1,2,\dots,N_C$; N_C = the number of

requirements) with allowable errors $\varepsilon^{(i)}$, the synthesis problem can be set up as

Formulation (A)

$$\begin{array}{ll}
 \text{Find} & \xi^A = \{\xi_1^A, \xi_2^A, \dots, \xi_{N_c}^A\}^T, \xi^k = \{\xi_1^k, \xi_2^k, \dots, \xi_{N_k}^k\}^T \\
 \text{Minimize} & 1 - \bar{\eta} \\
 \text{Subject to} & g_{i^*}^{(i)} = \psi_{i^*}^{(i)} - \varepsilon^{(i)} \leq 0 \quad (i = 1, 2, \dots, N_c)
 \end{array} \tag{3.32}$$

Depending on the type of synthesis problems, the constraint requirements could be stated as a specific motion at a few selected time steps or the entire actuation steps from $t^* = 0$ to $t^* = T$. The specific forms of $\psi_{i^*}^{(i)}$ will be described in the next section focused on synthesis case studies. In Formulation (A), work transmittance efficiency ($\bar{\eta}$) same as the one employed in Chapter 2 for planar mechanisms is used to control DOF of the suspension mechanisms.

While Formulation (A) is based on a ground structure with the discretizing finite element nodes fixed in space, it is also necessary to allow the nodes to move so that the design variable space can be expanded. In this case, the nodal coordinates (X_i, Y_i, Z_i) ($i = 1, 2, \dots, N_n$) can also be treated as design variables. If a new variable type ξ^x for controlling $\mathbf{X}_i = \{X_i, Y_i, Z_i\}^T$ is applied, Eq. (3.32) is replaced by

Formulation (B)

$$\begin{array}{ll}
 \text{Find} & \xi^A, \xi^k, \text{ and } \xi^x \\
 \text{Minimize} & 1 - \bar{\eta} \\
 \text{Subject to} & g_{i^*}^{(i)} = \psi_{i^*}^{(i)} - \varepsilon^{(i)} \leq 0 \quad (i = 1, 2, \dots, N_c)
 \end{array} \tag{3.33}$$

The resulting formulation (B) represents simultaneous topology and shape

optimization. When the shape optimization variables are employed, nodes may be overlapped during optimization iterations. Therefore, it needs to consider constraints restricting the distance between adjacent nodes to be larger than a certain value in addition to the kinematic requirements in (3.33). Detailed numerical values used for the distance constraints will be given in design case studies.

The main reason to consider Formulation (B) is that it could be difficult to find desired mechanisms with Formulation (A) using the fixed nodal points. Because the involved nonlinear analysis for kinematic analysis is computationally expensive, the use of fine mesh may not be practical. So, the simultaneous topology and shape optimization with a reasonable ground mesh is considered as a practical alternative. The effectiveness of the simultaneous topology and shape optimization compared with the topology optimization for fine mesh is discussed in APPENDIX A.3.

3.3.3 Design sensitivity analysis for design optimization

Because the mechanism synthesis will be performed numerically by the optimization formulation (A) in (3.32) or (B) in (3.33), the design variables should be updated iteratively by an optimizer. The method of moving asymptotes (MMA) [64], a gradient-based optimizer, will be used as an optimizer in this study. The method requires the design sensitivity of the objective function and constraint equations. We use the direct differentiation method to perform the sensitivity analysis and related equations will be given below.

The design sensitivity of the objective function \bar{r}_i with respect to the design variable ξ (representing ξ^A, ξ^k or ξ^X) can be expressed as:

$$\frac{d\bar{r}}{d\xi} = \frac{\partial \bar{r}}{\partial \xi} + \sum_{t^*=1}^T \left(\left[\frac{d\mathbf{x}_{t^*}}{d\xi} \right] \left[\frac{\partial \bar{r}}{\partial \mathbf{x}_t} \right]_{\mathbf{x}_t = \mathbf{x}_{t^*}} \right) \quad (3.34)$$

To find $d\mathbf{x}_{t^*}/d\xi$ in Eq. (3.34), equation (3.22b) will be used. To this end, $\mathbf{f}(\mathbf{x})=0$ is to be satisfied exactly (within numerical errors) for every $\mathbf{x} = \mathbf{x}_{t^*}$. Therefore, if (3.22b) is differentiated with respect to ξ and evaluated at $\mathbf{x} = \mathbf{x}_{t^*}$, the following equation will be satisfied regardless of the value of ξ .

$$\left[\frac{d\mathbf{f}}{d\xi} \right]_{\mathbf{x}_t = \mathbf{x}_{t^*}} = \left[\frac{\partial \mathbf{f}}{\partial \xi} \right]_{\mathbf{x}_t = \mathbf{x}_{t^*}} + \left[\frac{d\mathbf{x}_{t^*}}{d\xi} \right] \left[\frac{\partial \mathbf{f}}{\partial \mathbf{x}_t} \right]_{\mathbf{x}_t = \mathbf{x}_{t^*}} = \mathbf{0} \quad (3.35)$$

Equation (3.35) yields,

$$\left[\frac{d\mathbf{x}_{t^*}}{d\xi} \right] = - \left[\frac{\partial \mathbf{f}}{\partial \xi} \right]_{\mathbf{x}_t = \mathbf{x}_{t^*}} \left[\frac{\partial \mathbf{f}}{\partial \mathbf{x}_t} \right]_{\mathbf{x}_t = \mathbf{x}_{t^*}}^{-1} \quad (3.36)$$

Since $\partial \mathbf{f} / \partial \mathbf{x} = \nabla_{\mathbf{x}} \mathbf{f}(\mathbf{x})$, the expression in (3.27b) can be used to calculate $[\partial \mathbf{f} / \partial \mathbf{x}]^{-1}$. The accuracy in the calculation of $d\bar{r}/d\xi$ is strongly affected by the accuracy of solving $\mathbf{f}(\mathbf{x}(\xi))=0$. Accordingly, the solution to $\mathbf{f}(\mathbf{x}(\xi))=0$ should be found with little error.

3.4 Suspension mechanism synthesis by the proposed method

As case studies of suspension mechanism synthesis, two types of problems will be considered in this section. The first type of problems is to check if the proposed synthesis formulation can recover “known” suspension systems; for a selected suspension mechanism, the desired motion (\mathbf{q}_w) of the wheel center will be prescribed. The second type of problems is to synthesize suspension systems for prescribed ride and handling requirements as commonly used in automobile industry such as anti-squat. In these problems, no specific mechanism satisfying the requirements is assumed to be known – this is a challenging problem, so that some techniques needed to deal with this class of problems will be explained here. To deal with case studies considered in this work, the following values were used: $A_{\max} = 10,000 \text{ m}^2$ and $k_{\max} = 100,000 \text{ N/m}$. (These values were found to yield satisfactory results.)

3.4.1 Recovery of double wishbone and multilink suspensions

As the first type of problems, it needs to consider benchmark test problems, which are to check if the proposed formulation using the bar-spring model in Figure 3.1(a) is capable to recover known mechanisms. Here, it will be checked if double wishbone and 5-link suspension mechanisms which are represented by the bar-spring models in Figure 3.1(b) and Figure 3.3(a), respectively, can be synthesized when their output motions relative to input motions are prescribed. Because the

MacPherson type suspension has a strut which cannot be directly represented by the present bar-spring model, it is not considered here although some model modification could handle this type of suspensions as well.

The design domain for suspension mechanisms to be synthesized is $D_X \times D_Y \times D_Z = 0.3 \text{ m} \times 0.3 \text{ m} \times 0.3 \text{ m}$, and the number of the bar elements, nodes, and spring elements are $N_\ell = 315$, $N_n = 27$, and $N_k = 18$. Note that bar elements between hub-attached nodes are not necessary in the ground structure model because they are not needed for synthesis.

Formulation (A) will be used to solve this synthesis problem for which the input actuation motion is given by the Z -directional motion of the wheel center as (3.20) where \hat{q}_Z is stated as

$$\hat{q}_Z(t^*) = 100 \frac{t^*}{T} \text{ (unit: mm)} \quad \text{for } t^* = 1, 2, \dots, T = 10 \quad (3.37)$$

A larger value of T may be preferred for more precise description of input motion, but too large values could increase computational cost considerably. While $q_Z(t^*)$ is prescribed as an input motion, the time histories of the remaining variables, $q_X(t^*)$, $q_Y(t^*)$, $\theta_1(t^*)$, $\theta_2(t^*)$, and $\theta_3(t^*)$ are described as the target output motions. Therefore, the constraint equations ($\psi_{t^*}^{(i)}$) are expressed as

$$\psi_{t^*}^{(1)} = |q_X(t^*) - \hat{q}_X(t^*)| \quad (3.38a)$$

$$\psi_{t^*}^{(2)} = |q_Y(t^*) - \hat{q}_Y(t^*)| \quad (3.38b)$$

$$\psi_{t^*}^{(3)} = \left| \theta_1(t^*) - \hat{\theta}_1(t^*) \right| \quad (3.38c)$$

$$\psi_{t^*}^{(4)} = \left| \theta_2(t^*) - \hat{\theta}_2(t^*) \right| \quad (3.38d)$$

$$\psi_{t^*}^{(5)} = \left| \theta_3(t^*) - \hat{\theta}_3(t^*) \right| \quad (3.38e)$$

where $(\hat{\bullet})$ denotes the prescribed values. To generate $\psi_{t^*}^{(1)}$ to $\psi_{t^*}^{(5)}$ in Eq. (3.38), the trajectories of $\hat{q}_x(t^*)$, $\hat{q}_y(t^*)$, $\hat{\theta}_1(t^*)$, $\hat{\theta}_2(t^*)$, and $\hat{\theta}_3(t^*)$ should be defined. In case when a 5-link suspension is used as a target (or reference) suspension mechanism (“Design Case 2”), for instance, the trajectories shown in Figure 3.3(b) are used as the target output paths. Likewise, similar output trajectories by a double wishbone suspension (“Design Case 1”), shown in Figure 3.1(b), is selected as a target (or reference) suspension mechanism. (Because the trajectories are similarly obtained as those in Figure 3.3(b), the output trajectories for the double wishbone suspension mechanism are not explicitly plotted.)

In order to define the mean value of the work transmittance efficiency function $\bar{\eta}$ in Formulation (A), $\mathbf{F}_{t^*}^{\text{ext}}$ must be applied to the system. Among various choices of $\mathbf{F}_{t^*}^{\text{ext}}$ to make $W_{t^*}^{\text{out}}$ nonzero, the following form is selected as employed in Chapter 2:

$$\mathbf{F}_{t^*}^{\text{ext}} = F_0 \frac{\left\{ \hat{q}_{X,t^*-1}, \hat{q}_{Y,t^*-1}, 0 \right\}^T - \left\{ \hat{q}_{X,t^*}, \hat{q}_{Y,t^*}, 0 \right\}^T}{\left\| \left\{ \hat{q}_{X,t^*-1}, \hat{q}_{Y,t^*-1}, 0 \right\}^T - \left\{ \hat{q}_{X,t^*}, \hat{q}_{Y,t^*}, 0 \right\}^T \right\|} \quad (3.39)$$

with $F_0 = 1 \text{ N}$. To ensure that the desired path of the wheel center is traced

accurately, we choose the error bounds for constraint equations as $\varepsilon^{(1)} = \varepsilon^{(2)} = 1 \text{ mm}$ and $\varepsilon^{(3)} = \varepsilon^{(4)} = \varepsilon^{(5)} = 0.02^\circ$. In solving Eq. (3.32), five constraint equations in (3.38) are checked at 10 time steps from $t^* = 1$ to $t^* = T = 10$, so that 50 constraints in total are applied in optimization.

We will consider the numerical results obtained by the proposed synthesis method (Formulation A) applied to Design Cases 1 and 2. Figure 3.5 shows the iteration histories of $\bar{\eta}$ and $\max(\psi_{t^*}^{(i)})(i=1,2,\dots,5)$ over all time steps for Design Case 1. We set the maximum iteration number to be 200, for which the constraint equations in Formulation (A) meet the specified error bounds. (The main reason we choose 200 iterations, instead of using the stopping criteria, is to see the convergence behavior better.) In Figure 3.5, $\psi_{t^*}^{(1)}$ and $\psi_{t^*}^{(2)}$ denote the errors in the longitudinal and lateral displacements of the wheel center, while $\psi_{t^*}^{(3)}$, $\psi_{t^*}^{(4)}$ and $\psi_{t^*}^{(5)}$, the errors in the Tait-Bryant angles. After 125 iterations, the mean transmittance efficiency $\bar{\eta}$ reaches almost 100%. The value of $\bar{\eta}$ at the end of the synthesis, was 0.997, implying the condition of DOF=1 is accurately satisfied. Also, the errors in the constraint equations decrease stably. These findings support that good convergence can be achieved by the proposed formulation.

Figure 3.6 illustrates intermediate and final suspension layouts during optimization iterations for Design Case 1. For the three layouts at n_{iter} (iteration number) = 0, 100 and 200, the poses (positions and orientations) of the suspension

and wheel system at $q_z(t^* = 0) = 0 \text{ mm}$, $q_z(t^* = 5) = 50 \text{ mm}$, and $q_z(t^* = 10) = 100 \text{ mm}$ are also shown. The thickness of each line (bar element j) represents the value of the design variable ξ_j^A ($j = 1, 2, \dots, N_\ell$) assigned to the bar element j . Also, the size of each circular mark (in blue) denotes the value of the design variable ξ_i^k ($i = 1, 2, \dots, N_k$) allocated to the spring element i . The marks with fully-filled circles in Figure 3.6 denote the hard points. Examining the obtained suspension layout at $n_{\text{iter}} = 200$ shows that it looks quite different from the one shown in Figure 3.1(b). The main reason is that if there is no mass constraint on the suspension mechanism, it is not possible to obtain exactly the same layout as the suspension layout used to generate the target output trajectories. This is because it is possible to put additional link (bar) elements without changing output kinematic motion of a rigid-body mechanism (Here, lots of redundant elements are located between hard points). This issue was carefully addressed in Chapter 2 with a proposed post-processing algorithm. Using the post-processing algorithm such as pruning, the post-processed layout shown in Figure 3.6 can be obtained. The final post-processed layout shows that the proposed synthesis method successfully finds the desired mechanism; the post-processed suspension is identical to the double wishbone suspension in Figure 3.1(b).

A few more words regarding the results in Figures 3.5 and 3.6 are worth mentioning. From Figure 3.6, one can see that the system poses at $n_{\text{iter}} = 0$ are quite

different from those at $n_{\text{iter}} = 100$ and $n_{\text{iter}} = 200$. On the other hand, the poses at $n_{\text{iter}} = 100$ and $n_{\text{iter}} = 200$ are nearly the same. This behavior can be explained by examining the iteration history shown in Figure 3.5; the error values in $\psi_{t^*}^{(i)}$ decreased drastically during the first 60 iterations, and $\psi_{t^*}^{(i)} < \varepsilon^{(i)}$ were satisfied thereafter. Once the candidate solution enters the feasible region, then the objective function $(1 - \bar{\eta})$ starts to be minimized (equivalently, $\bar{\eta}$ starts to be maximized). Consequently, intermediate design variables will take on upper or lower bound values. Clearly, $\bar{\eta}$ rapidly increases from $n_{\text{iter}} = 100$.

Design Case 2 is concerned with the synthesis of the 5-link suspension shown in Figure 3.3(a). As in Design Case 1, $q_z(t^*)$ in (3.37) is given as an input bound motion of the wheel center and the trajectories of $\hat{q}_x(t^*)$, $\hat{q}_y(t^*)$, $\hat{\theta}_1(t^*)$, $\hat{\theta}_2(t^*)$, and $\hat{\theta}_3(t^*)$ that are calculated by using the model shown in Figure 3.3(a) are prescribed as the target path of the wheel center (The desired trajectories shown in Figure 3.3(b)). The intermediate and final suspension layouts are shown in Figure 3.7. The iteration histories of the objective and constraint functions are similar to those in Figure 3.5. Therefore, they are not plotted here.

3.4.2 Synthesis of suspensions satisfying R&H requirements

As the proposed synthesis approach for suspension mechanisms successfully recovered known suspension systems, now it needs to consider more realistic

problems. To this end, R&H (Ride & Handing) requirements that are typically used in automobile industry are specified. As specific data for the R&H requirements would differ from one car manufacturer to another, some representative data are chosen in this investigation to see if the proposed formulation is capable to deal with typical R&H requirements. Because there is no information about mechanisms to be synthesized for this type of problems, a more versatile approach is required than Formulation (A) based on the fixed ground nodes. In other words, there is no guarantee that a desired mechanism can be synthesized within the fixed-node ground model. Therefore, Formulation (B) in which the ground nodes are also allowed to move during the optimization based synthesis will be used. This means that Formulation (B) performs both topology and shape optimizations simultaneously. Indeed, this strategy was considered in earlier paper [34] where the potential of the simultaneous topology and shape optimization in linkage mechanism synthesis problems was shown. When formulation (B) is used, the additional variables ξ^x also need to be used as design variables, as mentioned earlier. Instead of using unscaled normal coordinates $(X_i, Y_i, Z_i) (i=1,2,\dots,N_n)$ as the design variables, it is convenient to use ξ^x such that

$$\xi^x = \{\xi_1^x, \xi_2^x, \xi_3^x; \dots; \xi_{3N_n-2}^x, \xi_{3N_n-1}^x, \xi_{3N_n}^x\}^T \quad (3.40a)$$

with

$$\{X_i, Y_i, Z_i\}^T = \{D_x(\xi_{3i-2}^x - 0.5), D_y(\xi_{3i-1}^x), D_z(\xi_{3i}^x - 0.5)\}^T (i=1,2,\dots,N_n) \quad (3.40b)$$

In defining ξ^x or $\psi_{i*}^{(i)} (i = 1, 2, \dots, N_C)$ in Formulation (B), the following R&H requirements are used:

$$\text{Initial toe-in angle rate} \quad \dot{\delta}_{\text{lower}} \leq \dot{\delta} \leq \dot{\delta}_{\text{upper}} \quad (3.41a)$$

$$\text{Toe-in angle at 50 mm bound stroke} \quad \delta_{\text{lower}}^{50\text{mm}} \leq \delta^{50\text{mm}} \leq \delta_{\text{upper}}^{50\text{mm}} \quad (3.41b)$$

$$\text{Initial Camber angle rate} \quad \dot{\gamma}_{\text{lower}} \leq \dot{\gamma} \leq \dot{\gamma}_{\text{upper}} \quad (3.41c)$$

$$\text{Camber angle at 50 mm bound stroke} \quad \gamma_{\text{lower}}^{50\text{mm}} \leq \gamma^{50\text{mm}} \leq \gamma_{\text{upper}}^{50\text{mm}} \quad (3.41d)$$

$$\text{Roll Center Height} \quad H_{\text{lower}}^{\text{RC}} \leq H^{\text{RC}} \leq H_{\text{upper}}^{\text{RC}} \quad (3.41e)$$

$$\text{Anti-Squat} \quad AS_{\text{lower}} \leq AS \leq AS_{\text{upper}} \quad (3.41f)$$

$$\text{Anti-Lift} \quad AL_{\text{lower}} \leq AL \leq AL_{\text{upper}} \quad (3.41g)$$

$$\begin{aligned} \text{Contact patch lateral displacement} \\ \text{at 50 mm bound stroke} \end{aligned} \quad \left| \Delta y_{50\text{mm}}^{\text{CP}} \right| \leq \Delta y_{\text{max}}^{\text{CP}} \quad (3.41h)$$

$$\begin{aligned} \text{Contact patch lateral displacement} \\ \text{at 100 mm bound stroke} \end{aligned} \quad \left| \Delta y_{100\text{mm}}^{\text{CP}} \right| \leq \Delta y_{\text{max}}^{\text{CP}} \quad (3.41i)$$

$$\begin{aligned} \text{Nodal distance} \\ (i, j = 1, 2, \dots, N_n, i \neq j) \end{aligned} \quad 100 \text{ mm} \leq \text{Dist}(i, j) \quad (3.41j)$$

As listed in (3.41), there are several ride and handling criteria to be considered for the design of suspension mechanisms. For the meaning of the terminology and the procedure to calculate the quantities (such as H^{RC} , AS , etc.) appearing in (3.41),

see [75, 80, 81]. For instance, the rates such as $\dot{\delta}$ and $\dot{\gamma}$ are defined as the derivatives of the initial toe-in and camber angle rates with respect to the vertical bound stroke, respectively. They are calculated by the forward difference method. The roll center height H^{RC} is calculated at the initial configuration (before being subjected to the bound stroke). Also, the anti-squat (AS) and the anti-lift (AL) are calculated at the initial configuration. The symbol $\text{Dist}(i, j)$ in (3.41j) denotes the distance between nodes i and j . This constraint requires that the relative distance between two nodes of the ground structure should be larger than 100 mm. The minimum distance of 100 mm between two adjacent nodes should be maintained in order to install a bush (or a ball joint) without interference in suspension mechanisms. The specific data used for (3.41) in the present study are chosen as:

$$\begin{aligned}
\dot{\delta}_{\text{lower}} &= 0.0027^\circ / \text{mm} ; & \dot{\delta}_{\text{upper}} &= 0.0033^\circ / \text{mm} \\
\delta_{\text{lower}}^{50\text{mm}} &= 0.225^\circ ; & \delta_{\text{upper}}^{50\text{mm}} &= 0.275^\circ \\
\dot{\gamma}_{\text{lower}} &= -0.022^\circ / \text{mm} ; & \dot{\gamma}_{\text{upper}} &= -0.018^\circ / \text{mm} \\
\gamma_{\text{lower}}^{50\text{mm}} &= -1.65^\circ ; & \gamma_{\text{upper}}^{50\text{mm}} &= -1.35^\circ \\
H_{\text{lower}}^{RC} &= 90 \text{ mm} ; & H_{\text{upper}}^{RC} &= 110 \text{ mm} \\
AS_{\text{lower}} &= 45\% ; & AS_{\text{upper}} &= 55\% \\
AL_{\text{lower}} &= 63\% ; & AL_{\text{upper}} &= 77\% \\
\Delta y_{\text{max}}^{\text{CP}} &= 5 \text{ mm}
\end{aligned} \tag{3.42}$$

The lateral movement of the center of the contact path Δy^{CP} has a negative effect

on the vehicle feature related to straight maneuvering on an irregular road [81] and large Δy^{CP} values deteriorate the NVH (Noise/Vibration/Harshness) performance of a vehicle due to side-to-side excitations from tire-road interfaces. Meanwhile, the condition imposed on Δy^{CP} conflicts with the design criteria on the roll center height because the roll center height is determined by the rate of the lateral movement of the contact patch with respect to vertical movement [75]. Because lower and upper bounds of the roll center height H^{RC} govern the amount of contact patch displacement when the suspension is placed near its initial configuration, the imposition of too small $\Delta y_{\text{max}}^{\text{CP}}$ values is quite difficult to achieve. Also, Δy^{CP} is affected by the size of a vehicle suspension in case of typical suspension types [82]. This implies that it is very difficult to find a feasible suspension layout if the design domain is small. Nevertheless, we attempt to use a small design domain in order to demonstrate advantages of the proposed method in synthesizing non-trivial suspension mechanisms.

Here, it should be noted that unlike the design problems in Section 4.1, the whole path of the wheel center under a Z-directional bound stroke is not given. Therefore, the external force $\mathbf{F}_{t*}^{\text{ext}}$ as given by Eq. (3.39) cannot be used for the present problems. Thus, an alternative scheme to define $\mathbf{F}_{t*}^{\text{ext}}$ should be devised here. By examining the constraints on $\dot{\gamma}$, $\gamma^{50\text{mm}}$, Δy^{CP} , and H^{RC} , one can anticipate the direction of lateral movement of the wheel center. Also, by considering the required anti-feature values and others, one can see that the backward movement of a wheel

center is required in rear suspensions. Based on these observations, we propose to choose $\mathbf{F}_{t^*}^{\text{ext}} = F_0 \{1, -1, 0\}^T / \sqrt{2}$ ($F_0 = 1 \text{ N}$).

The following two design cases are considered:

Design Case 3 with $[D_x \times D_y \times D_z] = [0.5 \text{ m} \times 0.5 \text{ m} \times 0.3 \text{ m}]$

Design Case 4 with $[D_x \times D_y \times D_z] = [0.3 \text{ m} \times 0.3 \text{ m} \times 0.3 \text{ m}]$

Design Case 4 deals with a problem with a tight design space. For both cases, the height of the weight center (H) from the ground is set to be 600 mm, and the tire radius (R) and the wheel base (W_b) are set to be 300 mm and 2600 mm, respectively. The braking force distribution ratio (α) between the front and rear tires is assumed to be 0.5.

Figure 3.8 shows the intermediate and final optimized suspension layouts for Design Cases 3 and 4. Also the configurations of the post-processed suspension layouts at $\hat{q}_z = 0$ and $\hat{q}_z = 100 \text{ mm}$ are shown. The same post-processing algorithm applied to Design Cases 1 and 2 was used to obtain the final layouts in Figure 3.8. As may be seen from Figure 3.8, the optimized mechanism for Design Case 3 turns out to be a conventional multi-link suspension mechanism while, the mechanism for Design Case 4, looks quite different from typical suspension mechanisms. The interpretation of the synthesized mechanisms by the present synthesis method for Design Cases 3 and 4 will be given in the next section.

The iteration histories of $\bar{\eta}$, $\gamma^{50\text{mm}}$, $\delta^{50\text{mm}}$ and H^{RC} for Design Case 3 are presented in Figure 3.9. At the initial iterations, the constraints imposed on the design

parameters such as $\gamma^{50\text{mm}}$, $\delta^{50\text{mm}}$, etc. are pushed to be satisfied at initial iterations so that candidate design points become feasible enough. In Figure 3.9, the feasible ranges of $\gamma^{50\text{mm}}$, $\delta^{50\text{mm}}$ and H^{RC} are indicated by shaded gray strips. Although not shown here, the constraints imposed on other design parameters behave similarly to those imposed on $\gamma^{50\text{mm}}$, $\delta^{50\text{mm}}$, and H^{RC} . After candidate design points become sufficiently feasible, the mean transmittance efficiency ($\bar{\eta}$) starts to be maximized from $n_{\text{iter}} \approx 50$ and rapidly reaches the value of 100%. Because the iteration histories for Design Case 4 were found to be very similar to those for Design Case 3, they are not plotted here.

When the simultaneous topology and shape optimization is carried out, some numerical issues could arise. Because the synthesis convergence behavior can be significantly affected by the magnitude of design variable variation during design variable update, some care must be taken to limit the maximum allowed variations. For instance, too much variation in the shape design variables typically could induce much oscillation in the objective and constraint functions, making convergence difficult. As a remedy, one can use small move limits in updating the design variables. Actually, all design variables are not allowed to vary more than 2% of $|\xi_{\text{max}} - \xi_{\text{min}}|$ for every iteration. Additionally, different values of MMA parameters are used to update the topology and shape optimization variables. MMA, the gradient-based algorithm employed in this research, has upper and lower asymptotes for each design variable, and they are increased or decreased according to the variation of the

assigned design variable [64]. So we can adjust the convergence speed of two types of variables by assigning different MMA interval adjusting parameters for topology and shape variables. To suppress oscillatory behavior of the design variables, a 5 % interval reducing strategy is used for topology variables and a 30 % interval reduction strategy, for shape variables. Larger reduction in the interval between asymptotes of the shape design variable contributes to more stable convergence (too much reduction rate makes convergence too late). By this scheme, we could obtain stable convergence history as Figure 3.9.

In Design Case 3, the nodal positions change significantly before $n_{iter} \approx 50$ as shown in Figure 3.8, and then shape change by nodal movements is slowed down and the optimization proceeds to satisfy the required DOF by maximizing $\bar{\eta}$ with more distinct topological layouts. Meanwhile, the iteration histories in Figure 3.9 show that optimization proceeds to satisfy the constraint equations from the initial state until $n_{iter} \approx 50$. After satisfying the constraints, the value of $\bar{\eta}$ is increased until it reaches 99.66% at the final step ($n_{iter} = 200$). The optimized values of the design parameters are summarized in Table 3.1.

3.4.3 Interpretation of the optimized suspension layouts

Figure 3.10 (a) and (b) show three-dimensional illustrations of the post-processed optimized linkage suspension mechanisms obtained by the proposed formulation for Design Cases 3 and 4, respectively. Note that the result for Design Case 4 is obtained

for a smaller design domain. The two-dimensional schematic illustrations of the optimized mechanisms are also plotted in the figures. In interpreting the layout configuration of the optimized suspension, we use capital letters (A, B, ...) to represent hub-attached points and numbers (1, 2, ...) for the other joint nodes not attached to hub. A link connecting point α and point β will be denoted by “Link $\alpha - \beta$.” And an arm composed of Link $\alpha_1 - \beta$ and Link $\alpha_2 - \beta$ will be denoted by “Arm $\alpha_1 - \beta - \alpha_2$ ” or “Arm $\alpha_2 - \beta - \alpha_1$.”

Let us examine the result in Figure 3.10(a) for Design Case 3. The layout configuration is similar to those of double wishbone or 5-link suspensions. Indeed, the synthesized mechanism in Figure 3.10(a) can be viewed as a hybrid of the two types of suspensions. In the obtained suspension, Link 1-A and Link 2-A meet at a point A so that they form a rigid arm with an equivalent revolute joint attached at the frame and a spherical joint at the wheel hub. The rigid arm formed by two links (Link 1-A and Link 2-A) connected to the common point “A” functioning as a ball joint can be denoted by “Arm 1-A-2.” In this notation, node “A” appearing in the middle of the Arm notation (Arm 1-A-2) is a spherical joint, and node 1 and node 2 form a revolute joint as a whole although each of them represents spherical joints. The axis of the revolute joint is a line connecting the two nodes 1 and 2 as shown in Figure 3.1(b).

In the schematic figure shown in the right side of Figure 3.10(a), the rigid arm is denoted by the line connecting a revolute joint (denoted by a cylinder with 1 & 2) and a spherical joint (denoted by a circle with “A”). Each spherical joint will be

denoted by a set of a ball and a semi-circle in the simplified schematic figure. Besides the rigid arm, there are three more links, Link 3-B, Link 4-C and Link 5-D, both ends of which are connected to the frame and the hub by spherical joints. Links 4-C and 5-D can be viewed as dual lower links, which are commonly used in conventional multi-link type suspensions. Although the extended lines along Links 4-C and 5-D do not meet exactly at a single point, they, as a whole, approximately function as a lower rigid arm of a double wishbone suspension mechanism. (Note that a typical dual link is known to have a virtual pivot position at the intersection point of the extended lines of two links forming a dual link set.) In this respect, the optimized mechanism in Figure 3.10(a) for Design Case 3 can be regarded as a double wishbone-like multi-link suspension in which its effective lower arm is virtually constructed by the two lower links (Links 4-C and 5-D).

Next, the optimized suspension layout in Figure 3.10(b), which was obtained for a smaller design domain than the domain used to obtain Figure 3.10(a), is examined. Apparently, the layout is considerably more complicated than typical suspension layouts so that its practicality may be an issue. Nevertheless, it can give an insight because alternative suspension mechanisms, as shall be demonstrated below, can be synthesized. To facilitate the analysis of the kinematic chain which the mechanism in Figure 3.10(b) represents, the post-processed three-dimensional layout is also cast into a two-dimensional schematic representation. It has 4 rigid arms and 6 rigid links. The 4 rigid arms are: Arm 1-5-2, Arm 2-7-4, Arm 3-6-4, Arm C-2-D. The 6 links are: Link 5-6, Link 6-7, Link 1-B, Link 5-A, link 6-D, and link 7-E. First of all, Arm C-

2-D looks like a typical arm that connects the frame and the hub-carrier but it has a spherical joint attached to the frame unlike an arm of a double-wishbone suspension (see Figure 3.1(b)) which has a spherical joint attached to the wheel-hub. Link 1-B is a typical link connecting one spherical joint at a point of the frame and another spherical joint at a point of the wheel-hub. However, other arms and links have unique configurations, which will be analyzed below in more details.

Arms 1-5-2, 2-7-4, and 3-6-4 have their equivalent revolute joints (axis of them passing through nodes 1 and 2 in case of Arm 1-5-2, for example) attached to the frame and their spherical joints at nodes 5, 6 or 7 are not directly attached either to the frame or the wheel-hub. Likewise, Links 5-6, 6-7, 5-A, 6-C, and 7-E have one of their end nodes not attached to either the frame or the wheel-hub. They are not typical components used in the conventional suspensions, which only have arm or link modules directly connecting the frame and hub-carrier like as Link 1-B in Figure 3.10(b). Among these unusual members, Link 5-6, 6-7, 5-A, 6-C, and 7-E correspond to the coupler links in planar linkage mechanisms. A coupler in a four-bar linkage mechanism is a rigid body not directly connected or restricted to a frame such as the hub-carrier in a double wishbone suspension. In fact, similar concepts have been used in some modern suspensions such as the “Integral Link” suspension mechanism [83] and the “RevoKnuckle” suspension mechanism [84, 85]. The main reason to employ coupler links in these advanced linkage mechanisms, in spite of complexity involved, is that without the use of additional coupler links, it is (nearly) impossible to design a suspension mechanism outperforming the conventional suspension

mechanisms such as the double-wishbone, 5-link and McPherson suspensions. For example, the “Integral Link” suspension was designed to surpass the Pareto frontier between longitudinal compliance and wind-up angle (spin angle) stiffness [83]. Besides, the “RevoKnuckle” suspension is known to relax the torque steer problem [85].

As remarked earlier, the suspension layout shown in Figure 3.10(b) for Design Case 4 may not be actually installed in automobiles because of its complexity. However, it is remarkable that even for a tight design domain which may be compared to the design domain of in-wheel suspensions, the proposed optimization-based synthesis mechanism yields a suspension mechanism that satisfies the given design requirements. It is well-known that the lateral movement of the tire contact patch and the camber angle change are very sensitive to the lower link lengths in conventional suspensions [82]. However, our approach yielded a mechanism that satisfies the design requirements in a tight design space by synthesizing coupler links.

Finally, we check the DOF of the synthesized mechanism in Figure 3.10(b). Among others, the mean work transmittance efficiency reached 99.66% at the final iteration stage, indicating almost the exact satisfaction of the correct DOF equal to 1. Nevertheless, it is worth calculating the DOF from the configuration shown in Figure 3.10(b) directly. Referring to the schematic linkage representation in Figure 3.10(b), we note that four arms and hub-carrier form five rigid bodies, resulting in $5 \times 6 = 30$ DOF's. Because each arm has a revolute joint, restricting 5 DOF's in each rigid body, 20 DOF's by 5 revolute joints are restricted. There is a spherical joint in

Arm C-2-D at node 2 that connects the arm to the chassis frame. This joint restricts 3 DOF's. Finally, each of the 6 links removes 1 DOF, restricting 6 DOF's altogether. Therefore, the total DOF of the suspension mechanism is $30 - 20 - 3 - 6 = 1$, which results in the required degree of freedom. This clearly demonstrates that the synthesized mechanism by the proposed method is indeed a mechanism satisfying the desired DOF exactly.

To see the effects of the R&H conditions on the optimized layout, the camber angle rate was changed for Case 3 from $-0.022^\circ/\text{mm} \leq \dot{\gamma} \leq -0.018^\circ/\text{mm}$ to $-0.011^\circ/\text{mm} \leq \dot{\gamma} \leq -0.009^\circ/\text{mm}$. The optimized result (not explicitly shown here) for the changed camber angle rate (with the same conditions for other R&H criteria) was found to have the same topological layout as the optimized result in Figure 3.10(a). The difference was only in the locations of the hub carried attached nodes and hard points. Because the R&H kinematic conditions cannot be dramatically changed for actual suspension mechanism design, different topological layouts may be not be found unless the size of the design domain is largely altered. On the other hand, a significantly different topological layout may be obtained if kinematics and compliance are simultaneously considered, which is beyond the scope of this study. (This study is mainly focused on kinematics without considering any compliance effects in the suspension mechanisms.)

3.5 Summary

Possibilities of using topology optimization for mechanism synthesis were suggested in earlier studies, but they were mainly limited to planar or simple three-dimensional problems. Therefore, the application of the topology optimization method to realistic mechanism synthesis problems, such as the synthesis of vehicle suspension mechanisms discussed here, has not been made. In this respect, this research presented the first successful implementation of the topology optimization of three-dimensional rear suspensions of a vehicle. To deal with such spatial mechanism design problems, a spatial truss ground model is employed and a gradient-based simultaneous topology and shape optimization method is developed. By controlling the design variables affecting the cross sectional areas of the truss elements, the existence of suspension components such as links and arms can be handled. To allow the existence of auxiliary links, the zero-length spring elements were also used to connect the finite element nodes of the truss model and the chassis frame (or car body). The coordinates of the nodes of the ground model are used as the shape design variables. By performing the additional shape optimization, a larger solution space was efficiently explored without dramatically increasing the resolution of the truss ground model for the topology optimization. Another practically important aspect in solving the present design problems was that many ride and handling constraints were given mainly in the bound form limiting the upper and lower values of the performance criteria such as anti-lift, anti-squat, etc. This contrasts with the conventional specification of full paths during motion but the proposed simultaneous

topology and shape optimization was found to yield converged results successfully.

In terms of the designed suspension mechanisms by the developed method, it was possible to obtain various suspension topologies ranging from the conventional double wishbone to the advanced multi-link solutions. Among others, an atypical suspension that involves the coupler links was obtained when a smaller design domain than the conventional one was used. The atypical suspension was more complicated due to several coupler links than commonly used suspensions without them, but the result clearly suggests the potential of the proposed suspension synthesis method in finding new alternative suspensions. To this end, one can see that a key point for obtaining the new-concept suspension is the layout constraint. From this aspect, the author tried to apply various design constraints for the limited design domain to achieve new-concept suspensions. From this effort, several suspension mechanisms are obtained such as atypical one shown in this chapter. Surprisingly, they have a common module which has not been shown in the conventional suspensions, so that author tried to analyze the new-concept module. The configuration of the new module and newly developed analyzing method for that will be introduced in Chapter 4.

Table 3.1 Optimized values of the design parameters for Cases 3 and 4 (All satisfy the R&H constraints specified by (3.41) and (3.42)).

Design Parameters	Design Case 3	Design Case 4
$\dot{\gamma}$	-0.0202 deg/mm	-0.220 deg/mm
$\gamma^{50\text{mm}}$	-1.57 deg	-1.35 deg
$\dot{\delta}$	0.00310 deg/mm	0.00271 deg/mm
$\delta^{50\text{mm}}$	0.238 deg	0.274 deg
H^{RC}	90.0 mm	90.0 mm
AS	55.0 %	55.0 %
AL	63.0 %	63.0 %
$\Delta y_{50\text{mm}}^{\text{CP}}$	-3.53 mm	-2.18 mm
$\Delta y_{100\text{mm}}^{\text{CP}}$	-5.00 mm	0.833 mm

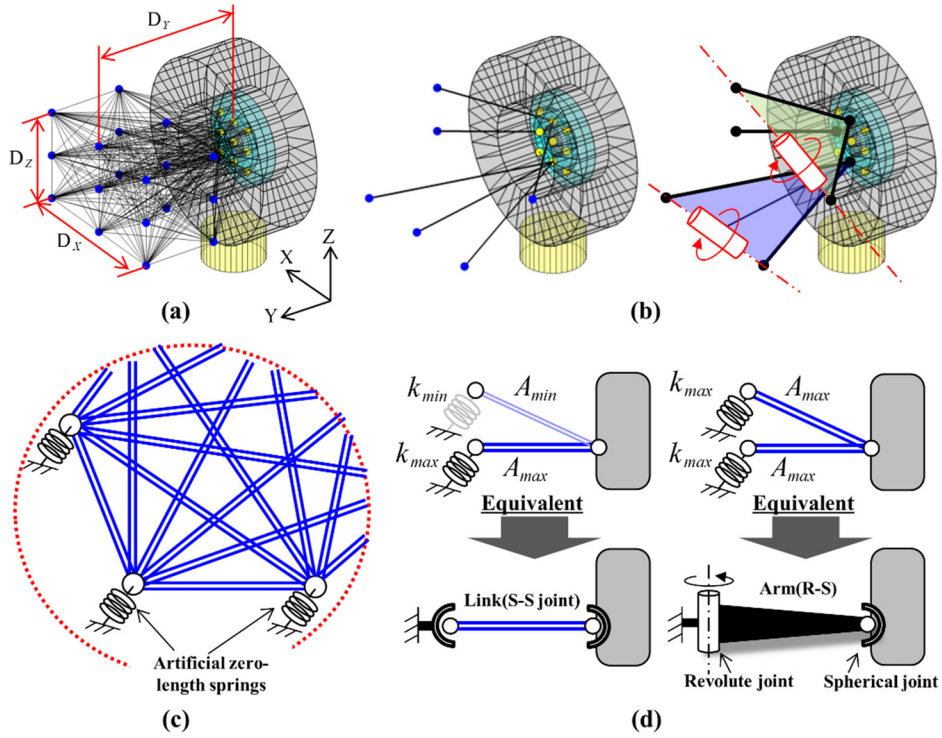


Figure 3.1 (a) Ground structure model composed of spatial bar elements and spring elements (spring elements are not shown). (b) Double wishbone suspension constructed from the ground structure. (c) Zoomed in view of the ground structure model with artificial zero-length springs. (d) Representation of a link and an arm by using the bar-spring ground structure model.

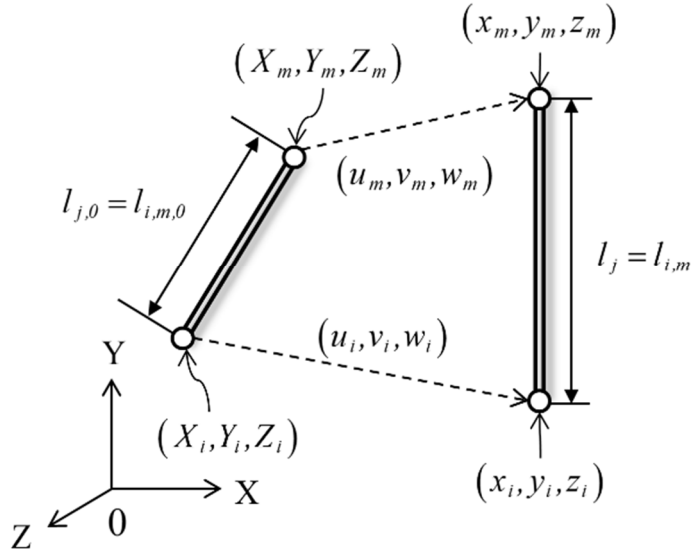
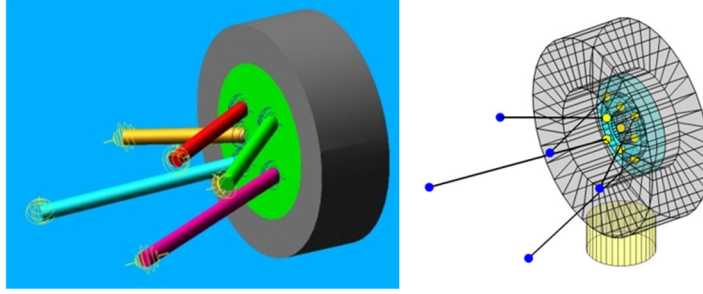
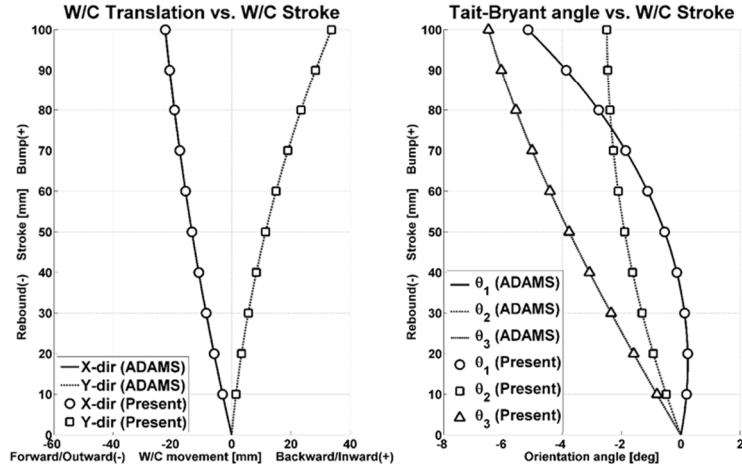


Figure 3.2 Undeformed (X, Y, Z) and deformed (x, y, z) configurations of a spatial bar element with two end-nodes.

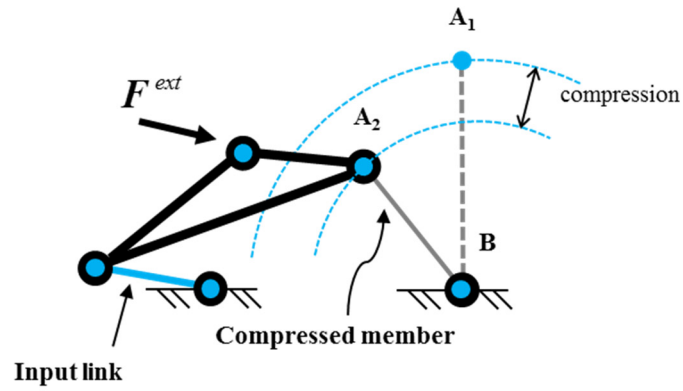


(a)

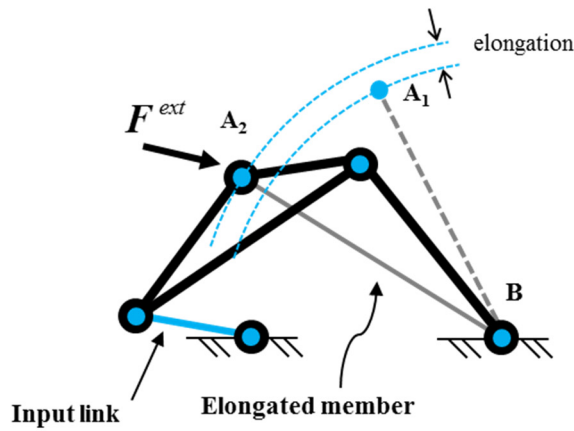


(b)

Figure 3.3 (a) Five-link suspension modeled by ADAMS (left) and by the present bar-spring ground structure model (right). (b) (left) Trajectories of (q_X, q_Y) and (right) those of $(\theta_1, \theta_2, \theta_3)$ or the 5-link suspension shown (a) when its Z -direction motion (q_Z) of the wheel center is prescribed as Eq. (3.37).



(a)



(b)

Figure 3.4 The planar mechanism behavior with a bar element of an intermediate design variable $\xi = \xi_{int}$, (say $\xi_{int} = 0.5$). — : $\xi = \xi_{max} = 1.0$, --- : $\xi = \xi_{int}$. (a) Mechanism in a quasi-redundant DOF state and (b) mechanism in a quasi-deficient DOF state.

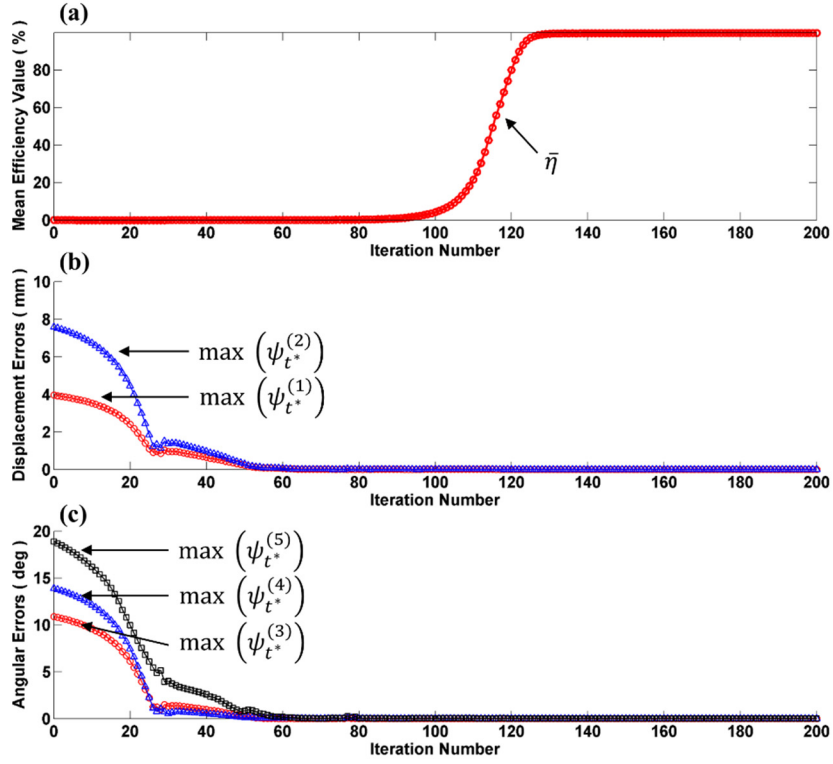


Figure 3.5 The iteration histories of (a) the mean transmittance efficiency ($\bar{\eta}$) and

(b) the path error measures for Design Case 1. ($\psi_{t^*}^{(1)} = |q_X(t^*) - \hat{q}_X(t^*)|$,

$$\psi_{t^*}^{(2)} = |q_Y(t^*) - \hat{q}_Y(t^*)|, \quad \psi_{t^*}^{(3)} = |\theta_1(t^*) - \hat{\theta}_1(t^*)|, \quad \psi_{t^*}^{(4)} = |\theta_2(t^*) - \hat{\theta}_2(t^*)|$$

$$\psi_{t^*}^{(5)} = |\theta_3(t^*) - \hat{\theta}_3(t^*)|)$$

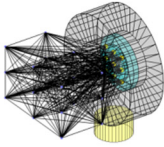
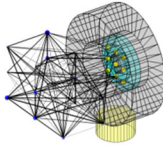
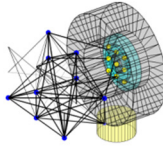
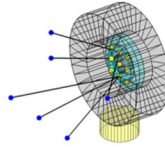
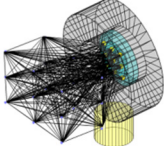
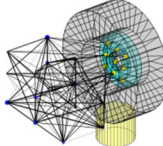
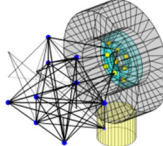
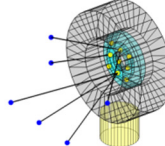
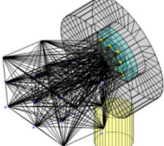
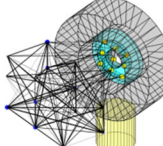
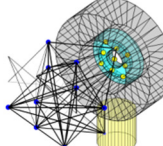
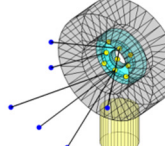
W/C Stroke	$n_i = 0$ (Initial)	$n_i = 100$	$n_i = 200$	Post-processed
0 mm				
50 mm				
100 mm				

Figure 3.6 Intermediate and final suspension layouts with their configurations for different wheel-center stroke values (\hat{q}_z) for Design Case 1 to synthesize a double wishbone suspension mechanism (n_i : iteration number).

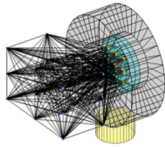
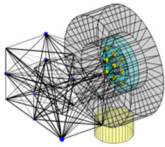
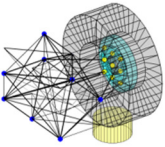
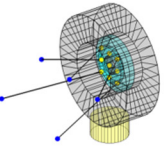
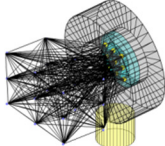
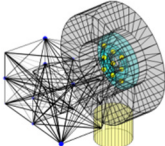
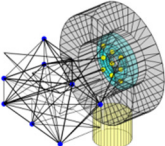
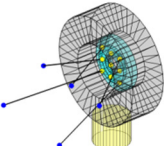
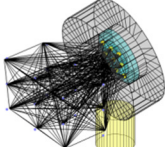
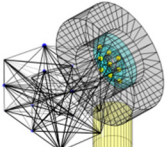
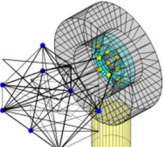
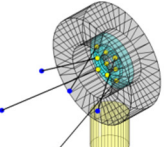
W/C Stroke	$n_i = 0$ (Initial)	$n_i = 100$	$n_i = 200$	Post-processed
0 mm				
50 mm				
100 mm				

Figure 3.7 Intermediate and final suspension layouts with their configurations for different wheel-center stroke values (\hat{q}_z) for Design Case 2 to synthesize a 5-link suspension mechanism (n_i : iteration number).

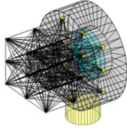
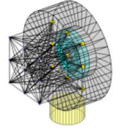
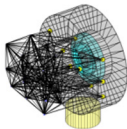
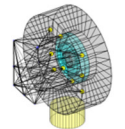
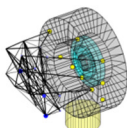
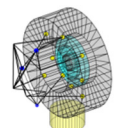
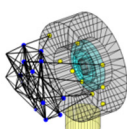
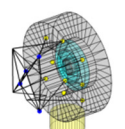
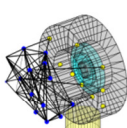
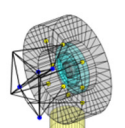
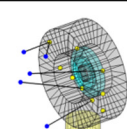
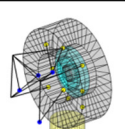
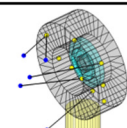
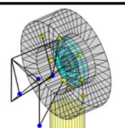
State	Design Case 3	Design Case 4
$n_i = 0$		
$n_i = 50$		
$n_i = 100$		
$n_i = 150$		
$n_i = 200$ (converged)		
Final post-processed layout at 0 mm stroke		
Final post-processed layout at 100 mm stroke		

Figure 3.8 Evolutions of the suspension mechanism layouts by the proposed synthesis method for Design Cases 3 and 4 (n_i : iteration number). The last two rows show the post-processed synthesized mechanism configurations at $\hat{q}_z = 0$ mm and $\hat{q}_z = 100$ mm .

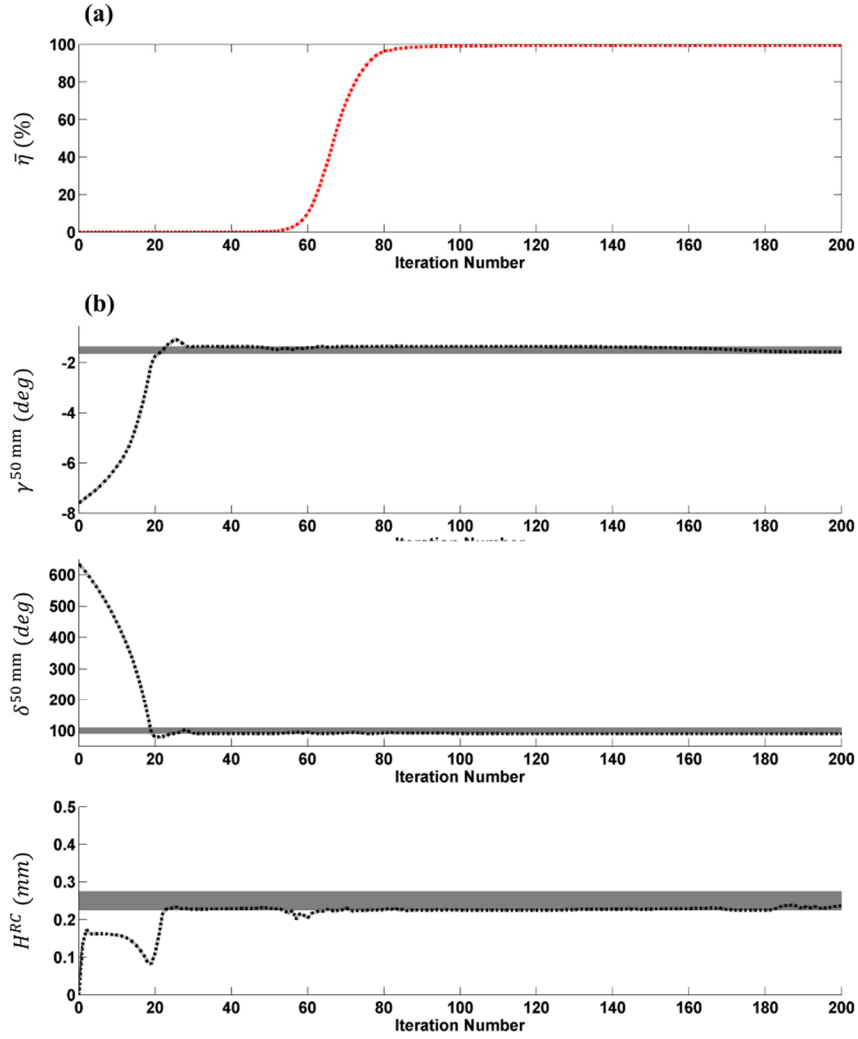


Figure 3.9 The iteration histories for Design Case 3. (a) The work transmittance efficiency and (b) some design parameters.

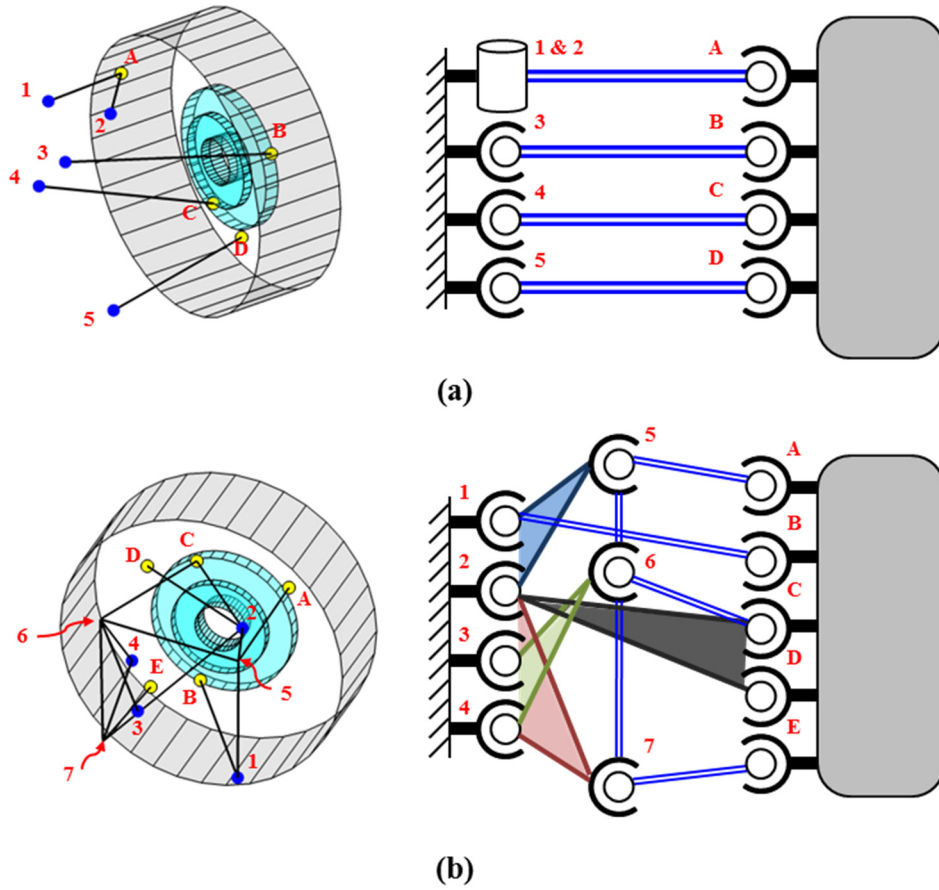


Figure 3.10 Illustration of the synthesized suspensions (a) for Design Case 3 and (b) Design Case 4. The two-dimensional schematic representation of the optimized suspensions can facilitate the kinematic chain analyses.

CHAPTER 4

NEW CONCEPT SUSPENSION INCLUDING HIDDEN LINK MODULE

4.1 Overview

A methodology for mechanism design through topology optimization is proposed in Chapter 2, and then it is extended to the three-dimensional suspension mechanism design problems in Chapter 3. As a result, it is confirmed that industrial problems such as suspension design problems can be dealt with successfully by the proposed automatic synthesis method, also being confirmed that new suspensions can be derived in addition to conventional suspensions through the proposed method. In particular, the entirely new suspension topology is obtained when performance conditions required for the conventional suspensions are applied to the smaller

design domain, where extremely restricted space is allowed to use.

After verifying the proposed suspension design methodology, several design case studies with variation of the design parameters, corresponding to equation (3.42), are implemented. As mentioned in Chapter 3, the results are quite similar in ordinary design domain. However, in smaller design domain, unconventional suspension types are obtained with auxiliary links. In particular, a specific module is obtained several times repeatedly among the design case studies, so that we decided to investigate the meaning of the results.

In this chapter, geometric feature and kinematic role of the newly obtained special module will be analyzed. During the analysis, a new method called “force transmission analysis” technique will be proposed based on screw-axis theory to investigate the role of the newly designed module. After analyzing what kinds of kinematic constraints the new module imposes to the wheel (or knuckle), an existing suspension component performs the same role as the new module will be found. According to the result of the investigation, it is confirmed that the concerned module gives the constraint force as the "link" component of the existing suspension, and from this point we named the new module as the "hidden link". The details of the procedure and result will be described in this chapter.

4.2 A new concept obtained from topology optimization

4.2.1 A special module included in the new concept

Topology optimization is performed for the two design domains as Figure 4.1 (Design Domain L is larger than Design Domain S), where the design conditions presented in (3.41) are applied. Figure 4.1 shows each optimization result; View 1 in Figure 4.1 corresponds to the front view. Black dots means hard points attached to the frame (or car body), and cyan-colored dots means knuckle points. The white dot location, where it corresponds to the point of which the spring stiffness is designed to have the minimum value in the topology optimization, is a point not directly connected to both the knuckle and the frame.

Design Case L in Figure 4.1 is applied to the design domain whose lengths in X, Y, and Z directions are 300 mm, respectively. Meanwhile, Design Case S in Figure 4.1 corresponds to a case where the design domain size is reduced to 200 mm in the X and Z directions. In Case L, a conventional multi-link type suspension is obtained, in which the lower arm is split into two lower links in a double wishbone type suspension. On the other hand, in Case S, a new suspension which has not been observed before was derived. It is the newly suggested suspension obtained from the topology optimization, and this new concept will be studied in this chapter.

Figure 4.2 is a simplified representation of the suspension obtained in Figure 4.1, where the cylinder shaped symbol represents a revolute joint, and the circle surrounded by the half-circle represents a ball joint. A simplified symbolic

expression of the suspension in Figure 4.2(a), corresponding to the Case L result, is consisting of one arm and three links. Here, an arm is defined as a component having two end points, where one is a revolute joint and the other end is a ball joint. And a link is a two-end point member whose both ends are ball joints. A suspension of Figure 4.2(b) corresponds to the Case S result. Compared with the Case L result, a link is replaced into the special module in the Case S result.

In detail, for the Case S result, there are several differences between the configuration obtained from the topology optimization (Figure 4.1) and symbolic expression (Figure 4.2(b)). In configuration depicted in Figure 4.1, one of the hard points of the upper arm and one of the hard points of the special module share the same node, and one of the knuckle points of the lower link and one of the knuckle points of the special module also share the same node. However, since the topology of suspension mechanism is not changed even if the shared points are separated into two different points, each joint was independently separated and analyzed as shown in Figure 4.2(b). This separation is helpful to interpret the special module.

From the simplified schematic illustration shown in Figure 4.2(b), one can see that two links connected to the knuckle in the special module are not directly connected to the frame. This part corresponds to the auxiliary link concept mentioned in Chapter 3, and it can be considered as a new suspension component which has not been found in existing conventional suspensions. It is a representative feature of the suggested new concept suspension, and the kinematic role of this special module will be analyzed in this chapter.

4.2.2 Strategy for interpretation of the special module

In raw data of the topology optimization result (Case S shown in Figure 4.1), four green-colored truss elements correspond to the special module in Figure 4.2(b). Here, the special module what we suggest as new-concept in this research can be interpreted as Figure 4.3(a) as well as Figure 4.3(b) according to the grouping strategy. Then, what is the effect of the four truss elements composing the special module? To see the role of them, it needs to consider both grouping strategies. Interpretation of the special module based on the grouping shown in Figure 4.3(a) will be implemented here, and analyzing the effects of the special module by grouping as shown in Figure 4.3(b) will be dealt with later.

First, consider the grouping shown in Figure 4.3(a), where three links are considered as one set. From this grouping strategy, the result of Case S can be interpreted as the modification of the multi-link suspension shown in Figure 4.2(a). The modification needs the following three steps:

Step1. Select one of the lower links in the suspension of 4.2(a)

Step 2. Remove a connection between the selected link and the sub-frame

Step 3. Attach three links to the hard point as shown in Figure 4.3(a)

In step 3, two of the three links are connected to the frame and the other one is connected to the knuckle. In general, the ball joint applied at the end of the link component has the effect of constraining three DOF's, however each additional link

component has only one DOF restricting effect. Accordingly, the three additional link elements are required to restrict three DOF's instead of the ball joint. In this case, the ball joint located at the end of the link, which was selected in Step 1, is no longer fixed to the frame, but has a relative motion with respect to the frame. That is, it is no longer a fixed mount point of the multi-link suspension, but a moving point in the newly suggested suspension.

If an end-point of the link moves, what is better than a link with a fixed hard point? The kinematic behavior of existing suspensions is strongly influenced by the located angle and length of the arms (or links). Especially, the sum and difference of the lengths of the two arms are very important in double wishbone suspensions, because camber, scuff changes, and anti-features are directly affected by them [82]. Each length of links also have an impact on roll center migration behavior [86]. Thus, a suspension having a moving (hard) point such as the suspension in Figure 4.3(a) may have totally different features compared with that of the conventional suspensions which has only the fixed mount points. It can be expected that the effective length of the link in Figure 4.3(a) will be changed during the kinematic motions. By using this effect well, it could be possible to flexibly change the effective length of the component in the desired direction. Therefore, it could be presumed to be the reason why a new concept solution was derived from Design Case S with a narrow design domain. However, there is no way to analyze the effect theoretically in this viewpoint, so that the numerical computation is the only method to analyze the concept shown in Figure 4.3(a). Also, it means that we need to rely on the numerical optimizations

rather than analytical methods to control design parameters of the newly suggested suspension module. In this research, to avoid this kind of problem, a new module interpretation method is proposed based on another grouping strategy as shown in Figure 4.3(b).

When considering the two links as one arm like Figure 4.3(b), the special module included in the new-concept suspension can be interpreted as "revolute-spherical-revolute" structure. We call it RSR-limb, which is occasionally employed in the parallel manipulators. For one's information, the RSR-limb structure corresponds to a limb composed of two RS structures, where the RS corresponds to the conventional arm component in suspensions. Then, how can we discuss the kinematic role of the RSR limb? In robotics, in addition to the RSR, there are a lot of limbs such as UPS, RCR, and others [87], and there is also a method so-called screw axis theory to calculate Jacobian of these limbs. In this research, the force that the car body supports the knuckle through the RSR limb will be interpreted by this screw axis theory, and it will be compared with the forces of the existing suspension components to analyze the kinematics role of the new special module.

4.3 Force transmission analysis

A key point determining the movement of the mechanism in kinematics is a constraint equations created by the kinematic components. If there are two suspensions which instantaneously impose the same constraints to the knuckle, the both suspensions can be considered as instantaneously equivalent systems. In this case, the same constraint means the same constraint force of the suspension imposed on the knuckle, which corresponds to the “point of action” of the force and the “direction of force”. For example, a link element commonly used in suspension gives the knuckle joint a lengthwise force in their located direction at the connected point, so that a 5-link suspension is able to control the five DOF’s of the wheel by imposing the five-lengthwise force of each link component to the knuckle.

The constraint force of the mechanism is expressed as the product of the Lagrange multiplier assigned to the constraint and derivative of the constraint with respect to state-variables, and the overall behavior of the constraints constituting the system is expressed through a Jacobian matrix that implicitly represents the constraint forces in total. The following equations correspond to the equations governing the behavior of the mechanism.

$$\begin{bmatrix} \mathbf{M} & \Phi_q^T \\ \Phi_q & \mathbf{0} \end{bmatrix} \begin{Bmatrix} \ddot{\mathbf{q}} \\ \lambda \end{Bmatrix} = \begin{Bmatrix} \mathbf{Q}^A \\ \gamma \end{Bmatrix} \quad (4.1)$$

$$\gamma \equiv -(\Phi_q \dot{\mathbf{q}})_q \dot{\mathbf{q}} - 2\Phi_{q'} \dot{\mathbf{q}} - \Phi_{tt} \quad (4.2)$$

In Eq. (4.1), \mathbf{M} denotes inertia matrix, and $\Phi_{\mathbf{q}}$ corresponds the derivative of the constraint equation (Φ) with respect to state variable (\mathbf{q}). External force vector and Lagrange multiplier vector are \mathbf{Q}^A and $\boldsymbol{\lambda}$, respectively. The Lagrange multiplier determines the magnitude of the corresponding constraint forces. Eq. (4.1) is the governing equation of the dynamics of multi-body systems, and $\boldsymbol{\gamma}$ defined as Eq. (4.2) is required for the dynamic effects. In the field of computational kinematics, Equation (4.1) is called DAE (Differential-Algebraic Equation) [63]. In Eq. (4.1), $\Phi_{\mathbf{q}}$ is the Jacobian matrix which includes information of “point of action” and “direction of force” of the constraint forces ($\Phi_{\mathbf{q}}^T \boldsymbol{\lambda}$). As one can see in the governing equations, by considering the constraint equations of the mechanism composing components, overall behavior of the mechanism systems can be analyzed. In this chapter, to see what kinds of the constraint forces are applied to the wheel through the RSR-limb, the force transmission analysis will be implemented based on the screw-axis theory. Then, conventional suspension components having the similar effects will also be found for interpretation of the RSR-limb which is obtained from the topology optimization in smaller design domain.

4.3.1 Introduction of the screw axis theory

The screw axis theory, one of the coordinate systems for representing spatial motions in three dimension, divides the motion into the translation motion parallel to an axis and the rotation motion around the axis (the ratio between translation and rotation is

defined as pitch). This screw axis theory could be employed to represent 6-DOF spatial motion as well as to express the generalized forces, where they are work-conjugate of each other. When the screw is applied for the displacements, it is called twist. However, it is called wrench for the generalized forces, which are forces and moments. To definitely represent three-dimensional motions and forces, the screw-axis theory needs six independent components, which are 4 line description components based on the Plücker coordinate (3 direction components and 1 intercept), 1 translational displacement (or force) magnitude along the designated axis, and 1 pitch information, respectively. By dealing with these six components well, one can easily describe the motion and force in the three-dimensional space. In robotics, screw axis is occasionally employed to calculate the Jacobian matrix of the parallel manipulators, and it is also used in automotive industry to find steering kingpin axis and car body roll axis [88, 89]. In this research, detailed description of the screw-axis theory for basic course will not be dealt with. For the basics, consider the references [87, 90].

Figure 4.4(a) depicts the initial and the final position of a rigid-body, and motion between the two states can be divided into rotation about an axis and translation along the same axis. This is the screw-axis theory, and every motion occurring in the three-dimension can be expressed through the translation and the rotation about an axis called screw-axis. In Figure 4.4(b) the divided motions are sequentially described, but they can occur at once with a helical trajectory. In the helix, the

translational magnitude per the unit rotation is defined as the pitch ($p = d/\theta$), where d and θ denote magnitude of the translation and rotation, respectively. Here, the rotation angle θ is equal to the angle observed in the view perpendicular to the rotation axis as described in Figure 4.4(c). If the direction vector of the screw axis, the rotation axis in Figure 4.4, is defined as \mathbf{s} and the screw axis pass through a point A , one can describe the twist screw representing the motion in Figure 4.4 as Eq. (4.3).

$$\mathbf{S} = \begin{bmatrix} \mathbf{s} \\ \mathbf{s}_o \times \mathbf{s} + p\mathbf{s} \end{bmatrix} \quad (4.3)$$

where, \mathbf{s}_o corresponds to the three-dimensional coordinates of the point A . By the similar way, one can describe the wrench screw corresponding to the generalized force. When the net force and moment applied to the body CM (Center of Mass) is equal to \mathbf{F} and \mathbf{c} , they can be converted to a equivalent force and moment applied to a point A_r , where the force has the direction in \mathbf{s}_r and the moment has an axis in the same direction. Here the ratio between moment and the force is defined as the pitch of wrench ($p_r = c/f$). To this end, c and f are couple and the force applied to the point A_r , respectively. When the coordinate of the point A_r is equal to \mathbf{s}_{ro} , the wrench screw can be expressed as Eq. (4.4).

$$\mathbf{S}_r = \begin{bmatrix} \mathbf{s}_r \\ \mathbf{s}_{ro} \times \mathbf{s}_r + p_r \mathbf{s}_r \end{bmatrix} \quad (4.4)$$

By employing the screw axis theory, the Jacobian matrix of the mechanism system can be obtained easily. Figure 4.5(a) depicts four independent motions of the arm components by using the twist screws, where point A corresponds to an arbitrary point located on the axis of the revolute joint. The four independent motions are screw \mathbf{S}_1 denoting revolute joint motion, and three independent rotations of the ball joint B described by $\mathbf{S}_2, \mathbf{S}_3$, and \mathbf{S}_4 , i.e. the ball joint can be divided into three revolute joints. Three independent rotations of the ball joint can be selected arbitrary if they are not linearly dependent, but in this research they are set to global X, Y, and Z axis for the convenience in calculation. Because each revolute joint does not have translational motion, pitch of the screw becomes 0. Therefore, the twist equation in (4.3) can be derived as (4.5) in case of Figure 4.5(a).

$$\mathbf{S}_1 = \begin{bmatrix} \mathbf{s}_1 \\ \mathbf{s}_A \times \mathbf{s}_1 \end{bmatrix} \quad (4.5a)$$

$$\mathbf{S}_2 = \begin{bmatrix} \mathbf{s}_2 \\ \mathbf{s}_B \times \mathbf{s}_2 \end{bmatrix} \quad (4.5b)$$

$$\mathbf{S}_3 = \begin{bmatrix} \mathbf{s}_3 \\ \mathbf{s}_B \times \mathbf{s}_3 \end{bmatrix} \quad (4.5c)$$

$$\mathbf{S}_4 = \begin{bmatrix} \mathbf{s}_4 \\ \mathbf{s}_B \times \mathbf{s}_4 \end{bmatrix} \quad (4.5d)$$

In Eq. (4.5), two vectors \mathbf{s}_A and \mathbf{s}_B correspond to position vector of the point A and the point B, and \mathbf{s}_1 denotes the direction vector of the revolute axis.

Direction vectors \mathbf{s}_2 , \mathbf{s}_3 , and \mathbf{s}_4 are unit vectors in global X, Y, and Z direction, respectively. If the magnitude of the twist screws described in (4.5) is q_i ($i = 1, 2, 3, 4$), relative motion of the knuckle/wheel with respect to the car-body is equal to Eq. (4.6).

$$\mathbf{S} = \sum_{i=1}^4 (q_i \mathbf{S}_i) \quad (4.6)$$

That is, the knuckle have four DOF's with respect to the car-body. Generally, when a rigid-body, such as the knuckle, is not restricted to any constraint, it has six DOF's corresponding to free motions in three-dimensional space. But, a knuckle attached to the arm only have the four free motions, so that one can see that there are two constraints applied to the knuckle through the arm (RS module). To calculate the constraints imposed to the knuckle by the arm, virtual work principle can be used. Because the (virtual) work of the constraints of perfect rigid joint is equal to 0, Eq. (4.7) should be satisfied to all kinematic joints. In (4.7), screw \mathbf{S}_r corresponds to the reciprocal screw of the twist screw \mathbf{S} , and it is called work conjugate. Here, it is the wrench screw corresponding to the constraint force.

$$\mathbf{S}_r^T (\delta \mathbf{S}) = 0 \quad (4.7)$$

In (4.7), $\delta \mathbf{S}$ is the virtual displacement, which is equal to $\sum_{i=1}^4 (\delta q_i) \mathbf{S}_i$. Additionally, in calculating the equation (4.7), the transpose should be dealt with carefully. According to the definition of screw theory, transpose of \mathbf{S} is equal to

$$\mathbf{S}^T = \{S_4, S_5, S_6, S_1, S_2, S_3\}, \text{ where } \mathbf{S} = \{S_1, S_2, S_3, S_4, S_5, S_6\}^T.$$

In case of Figure 4.5(a), one can obtain two reciprocal screws satisfying Eq. (4.7). They are pure forces \mathbf{S}_{r1} and \mathbf{S}_{r2} ($p_r = 0$), which are applied to the point B. These two wrench screws are located on the wrench plane, which is corresponding to the arm (RS) plane composed of the directional vector of the revolute joint axis (\mathbf{s}_1) and vector connecting the point A and B (\mathbf{s}_{BA}) as shown in Figure 4.5(b). It could be proved from the below proposition. The proof is well organized in APPENDIX B.2.

Proposition

A wrench screw described as Eq. (4.8) satisfies Eq. (4.7) with respect to twist screws defined in (4.5-4.6).

$$\tilde{\mathbf{S}}_r = \tilde{q}_r \begin{bmatrix} \tilde{\mathbf{s}}_r \\ \mathbf{s}_B \times \tilde{\mathbf{s}}_r \end{bmatrix} \quad (4.8a)$$

$$\tilde{\mathbf{s}}_r = c_1 \mathbf{s}_1 + c_2 (\mathbf{s}_B - \mathbf{s}_A) \quad (4.8b)$$

In Eq. (4.8), coefficients c_1 and c_2 are arbitrary values, but both them cannot be 0 at once.

Consequently, two arbitrary independent vectors located on the wrench plane of the Figure 4.5(b) could be the force vectors which support the knuckle through the arm (RS-module), and their action point becomes the locations of ball joint (B). It can also be proved by numerically calculated Jacobian matrix. Then, it needs to consider the wrench screws of the arm (RS) in the physical behavior aspect. If a force perpendicular to the arm plane is imposed on the ball joint position B, then it will excite rotational motion of the revolute axis. Otherwise, if moments are applied to the point B, they will excite rotation of the ball joints, which corresponds to the knuckle rotations with respect to the arm. Accordingly, only the in-plane pure forces applied to the ball joint, included in the wrench plane of the Figure 4.5(b), could be the forces which do not excite rigid-body motions of the joints in RS-component. That is, they are the constraint forces which the arm can apply to the knuckle in statics. In the next chapter, the screw axis theory will be applied to the RSR-limb to interpret behavior of the special module in the proposed new-concept suspension.

4.3.2 Force transmission analysis of the RSR-limb

A special module proposed in the new-concept suspension is the RSR-limb, which corresponds to the two arms connected through the ball joint. When there is no components attached to the knuckle, it will have the six free motions DOF's in 3-dimensional space. However, only the five free motions are remained after applying the RSR-limb to the knuckle, and it means that one DOF is restricted by the RSR-

limb. To this end, the screw-axis theory could be applied to see what kinds of the constraint force/moment is applied through the RSR-limb, and the result is equal to (4.9).

$$\bar{\mathbf{S}}_r = \begin{bmatrix} \bar{\mathbf{s}}_r \\ \mathbf{s}_B \times \bar{\mathbf{s}}_r \end{bmatrix} \quad (4.9a)$$

$$\bar{\mathbf{s}}_r \perp \{\mathbf{s}_1 \times (\mathbf{s}_A - \mathbf{s}_B)\} \quad (4.9b)$$

$$\bar{\mathbf{s}}_r \perp \{\mathbf{s}_1 \times (\mathbf{s}_B - \mathbf{s}_C)\} \quad (4.9c)$$

In Eq. (4.9), \mathbf{s}_i ($i = A, B, C$) is the position vector of the point A, B, and C, where the point B is the ball joint location and points A and C are points located on the rotation axis of each revolute joint as shown in Figure 4.6(a). Additionally, \mathbf{s}_1 and \mathbf{s}_5 are rotation axis vector of each revolute joint. In Eq. (4.9), $\bar{\mathbf{S}}_r$ is the wrench screw corresponding to the pure force acting on the point B in $\bar{\mathbf{s}}_r$ direction, where the direction of the force is perpendicular to the normal vectors of the both arms composing the RSR-limb, and it means that $\bar{\mathbf{s}}_r$ is the directional vector corresponding to an intersecting line of the two arms.

To verify the (4.9), it needs to employ the virtual work principle as described in Chapter 4.3.1. First, twist screws representing motion of the rigid joints in Figure 4.6(a) should be described for five independent motions, as written down in Eq. (4.10) by the screw-axis form.

$$\bar{\mathbf{S}}_1 = \begin{bmatrix} \mathbf{s}_1 \\ \mathbf{s}_A \times \mathbf{s}_1 \end{bmatrix} \quad (4.10a)$$

$$\bar{\mathbf{S}}_2 = \begin{bmatrix} \mathbf{s}_2 \\ \mathbf{s}_B \times \mathbf{s}_2 \end{bmatrix} \quad (4.10b)$$

$$\bar{\mathbf{S}}_3 = \begin{bmatrix} \mathbf{s}_3 \\ \mathbf{s}_B \times \mathbf{s}_3 \end{bmatrix} \quad (4.10c)$$

$$\bar{\mathbf{S}}_4 = \begin{bmatrix} \mathbf{s}_4 \\ \mathbf{s}_B \times \mathbf{s}_4 \end{bmatrix} \quad (4.10d)$$

$$\bar{\mathbf{S}}_5 = \begin{bmatrix} \mathbf{s}_5 \\ \mathbf{s}_C \times \mathbf{s}_5 \end{bmatrix} \quad (4.10e)$$

In Eq. (4.10b)-(4.10d), ball joints are divided into three independent revolute joints as the RS-module analysis implemented in Chapter 4.3.1. Also, the three bases of the revolute joints, \mathbf{s}_i ($i = 2, 3, 4$), are selected as the unit vectors of the global X, Y, and Z direction. After obtaining the twist screw of each joint, knuckle motion with respect to the fixed car body can be denoted as (4.11) by linear combination of the screws in (4.10).

$$\bar{\mathbf{S}} = \sum_{i=1}^5 (q_i \bar{\mathbf{S}}_i) \quad (4.11)$$

To check whether the wrench in (4.9) is a reciprocal screw of (4.11) or not, it needs to calculate the virtual work in (4.12).

$$\bar{\mathbf{S}}_r^T \delta \bar{\mathbf{S}} = 0 \quad (4.12)$$

Proposition

A wrench screw in Eq. (4.9) satisfies Eq. (4.12) with respect to twist screws defined in (4.10-4.11).

The proof for above proposition is introduced in Appendix B.3. From the proposition, a force imposed on the knuckle through the RSR-limb can be investigated. The force is equal the pure force, which has a direction in the interesting line of the two arm planes and acts on the ball joint located between the two arms. Figure 4.6(b) shows the constraint force, where two wrench planes correspond to each arm plane. Then, it needs to see the load flow from the knuckle to the car-body in detail.

First, the wrench plane 2 in Figure 4.6(b) has the normal vector perpendicular to both \mathbf{s}_C and $\mathbf{s}_C - \mathbf{s}_B$, and it includes the ball joint denoted as the point B . To this end, the force imposed on the knuckle will be transmitted to the ball joint located between two arms through the knuckle-attached arm, and only in-plane forces located on wrench plane 2 are transmittable as mentioned in Chapter 4.3.1. Here, the concept of the “transmittable” is the same with the concept used in Chapter 4.3.1 to analyze the arm (RS-module) component. The transmittable force corresponds to the force which can be supported in statics without any rigid joint motion. For example, a force perpendicular to the wrench plane 2 cannot be transmitted to the ball joint, because it will make knuckle-attached revolute joint rotate. Also, if the moments are

transmitted to the ball joint through the knuckle-attached arm, it will excite rotation of the knuckle-attached arm to rotate with respect to the car-body attached arm through the ball joint. Consequently, only the pure in-plane forces, which is belong to the wrench plane 2, can be transmitted from the knuckle to the ball joint through the knuckle-attached arm. In the same manner, the car-body attached arm can transmit only the in-plane forces located on the wrench plane 1, which is perpendicular to both vectors \mathbf{s}_A and $\mathbf{s}_A - \mathbf{s}_B$ and includes the ball joint. Accordingly, only a force along the intersecting line of both wrench planes could be transmitted from the knuckle to the car body, and it means that above-proved proposition is correct in physics. In Figure 4.6(b), $\bar{\mathbf{S}}_r$ is the transmittable force of the RSR-limb, and it is corresponding to the intersection set of the transmittable forces of both arms composing the RSR-limb.

In precise, the force flow could be described as Figure 4.7(a). The forces are imposed on the knuckle through the two points in suspensions, because the revolute joints are generally realized by the two ball joints (or bushes). Meanwhile, we need to focus on an important thing that net force of these two forces, \mathbf{F}_{C_1B} and \mathbf{F}_{C_2B} in Figure 4.7(a), are equivalent to a force acting on the ball joint, which has the magnitude of $\|\mathbf{F}_{C_1B} + \mathbf{F}_{C_2B}\|$ and direction same as that of the vector $\bar{\mathbf{s}}_r$ in (4.9a). It is the same as that described in (4.9), and it means that the pure force action point and direction is equal to \mathbf{s}_B and $\bar{\mathbf{s}}_r$, respectively. From that, it is possible to

suggest a concept shown in Figure 4.7(b). Even though the ball joint is not directly attached to the knuckle in the RSR-limb module, but it can be considered as a virtual joint attached to the knuckle rigidly in instantaneous case. That is, it is possible to think that the designated force $\mathbf{F}_{C_1B} + \mathbf{F}_{C_2B}$ is transmitted directly to the knuckle through this virtual joint, which is located on the ball joint location. Then, why do we need to consider the virtual joint concept? It will be helpful to analyze the effect of the RSR-limb in the new-concept suspension in the following chapters.

4.3.3 Suggestion of hidden link concept

From the force transmission analysis in Chapter 4.3.2, type of the constraint force could be analyzed, and also direction and action points of the constraint forces were investigated. Interestingly, the constraint force is the pure force applied to the ball joint located between two arms composing the RSR-limb. As mentioned in the introduction of Chapter 4.3, the constraint forces in rigid-body mechanisms govern behavior of the systems. Particularly, two systems will have the same motion if they have the same constraints, when the inertial is excluded like as quasi-static case. To this end, the same constraint means that the constraint forces have the same direction and action point. Then, what is the equivalent constraint of the RSR-limb according to this viewpoint? Fortunately, there is a well-known suspension component called link, which imposes the pure force on the knuckle. Accordingly, one can consider the RSR-limb to behave as the link component located along the transmittable force

direction. From that, in this research, the RSR-limb is defined as the “hidden link”.

Generally, topology optimization results of the normal sized design domains are conventional suspensions such as the multi-link type suspension shown in Figure 4.2 of Case L. But, when the design domain is reduced to be smaller than conventional one like as Case S in Figure 4.2, it is apparent that conventional suspension is difficult to satisfy the provided design criteria. In this case, a special module which replaces the link component may be required, and from this regard one can expect that the RSR-limb is obtained in Case S to resolve the problem.

The effect of the special module, RSR-limb, in instantaneous was well-investigated through the force transmission analysis. According to the investigation, the RSR-limb can work as a hidden link, and one end-point location of the hidden link is designated as the virtual joint in Figure 4.7(b), which is corresponding to the position of the ball joint located between the arms. That is, the ball joint can be regarded to be attached to the knuckle rigidly like as the real link-end point. However, another joint position corresponding to the frame-attached hard point is not yet determined by using the force transmission analysis. Indeed, no exact point exists corresponding to the equivalent chassis mount theoretically, so that it could not be defined through the instantaneous constraint force analysis, such as the method based on the screw-axis theory.

Then, how can we find a virtual mount position of the hidden link which gives a similar effect on the knuckle especially in large kinematic motions of the suspension. A parameter study and suggestion related to this issue will be dealt with in the

Chapter 4.4. Before examining the parameter study for determining the mount position, validation of the suggested hidden link for the system-level behavior will be implemented in the next chapter.

4.3.4 Validation of the hidden link concept

By implementing the compliance analysis of the suspension, one can verify if the hidden link gives the same effect compared with the conventional suspension link component. In this chapter, an arbitrary hidden link suspension including the RSR limb will be considered as shown in Figure 4.8(a), where the RSR limb can be considered as the hidden link. Then, a multi-link suspension which has the real-link instead of the RSR-limb in the location of the hidden-link will be modeled as shown in Figure 4.8(b), which has the same components except the RSR-limb compared with the hidden link suspension in Figure 4.8(a). If the compliance behaviors of the two suspensions in Figure 4.8 are equivalent to each other, the system-level proof of the hidden link concept will be completed. That is, from this numerical experiment, whether the RSR-limb works as the link component or not can be shown in suspension systems, beyond the part/module level.

From Eq. (4.1) corresponding to the governing equations of multi-body dynamics, one can see that constraint equations are included in the Jacobian matrix of the system. If the inertia effect is excluded from the Eq. (4.1) and the elastic effect is included, Eq. (4.13) can be derived as the governing equations of the system. Eq. (4.13) denotes the behavior of the deformable multi-body system constrained by the

rigid-joints. An interesting point is that Eq. (4.13) also employs the same Jacobian information which is used in Eq. (4.1) to describe the rigid-body systems [91]. To this end, directions and action points of the constraint forces are still included in the Jacobian matrix, where these two elements are essential components of the “three elements of the force” together with magnitude of the constraint force. Note that the magnitude of the constraint force is not included in the Jacobian matrix, but it is obtained from the calculation of the governing equations. The magnitude is determined by the Lagrange multipliers (λ), one of the state variables in Eq. (4.29), of the constraints.

$$\begin{bmatrix} \mathbf{K} & \Phi_q \\ \Phi_q^T & \mathbf{0} \end{bmatrix} \begin{Bmatrix} \Delta \mathbf{q} \\ \lambda \end{Bmatrix} = \begin{Bmatrix} \mathbf{F}^{\text{ext}} \\ \mathbf{0} \end{Bmatrix} \quad (4.13)$$

Eq. (4.13) is the linearized elasto-kinematic equation, where $\Delta \mathbf{q}$ is the state variable representing rigid-body motions including translation ($\Delta \mathbf{r}$) and virtual rotation ($\Delta \boldsymbol{\pi}$). Because three-dimensional rotation of the rigid-body is path-dependent quantity, it needs to define linearized path-independent rotation DOF's to derive potential. To this aspect, virtual rotation $\Delta \boldsymbol{\pi}$ is defined as $\Delta \boldsymbol{\pi} = (\Delta \mathbf{A}) \mathbf{A}^T$, by which linearized displacement of an arbitrary point according to rotation of the body could be calculated as $(\Delta \boldsymbol{\pi}) \times \mathbf{s}$. Here, \mathbf{s} denotes position vector with respect to the body-coordinate of the rigid-body, and one can see that this concept is the same as the description of the small displacement occurred due to the rotation DOF in the Timoshenko beam or Mindlin plate theory. That is, $\Delta \boldsymbol{\pi}$ is only valid in

very small rotation cases [63].

To calculate Eq. (4.13) for the suggested suspension systems, it needs to derive total stiffness matrix \mathbf{K} . To calculate the total stiffness, bush element stiffness matrix \mathbf{K}_e has to be derived.

$$\begin{Bmatrix} \mathbf{F}_i \\ \mathbf{T}_i \\ \mathbf{F}_j \\ \mathbf{T}_j \end{Bmatrix} = \mathbf{K}_e \begin{Bmatrix} \Delta \mathbf{r}_i \\ \Delta \boldsymbol{\pi}_i \\ \Delta \mathbf{r}_j \\ \Delta \boldsymbol{\pi}_j \end{Bmatrix} \quad (4.14a)$$

$$\mathbf{K}_e = \begin{bmatrix} \mathbf{K}_T & -\mathbf{K}_T \tilde{\mathbf{s}}_i & -\mathbf{K}_T & \mathbf{K}_T \tilde{\mathbf{s}}_j \\ \tilde{\mathbf{s}}_i \mathbf{K}_T & -\tilde{\mathbf{s}}_i \mathbf{K}_T \tilde{\mathbf{s}}_i + \mathbf{K}_R & -\tilde{\mathbf{s}}_i \mathbf{K}_T & \tilde{\mathbf{s}}_i \mathbf{K}_T \tilde{\mathbf{s}}_j - \mathbf{K}_R \\ -\mathbf{K}_T & \mathbf{K}_T \tilde{\mathbf{s}}_i & \mathbf{K}_T & -\mathbf{K}_T \tilde{\mathbf{s}}_j \\ -\tilde{\mathbf{s}}_j \mathbf{K}_T & \tilde{\mathbf{s}}_j \mathbf{K}_T \tilde{\mathbf{s}}_i - \mathbf{K}_R & \tilde{\mathbf{s}}_j \mathbf{K}_T & -\tilde{\mathbf{s}}_j \mathbf{K}_T \tilde{\mathbf{s}}_j + \mathbf{K}_R \end{bmatrix} \quad (4.14b)$$

The derivation process will not be written down in this research, but details could be found in Refs. [91, 92]. In (4.14), \mathbf{K}_e is the stiffness matrix of the bush element connecting the rigid body i and the rigid body j , and total stiffness matrix of the system in (4.13) can be obtained by assembling the stiffness matrix of each bush. In (4.14a), \mathbf{F}_i and \mathbf{T}_i are internal force and moment of the body i , which is corresponding to the work conjugate of the $\Delta \mathbf{r}_i$ and $\Delta \boldsymbol{\pi}_i$. In (4.14b), $\tilde{\mathbf{s}}_i$ is used to denote skew symmetric matrix of \mathbf{s}_i , which is the position vector of the bush with respect to the body coordinate of the rigid body i . The relation between $\tilde{\mathbf{s}}_i$ and \mathbf{s}_i is written down in Eq. (4.15). Finally, \mathbf{K}_T and \mathbf{K}_R denote translational and rotational stiffness matrix of the bush element, which are defined in (4.16).

$$\mathbf{s}_i = \{\mathbf{s}_{i,X} \quad \mathbf{s}_{i,Y} \quad \mathbf{s}_{i,Z}\}^T \quad (4.15a)$$

$$\tilde{\mathbf{s}}_i = \begin{bmatrix} 0 & -\mathbf{s}_{i,Z} & \mathbf{s}_{i,Y} \\ \mathbf{s}_{i,Z} & 0 & -\mathbf{s}_{i,X} \\ -\mathbf{s}_{i,Y} & \mathbf{s}_{i,X} & 0 \end{bmatrix} \quad (4.15b)$$

In (4.15), $\mathbf{s}_{i,X}$, $\mathbf{s}_{i,Y}$, and $\mathbf{s}_{i,Z}$ are X, Y, and Z components of the vector \mathbf{s}_i .

$$\mathbf{K}_T = \mathbf{T}^T \begin{bmatrix} k_{\text{radial}} & 0 & 0 \\ 0 & k_{\text{radial}} & 0 \\ 0 & 0 & k_{\text{axial}} \end{bmatrix} \mathbf{T} \quad (4.16a)$$

$$\mathbf{K}_R = \mathbf{T}^T \begin{bmatrix} k_{\text{conical}} & 0 & 0 \\ 0 & k_{\text{conical}} & 0 \\ 0 & 0 & k_{\text{rotation}} \end{bmatrix} \mathbf{T} \quad (4.16b)$$

In Eq. (4.16a), k_{radial} and k_{axial} denotes radial and axial stiffness of the bush, respectively. In (4.16b), k_{conical} and k_{rotation} are conical and rotation stiffness of the bush. In both equations, \mathbf{T} corresponds to the transformation matrix which have the information of the bush direction in global coordinates. In this research, (4.16a) and (4.16b) assumed an axis-symmetric bush which have the same stiffness in radial direction.

After deriving the stiffness matrix, it needs to derive derivative of the constraints for several joint types. Eq. (4.17) are the derivatives of the constraints corresponding to SS-joint (4.17a), In-plane joint (4.17b), and Spherical joint (4.17c).

$$\Phi_q^{\text{SS}} = \{2\mathbf{d}^T, -2\mathbf{d}^T \tilde{\mathbf{s}}_i, -2\mathbf{d}^T, 2\mathbf{d}^T \tilde{\mathbf{s}}_j\}^T \quad (4.17a)$$

$$\Phi_q^{\text{IP}} = \left\{ \mathbf{h}_j^T, -\mathbf{h}_j^T \tilde{\mathbf{s}}_i, -\mathbf{h}_j^T, \mathbf{h}_j^T \tilde{\mathbf{s}}_j + \mathbf{d}^T \mathbf{h}_j \right\}^T \quad (4.17b)$$

$$\Phi_q^{\text{S}} = \left\{ \mathbf{I}_3, -\tilde{\mathbf{s}}_i, -\mathbf{I}_3, \tilde{\mathbf{s}}_j \right\}^T \quad (4.17c)$$

In (4.17), $\tilde{\mathbf{s}}_i$ denotes skew symmetric matrix of \mathbf{s}_i , where \mathbf{s}_i corresponds to the position vector of the joint observed on the body-coordinate of the rigid-body i . In (4.17b), \mathbf{h}_j represents the normal vector of the In-plane joint which is observed on the body-coordinate of the rigid-body j , and \mathbf{I}_3 means the 3 by 3 identity matrix. Finally, \mathbf{d} is defined as (4.18a), which is the distance vector between two vectors represented in (4.18b-c).

$$\mathbf{d} = \mathbf{r}_j - \mathbf{r}_i \quad (4.18a)$$

$$\mathbf{r}_i = \Delta \mathbf{r}_i - \tilde{\mathbf{s}}_i (\Delta \boldsymbol{\pi}_i) \quad (4.18b)$$

$$\mathbf{r}_j = \Delta \mathbf{r}_j - \tilde{\mathbf{s}}_j (\Delta \boldsymbol{\pi}_j) \quad (4.18c)$$

Now, Eq. (4.13) can be applied to an arbitrary suspension system by employing Eq. (4.14)-(4.18). Figure 4.8(a) is a hidden link suspension including RSR-limb (hidden link), and Figure 4.8(b) corresponds to the multi-link type suspension which replaces the RSR-limb to a link (other suspension components are remained the same as those of the hidden link suspension in Figure 4.8(a)). Here, the replaced link in Figure 4.8(b) is located in the direction of the hidden link, which can be calculated from the hidden link suspension in Figure 4.8(a) according to the suggested force transmission analysis in previous chapters. Knuckle attached point of the link is also determined by the suggested analysis, which is the position of the ball joint which is

located between two arms of the RSR-limb. However, one cannot define the length of the hidden link by the suggested hidden link calculation method. Therefore, the other end point of the replaced link, which is a hard point attached to the chassis frame, is selected arbitrary on the hidden link. Here, an end-point and direction of the hidden link is already designated by the afore-mentioned idea, so that the arbitrary does not means entirely arbitrary one. To this end, the hard point is located on the line, which is starting from the known end-point of the hidden link (the ball joint location between two arms of the RSR-limb) and having direction in the calculated hidden link direction (intersection line of the both arms in the RSR-limb). That is, only the length of the link is remained arbitrary.

To verify the effectiveness of the RSR-limb in compliance analysis, it needs to set the numerical experiment not to be affected by the length of the replaced link (arbitrary selected in Figure 4.8(b)). To make proper condition in the verification, no bush is applied to the RSR-limb joints, though the other chassis-frame joints are composed of the bushes rather than rigid-joints. By applying the ball joints to the RSR-limb component, the location of the arbitrary selected hard point does not affect the elastic behavior in this experiment, so that constraint effect (direction on the constraint force and action point of that in knuckle) of the RSR-limb can be observed solely in the compliance analysis.

To see the elastic behavior of the two suspension systems shown in Figure 4.8, four LC's (Loading Cases) are imposed to the wheel. Each LC corresponds to lateral force, impact force, brake force, and aligning moment, respectively. The wheel

translation and rotation DOF's of the two suspensions in each LC are compared, and they are plotted in Figure 4.9. Blue bars in the figure stands for the magnitude of the each factor in hidden link suspension shown in Figure 4.8(a), and red bars for the multilink suspension shown in Figure 4.8(b) which replaces the RSR-limb to link component. The super-scripts "Im", "Lt", "Br", and "Am" represent impact force LC, lateral force LC, brake force LC, and aligning moment LC, respectively. The lower-scripts "WC" and "CP" means the observed locations, which are wheel center and contact patch center.

The hidden link suspension and the multi-link suspension in Figure 4.8 have the exactly same response to each LC. From this experiment one can verify that constraints included in the Jacobian of the governing equations are the same in both suspensions, so that a proposition dealt with in Chapter 4.3 is valid for the arbitrary hidden link suspensions including the RSR-limb.

To summarize what was suggested in Chapter 4.3, a new concept suspension obtained from the topology optimization is analyzed through the force transmission analysis. Here, the force transmission analysis presumes that two components which gives the constraint forces having the same direction and action point to the knuckle can be considered as the equivalent component in instantaneous case. To apply this concept, the RSR-limb included in the new concept suspension is analyzed by the screw-axis theory, and the wrench screw of the RSR-limb is confirmed to be the same as that of the link component. Therefore, one can expect that a new concept solution is obtained to replace the conventional link component into the RSR-limb

during the topology optimization, where desired kinematic requirements are provided in smaller design domain. To verify it in the system level, the compliance analysis is applied to the new-concept system. As a result, it is verified that the Jacobian matrix imposed on the knuckle, which governs the dynamic behavior of the multi-body system and elasto-kinematic behavior of the link-bush system, is the same for both systems employing the RSR-limb (hidden link) and the real link (adopted to replace the RSR-limb).

The analysis in Chapter 4.3 is implemented to the suspension systems in very small movements, and it means that the suggested hidden link concept is only valid in instantaneous cases. That is, the RSR-limb is instantaneously equivalent to the real link component in suspensions. Then, what about in general large motion cases? To see the effect of the RSR-limb in the general case, it needs to consider nonlinear kinematic analysis which implies the nonlinear effects. It will be dealt with in Chapter 4.4.

4.4 Nonlinear effects of the hidden link suspension

In Chapter 4.3, the hidden link concept is derived from the new-concept suspension including the RSR-limb through the constraint force transmission analysis, and the hidden link concept is verified in the system level through the linear compliance analysis. To this end, the instantaneous constraint force direction and action point corresponding to the end-point of the hidden link is obtained from the analytical method. But, the other end-point of the hidden link, i.e. hard point of the effective link, cannot be defined by the instantaneously equivalent systems analysis, so that position of the hard point attached to the chassis frame is remained in arbitrary on the line which includes the hidden link. Then, what is the kinematic factor affected by the hard point location? And how can we determine position of the hard point in the design procedure? To see that, it needs to consider large kinematic motions.

In general suspensions, the length of the link affects the motion of the knuckle in nonlinear kinematics. For example, with several assumptions, one can simply consider the effect of the upper and lower arm lengths on the behavior of the double wishbone suspension. The front view plane behavior of the knuckle, i.e. camber and lateral movements of wheel center and contact patch, is highly affected by the geometry of two arms. To this end, the knuckle motion with respect to the wheel center vertical stroke can be assumed to the 2nd order curve, where the coefficient of the first order term is determined by placement angle of the both arms [82]. Meanwhile, the coefficients of the second order terms are governed by the lengths

of the upper and lower arms [82]. Consider the bump scrub curve in the vertical stroke motion. When the shortness of each arm is defined as the reciprocal of the length of each arm, the larger summation value of the shortness of the both arms generates the larger bump scrub curvature [82], herein the curvature corresponds to the 2nd order coefficient of the curve. Otherwise, when the difference of the shortness of the both arms becomes larger, the curvature will be smaller [82]. As mentioned earlier, the slope of the curve relevant to the 1st order of the curve is only determined by the height of the knuckle joint and placement angle of the both arms with respect to horizontal ground plane [82]. Accordingly, to designate the location of the hard point in Figure 4.8(b), it needs to consider nonlinear motion corresponding to the 2nd order in the motion curves rather than the 1st order linear behaviors of them.

In this chapter, the large and nonlinear motion of the hidden link motion, shown in Figure 4.8(a), will be analyzed. Then, corresponding multi-link suspensions obtained by replacing the RSR-limb (i.e. the hidden link) into the real link component, as shown in Figure 4.8(b), will be analyzed in the same nonlinear kinematic aspects. In doing so, the length of the link (ℓ_{link}) adopted to replace the hidden link module in the multi-link suspension will be varied in the designated variation range, and the nonlinear kinematic analysis will be repeatedly implemented for each multi-link suspension. Next, the result of the kinematic motions will be compared with the original hidden link suspension. From this parameter study, it is possible to visualize the error values according to the arbitrary selection of the hard point (corresponding to the length variation of the link ℓ_{link}), and from that an

effective length of the hidden link which minimizes the error value between two suspensions, i.e. two systems in Figure 4.8(a) and Figure 4.8(b), can be found.

In chapter 4.4, after implementing the above parameter study, the result will be analyzed to suggest an effective length prediction method, By which it is also possible to design the hidden link suspension from the a given multi-link suspension when a link of that is difficult to install in the provided design domain. The detailed design case study will be introduced at the end of this chapter.

4.4.1 Effective length of the hidden link in nonlinear motion

The hidden link suspension of Figure 4.8(a) is instantaneously equivalent to the multi-link suspension of Figure 4.8(b) as shown in Chapter 4.3, however they have difference in large kinematic motions. In particular, the undetermined length of the link in the multi-link suspension is the key factor which affects the behavior of the multi-link suspension. In Figure 4.10, four suspension mechanisms are shown for comparing the behavior of two-types of suspensions. In Figure 4.10(a), the hidden link suspension with the same geometry of that in Figure 4.8(a) is analyzed for the vertical kinematic stroke motion. In Figure 4.10(b)-(d), multi-link suspensions having different link lengths (ℓ_{link}) is analyzed to the same kinematic motions. The length of the link is 200 mm, 400 mm, and 600 mm, respectively.

In Figure 4.10, the left side of each figure corresponds to the initial configurations of each suspension. The right side figure shows the variation of the constraint forces,

imposed on the knuckle through the hidden or corresponding real link components, in vertical stroke motion analysis. That is, in Figure 4.10(a), the constraint force vectors are drawn for showing the variation of the hidden link constraint force in the large kinematic motions. To the kinematics analysis, wheel center is in vertical motion from 100 mm rebound to 100 mm bound, and the constraint forces are plotted for 50 mm interval. For the analysis, Euler parameter method for the three-dimensional angular motion description is applied. Please see [63] for details of the three-dimensional nonlinear kinematic analysis.

In the force plot in Figure 4.10(a), the vectors look like to be focused on a point, but they are not exactly passing through a point. Otherwise, in Figure. 4.10(b)-(d), the constraint force vectors of each multi-link suspension pass through the exactly same point corresponding to the pivot (M) of the link.

From the above-mentioned figures, one can find that the constraint force of the hidden link has similar tendency compared with that of the real link. Therefore, if adequate link length is selected for the multi-link suspension, it will be possible to describe the similar behavior with the hidden link by the multi-link suspension. The length of the link ℓ_{link} which makes the minimum error between the hidden link suspension and the multi-link suspension is defined as the “effective length” of the hidden link in this research.

To calculate the effective length of the hidden link, a numerical test will be implemented. First, calculate the hidden link direction and action point on the knuckle by the proposed method. One can find the suspension in multi-link type by

this method like as Figure 4.8(b) from the hidden link suspension in Figure 4.8(a). Next, the length of the link (ℓ_{link}) applied instead of the hidden link module will be varied from 200 mm to 800 mm in this experiment for 10 mm variation interval. That is, 61 multi-link type suspensions are constructed according to the variation of the link lengths, and each suspension is analyzed by the nonlinear kinematic analysis.

Among the 61 experimental targets, behavior of the several suspensions are plotted in Figure 4.11, where four systems are selected as the sample points (having the link length of 200 mm, 400 mm, 600 mm, and 800 mm). One can see in qualitatively that motion curves varies according to the length of the link, and the suspension having the 400 mm length link looks like the equivalent system for the target suspension. To see the result in details, Figure 4.12 is plotted.

In Figure 4.12, the X-axis of the figure represents the variation of the link length, from the 200 mm to 800 mm. The Y-axis of the figure corresponding to the RMS error values are defined as (4.19).

$$E_X = \left[\frac{1}{N_{\text{step}}} \sum_{Z=Z_{\min}}^{Z=Z_{\max}} \left\{ \frac{q_X(Z; \ell_{\text{link}}) - \hat{q}_X(Z)}{\hat{q}_{X, \max}} \right\}^2 \right]^{1/2} \quad (4.19a)$$

$$E_Y = \left[\frac{1}{N_{\text{step}}} \sum_{Z=Z_{\min}}^{Z=Z_{\max}} \left\{ \frac{q_Y(Z; \ell_{\text{link}}) - \hat{q}_Y(Z)}{\hat{q}_{Y, \max}} \right\}^2 \right]^{1/2} \quad (4.19b)$$

$$E_\gamma = \left[\frac{1}{N_{\text{step}}} \sum_{Z=Z_{\min}}^{Z=Z_{\max}} \left\{ \frac{\gamma(Z; \ell_{\text{link}}) - \hat{\gamma}(Z)}{\hat{\gamma}_{\max}} \right\}^2 \right]^{1/2} \quad (4.19c)$$

$$E_{\phi} = \left[\frac{1}{N_{\text{step}}} \sum_{Z=Z_{\min}}^{Z=Z_{\max}} \left\{ \frac{\phi(Z; \ell_{\text{link}}) - \hat{\phi}(Z)}{\hat{\phi}_{\max}} \right\}^2 \right]^{1/2} \quad (4.19d)$$

$$E_{\delta} = \left[\frac{1}{N_{\text{step}}} \sum_{Z=Z_{\min}}^{Z=Z_{\max}} \left\{ \frac{\delta(Z; \ell_{\text{link}}) - \hat{\delta}(Z)}{\hat{\delta}_{\max}} \right\}^2 \right]^{1/2} \quad (4.19e)$$

In (4.19), E_X , E_Y , E_{γ} , E_{ϕ} , and E_{δ} represent RMS error values of the wheel center X-displacement, wheel center Y-displacement, camber angle, spin angle, and toe angle, respectively. In (4.19a-b), q_X and q_Y corresponds to the displacement of the wheel center in X and Y-direction, respectively. In (4.19c-e), camber angle is denoted as γ , spin and toe angles are ϕ and δ . For these five motion DOF's, hat represents that of original hidden link suspension, shown in Figure 4.8(a), which corresponds to the reference. For example, $\gamma(Z; \ell_{\text{link}})$ is the camber angle of the multi-link suspension in Figure 4.8(b) with a real link length of ℓ_{link} at stroke position Z . And $\hat{\gamma}(Z)$ corresponds to the camber angle of the hidden link suspension in Figure 4.8(a).

In (4.19), N_{step} is used commonly as the number of analysis steps in vertical stroke motion, herein Z_{\min} and Z_{\max} are the minimum and the maximum stroke position of the wheel center in Z-direction. The vertical stroke positions in the kinematic analysis are equally divided between in Z_{\min} and Z_{\max} .

One can see the similar result in Figure 4.12 compared with that of Figure 4.11. A multi-link type suspension having a replaced link length of about 400 mm has the

minimum error value in each DOF. The total sum of error value, a black line with circle marker corresponding to the summation of these error values in (4.19), has the minimum on 390 mm in the figure. From this experiment, a suspension shown in Figure 4.8(a) could be considered to have a hidden link, which has the effective length of about 390 mm.

Strictly speaking, the length of the hidden link cannot be defined theoretically. Only there is an effective length which generates the minimum error value, such as the concept suggested in Figure 4.11-4.12. Since the RSR-limb is not a real link component, it is natural that it cannot have the exactly same motion in large nonlinear kinematic analysis. That is, the hidden link concept is perfectly satisfied only in the instantaneous case with small linear motion, not in the whole nonlinear motion cases. Then, what is the main nonlinear effect which generates the difference between the hidden link and real link? And is it possible to predict effective length of the hidden link which generates the minimum error values? Here, the nonlinear effect will be investigated, and then a method for predicting the effective length will be suggested. From this proposition a design guideline will also be provided for the hidden link suspension.

It needs to see two main factors inducing the differences between the hidden link and real link in nonlinear large motions. First, during the stroke motion, direction of the intersection line of the two arms composing the RSR-limb will be changed. Accordingly, the direction of the hidden link will also be changed. The change of the link direction also appears in multi-link suspension when the knuckle (wheel center)

moves in vertical direction, and it is strongly depends on the length of the link as shown in Figure. 4.10(b)-(d).

Second, in real link component, the distance between the wheel center and knuckle joint of the link will not be changed, even though the knuckle moves in the vertical direction. The knuckle joint position is a perfectly fixed to the knuckle. However, in hidden link module, the (effective) end point of the hidden link will move with respect to the knuckle center position during the suspension vertical motion, because the virtual knuckle joint position corresponding to the ball joint of the RSR-limb is connected to the knuckle through a rotatable arm. The relative position vector between the knuckle and the ball joint could be changed, and it is one of the factors generating the difference between the hidden link and the multi-link suspensions. We call it an action point change, which only occurs in the hidden link suspension, not in the multi-link suspension.

From the above mentioned discussion on the nonlinearity factors, one can know about the reason of the difference between two suspensions. In the next chapter, a method for predicting the effective length without numerical parameter study will be proposed.

4.4.2 Prediction of the effective length of the hidden link

In Figure 4.10, it is shown that end-point trajectory of the link and direction change of the link are strongly determined by the length of the link. Accordingly, to predict the effective length of the hidden link, it is important to find the length of the link of

which end-point trajectory follows the trajectory of the hidden link. If it is found, the difference between the hidden link and the real link due to the first nonlinear factor, corresponding to the link direction change, will be reduced.

Then, what about the second nonlinear factor? Let us consider details of the second nonlinear effect, corresponding to the action point change occurring only in the hidden link suspension. Interestingly, the hidden link shows similar tendency compared with the real link as shown in Figure 4.10. To this end, it is possible to think that nonlinear motion is accumulation of the piece-wise linear motions, corresponding to the instantaneous small motion in kinematics. And it is expected to be a reason why the hidden link suspension shows very similar wrench movement compared with the multi-link suspension, even though the equivalent relation is exactly satisfied only in the very small linear motions. Accordingly, we can expect that the action point change of the hidden link will be very small as the action point change does not happen in the real link. Indeed, rotation angle of the knuckle attached arm is much smaller compared with that of the frame-attached arm in case studies, so that the second nonlinear effect is not so much dominant.

Therefore, we only focused on the end-point trajectory of the hidden link suspension to predict the effective length.

The trajectory of the ball joint of the hidden link module (RSR-limb) is described in Figure 4.13(a), where the joint rotates around the chassis frame attached arm, so that it is belong to the circular path as shown in Figure 4.13(b). Radius of the circular path R_{proj} is the distance between ball joint and a point corresponding to the “foot

of the perpendicular” of the ball joint with respect to rotational axis. From the circle with the radius R_{proj} and the rotation axis of the frame-attached arm, it is possible to draw a cone shown in Figure 4.13(c). Let us consider the effective length of the hidden link equal to L_{cone} , which is the generation line length of the cone. In this case, the position of the cone vertex will be the virtual mount position of the hidden link. As shown in Figure 4.13(c), the ROM (Range of the Movement) of the link includes the circular trajectory of the hidden knuckle joint with radius of R_{proj} , so that link-end point will have the similar curvature with that of the hidden link end point. Precisely, the link end point trajectory is not exactly equal to that of the hidden link end point, because the ROM of the link is the sphere, not the circle. But the projected curvature of the real link end-point path will be very similar with the curvature of the hidden link end-point trajectory.

Even though the selection of the cone vertex as the virtual mount position of hidden link is not perfect for predicting the effective length of the hidden link ℓ_{link} , this suggested prediction method shows quite good results in the previous parameter study. For example, the effective length of the suspension in Figure 4.8(a) found by the numerical experiment in Figure. 4.12 is 387 mm. Meanwhile, the result predicted by the suggested method is 431 mm. Two results shows difference due to the a little bit trajectory difference and the other nonlinearity (small change of the action point), but this method can be employed for the prediction of the effective length before the numerical studies. Also, it can be exploited for design when selecting the initial

design configuration before the detailed design. The usage in design procedure will be dealt with in Chapter 4.4.3. Before dealing with the design problem, one more parameter study will be considered for the verification of the effective length prediction method.

Figure 4.14(a) shows a hidden link suspension, and Figure 4.14(b) corresponds to the multi-link suspension which employs the real link instead of the hidden link module, where the suggested effective length calculation method is used to find the mount position of the converted link. In the same manner, hidden link suspension in Figure 4.14(c) could be replaced by the multi-link suspension in Figure 4.14(d). The difference between two suspensions in Figure 4.14(a) and (c) is the hard point locations of the hidden link module; locations of the two chassis frame connected points are different. The position of these two hard points will be the control variable in the parameter study, and they will be changed up to 300 mm in $-Y$ direction. The suspension in Figure 4.14(a) is the initial configuration, and the one shown in Figure 4.14(c) corresponds to a configuration of which hard points are changed 100 mm in $-Y$ direction.

In the second parameter study, the error value calculation for finding the effective length is implemented for each configuration. That is, the parameterized hard points are changed 1 mm in $-Y$ direction until it moves 300 mm from the initial configuration, and the numerical experiment which is the same as that of Figure 4.12 with variation of the length of link ℓ_{link} is implemented for each configuration. As a result, one can obtain error value curves shown in Figure 4.12 for each

configuration, and these curves can be plotted at once in 3-dimension like as Figure 4.15(a). Two axes applied to the Figure 4.15(a) is equal to that of the Figure 4.11, but the other axis employed in the Figure 4.15(b) is a new one corresponding to the predicted effective length of the hidden link calculated by the proposed cone-shape based method. For each data point, i.e. suspension configuration with parameterized hard point locations, the afore-mentioned cone can be drawn as Figure 4.13(c) to calculate the length of the generating line L_{cone} , which corresponds to the new axis value applied to the Figure 4.15.

Figure 4.15(b) is the planar view of the Figure 4.15(a), where the black line is data sets connecting the points having the minimum error, corresponding to the minimum error point in Figure 4.12, for each parameterized configuration. The ideal line is the set of the data points which are corresponding to $L_{\text{cone}} = \ell_{\text{link}}$. If the prediction is correct, the minimum error value will be located on this ideal line. Therefore, by investigating whether the minimum error plot line is close to the ideal line or not, one can confirm how much the suggested effective calculation method is correct. In Figure 4.15(b), the two lines are very close, particularly the minimum error set line is almost linear, so that the suggested prediction method could be considered to be effective.

4.4.3 Design guide line of the hidden link suspension

For an arbitrary multi-link type suspension, the hidden link suspension can be applied by deleting one of the links and inserting the RSR-limb, i.e. the hidden link module, to that position. However, to determine the position of the hard points, engineers need a guideline. To construct the design guideline, the suggested methods to analyze the effects of the hidden link module can be applied reversely. First, a link direction and action point calculation methods can be easily exploited to replace the link component, even though this concept is only valid for the instantaneous case. Then, the effective length prediction method can also be used for correcting the nonlinear and large motion behaviors. By using these methods inversely, an initial configuration for design can be selected. It means that engineers can apply the conventional chassis geometry optimization to the hidden link suspension to the initial configuration obtained by the design guideline. In this chapter, a following design case study will be introduced for this purpose.

A layout problem is one of the issues in suspension design. Because the layout problems deteriorate other performance factors, designers have been struggling to resolve it. Among them, keeping the link mount position from the other components is the very difficult, especially when the essential components such as powertrain require the same space for installation. Also, the suspension mount space is commonly yielded to enlarge the trunk or interior spaces when the car productivity is required to be enhanced. Figure 4.16 shows the case, where layout problem occurs due to the spacious car issue or other components. To this end, assume that previous

design is the multi-link type suspension corresponding to the Figure 4.16(a), but the red dotted box is not allowed to mount any suspension hard point. In regard to this matter, the hidden link suspension concept can be exploited like as Figure 4.16(b), and detailed procedure for design will be explained in this chapter step by step.

First, check the link component which induces the layout problem. In this design example, the rear lower link in Figure 4.16(a) is the component corresponding to the packaging issue. Then, the knuckle joint of the link position will be selected to the ball joint of the RSR-limb, because the virtual knuckle joint of the hidden link will be located on there.

Next, two arm planes should be selected to control the hidden link direction in the desired link direction, which is the rear lower link direction shown in Figure 4.16(a) in this example. However, when selecting the arm planes engineers have the redundant design DOF's, so that infinite set of arms can be chosen to realize the desired link direction. This design step has a lot of design potential depending on the engineers. As an example, several chassis design issues will be introduced here.

- Interference between the knuckle attached arm and the inside of the rim (wheel) should be prevented.
- The knuckle joints are recommended to be located as near as the wheel center. If not, the knuckle can be heavier (or the stiffness of the knuckle might be degraded), so that handling performance can be worse.

- Mount locations should be chosen with consideration of the frame structure, since the local stiffness of the frame highly affects the R&H (ride and handling) and NVH performances.
- It needs to consider other issues relevant to driving performance, maintenance, cost, weight distribution (e.g. height of CG), etc.

Figure 4.16(b) is one of the examples, which shows the selected locations of the arms to generate the desired hidden link effects. Here, after constructing two arm planes, the frame attached points are selected for the hidden link to have the target effective length based on the suggested prediction method. To this end, the line passing through the both mount points of the hidden link module is set to pass through the mount point of the target link, where it is located inside the red dotted box as shown in Figure 4.16(a).

Finally, chassis geometry optimization is implemented to slightly adjust all joint locations. From this optimization, it is possible to achieve the kinematic motions, which follows that of the original multi-link suspension. Figure 4.17 shows the kinematic curves before and after the chassis geometry optimization. Fore-and-aft directional movement of the wheel center (X-dir.) and spin motion of the wheel is quite different before the shape optimization, but they both have the similar motion after the optimization. Here, the joint positions are allowed to move ± 10 mm for all directions, and the proper optimization result is obtained under this side constraint. In optimization, a basic algorithm in MATLAB is applied.

From the above design case study, it was confirmed that the hidden link suspension can be applied to resolve the layout issue. Especially, when the battery pack or enlarged powertrain space is required for the next generation vehicles, e.g. hybrid vehicles, the suggested method can be used to solve the problem. Meanwhile, it is also expected that the hidden link is effective in enhancing the driving performances. In Formula 1, it is general to employ the half-track length arms for extremely enhanced handling quality. But it is impossible to realize that suspension in typical mass production cars, because of their lack of productivity related to interior space. In this regard, if the hidden link concept is employed, it will be able to give the similar effect of the half-track arms to the suspension in the mass production cars. Additionally, the hidden link suspension can be devised to give high ride quality. In conventional suspensions, a trailing link is occasionally employed to react to the impact forces, where the role of the trailing link is solely decoupled with other physics such as lateral force supporting. However, the mount position of this link is not attached to the sub-frame, but to the car body because of the mounting location problems. So, the noise and vibration are transferred to the passenger directly without being absorbed by the sub-frame mount bushes. If the hidden link is used to replace this trailing, this problem can be removed by attaching the mounts of the hidden link to the sub-frame rather than the car-body. Except the mentioned advantages, the hidden link can be employed in other ways according to the needs in engineering.

Finally, note that there are two important cautions who wants to use the hidden link suspension should consider. The one is the singularity issue, and the other is the articulation angle limit of the bushes.

First, when the arms composing the hidden link module are located on the same plane, the singularity problem will occur. As mentioned earlier, the two arms can deliver forces belong to each arm-plane, and the intersection of these planes correspond to the link direction, which is the direction of the hidden link. If these two arm-planes become the same plane, the set of intersection becomes not a unique line corresponding to the transmittable force, but it will be infinite set of the lines located on the common plane. Accordingly, the constraint imposed by the hidden link module will not be a 1-DOF restriction, but 2-DOF's like as an arm. It means that hidden link suspension system cannot be a definite system having 1-DOF constraint, and the singularity phenomenon of the linkage mechanisms [63] will occur. To prevent this problem, designer should elaborately consider the chassis geometry as follows.

- It is necessary to prevent the two planes from being completely flattened into one plane.
- It is necessary to prevent the two planes from folding into one plane.

Second, when applying the bushes to the mount of the hidden link, i.e. the chassis-connected arm mounts in RSR-limb, the rotation angle limit of the bushes should be checked. If the rigid-joint such as the ball joints or the revolute joint is applied to that position, it does not need to worry about that. In general, however, when the

rubber bushes are employed for insulating the noise/vibration or controlling the compliance steers, move-limits of the rubber bushes in bending and torsion should be considered in chassis geometry design stage. One of the remedies for this problem is employing the quite long arm in RSR-limb, but it can induce another layout issues. If it is impossible to satisfy the bush requirements, special bushes (e.g. sliding bush [80]) could be a solution for this problem.

To sum up, the proposed method to analyze the effectiveness of the hidden link can be applied to the inverse problem, i.e. the design problem. And the proper initial configuration can be selected according to this method as shown in Figure 4.17. If the chassis geometry optimization is implemented, the result can be further improved. Meanwhile, in consideration of the initial design configuration, the RSR-limb has more design freedoms compared with that of the target component, a link, so that engineers are able to select arbitrary set of the RSR-limb joint locations which have the similar effect. But there are another issues related to the chassis design, for example, interference or stiffness of the frame structure is one of the issues, which needs to be considered. With careful concerns, the hidden link suspension can be applied to the mass production cars, especially for the next generation vehicles with other powertrains or the high-performance vehicles.

4.5 Summary

It is confirmed that the new concept suspension can be derived by using the topology optimization technique that assists intuition of the users. In particular, the new concept suspension includes components that are not directly connected to the car body (or sub-frame). This in-directly connected components are the auxiliary links, which are common in the new concept suspensions, e.g. RevoKnuckle [85] and Integral link [83]. To this end, for the practical problem, it is the first research in which a concept difficult to be imagined by the engineers' intuition is systematically found through the mechanism topology optimization.

In this study, the newly derived module equivalent to the RSR-limb module in parallel manipulators is investigated in depth. In order to analyze its role and effect compared with the conventional suspension components, the force transmission analysis is developed based on the screw axis theory. As a result, it is confirmed that when the RSR-limb is used the knuckle is given the same constraint force as the conventional link is employed instead of that. According to this aspect, the newly derived module is named as the hidden link, then the concept of the hidden link is proved through elastic-kinematic coupled analysis in link-bush system.

The proposed concept of hidden link is theoretically valid only for a moment. That is, the knuckle is given the same constraint as a link through the hidden link in a specific direction at a specific instant. On the other hand, in large motion, the behavior of the link and its motion cannot be the same. Nevertheless, the length of the hidden link that behaves most like the RSR-limb can be defined and found by a

numerical test, in which the link length generating the minimum error is defined as the effective length. Besides the numerical test, a method to estimate the effective length is proposed and verified, where a cone is employed to predict the effective length.

By applying the force transmission analysis and the effective length prediction method in reverse, it is possible to select the initial position of the RSR-limb geometry in design case study to replace the link of the given multilink suspension. In this research, the initial geometry of the proposed new suspension was selected according to this method, and the chassis geometry optimization was performed after the selection of the initial design configuration. As a result, it is confirmed that the new concept suspension including the RSR-limb can replace the conventional multi-link suspension in a limited space. The proposed new concept suspension is likely to be used in the next-generation vehicles and high-performance vehicles.

The derived suspension shows the potential of the topology optimization methodology. Since the topology optimization method that assists the mechanism designer's intuition is successfully introduced, it will be possible to derive a new suspension with a high complexity which is completely different from the conventional one. In the future, it is also expected that the topology optimization methodology can be applied to new applications which have no accumulated experience, such as exo-skeletons.

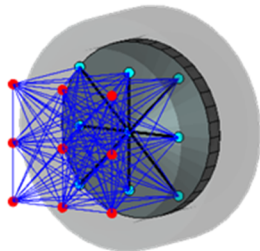
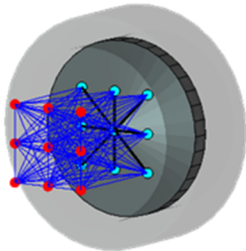
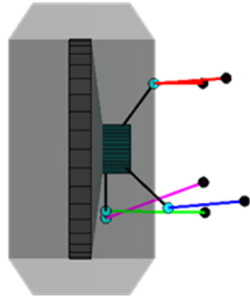
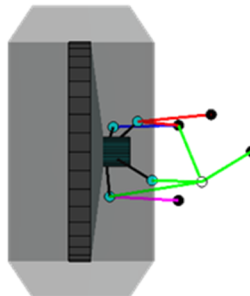
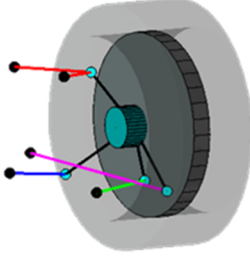
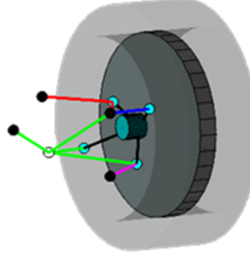
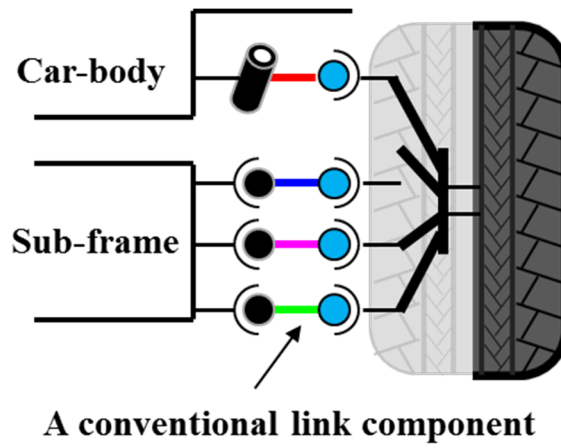
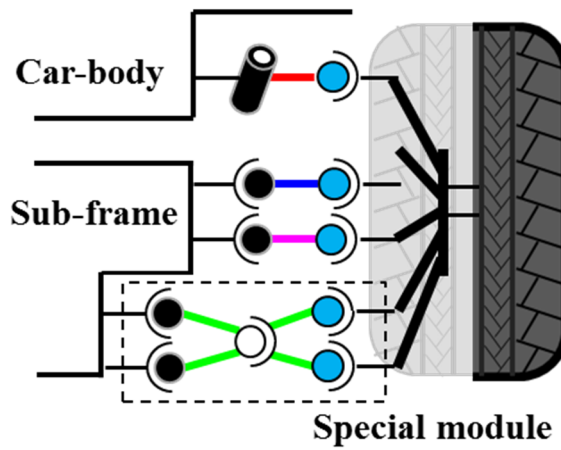
	Design Case L	Design Case S
Design domain		
Result (view 1)		
Result (view 2)		

Figure 4.1 Topology optimization result for Design Case L and Design Case S.



(a)



(b)

Figure 4.2 Schematic illustration of the topology optimization results (a) Result obtained from the Design Case L and (b) Result obtained from the Design Case S.



Figure 4.3 Two grouping strategies for investigating role of the new component. (a) Two groups composed of three links and remained one, respectively. (b) Two groups composed of two links, respectively. Each group can be considered as an arm component with revolute and ball joint.

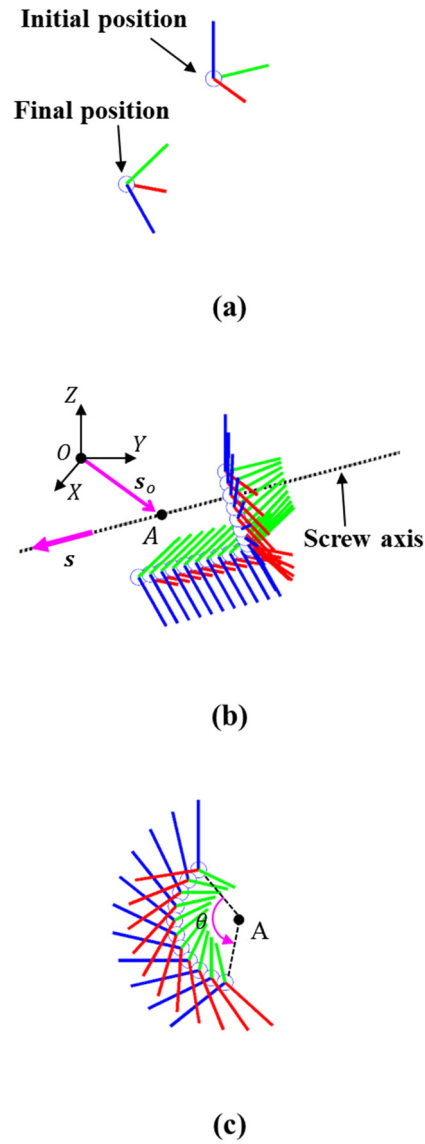
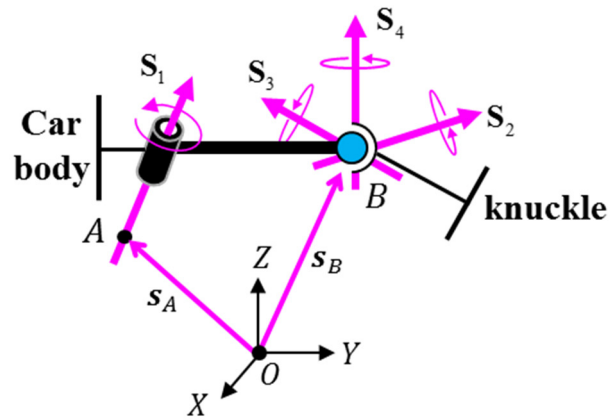
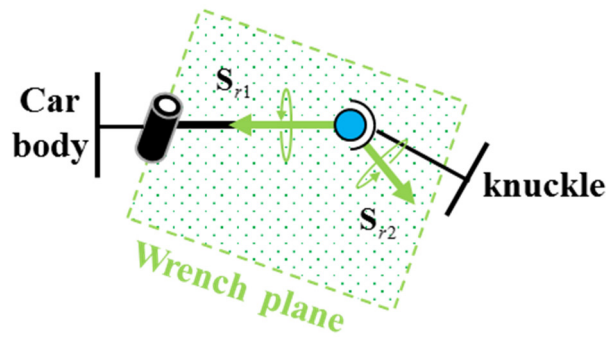


Figure 4.4 An example motion for explaining the screw axis theory. (a) Two configurations before and after movement. (b) Decoupled motions corresponding to translation and rotation about an axis. (c) Another motion view in perpendicular to the rotational axis.

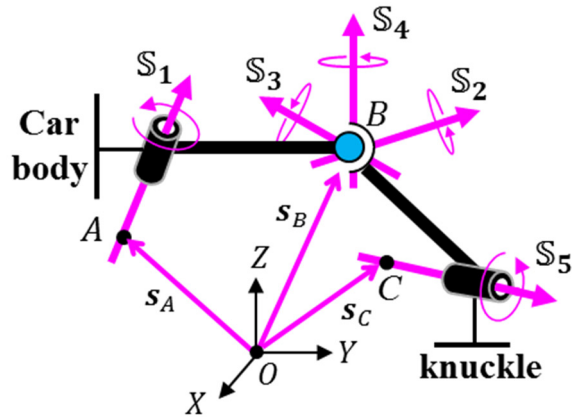


(a)

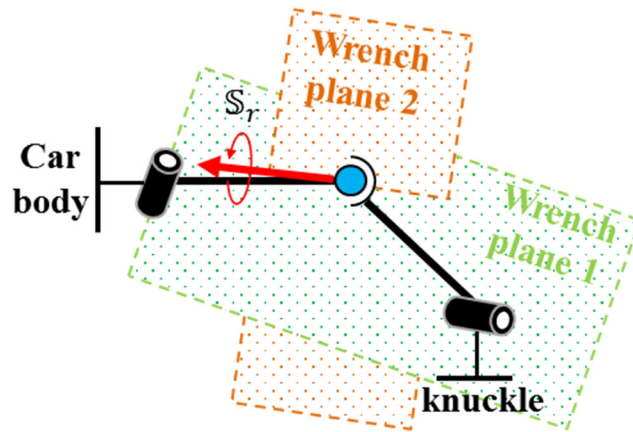


(b)

Figure 4.5 Twist and wrench screw description for RS (arm) component. (a) Twist screws of each joint and (b) Wrench screws corresponding to reciprocal screws of the twist screws.

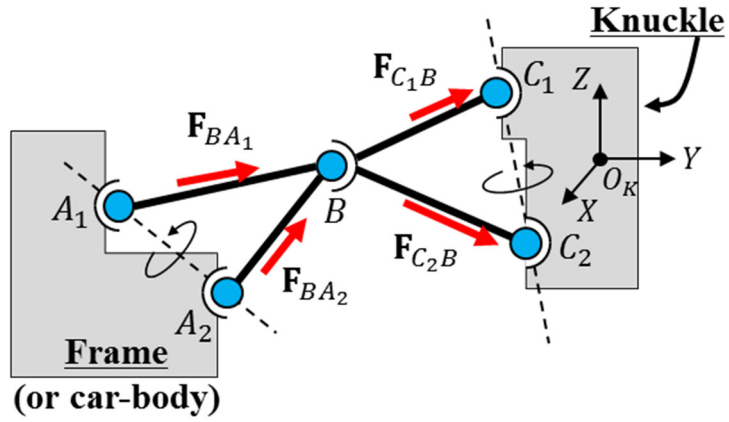


(a)

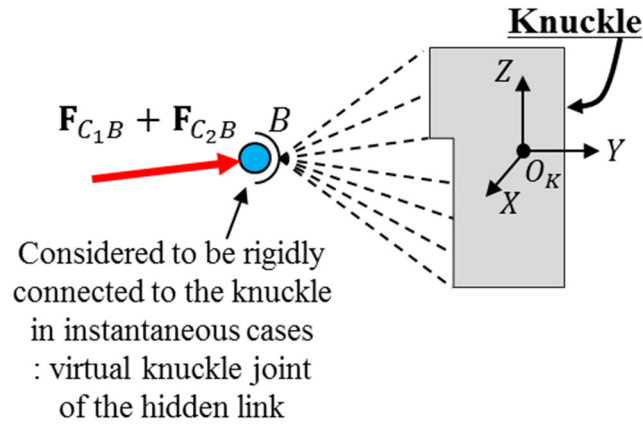


(b)

Figure 4.6 Twist and wrench screw description for RSR-limb. (a) Twist screws of each joint and (b) Wrench screws corresponding to reciprocal screws of the twist screws.



(a)



(b)

Figure 4.7 Load path of the supporting force imposed on the knuckle through the RSR-limb and equivalent force. (a) Description of the load flow from the frame (car-body) to the knuckle (wheel). (b) A constraint force equivalent to the forces applied on the knuckle in (a).

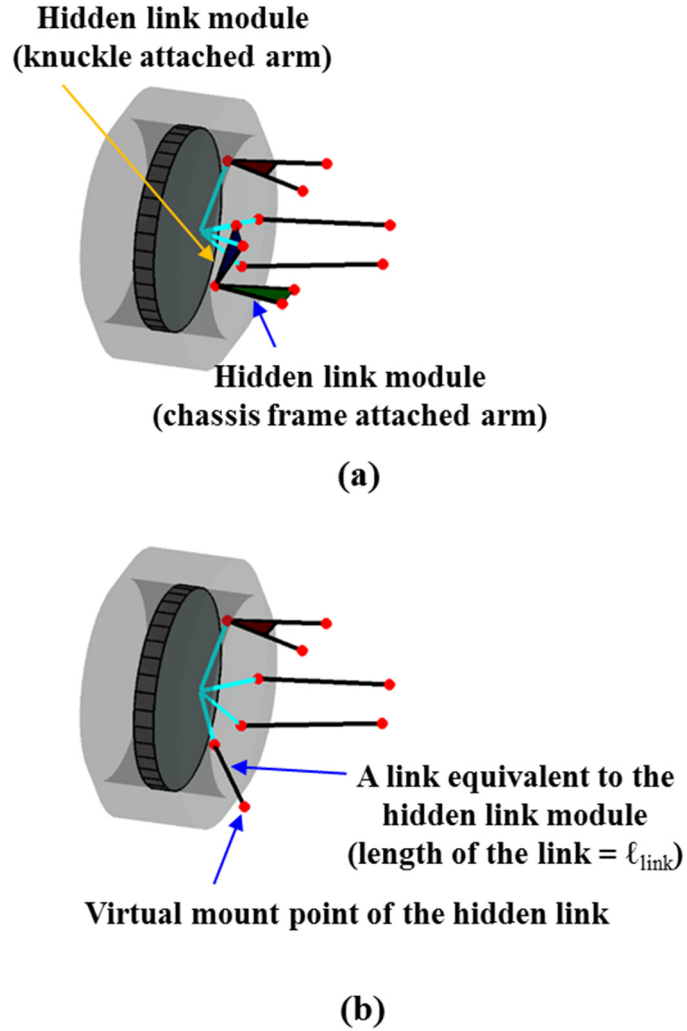


Figure 4.8 A new suspension proposed with a RSR-limb and its instantaneously equivalent system. (a) Newly suggested vehicle suspension including the RSR-limb and (b) Instantaneously equivalent system of the newly designed suspension in (a).

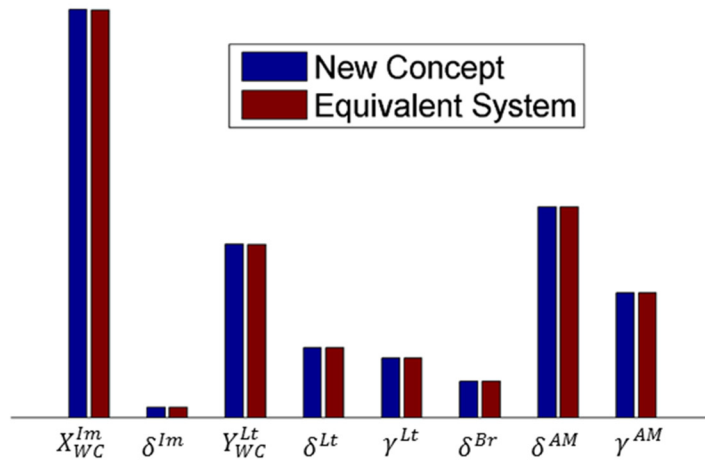


Figure 4.9 Comparison of the compliance behavior of the two suspensions in Figure 4.8(a) and (b). Amount of the response is depicted through bar plot.

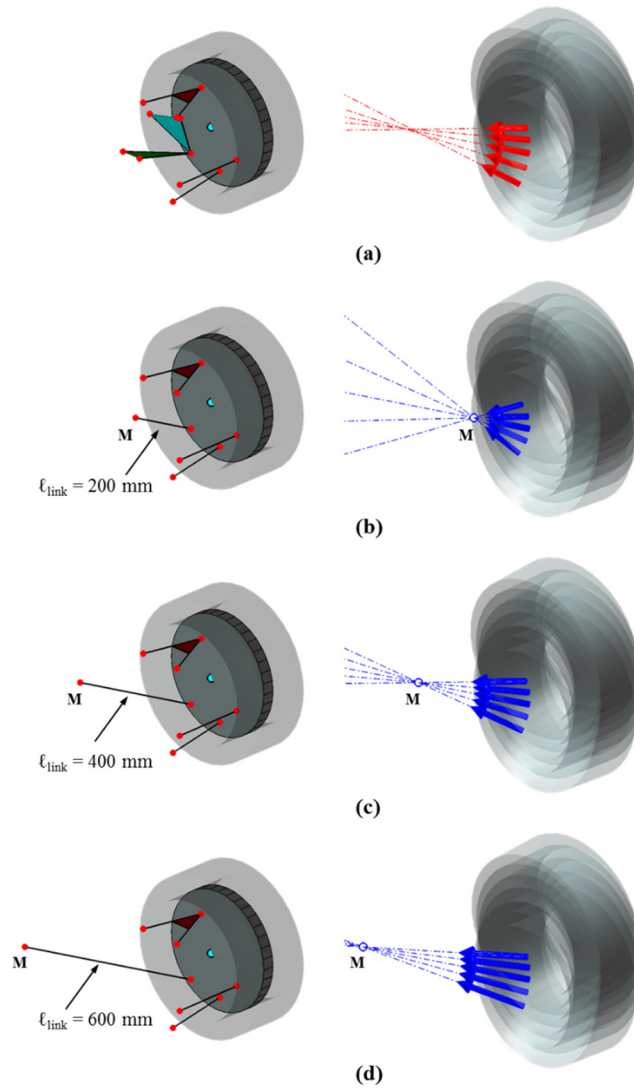


Figure 4.10 Configuration of the suspension (left) and constraint forces imposed on the knuckle (right) through the hidden link module and the real link for vertical stroke motions from -100 mm to 100 mm. (a) Hidden link suspension and multi-link suspension with the link length of (b) 200 mm, (c) 400 mm, and (d) 600 mm. (M: mount point of the real link in multi-link suspensions).

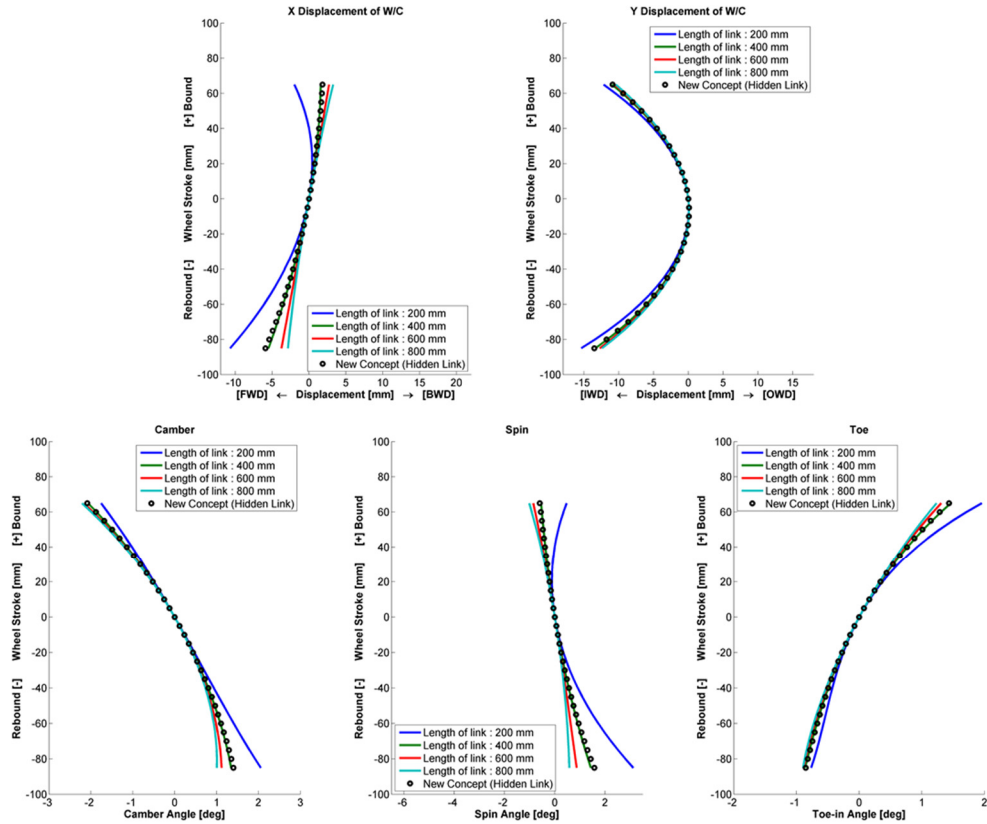


Figure 4.11 Comparison of the kinematic motion of the knuckle in vertical stroke. Circular marker corresponds to the motion of the new concept suspension in Figure 4.8(a), and other curves are that of the suspension in Figure 4.8(b). Length of the link corresponding to the hidden link is 200 mm, 400 mm, 600 mm, and 800 mm, respectively.

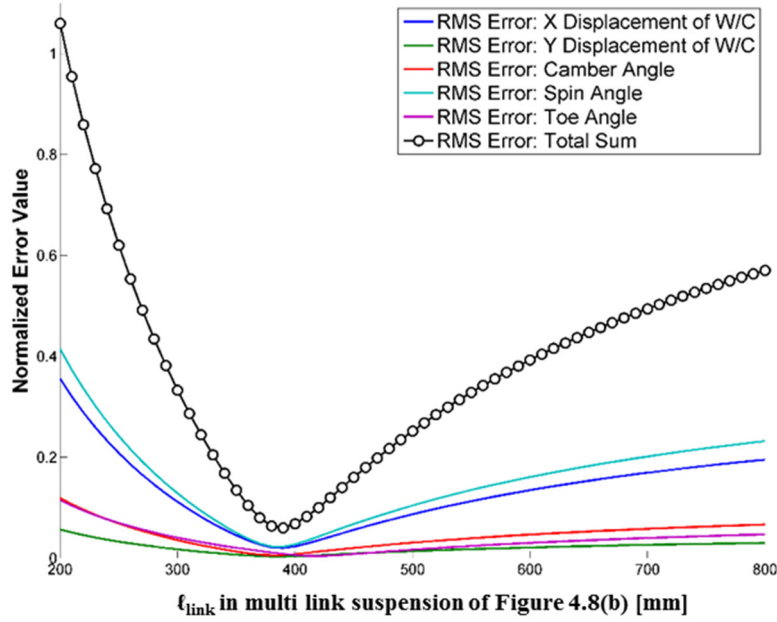


Figure 4.12 Variation of the RMS error value, defined in Eq. (4.19), according to the variation of the length of the link employed instead of the hidden link as shown in Figure 4.8(b).

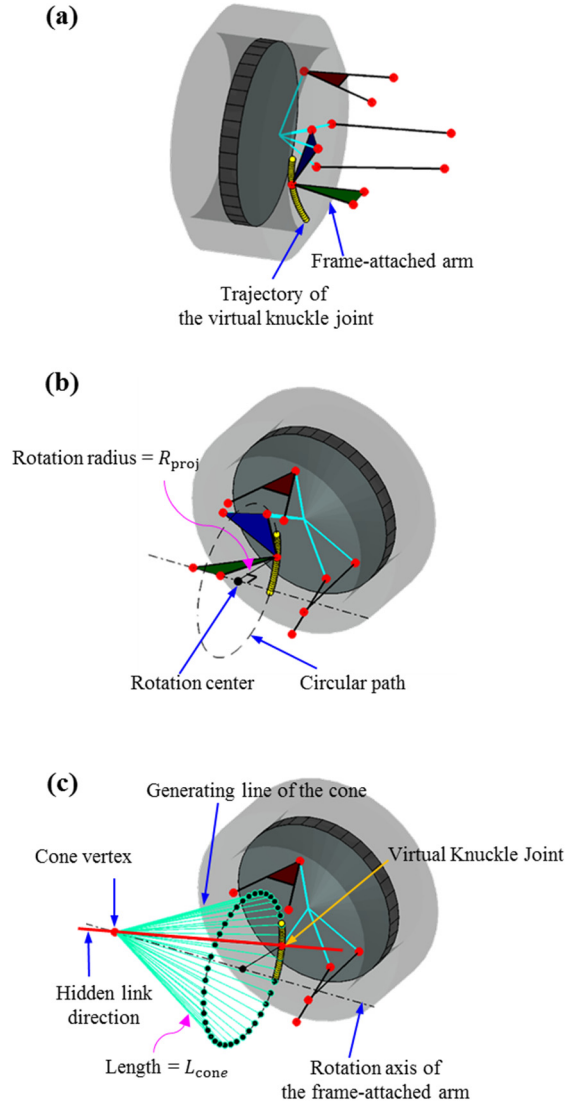


Figure 4.13 (a) Arc trajectory of the ball joint of the RSR-limb and (b) Radius of the circle which includes the arc trajectory of the ball joint. (c) Configuration of a cone which takes the circular path as the base plane, where the vertex of the cone is located at the intersection point of the extended line of the hidden link and the rotation axis of the frame-attached arm in RSR-limb.

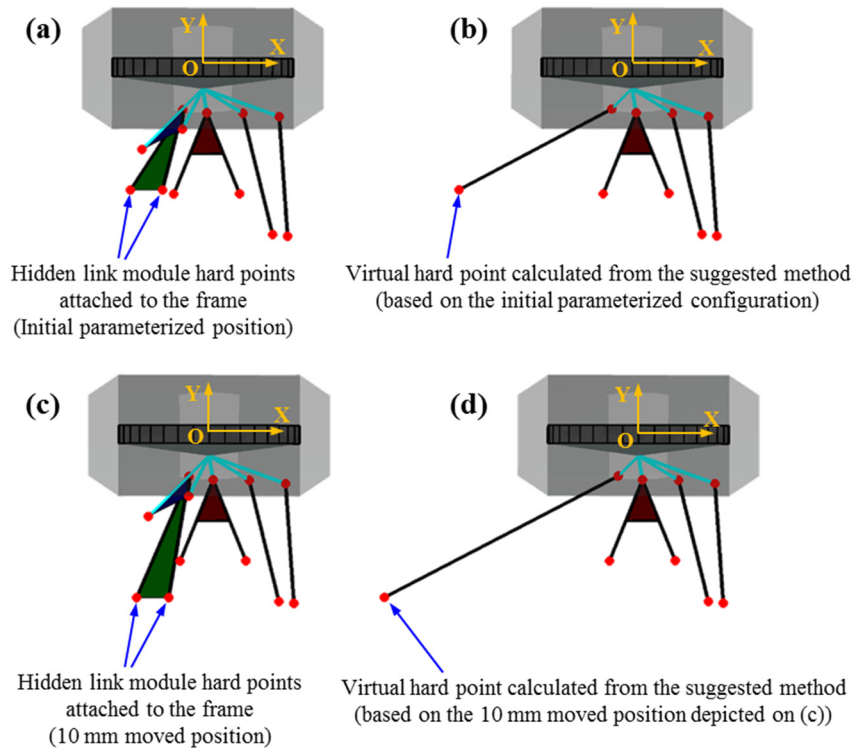


Figure 4.14 (a) A hidden link suspension corresponding to the initial configuration of the parameter study. (b) The equivalent multi-link suspension of (a) obtained by the proposed effective length calculation method. (c) A hidden link suspension with hard points 10 mm moved in $-Y$ direction by the parameter study. (d) The equivalent multi-link suspension of (c).

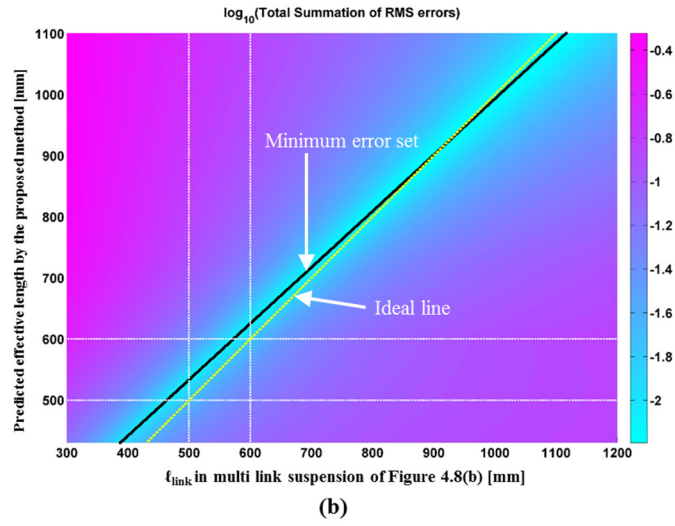
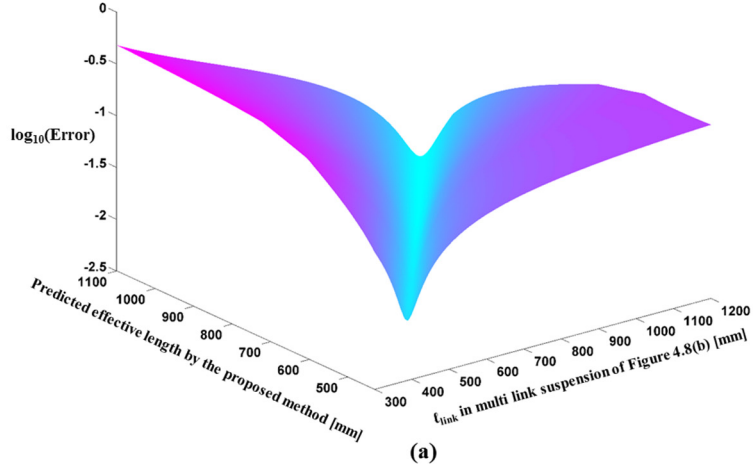


Figure 4.15 (a) Three dimensional view of the error plot and (b) 2D plane view of the error plot. Minimum error set is the line connecting the minimum error points. Ideal line is a set of points representing $X=Y$ (identity) in the 2D plane view.

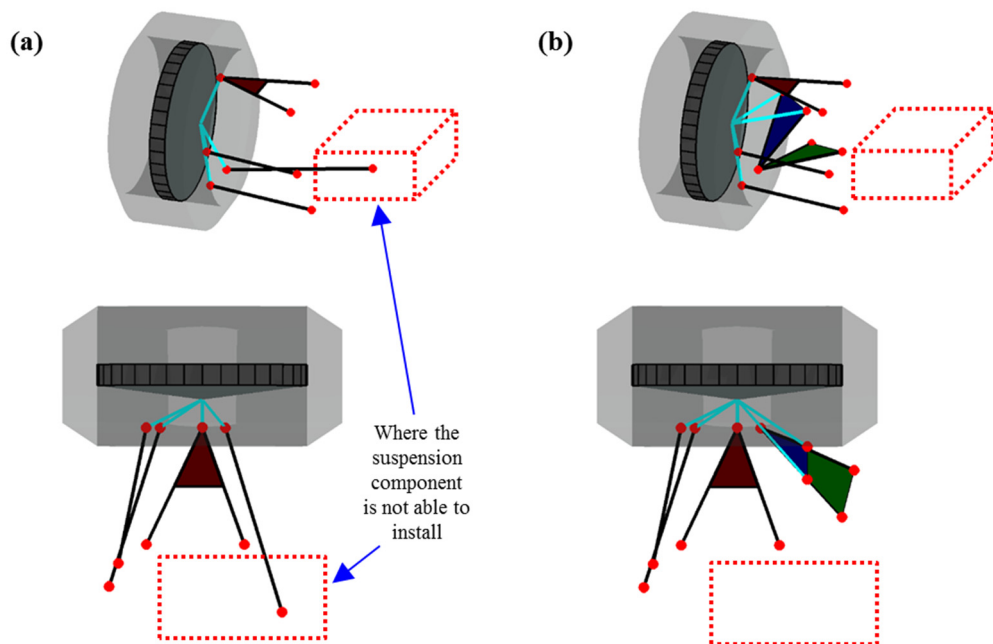


Figure 4.16 Design case study considering layout problem, where a zone depicted by the red dotted box is not allowed to mount any hard points. (a) A multi-link suspension and (b) A hidden link suspension.

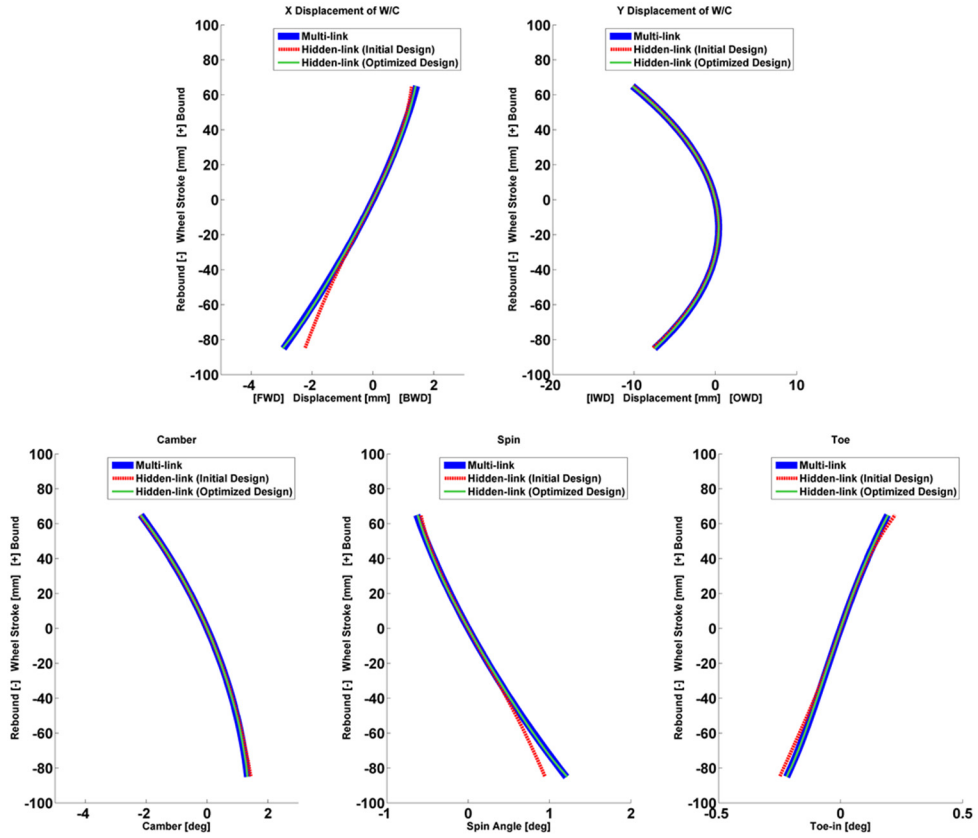


Figure 4.17 Comparison of the kinematic motion of the multi-link suspension in Figure 4.15(a) and hidden link suspension in Figure 4.15(b). In motion curves, hidden link (Initial Design) is the analysis result of the suspension in Figure 4.15(b), and hidden link (Optimized Design) corresponds to the result after adjusting the hard point locations by the chassis geometry optimization.

CHAPTER 5

CONCLUSIONS

In this thesis, a method to synthesize rigid link mechanisms without any baseline mechanism is developed. The developed method is an integrated one that unifies number synthesis and dimension synthesis based on the topology optimization formulation. It was shown through this study that various linkages from planar mechanisms to spatial mechanisms can be designed when the developed unified method is applied.

As the first step for the development of the methodology, some investigation was conducted on the conversion of the discrete-type DOF (Degree-of-Freedom) condition to a differentiable condition. Any rigid body mechanism must have the correct DOF for its operation. Since the DOF is a non-differentiable value corresponding to an integer value, a new physical quantity representing the DOF in differentiable form is introduced in this research. In contrast to the previous works

employing two physical quantities each of which represents the deficient-DOF state and redundant-DOF state, we showed that the degree of freedom can be controlled by only one unified physical quantity. In Chapter 2, the concept of the work transmittance efficiency function was proposed as the unified DOF control function, and it was confirmed that the planar link mechanisms satisfying the constraints can be synthesized by maximizing the efficiency function. Meanwhile, in the design process pre-matured convergence appeared due to the absence of a mass constraint. To resolve this problem, a new post-processing method was suggested. Using the proposed post-processing algorithm, we were able to design and identify industrial link mechanisms such as vehicle steering systems. This steering system design is the first successful application of any topology optimization method to two-dimensional industrial rigid-body mechanisms.

In Chapter 3, the proposed methodology was extended to spatial mechanism design problems. Accordingly, a three-dimensional ground structure was developed. The ground structure included ball joints, revolute joints, and links, which are the essential components necessary to construct spatial link mechanisms. In fact, we showed that a vehicle suspension system, one of the representative spatial mechanisms, can be designed by utilizing the proposed model and unified synthesis methodology. To check the validity of the developed synthesis method, it was made sure that the developed method successfully recovered the double wishbone and multi-link suspension mechanisms when the trajectories and orientations of their knuckles (or wheels) are supposed to be traced. As the provided trajectories, we

considered fore-and-aft motion and the lateral movement of the wheel center. We also considered the camber angle, spin angle (side view angle), and toe angle as the specified orientations of the wheel. Through these examples, it was confirmed that typical vehicle suspensions can be synthesized without intervention of a design engineer. Then, the developed synthesis methodology was applied to practical design problems with the design constraints mainly consisted of those used in automobile industries such as the roll center height, anti-lift and others. Depending on the size of the suspension design space, different types of suspensions were obtained. For a standard design space, a conventional multi-link type suspension, which is one of the most advanced types in the automotive industry, was obtained successfully by the developed linkage design method. More interestingly and importantly, a different type of suspension was synthesized when a smaller design space which is about 50% of the standard design space is applied. Actually, the newly synthesized one, having auxiliary links, may not be obtained without using the developed synthesis methodology based on the simultaneous topology and shape optimization algorithm. Here, the auxiliary link is defined as the suspension component which is not directly connected either to the frame or to the car-body. When the auxiliary link is used in the vehicle suspension, the number of link components increases considerably. For this reason, a suspension mechanism with auxiliary links would have been avoided in conventional design methods in the first place. In this respect, the developed method can be very useful because it searches for a candidate mechanism in a large-scale solution space. The detailed modeling and design procedure for the spatial

vehicle suspension mechanisms was given in Chapter 3.

Finally, some interpretation of the designed suspension with auxiliary links, which was obtained for a tight design space, was made. To investigate the role of the suspension module consisting of the auxiliary links, an analysis based on the screw-axis theory was carried out in Chapter 4. Because the behavior of a link mechanism can be analyzed by the constraint forces imposed through mechanism components, one can examine the role of the newly designed module by investigating the constraint force applied to the wheel (or knuckle) through the module. Through the analysis, it was proved that a pure force that is the same as the constraint force of the link is imposed on the knuckle by the new module. Therefore, the component is defined as the hidden link module in this thesis. Interestingly, the direction of the constraint force of the hidden link can be controlled easily, even though there is a layout restriction due to packaging problems. Therefore, it is clear that conventional multi-link type suspensions can be replaced by the hidden link suspensions when there is any design layout issue because of tight design space.

In this thesis, a new linkage module, i.e. the hidden link module, for the vehicle suspension, was found by the unified mechanism synthesis algorithm which was proposed in this work. In that the module was identified without any baseline design, the developed methodology can free design engineers' burden considerably and offer new insights. Although the successful application of the developed method was limited only to a few automotive applications, the proposed synthesis method can be a very powerful tool in finding new rigid-body mechanisms in short time. Certainly,

the developed method can be applied to industries other than automobile industries. For instance, one can apply this methodology for robot industries. Exo-skeleton robots have been developed for several decades, but it appears that optimal motion mechanisms are not yet identified. If the developed synthesis methodology is used for the design of exo-skeleton robot mechanisms, considerable improvements could be made. The developed methodology can also be used to design mechanisms used in flapping-wing UAVs because they require the use of a small number of actuators with tight mass constraint. In this case, a linkage mechanism would be appropriate because the required motion can be reliably realized with the minimum number of actuators.

To find new-concept mechanisms in various fields including the above-mentioned applications, the proposed method in this thesis need to be further developed. For instance, joints other than revolute joints need to be also synthesized. The consideration other physics, such as compliance, in addition to kinematics, needs to be investigated to enrich the developed methodology. These subjects can be interesting research subjects for future studies.

APPENDIX A

REMEDIES FOR THE MESH DEPENDENCY ISSUE

A.1 Overview

In ground structure based topology optimization, the mesh grid number is very important factor which affects the converged result. Likewise, in truss element based linkage design model employed in this thesis is also highly affected by the mesh grid.

In this chapter, we will see the planar linkage design problems in-depth with mesh dependency issues. The benchmark-type four-bar linkage design problem and the automotive steering design problem will be re-considered with several types of mesh grids.

Generally, the mesh dependency exist in ground structure approach, and we cannot avoid that. To this end, fine mesh has potential to satisfy more complicated solutions, so that we need to consider it. But, the fine mesh also has possibility to induce too much complicated solutions in practical aspects. Then, for both aspects

related to solution potential and complexity control, how can we control the converged results? As the remedies for this issue, two types of approaches, coarse-to-fine mesh converting approach and simultaneous topology-and-shape optimization approach, can be considered.

For the former approach, corresponding to the coarse-to-fine mesh converting approach, the automotive steering design problem is considered. And for the latter approach, the simultaneous topology-and-shape optimization, benchmark-type four-bar linkage design problem is re-considered in this chapter.

A.2 Coarse-to-fine mesh converting approach

In the automotive steering design problems considered in Chapter 2, we dealt with the design case studies for two types of mesh grids. The first one is the 6 by 3 grid, and the other one is the 7 by 3 grid. For both types of ground structure, we found six-bar and nine-bar linkage mechanisms, respectively. And it was shown in Chapter 2.3.2 that the nine-bar linkage result is composed of the two six-bar linkages, with redundant constraints. Then, what about if we consider the fine mesh grids such as 7 by 5 or 13 by 5. Figure A.1 shows the result obtained from various mesh grids with the same design condition considered in Chapter 2.

As one can see from the Figure A.1, the converged results for 7 by 3 mesh grid and 7 by 5 mesh grid in Figure A.1(b) and (c) are the same. However, the results of the mesh grid 13 by 3 and the 13 by 5 described in Figure A.1(d) and (e) are different with that of 7 by 3, and too complicated for manufacturing.

For the above mesh dependency issue, it will be better if we can control the complexity to obtain simple results such as the one from the coarse mesh and can find better solution with fine mesh grid. Here, to consider this problem, a method that applying a solution obtained from the 7 by 3 mesh grid to the 13 by 5 mesh grid as the initial guess is implemented. We call it “coarse-to-fine” mesh converting approach. Because the mesh grid is exactly doubled from “7 by 3” to “13 by 5”, all truss elements of 7 by 3 mesh grid are included in 13 by 5 mesh grid. Therefore, it is possible to apply the converged solution of 7 by 3 mesh grid into 13 by 5 mesh directly.

But, when applying the initial guess, a heuristic factor related to value of the initial guess is still remained with ambiguity. Here, we applied a strategy as follow.

Coarse-to-fine mesh converting approach

Step 1: Optimize the system in low-level mesh grid

Step 2: Double the mesh grid to high-level, e.g. [7 by 3] to [13 by 5]

Step 3: Allocate the initial guess with below rule

Step 3-1: Define user-defined control variable $\Delta\xi_{init}$

Step 3-2: Designate initial value for all design variables as $0.5 - \Delta\xi_{init}$

Step 3-3: Find truss and spring elements in fine mesh (high-level)

corresponding to converged solution of coarse mesh (low-level)

Step 3-4: Modify the initial value of design variables corresponding the

elements found in Step 3-3 to $0.5 + \Delta\xi_{init}$

Step 4: Optimize the system in fine mesh grid by using the initial guess of Step 3

In Figure A.2, there are several case studies for [13 by 5] mesh grid with variation of control parameter $\Delta\xi_{init}$, where the solution shown in Figure A.1(a) with [7 by 5] mesh grid is employed as the Step 1 solution. In three cases, 0.30, 0.15, and 0.10 are allocated as the $\Delta\xi_{init}$, respectively. From the results shown in Figure A.2(a) and (b), it is possible to see the same result compared with the 7 by 3 mesh grid. But, the result in Figure A.2(c) is quite different. To this end, it will be nearly impossible to

use this solution due to its complex configuration.

Then, what about if we apply this method to 12 by 3 mesh grid with the initial guess based on the converged solution of 6 by 3 mesh grid? We employed the post-processed result of the 6 by 3 ground structure solution, which is shown in Figure 2.14. And apply this solution into 12 by 3 mesh grid with two initial guess parameters. In the first case, we considered 12 by 3 mesh grid with initial guess of $\Delta\xi_{\text{init}} = 0.3$. Next, for the second case study, $\Delta\xi_{\text{init}} = 0.15$ case is considered. The obtained solution is shown in Figure A.3(a) and (b), respectively.

The results of the first case study is the exactly same with the 6 by 3 mesh grid solution, which is the 9-bar linkage. But the converged result of the second case study is entirely different, that corresponds to the 32-bar linkage mechanism as shown in Figure A.3(b). To see the performance of the newly designed steering mechanism, we simplified the solution and analyze by the multi-body analysis. The performance of the systems are compared in Figure A.4, and the 32-bar linkage solution shows better performance compared with that of the 9-bar linkage.

The coarse-to-fine mesh technique can be exploited by the users for better convergence in fine mesh when they want to high-performance systems. However, in coarse-to-fine mesh grid strategy, there is a still remained issue related to deciding initial guess factor, which is determined by heuristics. Also, the complexity of design results is not well controlled by the suggested rule, so that obtained solution is difficult to apply in practical applications. To avoid these difficulties, one can

consider simultaneous topology and shape optimization as shown in Chapter 3 and Chapter 4. In the next chapter, we will discuss the simultaneous topology and shape optimization in aspect of the mesh dependency issue.

A.3 Simultaneous topology and shape optimization approach

To consider this hybrid optimization approach, it needs to check the uniqueness of the solution compared with the fine mesh grid approach. In this chapter, we applied 3 by 3 mesh grid for topology and shape optimization at once, and compare the result of the pure topology optimization with the 5 by 5 mesh grid. Figure A.5 shows the reference benchmark type linkage with 5 by 5 mesh grid, which is used as the target system generating desired output path in this study.

First, in 3 by 3 mesh grid, we implemented pure topology optimization. But it fails to trace the desired path with proper DOF condition. The solution with efficiency value 1 is not found with satisfaction of the error constraint. Then, we applied the pure topology optimization again, with 5 by 5 mesh grid. As one can expect, the solution is properly obtained for this case, because there is a solution in the designated mesh grid. The result is shown in Figure A.6(a).

Next, 3 by 3 mesh grid is applied with topology and shape optimization variables. The way we define this hybrid optimization is exactly same with Formulation B, equation (3.33) in Chapter 3.3.2. Design variable for shape optimization is defined as (3.40), and nodal distance between nodes are applied as (3.41j) to prevent merging node (or called melting node) problem [93]. In this case, distance between each node is restricted to be larger than 0.1 m. Also, the end-effector position corresponding to the output is not included in the shape optimization. Figure A.6(b) is the result obtained for simultaneous topology and shape optimization with error bound 0.02 m. The converged solution has a little bit different coordinate compared with the

reference link. The right top corner point of the original reference link is located on $\{0.7500, 1.0000\}$ in Figure A.6(a), but the position of corresponding point in Figure A.6(b) is $\{0.7416, 0.9475\}$. Nonetheless, the output path trajectory is almost the same to each other.

Then, what about the convergence history of cases in Figure A.6(a) and (b)? They are compared in Figure A.7. Because the number of design variables are smaller in 3 by 3 topology-and-shape case compared with 5 by 5 pure topology case, it is easier to find the solution in former case with less iteration number. The number of design variables is 63 in former case and 325 in latter case. Also, the number of state variables corresponding to the FE DOF's is less in former case, for each case 18 and 50. Therefore, computation cost for nonlinear analysis can be reduced when we apply the topology-and-shape optimization strategy with coarse mesh grid. (In general, we used $O(n^2)$ type solver.)

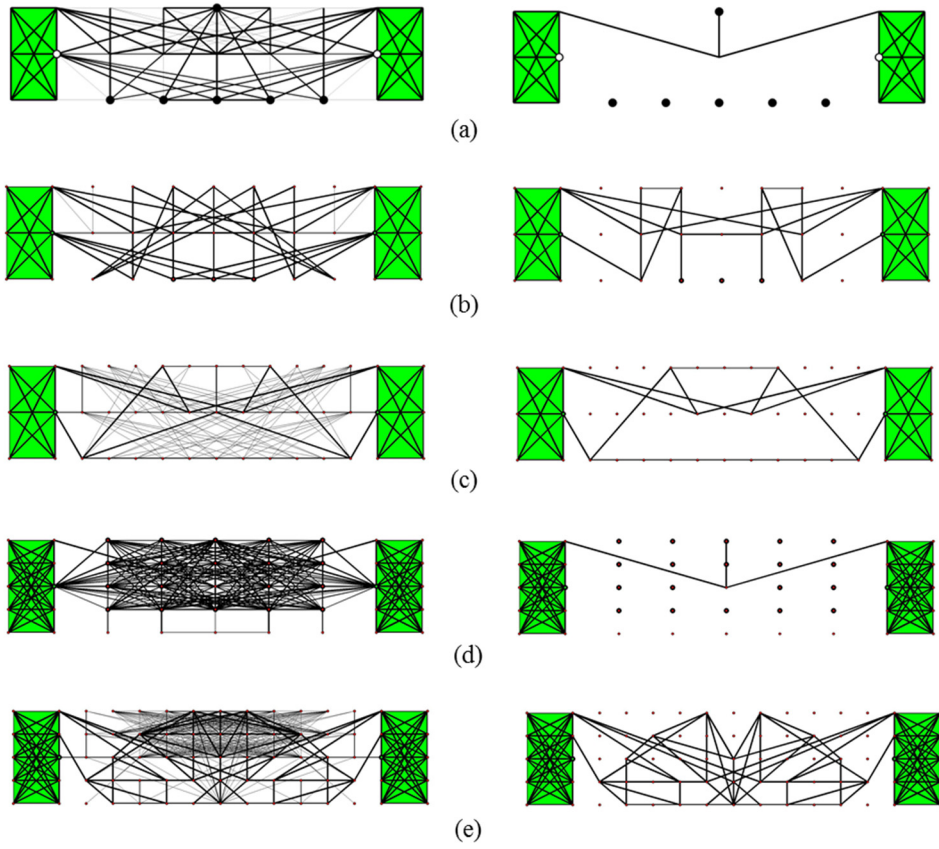


Figure A.1 Ground structure and design results for the various mesh grids. (a) 7 by 3 mesh grid, (b) 9 by 3 mesh grid, (c) 13 by 3 mesh grid, and (d) 7 by 5 mesh grid, and (e) 13 by 5 mesh grid.

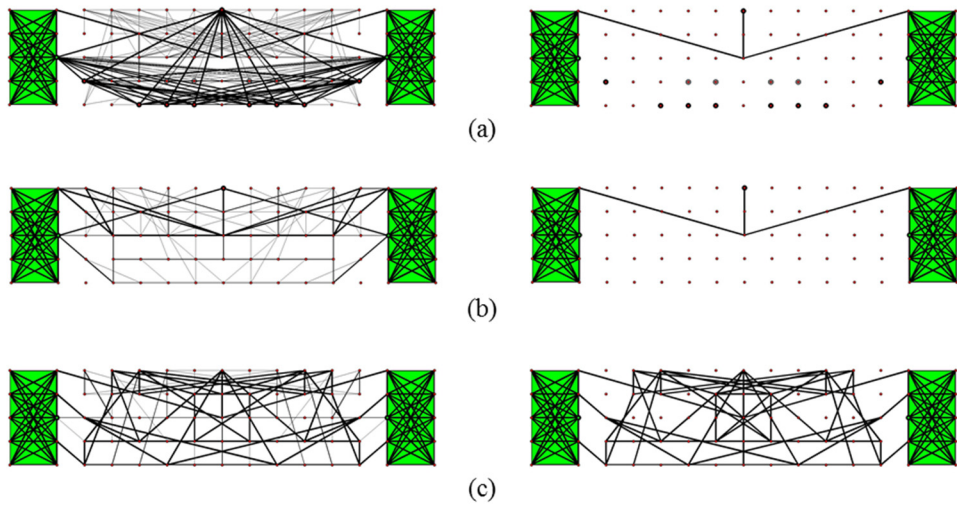


Figure A.2 Result of the coarse-to-fine mesh grid approach in 13 by 5 mesh grid, where the initial guess based on the converged result of 7 by 3 grid mesh shown in Figure A.1(a) is applied. For each case, (a) $\Delta\xi_{\text{init}} = 0.3$, (b) $\Delta\xi_{\text{init}} = 0.15$, and (c) $\Delta\xi_{\text{init}} = 0.10$ is allocated as the initial guess controlling parameter.

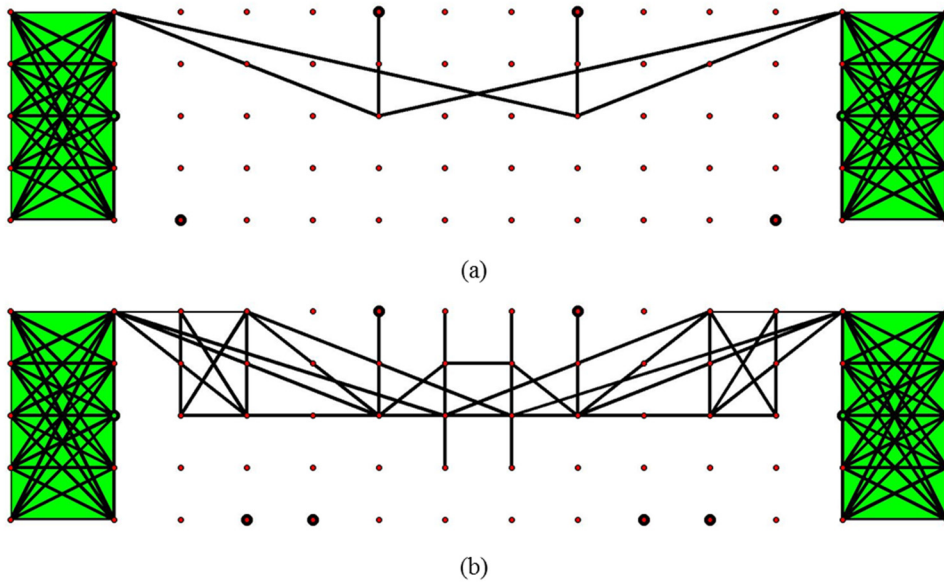


Figure A.3 Result of the coarse-to-fine mesh grid approach in 12 by 5 mesh grid, where the initial guess based on the converged result of 6 by 3 grid mesh (i.e. 9-bar linkage shown in Figure 2.14) is applied. For each case, (a) $\Delta\xi_{\text{init}} = 0.3$ and (b) $\Delta\xi_{\text{init}} = 0.15$ is allocated as the initial guess controlling parameter.

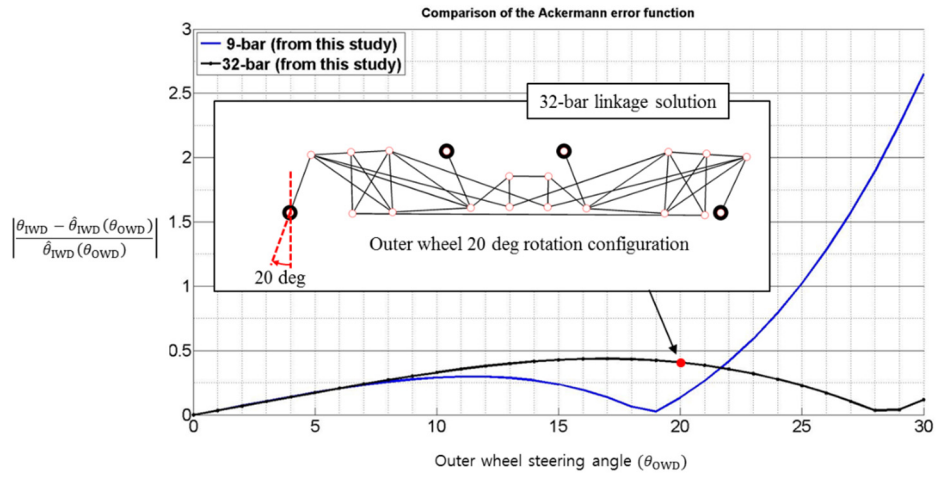


Figure A.4 Comparison of the post-processed result shown in Figure A.3.

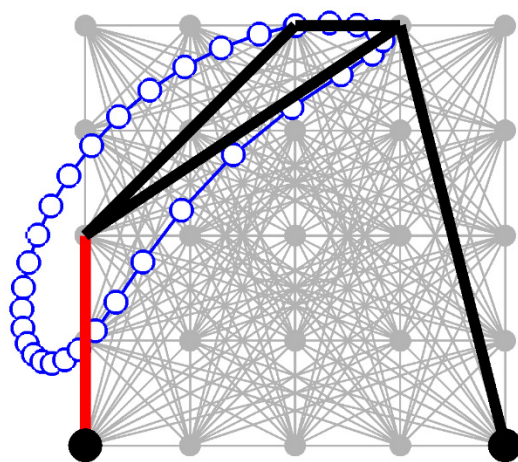


Figure A.5 Reference linkage mechanism configuration and output path trajectory.

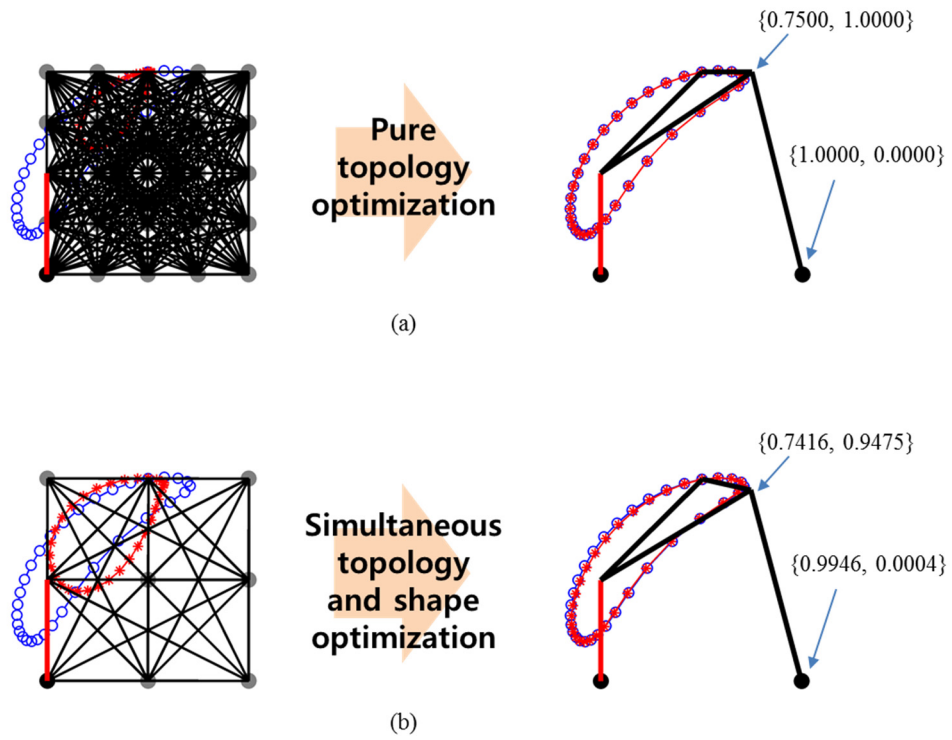


Figure A.6 Ground structure employed for the optimization and post-processed result obtained from the optimization. (a) 5 by 5 mesh grid result for pure topology optimization and (b) 3 by 3 mesh grid result with simultaneous topology and shape optimization.

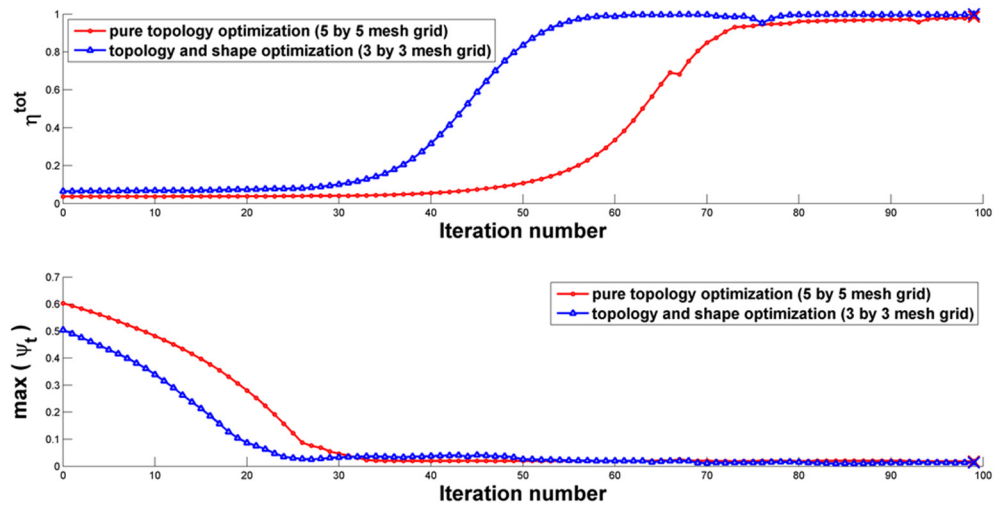


Figure A.7 Iteration history for comparing pure topology optimization (5 by 5 mesh grid) and simultaneous topology and shape optimization (3 by 3 mesh grid).

APPENDIX B

WRENCH SCREW ANALYSIS

B.1 Overview

To find force and moment applied to the knuckle by suspension components, we need to find wrench screw provided by the composing parts. For example, general link component which is composed of a rigid with ball joint at both end points can be analyzed by the screw axis theory. In the link case, the wrench screw will be lengthwise force without couple (moment), and the action point of the force will be ball joint of the link.

The constraint force applied to the connected component, or moving platform, can be obtained by calculating the reciprocal screw of the twist. In the subsequent sub-chapters wrench screw of “arm” and “RSR-limb” will be found by this method.

B.2 Wrench screw of arm component

As described in Chapter 4, twist screw can be defined as (4.5) and (4.6). Here, the related equations are introduced again as below.

$$\mathbf{S}_1 = \begin{bmatrix} \mathbf{s}_1 \\ \mathbf{s}_A \times \mathbf{s}_1 \end{bmatrix} \quad (\text{B.1a})$$

$$\mathbf{S}_2 = \begin{bmatrix} \mathbf{s}_2 \\ \mathbf{s}_B \times \mathbf{s}_2 \end{bmatrix} \quad (\text{B.1b})$$

$$\mathbf{S}_3 = \begin{bmatrix} \mathbf{s}_3 \\ \mathbf{s}_B \times \mathbf{s}_3 \end{bmatrix} \quad (\text{B.1c})$$

$$\mathbf{S}_4 = \begin{bmatrix} \mathbf{s}_4 \\ \mathbf{s}_B \times \mathbf{s}_4 \end{bmatrix} \quad (\text{B.1d})$$

Equation (B.1) is the same with (4.5), and details can be found in Chapter 4.

$$\mathbf{S} = \sum_{i=1}^4 (q_i \mathbf{S}_i) \quad (\text{B.2})$$

Equation (B.2) is the same with (4.6).

$$\mathbf{S}_r^T (\delta \mathbf{S}) = 0 \quad (\text{B.3})$$

Equation (B.3) is the same with (4.7).

To see whether (B.4), which is the same with (4.8), is the reciprocal screw of twist shown in (B.2), it needs to check the reciprocal relation of (B.3).

$$\tilde{\mathbf{S}}_r = \tilde{q}_r \begin{bmatrix} \tilde{\mathbf{s}}_r \\ \mathbf{s}_B \times \tilde{\mathbf{s}}_r \end{bmatrix} \quad (\text{B.4a})$$

$$\tilde{\mathbf{s}}_r = c_1 \mathbf{s}_1 + c_2 (\mathbf{s}_B - \mathbf{s}_A) \quad (\text{B.4b})$$

First, substitute Eq. (B.1), (B.2), and (B.4a) into Eq. (B.3).

$$\begin{aligned} \tilde{\mathbf{S}}_r^T \delta \mathbf{S} = & \tilde{q}_r \delta q_1 \begin{bmatrix} (\mathbf{s}_B \times \tilde{\mathbf{s}}_r)^T & \tilde{\mathbf{s}}_r^T \end{bmatrix} \begin{bmatrix} \mathbf{s}_1 \\ \mathbf{s}_A \times \mathbf{s}_1 \end{bmatrix} + \tilde{q}_r \delta q_2 \begin{bmatrix} (\mathbf{s}_B \times \tilde{\mathbf{s}}_r)^T & \tilde{\mathbf{s}}_r^T \end{bmatrix} \begin{bmatrix} \mathbf{s}_2 \\ \mathbf{s}_B \times \mathbf{s}_2 \end{bmatrix} \\ & + \tilde{q}_r \delta q_3 \begin{bmatrix} (\mathbf{s}_B \times \tilde{\mathbf{s}}_r)^T & \tilde{\mathbf{s}}_r^T \end{bmatrix} \begin{bmatrix} \mathbf{s}_3 \\ \mathbf{s}_B \times \mathbf{s}_3 \end{bmatrix} + \tilde{q}_r \delta q_4 \begin{bmatrix} (\mathbf{s}_B \times \tilde{\mathbf{s}}_r)^T & \tilde{\mathbf{s}}_r^T \end{bmatrix} \begin{bmatrix} \mathbf{s}_4 \\ \mathbf{s}_B \times \mathbf{s}_4 \end{bmatrix} \end{aligned} \quad (\text{B.5})$$

If Eq. (B.6a-d) become zero, $\tilde{\mathbf{S}}_r^T \delta \mathbf{S}$ in Eq. (B.5) will be zero regardless of the coefficients \tilde{q}_r and q_i ($i=1,2,3,4$).

$$\tilde{\mathbf{S}}_r^T \delta \mathbf{S}_1 = \tilde{q}_r \delta q_1 \begin{bmatrix} \mathbf{s}_B \times \tilde{\mathbf{s}}_r & \tilde{\mathbf{s}}_r \end{bmatrix} \begin{bmatrix} \mathbf{s}_1 \\ \mathbf{s}_A \times \mathbf{s}_1 \end{bmatrix} = \tilde{q}_r \delta q_1 \{ (\mathbf{s}_B \times \tilde{\mathbf{s}}_r) \cdot \mathbf{s}_1 + \tilde{\mathbf{s}}_r \cdot (\mathbf{s}_A \times \mathbf{s}_1) \} \quad (\text{B.6a})$$

$$\tilde{\mathbf{S}}_r^T \delta \mathbf{S}_2 = \tilde{q}_r \delta q_2 \begin{bmatrix} \mathbf{s}_B \times \tilde{\mathbf{s}}_r & \tilde{\mathbf{s}}_r \end{bmatrix} \begin{bmatrix} \mathbf{s}_2 \\ \mathbf{s}_B \times \mathbf{s}_2 \end{bmatrix} = \tilde{q}_r \delta q_2 \{ (\mathbf{s}_B \times \tilde{\mathbf{s}}_r) \cdot \mathbf{s}_2 + \tilde{\mathbf{s}}_r \cdot (\mathbf{s}_B \times \mathbf{s}_2) \} \quad (\text{B.6b})$$

$$\tilde{\mathbf{S}}_r^T \delta \mathbf{S}_3 = \tilde{q}_r \delta q_3 \begin{bmatrix} \mathbf{s}_B \times \tilde{\mathbf{s}}_r & \tilde{\mathbf{s}}_r \end{bmatrix} \begin{bmatrix} \mathbf{s}_3 \\ \mathbf{s}_B \times \mathbf{s}_3 \end{bmatrix} = \tilde{q}_r \delta q_3 \{ (\mathbf{s}_B \times \tilde{\mathbf{s}}_r) \cdot \mathbf{s}_3 + \tilde{\mathbf{s}}_r \cdot (\mathbf{s}_B \times \mathbf{s}_3) \} \quad (\text{B.6c})$$

$$\tilde{\mathbf{S}}_r^T \delta \mathbf{S}_4 = \tilde{q}_r \delta q_4 \begin{bmatrix} \mathbf{s}_B \times \tilde{\mathbf{s}}_r & \tilde{\mathbf{s}}_r \end{bmatrix} \begin{bmatrix} \mathbf{s}_4 \\ \mathbf{s}_B \times \mathbf{s}_4 \end{bmatrix} = \tilde{q}_r \delta q_4 \{ (\mathbf{s}_B \times \tilde{\mathbf{s}}_r) \cdot \mathbf{s}_4 + \tilde{\mathbf{s}}_r \cdot (\mathbf{s}_B \times \mathbf{s}_4) \} \quad (\text{B.6d})$$

To simplify the Eq. (B.6), substitute Eq. (B.4b) into $\tilde{\mathbf{s}}_r$. Then, $\mathbf{s}_B \times \tilde{\mathbf{s}}_r$ in Eq. (B.6) could be calculated as (B.7).

$$\begin{aligned}\mathbf{s}_B \times \tilde{\mathbf{s}}_r &= \mathbf{s}_B \times \{c_1 \mathbf{s}_1 + c_2 (\mathbf{s}_B - \mathbf{s}_A)\} \\ &= c_1 (\mathbf{s}_B \times \mathbf{s}_1) - c_2 (\mathbf{s}_B \times \mathbf{s}_A)\end{aligned}\quad (\text{B.7})$$

Eq. (B.8) is the result of substitution of (B.7) into (B.6a).

$$\begin{aligned}\tilde{\mathbf{S}}_r^T \delta \mathbf{S}_1 &= \tilde{q}_r \delta q_1 \left[\{c_1 (\mathbf{s}_B \times \mathbf{s}_1) - c_2 (\mathbf{s}_B \times \mathbf{s}_A)\} \cdot \mathbf{s}_1 + \{c_1 \mathbf{s}_1 + c_2 (\mathbf{s}_B - \mathbf{s}_A)\} \cdot (\mathbf{s}_A \times \mathbf{s}_1) \right] \\ &= \tilde{q}_r \delta q_1 \{c_1 (\mathbf{s}_B \times \mathbf{s}_1) \cdot \mathbf{s}_1 - c_2 (\mathbf{s}_B \times \mathbf{s}_A) \cdot \mathbf{s}_1 \\ &\quad + c_1 \mathbf{s}_1 \cdot (\mathbf{s}_A \times \mathbf{s}_1) + c_2 \mathbf{s}_B \cdot (\mathbf{s}_A \times \mathbf{s}_1) - c_2 \mathbf{s}_A \cdot (\mathbf{s}_A \times \mathbf{s}_1)\}\end{aligned}\quad (\text{B.8})$$

Because $\mathbf{s}_B \times \mathbf{s}_1$ is perpendicular to the \mathbf{s}_1 , a term $(\mathbf{s}_B \times \mathbf{s}_1) \cdot \mathbf{s}_1$ in (B.8) becomes zero. In the same manner, $\mathbf{s}_1 \cdot (\mathbf{s}_A \times \mathbf{s}_1)$ and $\mathbf{s}_A \cdot (\mathbf{s}_A \times \mathbf{s}_1)$ also become zero, then (B.8) could be simplified as (B.9).

$$\tilde{\mathbf{S}}_r^T \delta \mathbf{S}_1 = \tilde{q}_r \delta q_1 c_2 \{-(\mathbf{s}_B \times \mathbf{s}_A) \cdot \mathbf{s}_1 + \mathbf{s}_B \cdot (\mathbf{s}_A \times \mathbf{s}_1)\} \quad (\text{B.9})$$

For more simplification of the (B.9), a vector calculation rule in Eq. (B.10) is employed.

$$\mathbf{A} \cdot (\mathbf{B} \times \mathbf{C}) = \mathbf{C} \cdot (\mathbf{A} \times \mathbf{B}) = \mathbf{B} \cdot (\mathbf{C} \times \mathbf{A}) \quad (\text{B.10})$$

From (B.10), Eq. (B.9) can be simplified as (B.11).

$$\tilde{\mathbf{S}}_r^T \delta \mathbf{S}_1 = \tilde{q}_r \delta q_1 c_2 \{-(\mathbf{s}_B \times \mathbf{s}_A) \cdot \mathbf{s}_1 + (\mathbf{s}_B \times \mathbf{s}_A) \cdot \mathbf{s}_1\} \quad (\text{B.11})$$

Accordingly, $\tilde{\mathbf{S}}_r^T \delta \mathbf{S}_1 = 0$ is satisfied regardless of the coefficients. Then, what about equations (B.6b)-(B.6d) if the Eq. (B.7) is substituted like as Eq. (B.6a). Consider the substitution of the Eq. (B.7) into (B.6b)-(B.6d).

$$\begin{aligned}
\tilde{\mathbf{S}}_r^T \delta \mathbf{S}_2 &= \tilde{q}_r \delta q_2 \left[\{c_1 (\mathbf{s}_B \times \mathbf{s}_1) - c_2 (\mathbf{s}_B \times \mathbf{s}_A)\} \cdot \mathbf{s}_2 + \{c_1 \mathbf{s}_1 + c_2 (\mathbf{s}_B - \mathbf{s}_A)\} \cdot (\mathbf{s}_B \times \mathbf{s}_2) \right] \\
&= \tilde{q}_r \delta q_2 \{c_1 (\mathbf{s}_B \times \mathbf{s}_1) \cdot \mathbf{s}_2 - c_2 (\mathbf{s}_B \times \mathbf{s}_A) \cdot \mathbf{s}_2 \\
&\quad + c_1 \mathbf{s}_1 \cdot (\mathbf{s}_B \times \mathbf{s}_2) + c_2 \mathbf{s}_B \cdot (\mathbf{s}_B \times \mathbf{s}_2) - c_2 \mathbf{s}_A \cdot (\mathbf{s}_B \times \mathbf{s}_2)\}
\end{aligned}
\tag{B.12a}$$

$$\begin{aligned}
\tilde{\mathbf{S}}_r^T \delta \mathbf{S}_3 &= \tilde{q}_r \delta q_3 \left[\{c_1 (\mathbf{s}_B \times \mathbf{s}_1) - c_2 (\mathbf{s}_B \times \mathbf{s}_A)\} \cdot \mathbf{s}_3 + \{c_1 \mathbf{s}_1 + c_2 (\mathbf{s}_B - \mathbf{s}_A)\} \cdot (\mathbf{s}_B \times \mathbf{s}_3) \right] \\
&= \tilde{q}_r \delta q_3 \{c_1 (\mathbf{s}_B \times \mathbf{s}_1) \cdot \mathbf{s}_3 - c_2 (\mathbf{s}_B \times \mathbf{s}_A) \cdot \mathbf{s}_3 \\
&\quad + c_1 \mathbf{s}_1 \cdot (\mathbf{s}_B \times \mathbf{s}_3) + c_2 \mathbf{s}_B \cdot (\mathbf{s}_B \times \mathbf{s}_3) - c_2 \mathbf{s}_A \cdot (\mathbf{s}_B \times \mathbf{s}_3)\}
\end{aligned}
\tag{B.12b}$$

$$\begin{aligned}
\tilde{\mathbf{S}}_r^T \delta \mathbf{S}_4 &= \tilde{q}_r \delta q_4 \left[\{c_1 (\mathbf{s}_B \times \mathbf{s}_1) - c_2 (\mathbf{s}_B \times \mathbf{s}_A)\} \cdot \mathbf{s}_4 + \{c_1 \mathbf{s}_1 + c_2 (\mathbf{s}_B - \mathbf{s}_A)\} \cdot (\mathbf{s}_B \times \mathbf{s}_4) \right] \\
&= \tilde{q}_r \delta q_4 \{c_1 (\mathbf{s}_B \times \mathbf{s}_1) \cdot \mathbf{s}_4 - c_2 (\mathbf{s}_B \times \mathbf{s}_A) \cdot \mathbf{s}_4 \\
&\quad + c_1 \mathbf{s}_1 \cdot (\mathbf{s}_B \times \mathbf{s}_4) + c_2 \mathbf{s}_B \cdot (\mathbf{s}_B \times \mathbf{s}_4) - c_2 \mathbf{s}_A \cdot (\mathbf{s}_B \times \mathbf{s}_4)\}
\end{aligned}
\tag{B.12c}$$

Because $\mathbf{s}_B \times \mathbf{s}_2$ is perpendicular to the \mathbf{s}_2 , a term $\mathbf{s}_B \cdot (\mathbf{s}_B \times \mathbf{s}_2)$ in (B.12a) becomes zero. In the same manner, $\mathbf{s}_B \cdot (\mathbf{s}_B \times \mathbf{s}_3)$ in Eq. (B.12b) and $\mathbf{s}_B \cdot (\mathbf{s}_B \times \mathbf{s}_4)$ in Eq. (B.12c) can be removed. Then, remained terms could be calculated according to the Eq. (B.10) as follow.

$$\begin{aligned}
\tilde{\mathbf{S}}_r^T \delta \mathbf{S}_2 &= \tilde{q}_r \delta q_2 \left[c_1 \{(\mathbf{s}_B \times \mathbf{s}_1) \cdot \mathbf{s}_2 + \mathbf{s}_1 \cdot (\mathbf{s}_B \times \mathbf{s}_2)\} - c_2 \{(\mathbf{s}_B \times \mathbf{s}_A) \cdot \mathbf{s}_2 + \mathbf{s}_A \cdot (\mathbf{s}_B \times \mathbf{s}_2)\} \right] \\
&= \tilde{q}_r \delta q_2 \left[c_1 \{(\mathbf{s}_B \times \mathbf{s}_1) \cdot \mathbf{s}_2 - (\mathbf{s}_B \times \mathbf{s}_1) \cdot \mathbf{s}_2\} - c_2 \{(\mathbf{s}_B \times \mathbf{s}_A) \cdot \mathbf{s}_2 - (\mathbf{s}_B \times \mathbf{s}_A) \cdot \mathbf{s}_2\} \right] \\
&= 0
\end{aligned}
\tag{B.13a}$$

$$\begin{aligned}
\tilde{\mathbf{S}}_r^T \delta \mathbf{S}_3 &= \tilde{q}_r \delta q_3 \left[c_1 \left\{ (\mathbf{s}_B \times \mathbf{s}_1) \cdot \mathbf{s}_3 + \mathbf{s}_1 \cdot (\mathbf{s}_B \times \mathbf{s}_3) \right\} - c_2 \left\{ (\mathbf{s}_B \times \mathbf{s}_A) \cdot \mathbf{s}_3 + \mathbf{s}_A \cdot (\mathbf{s}_B \times \mathbf{s}_3) \right\} \right] \\
&= \tilde{q}_r \delta q_3 \left[c_1 \left\{ (\mathbf{s}_B \times \mathbf{s}_1) \cdot \mathbf{s}_3 - (\mathbf{s}_B \times \mathbf{s}_1) \cdot \mathbf{s}_3 \right\} - c_2 \left\{ (\mathbf{s}_B \times \mathbf{s}_A) \cdot \mathbf{s}_3 - (\mathbf{s}_B \times \mathbf{s}_A) \cdot \mathbf{s}_3 \right\} \right] \\
&= 0
\end{aligned}
\tag{B.13b}$$

$$\begin{aligned}
\tilde{\mathbf{S}}_r^T \delta \mathbf{S}_4 &= \tilde{q}_r \delta q_4 \left[c_1 \left\{ (\mathbf{s}_B \times \mathbf{s}_1) \cdot \mathbf{s}_4 + \mathbf{s}_1 \cdot (\mathbf{s}_B \times \mathbf{s}_4) \right\} - c_2 \left\{ (\mathbf{s}_B \times \mathbf{s}_A) \cdot \mathbf{s}_4 + \mathbf{s}_A \cdot (\mathbf{s}_B \times \mathbf{s}_4) \right\} \right] \\
&= \tilde{q}_r \delta q_4 \left[c_1 \left\{ (\mathbf{s}_B \times \mathbf{s}_1) \cdot \mathbf{s}_4 - (\mathbf{s}_B \times \mathbf{s}_1) \cdot \mathbf{s}_4 \right\} - c_2 \left\{ (\mathbf{s}_B \times \mathbf{s}_A) \cdot \mathbf{s}_4 - (\mathbf{s}_B \times \mathbf{s}_A) \cdot \mathbf{s}_4 \right\} \right] \\
&= 0
\end{aligned}
\tag{B.13c}$$

Accordingly, $\tilde{\mathbf{S}}_r^T \delta \mathbf{S}_i = 0$ ($i = 2, 3, 4$) is satisfied regardless of the coefficients, and

$$\tilde{\mathbf{S}}_r^T \delta \mathbf{S} = 0.$$

B.3 Wrench screw of RSR limb module

As described in Chapter 4, twist screw can be defined as (4.10) and (4.11). Here, the related equations are introduced again as below.

$$\bar{\mathbf{S}}_1 = \begin{bmatrix} \mathbf{s}_1 \\ \mathbf{s}_A \times \mathbf{s}_1 \end{bmatrix} \quad (\text{B.14a})$$

$$\bar{\mathbf{S}}_2 = \begin{bmatrix} \mathbf{s}_2 \\ \mathbf{s}_B \times \mathbf{s}_2 \end{bmatrix} \quad (\text{B.14b})$$

$$\bar{\mathbf{S}}_3 = \begin{bmatrix} \mathbf{s}_3 \\ \mathbf{s}_B \times \mathbf{s}_3 \end{bmatrix} \quad (\text{B.14c})$$

$$\bar{\mathbf{S}}_4 = \begin{bmatrix} \mathbf{s}_4 \\ \mathbf{s}_B \times \mathbf{s}_4 \end{bmatrix} \quad (\text{B.14d})$$

$$\bar{\mathbf{S}}_5 = \begin{bmatrix} \mathbf{s}_5 \\ \mathbf{s}_C \times \mathbf{s}_5 \end{bmatrix} \quad (\text{B.14e})$$

Equation (B.14) is the same with (4.10), and details can be found in Chapter 4.

$$\bar{\mathbf{S}} = \sum_{i=1}^5 (q_i \bar{\mathbf{S}}_i) \quad (\text{B.15})$$

Equation (B.15) is the same with (4.11).

$$\bar{\mathbf{S}}_r^T \delta \bar{\mathbf{S}} = 0 \quad (\text{B.16})$$

Equation (B.16) is the same with (4.12).

To see whether (B.17), which is the same with (4.9), is the reciprocal screw of

twist shown in (B.15), it needs to check the reciprocal relation of (B.16).

$$\bar{\mathbf{S}}_r = \begin{bmatrix} \bar{\mathbf{s}}_r \\ \mathbf{s}_B \times \bar{\mathbf{s}}_r \end{bmatrix} \quad (\text{B.17a})$$

$$\bar{\mathbf{s}}_r \perp \{\mathbf{s}_1 \times (\mathbf{s}_A - \mathbf{s}_B)\} \quad (\text{B.17b})$$

$$\bar{\mathbf{s}}_r \perp \{\mathbf{s}_5 \times (\mathbf{s}_C - \mathbf{s}_B)\} \quad (\text{B.17c})$$

A twist screw described in (B.17) can be written as Eq. (B.18).

$$\bar{\mathbf{S}}_r = \begin{bmatrix} \bar{\mathbf{s}}_r \\ \mathbf{s}_B \times \bar{\mathbf{s}}_r \end{bmatrix} \quad (\text{B.18a})$$

$$\bar{\mathbf{s}}_r = c \mathbf{N}_1 \times \mathbf{N}_2 \quad (\text{B.18b})$$

$$\mathbf{N}_1 = \{\mathbf{s}_1 \times (\mathbf{s}_B - \mathbf{s}_A)\} \quad (\text{B.18c})$$

$$\mathbf{N}_2 = \{\mathbf{s}_5 \times (\mathbf{s}_B - \mathbf{s}_C)\} \quad (\text{B.18d})$$

First, substitute (B.15), and (B.18a) into (B.16).

$$\bar{\mathbf{S}}_r^T \delta \bar{\mathbf{S}} = \delta q_1 \bar{\mathbf{S}}_r^T \bar{\mathbf{S}}_1 + \delta q_2 \bar{\mathbf{S}}_r^T \bar{\mathbf{S}}_2 + \delta q_3 \bar{\mathbf{S}}_r^T \bar{\mathbf{S}}_3 + \delta q_4 \bar{\mathbf{S}}_r^T \bar{\mathbf{S}}_4 + \delta q_5 \bar{\mathbf{S}}_r^T \bar{\mathbf{S}}_5 \quad (\text{B.19})$$

Then, substitute (B.14) into each term of the (B.19).

$$\bar{\mathbf{S}}_r^T \bar{\mathbf{S}}_1 = \begin{bmatrix} (\mathbf{s}_B \times \bar{\mathbf{s}}_r)^T & \bar{\mathbf{s}}_r^T \end{bmatrix} \begin{bmatrix} \mathbf{s}_1 \\ \mathbf{s}_A \times \mathbf{s}_1 \end{bmatrix} \quad (\text{B.20a})$$

$$\bar{\mathbf{S}}_r^T \bar{\mathbf{S}}_2 = \begin{bmatrix} (\mathbf{s}_B \times \bar{\mathbf{s}}_r)^T & \bar{\mathbf{s}}_r^T \end{bmatrix} \begin{bmatrix} \mathbf{s}_2 \\ \mathbf{s}_B \times \mathbf{s}_2 \end{bmatrix} \quad (\text{B.20b})$$

$$\bar{\mathbf{S}}_r^T \bar{\mathbf{S}}_3 = \begin{bmatrix} (\mathbf{s}_B \times \bar{\mathbf{s}}_r)^T & \bar{\mathbf{s}}_r^T \end{bmatrix} \begin{bmatrix} \mathbf{s}_3 \\ \mathbf{s}_B \times \mathbf{s}_3 \end{bmatrix} \quad (\text{B.20c})$$

$$\bar{\mathbf{S}}_r^T \bar{\mathbf{S}}_4 = \begin{bmatrix} (\mathbf{s}_B \times \bar{\mathbf{s}}_r)^T & \bar{\mathbf{s}}_r^T \end{bmatrix} \begin{bmatrix} \mathbf{s}_4 \\ \mathbf{s}_B \times \mathbf{s}_4 \end{bmatrix} \quad (\text{B.20d})$$

$$\bar{\mathbf{S}}_r^T \bar{\mathbf{S}}_5 = \begin{bmatrix} (\mathbf{s}_B \times \bar{\mathbf{s}}_r)^T & \bar{\mathbf{s}}_r^T \end{bmatrix} \begin{bmatrix} \mathbf{s}_5 \\ \mathbf{s}_C \times \mathbf{s}_5 \end{bmatrix} \quad (\text{B.20e})$$

Substitute (B.18b) into (B.20).

$$\bar{\mathbf{S}}_r^T \bar{\mathbf{S}}_1 = (\mathbf{s}_B \times c(\mathbf{N}_1 \times \mathbf{N}_2)) \cdot \mathbf{s}_1 + c(\mathbf{N}_1 \times \mathbf{N}_2) \cdot (\mathbf{s}_A \times \mathbf{s}_1) \quad (\text{B.21a})$$

$$\bar{\mathbf{S}}_r^T \bar{\mathbf{S}}_2 = (\mathbf{s}_B \times c(\mathbf{N}_1 \times \mathbf{N}_2)) \cdot \mathbf{s}_2 + c(\mathbf{N}_1 \times \mathbf{N}_2) \cdot (\mathbf{s}_B \times \mathbf{s}_2) \quad (\text{B.21b})$$

$$\bar{\mathbf{S}}_r^T \bar{\mathbf{S}}_3 = (\mathbf{s}_B \times c(\mathbf{N}_1 \times \mathbf{N}_2)) \cdot \mathbf{s}_3 + c(\mathbf{N}_1 \times \mathbf{N}_2) \cdot (\mathbf{s}_B \times \mathbf{s}_3) \quad (\text{B.21c})$$

$$\bar{\mathbf{S}}_r^T \bar{\mathbf{S}}_4 = (\mathbf{s}_B \times c(\mathbf{N}_1 \times \mathbf{N}_2)) \cdot \mathbf{s}_4 + c(\mathbf{N}_1 \times \mathbf{N}_2) \cdot (\mathbf{s}_B \times \mathbf{s}_4) \quad (\text{B.21d})$$

$$\bar{\mathbf{S}}_r^T \bar{\mathbf{S}}_5 = (\mathbf{s}_B \times c(\mathbf{N}_1 \times \mathbf{N}_2)) \cdot \mathbf{s}_5 + c(\mathbf{N}_1 \times \mathbf{N}_2) \cdot (\mathbf{s}_C \times \mathbf{s}_5) \quad (\text{B.21e})$$

To simplify (B.21), vector calculation equations in (B.22) needs to be applied.

$$\mathbf{A} \times (\mathbf{B} \times \mathbf{C}) = \mathbf{B}(\mathbf{A} \cdot \mathbf{C}) - \mathbf{C}(\mathbf{A} \cdot \mathbf{B}) \quad (\text{B.22a})$$

$$(\mathbf{A} \times \mathbf{B}) \cdot (\mathbf{C} \times \mathbf{D}) = (\mathbf{A} \cdot \mathbf{C})(\mathbf{B} \cdot \mathbf{D}) - (\mathbf{A} \cdot \mathbf{D})(\mathbf{B} \cdot \mathbf{C}) \quad (\text{B.22b})$$

Eq. (B.23) is calculated from the (B.21) by applying (B.22).

$$\begin{aligned}
\overline{\mathbf{S}}_r^T \overline{\mathbf{S}}_1 &= c \{ \mathbf{N}_1 (\mathbf{N}_2 \cdot \mathbf{s}_B) - \mathbf{N}_2 (\mathbf{N}_1 \cdot \mathbf{s}_B) \} \cdot \mathbf{s}_1 \\
&\quad + c \{ (\mathbf{N}_1 \cdot \mathbf{s}_A) (\mathbf{N}_2 \cdot \mathbf{s}_1) - (\mathbf{N}_1 \cdot \mathbf{s}_1) (\mathbf{N}_2 \cdot \mathbf{s}_A) \} \\
&= c \left[(\mathbf{N}_1 \cdot \mathbf{s}_1) \{ \mathbf{N}_2 \cdot (\mathbf{s}_B - \mathbf{s}_A) \} - (\mathbf{N}_2 \cdot \mathbf{s}_1) \{ \mathbf{N}_1 \cdot (\mathbf{s}_B - \mathbf{s}_A) \} \right] \\
&= c (\mathbf{N}_1 \times \mathbf{N}_2) \cdot \{ \mathbf{s}_1 \times (\mathbf{s}_B - \mathbf{s}_A) \}
\end{aligned} \tag{B.23a}$$

$$\begin{aligned}
\overline{\mathbf{S}}_r^T \overline{\mathbf{S}}_2 &= c \{ \mathbf{N}_1 (\mathbf{N}_2 \cdot \mathbf{s}_B) - \mathbf{N}_2 (\mathbf{N}_1 \cdot \mathbf{s}_B) \} \cdot \mathbf{s}_2 \\
&\quad + c \{ (\mathbf{N}_1 \cdot \mathbf{s}_B) (\mathbf{N}_2 \cdot \mathbf{s}_2) - (\mathbf{N}_1 \cdot \mathbf{s}_2) (\mathbf{N}_2 \cdot \mathbf{s}_B) \} \\
&= c \{ (\mathbf{N}_1 \cdot \mathbf{s}_2) (\mathbf{N}_2 \cdot \mathbf{s}_B) - (\mathbf{N}_2 \cdot \mathbf{s}_2) (\mathbf{N}_1 \cdot \mathbf{s}_B) \} \\
&\quad + c \{ (\mathbf{N}_1 \cdot \mathbf{s}_B) (\mathbf{N}_2 \cdot \mathbf{s}_2) - (\mathbf{N}_1 \cdot \mathbf{s}_2) (\mathbf{N}_2 \cdot \mathbf{s}_B) \} \\
&= 0
\end{aligned} \tag{B.23b}$$

$$\begin{aligned}
\overline{\mathbf{S}}_r^T \overline{\mathbf{S}}_3 &= c \{ \mathbf{N}_1 (\mathbf{N}_2 \cdot \mathbf{s}_B) - \mathbf{N}_2 (\mathbf{N}_1 \cdot \mathbf{s}_B) \} \cdot \mathbf{s}_3 \\
&\quad + c \{ (\mathbf{N}_1 \cdot \mathbf{s}_B) (\mathbf{N}_2 \cdot \mathbf{s}_3) - (\mathbf{N}_1 \cdot \mathbf{s}_3) (\mathbf{N}_2 \cdot \mathbf{s}_B) \} \\
&= c \{ (\mathbf{N}_1 \cdot \mathbf{s}_3) (\mathbf{N}_2 \cdot \mathbf{s}_B) - (\mathbf{N}_2 \cdot \mathbf{s}_3) (\mathbf{N}_1 \cdot \mathbf{s}_B) \} \\
&\quad + c \{ (\mathbf{N}_1 \cdot \mathbf{s}_B) (\mathbf{N}_2 \cdot \mathbf{s}_3) - (\mathbf{N}_1 \cdot \mathbf{s}_3) (\mathbf{N}_2 \cdot \mathbf{s}_B) \} \\
&= 0
\end{aligned} \tag{B.23c}$$

$$\begin{aligned}
\overline{\mathbf{S}}_r^T \overline{\mathbf{S}}_4 &= c \{ \mathbf{N}_1 (\mathbf{N}_2 \cdot \mathbf{s}_B) - \mathbf{N}_2 (\mathbf{N}_1 \cdot \mathbf{s}_B) \} \cdot \mathbf{s}_4 \\
&\quad + c \{ (\mathbf{N}_1 \cdot \mathbf{s}_B) (\mathbf{N}_2 \cdot \mathbf{s}_4) - (\mathbf{N}_1 \cdot \mathbf{s}_4) (\mathbf{N}_2 \cdot \mathbf{s}_B) \} \\
&= c \{ (\mathbf{N}_1 \cdot \mathbf{s}_4) (\mathbf{N}_2 \cdot \mathbf{s}_B) - (\mathbf{N}_2 \cdot \mathbf{s}_4) (\mathbf{N}_1 \cdot \mathbf{s}_B) \} \\
&\quad + c \{ (\mathbf{N}_1 \cdot \mathbf{s}_B) (\mathbf{N}_2 \cdot \mathbf{s}_4) - (\mathbf{N}_1 \cdot \mathbf{s}_4) (\mathbf{N}_2 \cdot \mathbf{s}_B) \} \\
&= 0
\end{aligned} \tag{B.23d}$$

$$\begin{aligned}
\overline{\mathbf{S}}_r^T \overline{\mathbf{S}}_5 &= c \{ \mathbf{N}_1 (\mathbf{N}_2 \cdot \mathbf{s}_B) - \mathbf{N}_2 (\mathbf{N}_1 \cdot \mathbf{s}_B) \} \cdot \mathbf{s}_5 \\
&\quad + c \{ (\mathbf{N}_1 \cdot \mathbf{s}_C) (\mathbf{N}_2 \cdot \mathbf{s}_5) - (\mathbf{N}_1 \cdot \mathbf{s}_5) (\mathbf{N}_2 \cdot \mathbf{s}_C) \} \\
&= c \left[(\mathbf{N}_1 \cdot \mathbf{s}_5) \{ \mathbf{N}_2 \cdot (\mathbf{s}_B - \mathbf{s}_C) \} - (\mathbf{N}_2 \cdot \mathbf{s}_5) \{ \mathbf{N}_1 \cdot (\mathbf{s}_B - \mathbf{s}_C) \} \right] \\
&= c (\mathbf{N}_1 \times \mathbf{N}_2) \cdot \{ \mathbf{s}_5 \times (\mathbf{s}_B - \mathbf{s}_C) \}
\end{aligned} \tag{B.23e}$$

From the simplified equations (B.23b-d), one can see that $\bar{\mathbf{S}}_r^T \bar{\mathbf{S}}_i = 0$ ($i = 2, 3, 4$) is satisfied. Finally, substitute (B.18c,d) into (B23a,e) to derive (B24).

$$\bar{\mathbf{S}}_r^T \bar{\mathbf{S}}_1 = c(\mathbf{N}_1 \times \mathbf{N}_2) \cdot \mathbf{N}_1 \quad (\text{B.24a})$$

$$\bar{\mathbf{S}}_r^T \bar{\mathbf{S}}_5 = c(\mathbf{N}_1 \times \mathbf{N}_2) \cdot \mathbf{N}_2 \quad (\text{B.24b})$$

Because $(\mathbf{N}_1 \times \mathbf{N}_2)$ is perpendicular to both vectors \mathbf{N}_1 and \mathbf{N}_2 , simplified results of $\bar{\mathbf{S}}_r^T \bar{\mathbf{S}}_1$ and $\bar{\mathbf{S}}_r^T \bar{\mathbf{S}}_5$ is zero. Therefore, $\bar{\mathbf{S}}_r^T \delta \bar{\mathbf{S}}$ is equal to zero.

APPENDIX C

VIRTUAL PRODUCT DEVELOPMENT FOR VALIDATION OF HIDDEN LINK CONCEPT

C.1 Overview

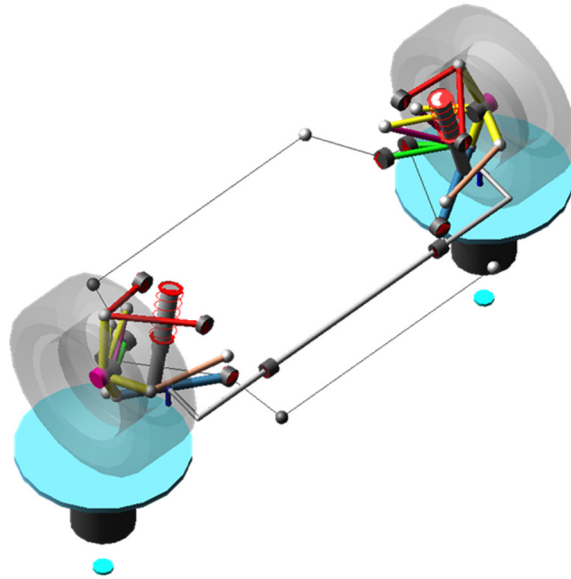
To see possibility of employing the hidden link type suspension system, virtual product development based on the CAE and prototype development is implemented in this thesis.

For the CAE validation, ADAMS/Car model is developed for half-car and full vehicle model. From the half-car model, rig test can be implemented for checking the kinematics and compliance behavior. By using the full-vehicle model, general vehicle dynamics test, such as lane change or constant radius circle test, can be implemented. Also, by developing the CAD model and manufacturing based on the 3D model, it is possible to see the interference between the composing components. In this 3D printer based prototype manufacturing procedure is conducted.

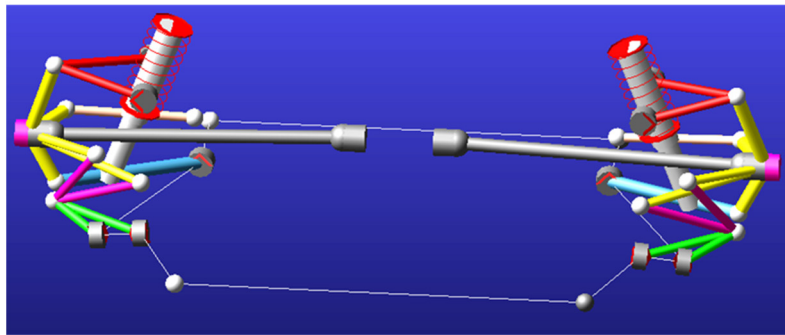
C.2 Virtual Product development process

Figure C.1 shows the half-car model of hidden link suspension model developed by the commercial software ADAMS/Car. Since there is no template for this newly designed topology, we developed a new template including hidden link module in this case. After checking the K&C (Kinematic and Compliance) behavior, vehicle dynamic analysis is also implemented based on the full vehicle model shown in Figure C.2 for several representative events, such as double lane change. Consequently, the possibility of applying the hidden link suspension is confirmed in the virtual development environment. In the near future, we have a plan to generate real-sized prototype for further consideration.

Next, the three-dimensional CAD model is also developed for rapid prototype model construction. Here, we applied 1/4-sized model with a ball-and-socket model. The details are shown in Figure C.3. The prototype model is also manufactured by the SLA (Stereo-Lithography Apparatus) method type 3D printer as shown in Figure C.4. From the additive manufacturing based rapid prototype model, we could confirm the possibility of operating the newly-designed mechanism with consideration of interference between suspension composing structures, including the hidden link module.

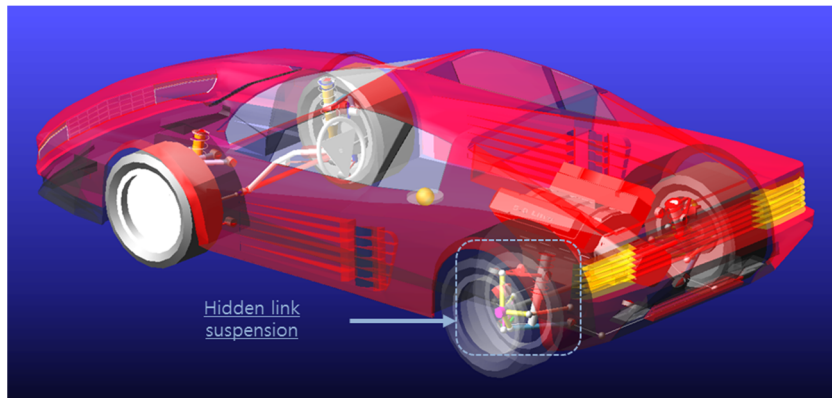


(a)

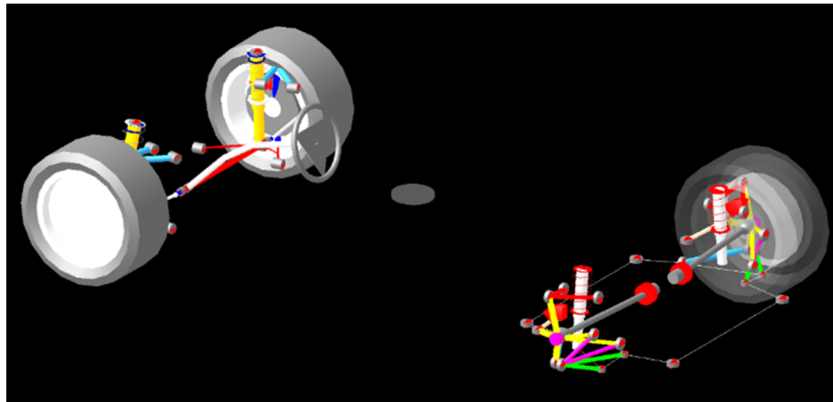


(b)

Figure C.1 Half car model of the hidden link suspension mechanism developed by the commercial software ADAMS/Car. (a) Suspension model with rig module, (b) without rig module.



(a)



(b)

Figure C.2 Full vehicle model of the hidden link suspension mechanism developed by the commercial software ADAMS/Car. (a) Chassis and car body, (b) with only chassis components.

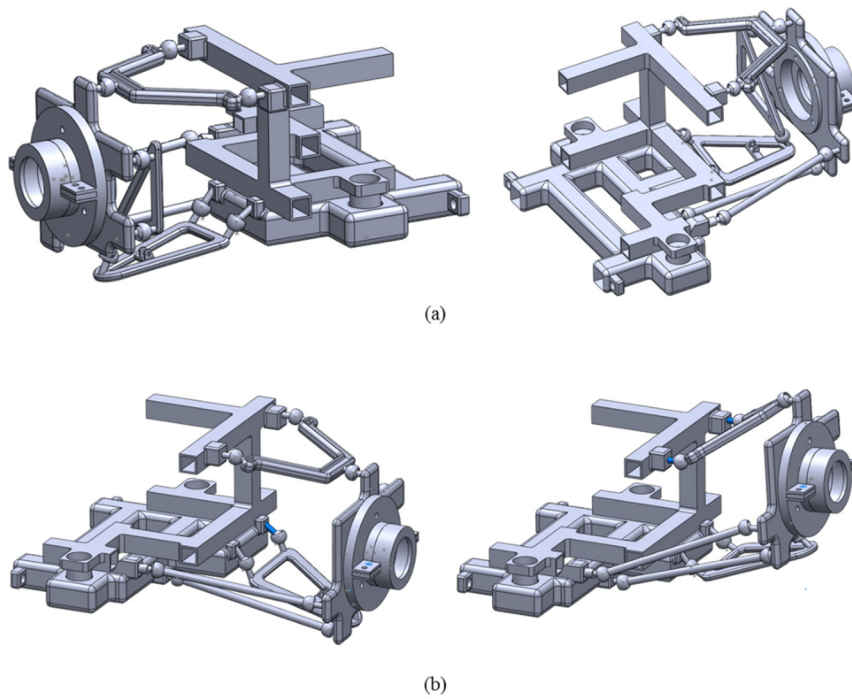
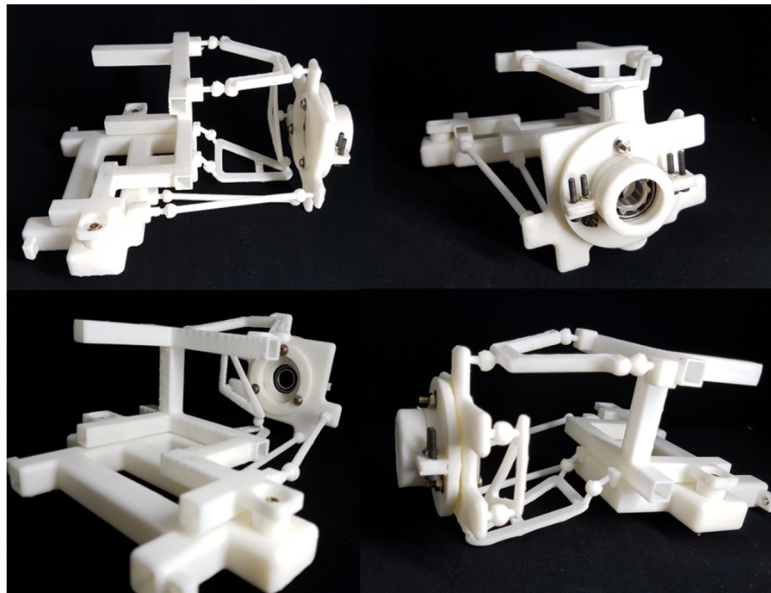
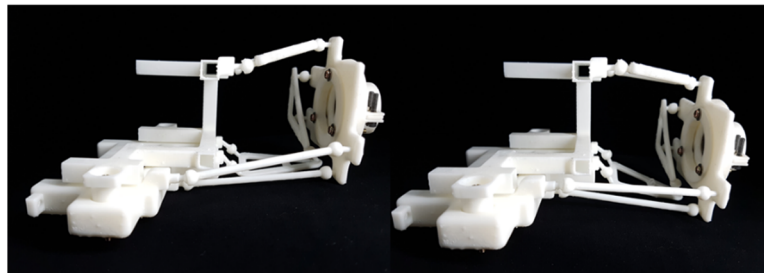


Figure C.3 (a) Developed 1/4-sized hidden link suspension CAD model and (b) its vertical stroke motion.



(a)



(b)

Figure C.4 (a) Prototype manufactured by the SLA type 3D printer (b) its vertical stroke motion.

REFERENCES

- [1] R.L. Norton, Kinematics and Dynamics of Machinery, Mcgraw hill higher education, New York, 2009.
- [2] F.E. Crossley, On an unpublished work of Alt, Journal of Mechanisms, 1 (1966) 165-170.
- [3] T. Mruthyunjaya, Kinematic structure of mechanisms revisited, Mech. Mach. Theory, 38 (2003) 279-320.
- [4] J. Uicker, A. Raicu, A method for the identification and recognition of equivalence of kinematic chains, Mech. Mach. Theory, 10 (1975) 375-383.
- [5] A. Ambekar, V. Agrawal, Canonical numbering of kinematic chains and isomorphism problem: min code, Mech. Mach. Theory, 22 (1987) 453-461.
- [6] S. Kota, S.-J. Chiou, Conceptual design of mechanisms based on computational synthesis and simulation of kinematic building blocks, Research in engineering design, 4 (1992) 75-87.
- [7] S.-J. Chiou, K. Sridhar, Automated conceptual design of mechanisms, Mech. Mach. Theory, 34 (1999) 467-495.
- [8] A.G. Erdman, Advanced mechanism design, 1984.
- [9] N.P. Suh, Axiomatic Design: Advances and Applications (The Oxford Series on Advanced Manufacturing), (2001).
- [10] C.W. Wampler, A.P. Morgan, A.J. Sommese, Complete solution of the nine-point path synthesis problem for four-bar linkages, J. Mech. Des., 114 (1992) 153-

159.

[11] J.L. Blechschmidt, J.J. Uicker, Linkage synthesis using algebraic curves, *Journal of Mechanisms, Transmissions, and Automation in Design*, 108 (1986) 543-548.

[12] S.N. Kramer, G.N. Sandor, Selective precision synthesis—a general method of optimization for planar mechanisms, *Journal of Engineering for Industry*, 97 (1975) 689-701.

[13] Y. Liu, J. McPhee, Automated type synthesis of planar mechanisms using numeric optimization with genetic algorithms, *J. Mech. Des.*, 127 (2005) 910-916.

[14] Y. Liu, J. McPhee, Automated Kinematic Synthesis of Planar Mechanisms with Revolute Joints#, *Mechanics Based Design of Structures and Machines*, 35 (2007) 405-445.

[15] M.P. Bendsøe, N. Kikuchi, Generating optimal topologies in structural design using a homogenization method, *Comput. Methods Appl. Mech. Eng.*, 71 (1988) 197-224.

[16] O. Sigmund, On the Design of Compliant Mechanisms Using Topology Optimization, *Journal of Structural Mechanics*, 25 (1997) 493-524.

[17] A. Kawamoto, M.P. Bendsøe, O. Sigmund, Articulated mechanism design with a degree of freedom constraint, *Int. J. Numer. Methods Eng.*, 61 (2004) 1520-1545.

[18] L. Krog, A. Tucker, M. Kemp, R. Boyd, Topology optimization of aircraft wing box ribs, 10th AIAA/ISSMO multidisciplinary analysis and optimization conference, 2004, pp. 2004-4481.

- [19] M. Cavazzuti, A. Baldini, E. Bertocchi, D. Costi, E. Torricelli, P. Moruzzi, High performance automotive chassis design: a topology optimization based approach, *Struct. Multidiscip. Optim.*, 44 (2011) 45-56.
- [20] L.L. Stromberg, A. Beghini, W.F. Baker, G.H. Paulino, Application of layout and topology optimization using pattern gradation for the conceptual design of buildings, *Struct. Multidiscip. Optim.*, 43 (2011) 165-180.
- [21] K. Besserud, N. Katz, A. Beghini, Structural emergence: architectural and structural design collaboration at SOM, *Architectural Design*, 83 (2013) 48-55.
- [22] O. Sigmund, A 99 line topology optimization code written in Matlab, *Struct. Multidiscip. Optim.*, 21 (2001) 120-127.
- [23] M.P. Bendsoe, O. Sigmund, *Topology optimization: theory, methods and applications*, Springer, Berlin, 2003.
- [24] J.D. Deaton, R.V. Grandhi, A survey of structural and multidisciplinary continuum topology optimization: post 2000, *Struct. Multidiscip. Optim.*, 49 (2014) 1-38.
- [25] J.-H. Zhu, W.-H. Zhang, L. Xia, Topology optimization in aircraft and aerospace structures design, *Archives of Computational Methods in Engineering*, (2015) 1-28.
- [26] S.I. Kim, Y.Y. Kim, Topology optimization of planar linkage mechanisms, *Int. J. Numer. Methods Eng.*, 98 (2014) 265-286.
- [27] S.I. Kim, S.W. Kang, S.M. Han, Y.-S. Yi, J. Park, Y.Y. Kim, Automated computational synthesis of suspension mechanisms: new design paradigm, in: P.E. Pfeffer (Ed.) *7th International Munich Chassis Symposium 2016 (chassis.tech plus)*,

ATZ lilve, 2016, pp. 457-474.

[28] S.I. Kim, S.W. Kang, Y.-S. Yi, J. Park, Y.Y. Kim, Topology optimization of vehicle rear suspension mechanisms, *Int. J. Numer. Methods Eng.*, Special Issue on Advanced Topology Optimization (2017).

[29] T.A. de Jong, Topology optimization of 3D linkages with application to morphing winglets, TU Delft, Delft University of Technology, 2016.

[30] C. Felter, O. Sigmund, Topology optimization of rigid body mechanisms, Master's Thesis, Department of Mechanical Engineering, Technical University of Denmark, (2003).

[31] A. Kawamoto, Generation of Articulated Mechanisms by Optimization Techniques, Danish Center for Applied Mathematics and Mechanics, Technical University of Denmark, 2004.

[32] A. Kawamoto, M.P. Bendsøe, O. Sigmund, Planar articulated mechanism design by graph theoretical enumeration, *Struct. Multidiscip. Optim.*, 27 (2004) 295-299.

[33] M. Stolpe, A. Kawamoto, Design of planar articulated mechanisms using branch and bound, *Mathematical programming*, 103 (2005) 357-397.

[34] A. Kawamoto, Path-generation of articulated mechanisms by shape and topology variations in non-linear truss representation, *Int. J. Numer. Methods Eng.*, 64 (2005) 1557-1574.

[35] Y.Y. Kim, G.-W. Jang, J.H. Park, J.S. Hyun, S.J. Nam, Automatic synthesis of a planar linkage mechanism with revolute joints by using spring-connected rigid block models, *J. Mech. Des.*, 129 (2007) 930-940.

- [36] M. Ohsaki, S. Nishiwaki, Generation of link mechanism by shape-topology optimization of trusses considering geometrical nonlinearity, *J. Comput. Sci. Tech.*, 3 (2009) 46-53.
- [37] S.J. Nam, G.-W. Jang, Y.Y. Kim, The spring-connected rigid block model based automatic synthesis of planar linkage mechanisms: numerical issues and remedies, *J. Mech. Des.*, 134 (2012) 051002.
- [38] S.W. Kang, S.I. Kim, Y.Y. Kim, Topology optimization of planar linkage systems involving general joint types, *Mech. Mach. Theory*, 104 (2016) 130-160.
- [39] S.M. Han, S.I. Kim, Y.Y. Kim, Topology Optimization of planar linkage mechanisms for path generation without prescribed timing, *Struct. Multidiscip. Optim.*, (accepted).
- [40] M. Ohsaki, Y. Kanno, S. Tsuda, Linear programming approach to design of spatial link mechanism with partially rigid joints, *Struct. Multidiscip. Optim.*, 50 (2014) 945-956.
- [41] H. Lipson, J.B. Pollack, Automatic design and manufacture of robotic lifeforms, *Nature*, 406 (2000) 974-978.
- [42] S. Coros, B. Thomaszewski, G. Noris, S. Sueda, M. Forberg, R.W. Sumner, W. Matusik, B. Bickel, Computational design of mechanical characters, *ACM Transactions on Graphics (TOG)*, 32 (2013) 83.
- [43] M. Langelaar, G.H. Yoon, Y.Y. Kim, F. van Keulen, Topology optimization of planar shape memory alloy thermal actuators using element connectivity parameterization, *Int. J. Numer. Methods Eng.*, 88 (2011) 817-840.

- [44] S.J. Moon, G.H. Yoon, A newly developed qp-relaxation method for element connectivity parameterization to achieve stress-based topology optimization for geometrically nonlinear structures, *Comput. Methods Appl. Mech. Eng.*, 265 (2013) 226-241.
- [45] G.H. Yoon, Y.Y. Kim, Topology optimization of material-nonlinear continuum structures by the element connectivity parameterization, *Int. J. Numer. Methods Eng.*, 69 (2007) 2196-2218.
- [46] B.S. Kim, H.H. Yoo, Unified synthesis of a planar four-bar mechanism for function generation using a spring-connected arbitrarily sized block model, *Mech. Mach. Theory*, 49 (2012) 141-156.
- [47] B.S. Kim, H.H. Yoo, Unified mechanism synthesis method of a planar four-bar linkage for path generation employing a spring-connected arbitrarily sized rectangular block model, *Multibody Sys. Dyn.*, 31 (2014) 241-256.
- [48] B.S. Kim, H.H. Yoo, Body guidance syntheses of four-bar linkage systems employing a spring-connected block model, *Mech. Mach. Theory*, 85 (2015) 147-160.
- [49] J.C. Heo, G.H. Yoon, Size and configuration syntheses of rigid-link mechanisms with multiple rotary actuators using the constraint force design method, *Mech. Mach. Theory*, 64 (2013) 18-38.
- [50] M. Ohsaki, S. Tsuda, Y. Miyazu, Design of linkage mechanisms of partially rigid frames using limit analysis with quadratic yield functions, *International Journal of Solids and Structures*, 88 (2016) 68-78.

- [51] K. Sedlacek, P. Eberhard, Topology Optimization of Large Motion Rigid Body Mechanisms With Nonlinear Kinematics, *Journal of Computational and Nonlinear Dynamics*, 4 (2009) 021011-021011~021018.
- [52] G.H. Yoon, J.C. Heo, Constraint force design method for topology optimization of planar rigid-body mechanisms, *Computer-Aided Design*, 44 (2012) 1277-1296.
- [53] J.C. Ryu, F.C. Park, Y.Y. Kim, Mobile robot path planning algorithm by equivalent conduction heat flow topology optimization, *Struct. Multidiscip. Optim.*, 45 (2012) 703-715.
- [54] R.N. Jazar, *Vehicle Dynamics: Theory and Application*, Springer, New York, 2008.
- [55] M.A. Crisfield, *Non-linear finite element analysis of solids and structures (Vol. 1)*, Wiley, New York, 1991.
- [56] P. Wriggers, *Nonlinear finite element methods*, Springer, 2008.
- [57] T.E. Bruns, Topology optimization by penalty (TOP) method, *Comput. Methods Appl. Mech. Eng.*, 196 (2007) 4430-4443.
- [58] A. Kawamoto, Stabilization of geometrically nonlinear topology optimization by the Levenberg–Marquardt method, *Struct. Multidiscip. Optim.*, 37 (2009) 429-433.
- [59] G.A. Kramer, *Solving geometric constraint systems: a case study in kinematics*, MIT press, Massachusetts, 1992.
- [60] T. Bruns, O. Sigmund, Toward the topology design of mechanisms that exhibit snap-through behavior, *Comput. Methods Appl. Mech. Eng.*, 193 (2004) 3973-4000.

- [61] M.A. Crisfield, An arc-length method including line searches and accelerations, *Int. J. Numer. Methods Eng.*, 19 (1983) 1269-1289.
- [62] R. Kemmler, A. Lipka, E. Ramm, Large deformations and stability in topology optimization, *Struct. Multidiscip. Optim.*, 30 (2005) 459-476.
- [63] E.J. Haug, Computer aided kinematics and dynamics of mechanical systems, Allyn and Bacon Boston, Boston, 1989.
- [64] K. Svanberg, The method of moving asymptotes—a new method for structural optimization, *Int. J. Numer. Methods Eng.*, 24 (1987) 359-373.
- [65] M.I. Frecker, G.K. Ananthasuresh, S. Nishiwaki, N. Kikuchi, S. Kota, Topological synthesis of compliant mechanisms using multi-criteria optimization, *J. Mech. Des.*, 119 (1997) 238-245.
- [66] J. Hetrick, S. Kota, An energy formulation for parametric size and shape optimization of compliant mechanisms, *J. Mech. Des.*, 121 (1999) 229.
- [67] T.E. Bruns, D.A. Tortorelli, Topology optimization of non-linear elastic structures and compliant mechanisms, *Comput. Methods Appl. Mech. Eng.*, 190 (2001) 3443-3459.
- [68] L.L. Howell, *Compliant Mechanisms*, Wiley-Interscience, New York, 2001.
- [69] C.B.W. Pedersen, T. Buhl, O. Sigmund, Topology synthesis of large-displacement compliant mechanisms, *Int. J. Numer. Methods Eng.*, 50 (2001) 2683-2705.
- [70] A. Saxena, G.K. Ananthasuresh, Topology synthesis of compliant mechanisms for nonlinear force-deflection and curved path specifications, *J. Mech. Des.*, 123

(2001) 33.

[71] P. Simionescu, M. Smith, Applications of Watt II function generator cognates, *Mech. Mach. Theory*, 35 (2000) 1535-1549.

[72] P. Simionescu, M. Smith, Four-and six-bar function cognates and overconstrained mechanisms, *Mech. Mach. Theory*, 36 (2001) 913-924.

[73] P.E. Nikravesh, *Planar Multibody Dynamics: Formulation, Programming and Applications*, CRC Press, Inc., Boca Raton, 2007.

[74] L.W. Tsai, *Mechanism design: enumeration of kinematic structures according to function*, CRC-Press, New York, 2000.

[75] P.A. Simionescu, D. Beale, Synthesis and analysis of the five-link rear suspension system used in automobiles, *Mech. Mach. Theory*, 37 (2002) 815-832.

[76] Y.-S. Yi, J. Park, K.-J. Hong, Design optimization of suspension kinematic and compliance characteristics, *SAE Technical Paper*, (2014) 2014-2001-0394.

[77] T.S. Liu, C.C. Chou, Type synthesis of vehicle planar suspension mechanism using graph theory, *J. Mech. Des.*, 115 (1993) 652-657.

[78] M. Raghavan, Number and dimensional synthesis of independent suspension mechanisms, *Mech. Mach. Theory*, 31 (1996) 1141-1153.

[79] D.L. Logan, *A first course in the finite element method*, Thomson, Toronto, 2007.

[80] B. Heißing, M. Ersoy, *Chassis handbook: fundamentals, driving dynamics, components, mechatronics, perspectives*, Springer Science & Business Media, Berlin, 2010.

- [81] W.F. Milliken, D.L. Milliken, Race car vehicle dynamics, Society of Automotive Engineers, Pittsburgh, 1995.
- [82] J.C. Dixon, Suspension geometry and computation, John Wiley & Sons, Chichester, 2009.
- [83] P. Zandbergen, A.G. Consolaro, Ford Motor Company's new rear suspension architecture for the global CD platform, Proceedings of the FISITA 2012 World Automotive Congress, (2013) 9-20.
- [84] M. Frantzen, W. David, M. Simon, L. Ohra-aho, Reduktion störender Lenkmomente, ATZ-Automobiltechnische Zeitschrift, 106 (2004) 434-440.
- [85] M. Simon, T. Gerhards, M. Frantzen, W. David, Suspension of the Ford focus RS 500, ATZ worldwide, 112 (2010) 48-51.
- [86] M. Raghavan, Suspension synthesis for N: 1 roll center motion, J. Mech. Des., 127 (2005) 673-678.
- [87] L.-W. Tsai, Robot analysis: the mechanics of serial and parallel manipulators, John Wiley & Sons, 1999.
- [88] J. Heo, U. Lee, S. Lee, Development of a method to compute the kingpin axis using screw axis theory based on suspension-parameter-measuring device data, Proceedings of the Institution of Mechanical Engineers, Part D: Journal of Automobile Engineering, 223 (2009) 519-531.
- [89] J. Lee, J. Shim, Validity and limitations of the kinematic roll center concept from the viewpoint of spatial kinematics using screw theory, International Journal of Automotive Technology, 12 (2011) 769.

- [90] J.K. Lee, Applications of screw axis theory to the behavior analysis of full-vehicle models and the synthesis of suspension system, Department of Mechanical Engineering Graduate School Korea University, (2007).
- [91] J.S. Kang, J.R. Yun, J.M. Lee, T.O. Tak, Elastokinematic analysis and optimization of suspension compliance characteristics, SAE Technical Paper, 1997.
- [92] J.R. Yun, The design of a new multi-link suspension system and the development of a dynamic model of vehicle for the application of four-wheel-steering, Department of Mechanical and Aerospace Engineering, Seoul National University, 2000.
- [93] G. Rozvany, M. Bendsoe, U. Kirsch, Layout optimization of structures, Applied Mechanics Reviews, 48 (1995) 41-119.

ABSTRACT (KOREAN)

기구 위상 및 치수 통합 합성 기법 개발과 이를 응용한 차량 현가 장치 개념설계

김 서 인

서울대학교 대학원

기계항공공학부

강체 기구(rigid-body mechanism)의 위상 최적화(topology optimization) 기법은 기본 설계 없이도 사용자에게 주어진 기구학적 요구조건을 만족하는 기본설계를 도출하기 위한 방법으로, 차량 및 항공 산업 분야 등에서 유용하게 적용 될 수 있는 새로운 설계 패러다임(paradigm)에 해당된다. 하지만, 기존 연구들은 단순한 평면 링크 기구(link mechanism)를 설계하는 수준에만 머무르고 있다.

본 연구에서는 평면과 공간 링크 기구의 위상과 형상을 동시에 설계하기 위한 새로운 정식화(formulation)가 구축되었다. 링크 기구의 위상 최적화 시에는 자유도(Degree-of-Freedom)를 미분 가능한 연속적인 값으

로 표현하는 정식화 기법이 필수적이다. 여기서 자유도란 기구 위치를 결정하기 위한 최소한의 액츄에이터(actuator) 수를 의미한다. 기존 연구들은 움직임 유연성(motion compliance) 및 하중 강성(load stiffness)이라는 두 가지 목적 함수를 적용하여 자유도가 남거나 부족해지는 부적절한 자유도 상황을 각각 통제하여왔다. 여기서 움직임 유연성이란 입력 운동과 같은 주어진 변위 가진(displacement excitation)에 대한 시스템의 유연성을 의미한다. 또한, 하중 강성이란 외부 저항력과 같은 힘 가진(force excitation)에 대한 시스템의 강성을 의미한다. 하지만, 이 방법은 다목적 함수 최적화(multi-objective optimization) 관점에서 서로 상반되는 두 목적 함수를 동시에 다루기 위한 가중치를 인위적으로 결정하기 어렵다는 문제점이 있었다. 반면, 본 연구에서 제안하는 일 전달 효율함수 기반의 통합된 자유도 통제 방식 하에서는 단일 목적함수만으로 자유도가 남거나 부족한 상황을 회피할 수 있기 때문에, 기존과 같은 두 목적함수의 선호도(preference) 조절 문제가 발생하지 않는다. 그러므로 기존과 달리 자유도 조건을 손쉽게 통제할 수 있고, 결과적으로 기존 연구보다 복잡한 시스템을 설계하는 것 또한 가능하다.

제안된 방법은 예제들을 통해 검증되었다. 평면 기구 설계 예제에서는 검증용 4절 링크 기구 및 차량 조향 (steering) 장치 문제가 검토되었다. 공간 기구 설계 예제에서는 제안하는 방법을 통해 차량의 현가

(suspension) 장치를 설계하였다. 현가 장치 설계 시, 보다 나은 해를 도출하기 위해 위상 및 형상 동시 최적화 기법을 적용하였다. 결과적으로, 통상적인 경우보다 작은 설계 공간이 주어졌을 때, 위상 및 치수 통합 합성 기법에 의해 새로운 형태의 현가 기구를 도출할 수 있었다. 새롭게 설계된 현가 장치의 거동 해석을 위해 나선축 이론(screw axis theory)을 도입하였는데, 특수한 모듈이 결과물에 포함되어 있고 그것이 기존의 링크(link)와 같은 역할을 수행한다는 점을 밝혀낼 수 있었다. 본 논문에서는 이와 같은 특성을 고려하여 새로운 현가 장치를 히든 링크 (hidden link) 현가 장치로 명명하였다. 해당 모듈 활용 시 현가 장치 설치 공간을 기존 멀티 링크 (multi-link) 방식보다 절약할 수 있음도 확인하였다.

본 논문의 연구 결과는 차량 산업 적용에 기구 위상최적화 기법을 성공적으로 적용한 첫 사례에 해당된다. 특히, 본 연구에서 보인 것처럼, 제안된 방법론은 완전히 새로운 개념설계를 통해 제품의 품질을 향상시키고자 하는 엔지니어들에게 새로운 통찰력을 제공할 수 있다. 향후, 제안된 링크 기구 설계 방법론은 차량 산업 외 다양한 실용 문제에서도 보다 진보된 기구 도출을 위해 적용 가능할 것으로 본다.

주요어: 강체 기구, 위상최적화, 차량 현가 장치, 히든 링크 현가 장치

학번: 2011-20691

